EXPERIMENTAL CHARACTERISATION OF BREAST TISSUES AND ITS APPLICATION TO A NUMERICAL MODEL OF A HEALTHY BREAST

by

JOSE LUIS CALVO GALLEGO

A thesis submitted in fulfilment of the requirements for the degree of

DOCTOR OF PHILOSOPHY

presented at the

ENGINEERING SCHOOL OF THE UNIVERSITY OF SEVILLE

supervised by the professors

JAVIER MARTÍNEZ REINA

and

JAIME DOMÍNGUEZ

December 2016

Nomenclature

Throughout this text, scalars, vectors and tensors are going to be used. For scalars, lowercase Greek and uppercase and lowercase italics letters are going to be used (i.e. t, α, J). For vectors referring to the material configuration, uppercase bold-face Latin letters (i.e. $\mathbf{N}$, $\mathbf{X}$) and for vectors referring to the current configuration, lowercase bold-face Latin letters (i.e. $\mathbf{n}$, $\mathbf{x}$). For second-order tensors in the reference configuration, uppercase bold-face Latin letters (i.e. $\mathbf{S}$, $\mathbf{E}$) and for second-order tensors in the spatial configuration, lowercase bold-face Greek or Latin letters (i.e. $\boldsymbol{\sigma}$, $\mathbf{e}$). For third-order tensors, uppercase bold-face calligraphic letters (i.e. $\boldsymbol{\mathcal{E}}$). For fourth-order tensors in the material configuration, uppercase blackboard Latin letters (i.e. $\mathbb{C}$) and for fourth order tensors in the spatial configuration, lowercase blackboard Latin letters (i.e. $\mathbb{c}$).

Symbol	Description
β_j^{∞}	Strain energy factor
$\boldsymbol{\Gamma}_j$	Tensor which determines the relaxation/creep behaviour
λ_a	Principal stretches, with $a = 1, 2, 3$
$\bar{\lambda}_a$	Modified principal stretches, with $a = 1, 2, 3$
ρ_0	Density in the reference configuration
ρ	Density in the current configuration
$\bar{\sigma}$	Recorded experimental Cauchy stress
$\tilde{\sigma}$	Treated experimental Cauchy stress
$\boldsymbol{\sigma}$	Cauchy stress tensor
$\boldsymbol{\sigma}_{\text{vol}}$	Volumetric part of the Cauchy stress tensor
$\boldsymbol{\sigma}_{\text{iso}}$	Isochoric part of the Cauchy stress tensor
$\bar{\boldsymbol{\sigma}}$	Fictitious Cauchy stress tensor
τ_i	Relaxation time constants
$\boldsymbol{\tau}$	Kirchhoff stress tensor
$\boldsymbol{\tau}_{\text{iso}}$	Isochoric part of the Kirchhoff stress tensor
$\bar{\boldsymbol{\tau}}$	Fictitious Kirchhoff stress tensor
Υ_j	Dissipative potentials
ϕ_*	Push-forward operation
ϕ^*	Pull-back operation
Ψ	Helmholtz free-energy function
Ψ_{vol}	Volumetric part of the strain energy function
Ψ_{iso}	Isochoric part of the strain energy function
$\Psi_{\text{vol}}^{\infty}$	Strain energy function describing the volumetric elastic response as $t \to \infty$
$\Psi_{\text{iso}}^{\infty}$	Strain energy function describing the isochoric elastic response as $t \to \infty$

Symbol	Description
$\Psi_{\mathrm{iso}\,j}$	Isochoric part of the strain energy function responsible for the j relaxation process
Ω_0	Initial or reference configuration
Ω	Current or deformed configuration
$\boldsymbol{a}_0$, $\boldsymbol{g}_0$	Fibre directions in the reference configuration
$\boldsymbol{a}$, $\boldsymbol{g}$	Fibre directions in the deformed configuration
$\mathbf{b}$	Left Cauchy-Green tensor
$\bar{\boldsymbol{b}}$	Modified left Cauchy-Green tensor
$\mathbf{C}$	Right Cauchy-Green tensor
$\bar{\boldsymbol{C}}$	Modified right Cauchy-Green tensor
$\mathbb{C}$	Elasticity tensor in material description
$\mathbb{C}_{\mathrm{vol}}$	Volumetric part of the elasticity tensor in material description
$\mathbb{C}_{\mathrm{iso}}$	Isochoric part of the elasticity tensor in material description
$\mathbb{c}$	Elasticity tensor in spatial description
$\mathbb{c}_{\mathrm{vol}}$	Volumetric part of the elasticity tensor in spatial description
$\mathbb{c}_{\mathrm{iso}}$	Isochoric part of the elasticity tensor in spatial description
$\bar{\mathbb{c}}^*$	Fictitious elasticity tensor in spatial description
$\mathcal{D}_{int}$	Internal dissipation
D	Compressibility constant
f	Fat volume ratio
$F(t)$	Force
$\mathbf{F}$	Deformation gradient tensor
$\bar{\boldsymbol{F}}$	Modified deformation gradient tensor
$G(t)$	Relaxation function
$\bar{G}(t)$	Reduced relaxation function
g_i	Prony constants
I_a	Invariants of $\mathbf{C}$, with $a = 1, 2, 3$
I_a	Pseudo-invariants of $\mathbf{C}$ and $\boldsymbol{a}_0 \otimes \boldsymbol{a}_0$ or $\boldsymbol{g}_0 \otimes \boldsymbol{g}_0$, with $a = 4, 5, 6, 7, 8$
$\bar{I}_a$	Modified invariants of $\mathbf{C}$, with $a = 1, 2, 3$
$\mathbf{I}$	Second-order unit tensor
$\mathbb{I}$	Fourth-order unit tensor
J	Volume ratio
$J(t)$	Creep function
p	Hydrostatic pressure
$\tilde{p}$	Modified hydrostatic pressure
$\mathbf{P}$	First Piola-Kirchhoff stress tensor
$\mathbb{P}$	Projection tensor
$\mathbf{Q}$	Rotation tensor
$\mathbf{Q}_j$	Non-equilibrium stress
$\mathbf{S}$	Second Piola-Kirchhoff stress tensor
$\bar{\mathbf{S}}$	Fictitious second Piola-Kirchhoff stress tensor
$\mathbf{S}_{\mathrm{vol}}$	Volumetric part of the second Piola-Kirchhoff stress tensor
$\mathbf{S}_{\mathrm{iso}}$	Isochoric part of the second Piola-Kirchhoff stress tensor
$\mathbf{S}_{\mathrm{vol}}^{\infty}$	Volumetric part of the second Piola-Kirchhoff stress tensor when $t \to \infty$
$\mathbf{S}_{\mathrm{iso}}^{\infty}$	Isochoric part of the second Piola-Kirchhoff stress tensor when $t \to \infty$
$\mathbf{S}_{\mathrm{iso}\,j}$	Isochoric part of the second Piola-Kirchhoff stress tensor corresponding to $\Psi_{\mathrm{iso}\,j}$
$\bar{\mathbf{S}}_j$	Fictitious second Piola-Kirchhoff stress tensor corresponding to the j relaxation process

Symbol	Description
t	Time
T^e	Elastic response function
$\mathbf{U}$	Displacement field vector in the material description
$\mathbf{u}$	Displacement field vector in the spatial description

Contents

Chapter 1

Introduction

1.1 Why studying the breast?

Breast cancer is by far the leading type of cancer in women in the world, regarding incidence, as well as mortality or 5-years prevalence. The figures are quite similar both in developed and underdeveloped countries. It comprises the 11.9% of all new cases of cancer in the world, the 2^{nd} in incidence after lung cancer, and the 25.1% of all female cancers, being the 1^{st} in incidence. It is the 5^{th} cause of cancer death overall and, although it is the most frequent cause of death by cancer in women in underdeveloped regions, in developed regions it is now the second one after lung cancer. Talking about prevalence, it occupies the 1^{st} position[1] [1, 2]. In table 1.1, the data for Spain and Europe are also presented. As can be seen, the figures are quite similar.

	Incidence				Mortality				5-years prevalence			
	Global		Women		Global		Women		Global		Women	
	%	Ranking	%	Ranking	%	Ranking	%	Ranking	%	Ranking	%	Ranking
Spain	11.7	4^{th}	29	1^{st}	6.1	3^{rd}	15.5	1^{st}	17.9	1^{st}	40.8	1^{st}
Europe	13.7	1^{st}	30	1^{st}	7.2	3^{rd}	16.3	1^{st}	20.2	1^{st}	41.7	1^{st}
World	11.9	2^{nd}	25.1	1^{st}	6.4	5^{th}	14.7	1^{st}	19.2	1^{st}	36.3	1^{st}

Table 1.1: Incidence, mortality and 5-years prevalence of breast cancer in Spain, Europe and the World[1].

In view of these statistics, it is normal that many scientists in the world, working in different fields, are concerned about breast cancer. On the one hand physicians, trying to improve prevention, detection and treatment of the disease. On the other hand, many other professionals researching and creating or improving tools to help physicians in the battle against the disease, for instance, researching in medicines or improving the imaging methods to facilitate the detection.

[1] All the statistics belong to 2012, the last actualization of GLOBOCAN (Estimated cancer incidence, mortality and prevalence worldwide, by the International Agency for Research on Cancer).

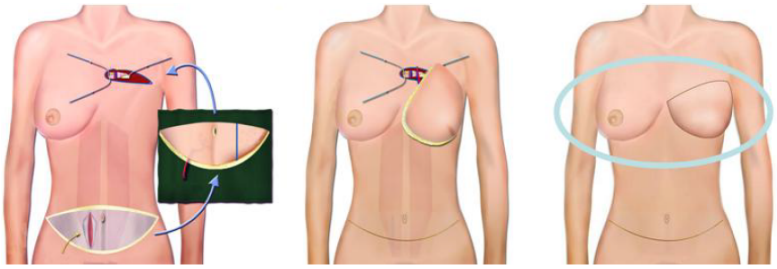

Figure 1.1: Reconstruction surgery with a DIEAP flap.

In the cases in which surgery is possible, the breast (or breasts) is partially or fully removed to eliminate the tumoral tissue and thus to prevent the reappearance of cancer. After surgery, women normally have serious psychological problems due to the loss of one or both breasts. When they look at themselves in a mirror, they feel they have lost a part of their bodies and that they are not attractive anymore. Moreover, they feel different to the other women. This is the reason why reconstruction surgeries are so important for the women health.

There are many reconstruction techniques, using implants or autologous tissue, but they all pursue the same aim: obtaining the most similar breast shape compared to the real one while minimizing the intervention and the rejection of the material used for the reconstruction.

In particular, there are several reconstruction techniques using autologous tissue that mainly differ on the area where the tissue is extracted from. So, the tissue can be obtained from the abdomen (DIEAP, deep inferior epigastric artery perforator flap; SIEA, superficial inferior epigastric artery flap; TRAM, transverse rectus abdominis myocutaneous flap), the back (LAT, latissimus dorsi flap; TDAP, thoracodorsal artery perforator flap) and other areas (lateral transverse thigh flap; SGAP, superior gluteal artery perforator flap, etc.).

If implants are going to be used, the procedure is called tissular expansion. After mastectomy, the physician reconstructs the skin layer introducing a breast tissue expander in order to periodically fill the expander over several months. When the skin has stretched enough, a second surgery is performed to extract the expander and introduce an implant. There are different implant shapes, from which the best is chosen according to the particular patient. Finally, the nipple and the mammary areola are reconstructed.

In general, surgeons prefer the flap reconstruction technique because it has many advantages against implants. Implants are indicated in the cases in which women do not have enough adipose tissue to conduct a reconstruction with autologous tissue. The main advantage of implants over flap reconstruction is a shorter and less complex surgery. However, the disadvantages are more numerous. First, the flap is tissue excised from the own patient (normally from de abdomen or the back), thus minimising rejection, whereas implants are a foreign body made of a silicon rubber shell filled with saline solution or silicone. Indeed, problems of rupture, deflation or capsular contracture are quite common in patients with implants. Also, implants are

less likely to look, feel and move like a natural breast. And very importantly, implants do not last forever. Normally, after 10 or 20 years they should be replaced, which implies more surgeries.

In any case, the majority of surgeons conduct this type of procedures based on their own experience more than in established guides, because of the lack of protocols. Therefore, the success of the surgery depends not only on the particular case and patient, as normal, but also in the surgeon's expertise. And here it comes the contribution of this thesis, a collaboration with the *Virgen del Rocío* University Hospital to help in the improvement of the reconstruction surgery. A group from this hospital is developing a virtual reality tool called VirSSPA (***Vir****tual* ***S****ervicio* ***S****anitario* ***P****úblico* ***A****ndaluz*) for the planning and improvement of surgeries, among which the breast reconstruction surgery is one of the most relevant types included in this programme. The surgeons from this hospital normally apply an autologous technique using adipose tissue and skin from the abdomen to reconstruct the breast. In a simplified way, the steps they follow to carry out the surgery are:

- Opening the scar made in the mastectomy surgery to partially or totally remove the breast. The surgeons draw some lines in the patient's skin to mark some important points, for example, the infra-mammary fold.
- Extraction of the abdominal flap.
  - The available tissue is that below the umbilicus. Surgeons try to leave a scar in the abdomen as low as possible, for aesthetic reasons.
  - Surgeons separate the adipose tissue, reaching the abdominal fascia. They only leave the arterial and venous connection to the flap, in order to minimize the time of ischemia.
  - They analyse the situation of the arteries and check if the artery is able to supply blood to all the flap. If there is a part in the tissue that is not well irrigated, it is eliminated.
  - The vessels are cut and blocked. From now on, ischemia starts.
  - The flap is weighted and wrapped in gauze with saline solution. At first, it is not known how much adipose tissue and skin are available.
  - During the rest of the surgery, the abdominal region is repaired and the wound is closed by some surgeons, while others continue working in the breast area.
- Circulatory anastomosis. The vessels of the flap are connected with the vessels of the breast in order to supply blood to the flap. Surgeons check that there is no blood leak and that the flap is well irrigated, eliminating the tissues which are not.
- Breast reconstruction.

Figure 1.2: Breast implants with different shapes.

- The whole flap is introduced inside the space between the skin and the pectoral muscle and the shape of the breast is checked.

- An iterative procedure starts in which the surgeons cut some parts of the flap or open more space until they are satisfied with the shape of the breast. If possible, the reconstructed breast is compared with the healthy one. In case both breasts were removed, the aim is to make both symmetric and with the best shape possible.

- The surplus skin of the flap is cut off and the remaining skin is sutured to the chest.

In case the woman is very thin and she has not enough adipose tissue to reconstruct the breast, it is not possible to use autologous tissue, so the breast is reconstructed using the tissular expansion.

As introduced previously, the main problem surgeons have in any reconstruction surgery is that the final shape of the breast is almost completely dependent on the expertise of the surgeon. And this is even more critical with the autologous methodology. Working with implants, surgeons have a set of available accepted implants with a specific shape that somehow mimic the breast shape (see figure 1.2). However, in reconstruction surgeries with flaps, they do not have a predefined shape but they have to reproduce it with the tissue they have from the abdomen. Moreover, the extracted tissue is highly deformable, so it is not easy to handle and, more precisely, to estimate the quantity and shape needed to suitably reconstruct the breast. As a consequence, the own expertise and skills of the surgeon are even more important when using flaps than in implant reconstruction surgery. Also, sometimes more than one surgery is needed in order to correct or improve the shape of the breast.

It would be very helpful for the physicians to have some tools to make the procedure less heuristic and more deterministic. And this is the principal aim this work is focused on.

1.2 Motivation

As said above, the principal aim of this thesis is to help physicians in their work with the breast. To date the problem is that nobody has been able to correctly simulate the position change from supine to prone, to the best of the author's knowledge. From supine to standing up position neither, but the first one is considerably more complicated as the deformations are higher. That is to say, the information available in the literature about breast biomechanics, including finite element (FE) models, material parameters, boundary conditions, etc., are not enough to reproduce this apparently easy simulation. Obviously, it is not easy at all, because it involves the complex anatomy of the breast, but apart from this, not much is known about how the different types of tissue are interacting with each other during that deformation. Many authors have worked in the field of breast biomechanics, constructing FE models for different applications: to predict the location of a tumour [3, 4], to simulate the compression of the breast between two plates as in a mammography [3, 5, 6, 7, 4], for image registration, normally based also in compression [8, 9, 10, 11, 12, 13, 14, 15], to simulate gravity loading [16, 17, 18, 19, 20], to simulate a prosthesis insertion for augmentation mammoplasty [21], etc. Some authors have worked trying to determine the reference configuration of the breast, e.g., the shape the breast would have if not subjected to any load [22, 16, 6, 20, 23].

Comparing these models with the reality, none of them provides reliable results. Moreover, they are normally used for a certain application, but when they are used to simulate a different scenario, they do not work. Pérez del Palomar [18] and Zain-Ul-Abdein et al. [20] validate their models measuring the distance between some points of the model. But simply seeing their deformed shapes with the naked eye, it is clear that they are far from the real deformation. Many authors validate their models using a simulation of a compression of the breast and comparing the deformed shape with a real image [3, 24, 7, 14, 4], but this deformation is obtained imposing displacements in the contact between the breast and the plates and considering the materials as incompressible. Therefore, it was expected that the deformed configurations were close to reality, provided that they are comparing displacements and not stresses. Anyway, none of the material parameters or models that all these works suggest is valid to simulate its position change under gravity loads. The goal should be to try to construct a more versatile model, which would be able to mimic the real behaviour of the breast in general conditions, such as the change in position between supine and prone.

1.3 Objective of the thesis

Our aim is to shed light on the use of a computational FE model to reproduce the behaviour of the healthy breast and particularly to obtain its deformed shape under gravity loads in different positions. The importance of this work lies in the fact that this is the first step to develop further models of the breast, such

us diseased breasts or simulation of surgical procedures. In order to develop a model of the breast for any application to help clinicians in their daily work, it is crucial to understand how the breast behaves internally in the normal conditions, to be able to extend the model to more complex cases. Once the healthy breast FE model is constructed and validated, it is possible to add characteristics or change the properties of the tissue, to see how this new model behaves and to compare it to the healthy breast model, for instance, a breast with a tumour inclusion. It can also be helpful in the field of image analysis to track certain points in the images or to compare images in different positions or conditions. Regarding the breast reconstruction, having a validated healthy breast model is the first step in the process of simulating the surgery. Subsequently, the healthy model can be modified to reproduce the reconstructive surgery and it is also possible to optimize some parameters in the model (quantity of adipose tissue, shape, skin tension, etc.) in order to make the behaviour similar to the healthy one.

To develop a FE model of the healthy breast, it is key to correctly characterise the mechanical properties of the breast tissues, which is then another important objective of this work. The abdominal adipose tissue will also be characterised, what can be useful for the reconstructive surgery simulation and, in general, for any other simulation conducted in the abdomen. Moreover, assuming the properties assessed here for the adipose tissue of the abdomen as valid for other regions, the applications could be quite numerous.

1.4 Contents of the work

To develop the FE model of the healthy breast it is necessary to define its geometry, the load and displacement boundary conditions, the mechanical properties of the tissues involved and the interaction between these tissues. Therefore, this thesis can be divided in three big parts: an anatomical study of the structures and tissues which compose the breast, an experimental work in which the properties of the tissues are determined and a computational work in which the FE model is constructed and the simulations carried out. All these parts are explained subsequently divided into chapters.

In chapter 2, the anatomy of the female breast is shortly presented. The different types of tissue which compose it are described, as well as their distribution and structure. Some methods to determine the fat proportion in the breast are also included. Finally, breast cancer is shortly introduced.

In chapter 3, some fundamental concepts of Nonlinear Continuum Mechanics needed to understand this work are presented. This chapter is not intended to be a comprehensive text. Only the most important concepts are reminded. Some mathematical developments which are used in the subsequent chapters are also presented.

Chapter 4 is about the mechanical properties of breast tissues. First, the previous experimental studies are described. Then, a homogenization procedure for the mixture of fat and glandular tissue is presented. Finally, the experimental test conducted is explained, including the test protocol, the algorithm developed

to fit the experimental curves and the results obtained.

Chapter 5 is devoted to the FE models of the breast. As in chapter 4, the most relevant literature is introduced first. Then, the construction of the model is explained as well as the method to validate it. Finally, the different models are presented, explaining the differences between them and their performance to obtain the real breast deformation.

In chapter 6, the thesis is summarised and the main conclusions extracted. The original contributions of this thesis and the future works are also presented.

Appendix A includes the procedure to obtain the analytical stress in the QLV formulation. It implies a high number of integrals which have not been included in the main text for clarity.

Finally, in appendix B, the safety manual developed for the Biomechanics Laboratory of the Department of Mechanical Engineering is attached. This manual was mainly made to work with human tissue specimens.

Chapter 2

The female breast

In this chapter, the anatomy of the female breast is shortly presented. Knowing the inner structure of the breast, the tissues which compose it and their distribution is of great importance to understand how the breast is deformed. Moreover, this knowledge is the starting point to develop a computational model of the breast. When modelling a biological system in a computational framework, the modeller should make some assumptions and simplifications through the process, relating the boundary conditions, the mechanical properties of the materials, the connections between them, etc. It is very important to always keep in mind the real anatomy, in order to know at any point if the subsequent simplifications and assumptions are correct, or at least, suitable. Finally, breast cancer is shortly introduced.

2.1 A global picture

Breasts or mammary glands are the distinctive characteristic of mammals. In humans, these organs cover the female chest, but are not normally developed in men. The female breast is an organ which is present in the women's body with a clear purpose: the breastfeeding of their children.

The breast is located overlaying the women's chest. It extends inferiorly from the second or third rib to the inframammary fold, which is approximately about the level of the sixth or seventh rib. Laterally, it extends form the sternum to the anterior axillary line. The extension into the axilla, known as the glandular Tail of Spence, is highly variable between subjects. The posterior face of the mammary gland is delimited by the fasciae of the pectoralis major, serratus anterior, external abdominal oblique and rectus abdominis muscles. The anterior part is covered by the skin [25, 26, 27, 28].

The female breast is mainly composed of glandular tissue, fat, connective tissue and skin. There also exist nervous tissue innerving the breast and blood vessels irrigating it. The glandular tissue is formed by lobules which are connected to the nipple through the lactiferous ducts in a radial arrangement. These lobules are separated by connective tissue and some fat is intermingled between them. The rest of the fat

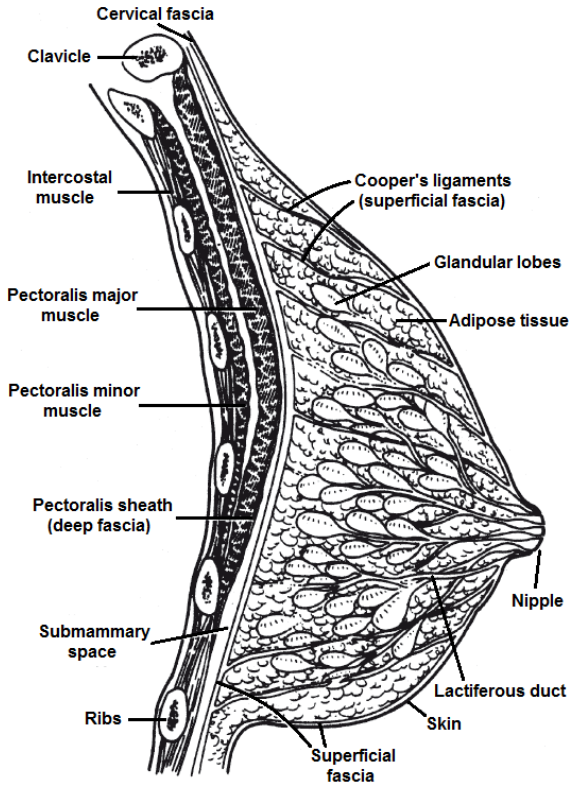

Figure 2.1: Global view of the female breast (adapted from [26]).

is surrounding the glandular tissue. There is some more connective tissue in the interface between the fat and the muscles, between the fat and the skin, and as ligaments inside the breast which are called Cooper's ligaments (suspensory ligaments). Finally, the skin is externally covering the organ.

The mammary development is initially identical in males and females. It starts approximately in the 4^{th} - 6^{th} week of gestation with the appearance of the milk lines (ectodermal thickening) on the ventral area. It extends from the axilla to the medial thigh (figure 2.2). In humans, the proximal and distal parts of the milk lines become atrophied while the pectoral part is the one responsible of the genesis of the breast. Inherited disorders may appear in 1% of women, as the development of an additional breast (polymastia) or a supernumerary nipple (polythelia). They can also appear in men. Once the milk lines have been created, during the remainder of gestation, they start to proliferate forming the lactiferous ducts. The areola is created during the 5^{th} month.

At birth, the breast, identical in men and women, is composed of radially arranged mammary lobes connected to the nipple through lactiferous ducts. This nipple is a little hollow formed by some Montgomery glands. Just after birth, the breasts may be active (with secretion of milk) due to the mother's hormones. Then the mammary activity is stopped until puberty. Shortly after birth, the nipple is everted due to the proliferation of the mesoderm, and the pigmentation of the areola increases.

In men, after birth, there is little mammary development. The presence of testosterone leads to the

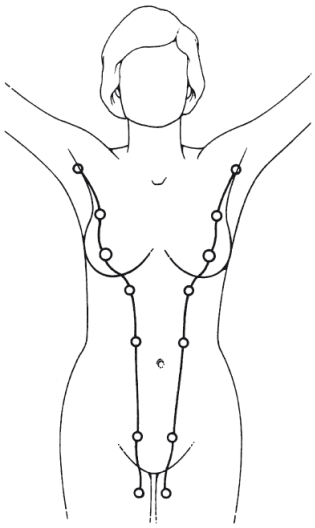

Figure 2.2: Milk lines (adapted from [26]).

involution of the mammary gland. However, in female, the breast continues developing due to the action of hormones. Three phases can be differentiated. In the first one, the stroma and glandular tissue of the breast slowly grow from the birth to the puberty, but no lobular growing takes place. Then, from puberty to approximately 20 years old, there exists a fast growth because of the development of fat and connective tissue, but also due to the thickening of the ductal system. This phase takes place under the effect of estrogens, growth hormone and prolactin. Finally, when pregnancy occurs the breasts reach their functional state and, under the influence of progesterone, estrogens, prolactin and lactogen, the development is completed. They become secretory alveoli and start to accumulate the necessary substances to generate milk in the postpartum period. When nursing is abandoned, the alveoli return to their non-functioning state. By the age of 40 years the mammary glands start to atrophy. Then the glandular lobes begin to be replaced by connective tissue and fat.

2.2 Adipose tissue

Adipose tissue is a loose connective tissue in which the adipocytes are the main cellular components. Adipocytes play a fundamental role in energy homeostasis. To survive, the human body should assure a constant energy contribution, despite of the fact that the availability of nutrients from the exterior may be variable. To compensate the energy demand of the body when there is not enough energy intake, the adipose tissue is able to store energy in an efficient way. The energy is stored in the lipid droplets as triglycerides (triacylglycerols). When food intake is higher than waste (in terms of energy), the excess is stored in the adipocytes. The triglycerides are the most concentrated way of storing energy in the human body. Moreover, the adipocytes have another functions besides the storing one. They secrete paracrine and endocrine

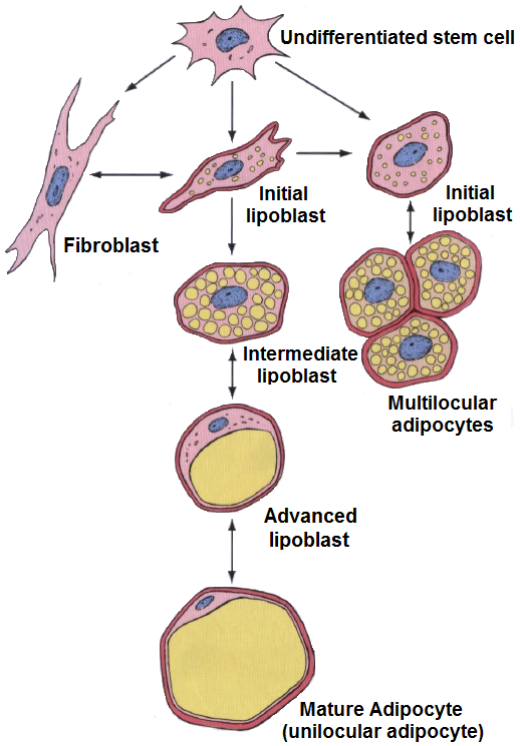

Figure 2.3: Development of an adipocyte (adapted from [27]).

substances to regulate the energy metabolism. The fat also has a structural function, serving as a padding to protect other organs.

There are two types of adipose tissue: white (unilocular) and brown (multilocular). The names come from the aspect that the cells have under the microscope and the color of the tissue when it is fresh. The white adipose tissue is predominant in the human body. The brown one is present during the fetal stage, but its quantity decreases along the first ten years after birth.

The unilocular adipose tissue forms a subcutaneous layer. It has an important isolating function. In the body it is normal to find big amounts of this adipose tissue in the abdominal region, the gluteal area, the axilla and the thigh. In both sexes the pectoral region is a preferential area to store fat. In fact, the fat is the main component of the non lactating breast. The origin of these adipocytes is an undifferentiated mesenchymal stem cell (figure 2.3). They have a spheroidal shape when they are isolated, but become an oval or a polyhedron when grouped. The big size of these cells is due to the storage of lipids, which causes the movement of the nucleus towards the border and its flattening. They are surrounded by reticular fibres (type III collagen) generated by them (figure 2.4). Moreover, the adipose tissue has a high blood supply, with many capillaries within its structure.

The amount of white adipose tissue in the body is regulated by two physiological systems. The first one, related with the regulation of weight in the short-term, controls the appetite and the daily metabolism. The second one, related with the regulation of weight in the long-term, controls the appetite in a continuous way

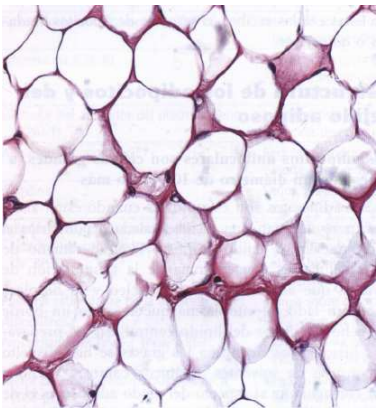

Figure 2.4: Adipocytes (adapted from [27]).

(during months or years).

The cells of the multilocular adipose tissue are smaller than those of the unilocular one. The nucleus of the multilocular adipocyte is eccentric but not flattened as in the unilocular one. They also derive from undifferentiated mesenchymal stem cells (figure 2.3).

In the breast, the fat (as said before, white adipose tissue) is surrounding the glandular tissue and filling the spaces between the lobes. The amount of fat in the breast is highly variable. It is responsible for the main part of the volume, shape and consistency of the breast. The percentage of body fat has an influence on the amount of adipose tissue in the breast, although it seems that some women, independently of their body fat, are more prone to accumulate fat in their breasts. The breasts with a higher percentage of fat are softer, while those with a higher percentage of glandular tissue are normally firmer and nodular. The amount of fat in the breast is increased once the glands start to atrophy after lactation and menopause.

2.3 Glandular tissue

Mammary glands are modified apocrine sweat glands (sudoriparous glands) which are developed due to the action of sex hormones. The mature inactive breast is composed of $15 - 20$ irregular lobes of ramified tubuloalveolar glands. The lobes, separated from each other by fibrous connective tissue, have a radial distribution starting from the nipple. Around 20 main lactiferous ducts ($2 - 4.5\,mm$ in diameter) drain the mammary lobes to the nipple. Each lobe is subdivided into little lobes ($200 - 600\,\mu m$), called terminal duct lobular units (TDLU) or lobules, composed of hundreds of secretory acini each one of which is connected to the lactiferous ducts through individual interlobular ducts ($40 - 60\,\mu m$ in diameter) [27, 29, 30]. All the system is inside the connective stroma and the adipose tissue.

The nipple and the areola are highly pigmented in contrast to the surrounding skin and a little bit wrinkled. Beneath the skin, there are smooth muscle fibre bundles arranged radially and circumferentially, and in a longitudinal direction along the lactiferous ducts. These muscle fibres are responsible for the erection

of the nipple in response to different stimuli. The areola has sebaceous glands, sweat glands and modified mammary glands (Montgomery glands). These glands, which have an intermediate structure between the sweat glands and the mammary glands, produce little lumps in the skin of the areola. The lactiferous ducts end in the nipple through a small pore. Under the areola, each duct has a dilated portion called lactiferous sinus.

When the mammary glands are inactive, the glandular component is limited and it mainly consists of ducts. During menstruation, and principally when the ovulation is about to start, secretory cells get bigger and ducts get wider, due to the action of oestrogen. During pregnancy, glandular tissue suffers some changes and fat and connective tissue are decreased.

2.4 Connective tissue

In the breast there are several structures made from connective tissue. The breast is developed and contained inside some supporting layers of the superficial fascia. The superficial layer of the superficial fascia is located near the skin, and is not always differentiated from it. The superficial layer of the superficial fascia is the external layer which covers the breast parenchyma. A variable amount of fat can be found between the dermis and the parenchyma. The deep layer of the superficial fascia is on the posterior surface of the breast. Some loose connective tissue is between the deep layer of the superficial fascia and the deep fascia which is covering the pectoralis mayor muscle, the rectus abdominis muscle, the serratus anterior muscle and the external abdominal oblique muscle (see figure 2.1).

The deep layer of the superficial fascia is pierced by some fibrous supports, called Cooper's ligaments, and by blood vessels, nerves and lymph vessels. Cooper's ligaments connect the deep layer of the superficial fascia and the skin which covers the breast, passing through all the breast. These suspensory ligaments are connected to the deep muscle fascia. Due to the fact that these ligaments are not tense, they allow the movement of the breast over the deep muscle fascia. These ligaments can be stretched and elongated because of pregnancy, ageing or fluctuations in weight.

The loss of the stiffness of these connective tissues contributes to the ptosis of the breast.

2.5 Skin

The skin is the biggest organ in the body. It is composed of two main layers (figure 2.5):

- The epidermis, formed by a keratinized stratified epithelium which is constantly growing though it always maintains its normal thickness due to the desquamation process (skin peeling).
- The dermis, composed of a dense connective tissue to provide mechanical support.

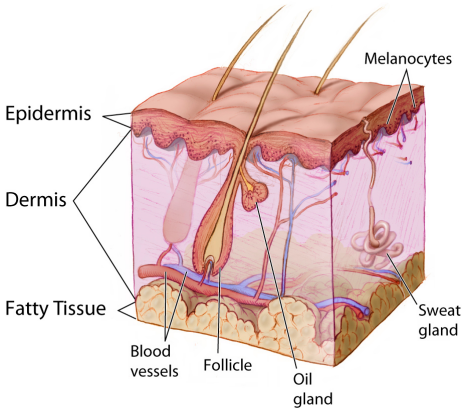

Figure 2.5: Layers of the skin.

The skin is involved in many functions and processes of the human body:

- It is a protection barrier against physical, chemical or biological agents from the surroundings.
- It provides immune information.
- It takes part in the body temperature homeostasis by regulating the heat exchange and the loss of water.
- It sends information about the surroundings obtained through the senses.
- It has endocrine functions.
- It plays a role in the excretion.

The thickness of the skin varies from less than $1mm$ to more than $5mm$ depending on the body region. Obviously, there are two regions in the body where the skin is clearly different: the palm of the hands and the sole of the feet. These regions are subjected to intense friction, they do not have hair and they have a much thicker epidermis than in any other part of the body.

In the breast, the quality, thickness and elasticity of the skin have a big influence in its appearance. The skin is influenced by hormonal changes, weight variations, gravity and ageing, which can cause a reduction in the thickness or a loss of elasticity. Stretch marks normally appear after a weight loss or a labour.

2.6 Methods to determine the fat proportion in the breast

Knowing the fat proportion in the breast is important for many reasons. The main one is based on the fact that breast tissue density has been identified as an important risk factor for cancer development and its analysis is useful for quantitative mammographic assessment. Moreover, for many surgeries it is useful to have an estimation of the fat proportion beforehand. This is linked to the availability of assessing the fat

volume ratio within the breast in a straightforward way, at least approximately. Several techniques exist to measure that fat volume ratio.

Visual assessment through mammography images is probably the simplest one, but it can only provide a qualitative measurement. With this technique an individual can be sorted out into categories, e.g. 0-25%, 25-50%, 50-75% and 75-100% [31]. The accuracy of the segmentation can be easily increased if some mathematical algorithms are applied [32, 31]. With the use of Magnetic Resonance (MR) imaging and tissue segmentation the accuracy can be increased further, though paying a high price in manipulation and computation time [33]. Depending on the particular application and on the desired accuracy, one of these methods or another will be chosen. For some purposes, a quick visual assessment of the fat volume ratio through mammography will be enough, whereas in other cases, a higher accuracy will be needed.

These methods to determine the fat proportion will be key in the development of a homogenized model for the mixture of fat and fibroglandular tissue in the breast, which will be introduced later in this document in section 4.2.

2.7 Breast cancer

There are some different types of cancer. They can be classified based on how the cancer cells look like under the microscope. The majority of cancers are carcinomas, a type of cancer which starts in the epithelial cells. In fact, breast cancers are often a type of carcinoma called adenocarcinoma, starting in the glandular tissue. There are other types such as sarcomas which start in the cells of fat, muscle or connective tissue. Sometimes, a breast tumour can be a combination of different types or it is even possible to develop a cancer without forming a tumour at all. The most frequent breast cancers are:

- The ductal carcinoma in situ (DCIS; intraductal carcinoma), a type of cancer in which the cells in the ducts change to look like cancer cells. The difference with an invasive cancer is that the tumoral cells do not spread through the walls of the ducts into the surrounding tissue of the breast. There is no way to know for sure which ones will become invasive and which ones will not. Nearly all women diagnosed of a DCIS can be cured. See figure 2.6.

- The invasive ductal carcinoma (IDC) is the most common type of breast cancer. It starts in the ducts, passes through the wall of the ducts and spreads into the surrounding fatty tissue. From that moment on, the cancer can metastasize (spread to other parts of the body) through the lymphatic system and the bloodstream. See figure 2.6.

- The invasive lobular carcinoma (ILC) is similar to the IDC, but starting in the lobules which produce the milk. It can easily metastasize too. It is more difficult to detect in a mammogram than IDC. (Figure 2.6).

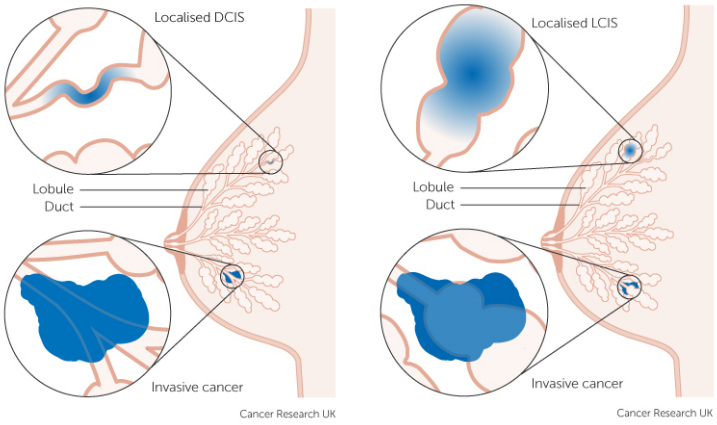

Figure 2.6: Left: Ductal carcinoma in situ and invasive ductal carcinoma. Right: Lobular carcinoma in situ and invasive lobular carcinoma [34].

Figure 2.7: Paget's disease of the breast.

There are some other types of cancer, less common than the previous ones:

- In the inflammatory breast cancer (IBC), the cancer cells block the lymph vessels making the skin look red and feel warm. It is normally mistaken for an infection known as mastitis. It is difficult to see it in a mammogram and to detect it in an early stage; therefore it has a worse prognosis (prediction) than IDC or ILC.

- The Paget's disease starts in the milk ducts and spreads to the nipple and the areola. The skin of the nipple and areola looks red and scaly, with areas of bleeding or oozing. Paget disease is almost always associated with either DCIS or IDC. If the biopsy shows a DCIS, the prognosis is better than revealing a IDC.

- The Phyllodes tumour (cystosarcoma phyllodes) is a very unusual tumour developed in the connective tissue of the breast. They are normally benign but in rare occasions may be malignant.

- The angiosarcoma starts in blood cells or lymph vessels. It rarely happens in the breast, but when it does, it tends to grow and spread quickly and may bring complications [35].

Chapter 3

Basic concepts of Nonlinear Continuum Mechanics

3.1 Introduction

Continuum Mechanics is a very useful tool in many engineering fields, and in particular, in the Biomechanics field. It permits to model a body as a continuum, which broadly means that every property or function is defined in every point of the body as a continuous function. It allows averaging these properties and there is no need to go deep inside the microstructure to model every detail of the body, simplifying enormously the modelling and computation processes. Even though nowadays there is a tendency to model and understand what is happening in the microstructure, Continuum Mechanics continues being a powerful tool due to two main reasons: the lack of knowledge about how to model many microstructures and how they behave, and the computational costs of simulating a process in the macro level taking into account what is happening in the micro or nano level. In general terms, Continuum Mechanics is based on:

1. The study of the movement and the deformation of a body (kinematics).
2. The study of the stress in the continuum media.
3. The mathematical description of the principal laws of physics which governs the behaviour of a continuum media (balance principles).

In the Biomechanics field, the nonlinear theory is needed. The human body is a complex machine, involving large displacements, large deformations and nonlinearities in the material behaviour and in the boundary conditions. Moreover, the human body is alive, what means that it is able to respond to stimuli, to change, to regenerate and many more actions which are really difficult to model because, among other reasons, the human technology is not able to reproduce many of these processes and we do not even understand many

of them yet. Throughout this chapter, some fundamental concepts of Nonlinear Continuum Mechanics which are needed to understand this work are presented. This chapter is not intended to be a comprehensive text in Continuum Mechanics. For this, the reader is referred to many books in the literature which cover this topic, as for example [36]. Here, only the fundamental concepts or theories which are not so common are reminded.

3.2 Hyperelasticity

3.2.1 Introduction

The equations governing the kinematics and the balance principles are valid for any continuum body and time t. The conservation of mass and the momentum equations provide 4 equations for 10 unknowns: the density ρ (in the current configuration), the Cauchy stress tensor $\boldsymbol{\sigma}$ (6 components) and the displacement vector $\mathbf{u}$ in the spatial description (3 components). The energy balance provides additional equations, but it also introduces new unknowns. The balance principles are derived in a general way, without taking into account the inner behaviour of the materials. This is the reason why this set of equations must be completed with another group of equations to characterise the specific material. These equations are called constitutive equations and relate the stresses with the kinematic variables in purely mechanical problems. The continuum mechanics theory is subdivided in different fields, depending on the type of material these equations are valid for.

A hyperelastic material, also called Green-elastic material, postulates the existence of a Helmholtz free-energy function Ψ, defined per unit reference volume. When it is defined as a function of the deformation gradient tensor, $\mathbf{F}$, that is $\Psi = \Psi(\mathbf{F})$, it is called strain-energy function.

A perfectly elastic material is by definition a material which locally produces no entropy, that is to say, the internal dissipation is defined as:

$$\mathcal{D}_{int} = \mathbf{P} : \dot{\mathbf{F}} - \dot{\Psi} \; = \; 0 \, , \tag{3.1}$$

where $\mathbf{P}$ is the first Piola-Kirchhoff stress tensor. A body made of this type of material recovers its original configuration when the forces causing the deformation disappear. Knowing that $\dot{\Psi}(\mathbf{F}) = \partial\Psi(\mathbf{F})/\partial\mathbf{F} : \dot{\mathbf{F}}$, equation (3.1) can be rewritten as:

$$\mathcal{D}_{int} = \left(\mathbf{P} - \frac{\partial \Psi(\mathbf{F})}{\partial \mathbf{F}} \right) : \dot{\mathbf{F}} \; = \; 0 \, . \tag{3.2}$$

Due to the fact that (3.2) must hold for any $\mathbf{F}$, and therefore $\dot{\mathbf{F}}$:

$$\mathbf{P} = \frac{\partial \Psi(\mathbf{F})}{\partial \mathbf{F}} \ . \tag{3.3}$$

Thus, equation (3.3) constitutes the definition of a hyperelastic material, as a subclass of elastic material whose response function has the form shown in the equation.

It is required that the strain energy function vanishes in the reference configuration, which is called the normalization condition:

$$\Psi = \Psi(\mathbf{I}) = 0 \ , \tag{3.4}$$

with $\mathbf{I}$ the second-order unit tensor. From the physical observation it is known that the strain energy function increases with deformation $\Psi(\mathbf{F}) \geq 0$. That means that the strain energy function has a global minimum for $\mathbf{F} = \mathbf{I}$. These conditions state that the stresses in the reference configuration, called residual stresses, are equal to zero.

The strain energy function should be objective. So when a body is subjected to deformation, the strain energy function reaches a certain value unequal to zero, but, if a rotation or a translation is applied to the body after this deformation, the strain energy function must remain unchanged. The superposition of deformation ($\mathbf{F}$) and rigid body motion, defined by an orthogonal tensor $\mathbf{Q}$, produces a new deformation gradient tensor $\boldsymbol{F}^{+} = \mathbf{QF}$. Mathematically, objectivity is expressed as:

$$\Psi(\mathbf{F}) = \Psi(\boldsymbol{F}^{+}) = \Psi(\mathbf{QF}) \tag{3.5}$$

for all orthogonal rotation tensors $\mathbf{Q}$.

3.2.2 Isotropic hyperelastic materials

Isotropic materials are those whose behaviour is identical in any direction. That means that the relation between Ψ and the right Cauchy-Green tensor $\mathbf{C}$ must be independent of the chosen material axes. As a consequence, Ψ can be expressed as a function of the invariants I_a (with $a = 1, 2, 3$) of $\mathbf{C}$ (or the left Cauchy-Green tensor $\mathbf{b}$, since they have the same eigenvalues):

$$\Psi = \Psi[I_1(\mathbf{C}), I_2(\mathbf{C}), I_3(\mathbf{C})] = \Psi[I_1(\mathbf{b}), I_2(\mathbf{b}), I_3(\mathbf{b})] \ . \tag{3.6}$$

Equation (3.6) is only valid for isotropic hyperelastic materials. Using equation (3.3), the first, $\mathbf{P}$, and second Piola-Kirchhoff stress tensor, $\mathbf{S}$, can be expressed as:

$$\mathbf{P} = 2\mathbf{F}\frac{\partial \Psi(\mathbf{C})}{\partial \mathbf{C}} \,, \tag{3.7a}$$

$$\mathbf{S} = 2\frac{\partial \Psi(\mathbf{C})}{\partial \mathbf{C}} = 2\left[\frac{\partial \Psi}{\partial I_1}\frac{\partial I_1}{\partial \mathbf{C}} + \frac{\partial \Psi}{\partial I_2}\frac{\partial I_2}{\partial \mathbf{C}} + \frac{\partial \Psi}{\partial I_3}\frac{\partial I_3}{\partial \mathbf{C}}\right] = 2\left[\left(\frac{\partial \Psi}{\partial I_1} + I_1\frac{\partial \Psi}{\partial I_2}\right)\mathbf{I} - \frac{\partial \Psi}{\partial I_2}\mathbf{C} + I_3\frac{\partial \Psi}{\partial I_3}\mathbf{C}^{-1}\right] \,. \tag{3.7b}$$

Recalling the relation between the Cauchy stress tensor and the second Piola-Kirchhoff stress tensor, $\boldsymbol{\sigma} = J^{-1}\mathbf{F}\mathbf{S}\mathbf{F}^T$, with $J = \det(\mathbf{F})$ the volume ratio, and using equation (3.7b) and the definition of the left Cauchy-Green tensor $\mathbf{b} = \mathbf{F}\mathbf{F}^T$, it is possible to express the Cauchy stress tensor in terms of the three invariants:

$$\boldsymbol{\sigma} = 2J^{-1}\left[I_3\frac{\partial \Psi}{\partial I_3}\mathbf{I} + \left(\frac{\partial \Psi}{\partial I_1} + I_1\frac{\partial \Psi}{\partial I_2}\right)\mathbf{b} - \frac{\partial \Psi}{\partial I_2}\mathbf{b}^2\right] \,. \tag{3.8}$$

3.2.3 Incompressible hyperelasticity

In practice, there are many processes in which the materials involved behave as incompressible or at least very close to it (nearly incompressible or quasi-incompressible). In the case of biological tissues, as many of them are mainly composed of water, and water is an incompressible material, they can be treated as incompressible as well. Modelling incompressible materials can lead to numerical problems that may compromise the convergence of the problem. This is the reason why it is advisable to model the incompressible materials as quasi-incompressible, that is to say, allowing a certain volumetric deformation in order to facilitate convergence. The restriction which characterises incompressibility is $J = 1$. A material subjected to an internal constraint is called a constrained material. In this case, the strain energy function can be written as:

$$\Psi = \Psi(\mathbf{F}) - p(J-1) \,, \tag{3.9}$$

where p can be seen as a Lagrange multiplier, which can be identified with the hydrostatic pressure. The scalar p can only be determined from the equilibrium equations and the boundary conditions.

Equation (3.7b) and (3.8) can be rewritten for an incompressible isotropic hyperelastic material as:

$$\mathbf{S} = 2\frac{\partial \Psi(I_1, I_2)}{\partial \mathbf{C}} - \frac{\partial [p(I_3^{1/2} - 1)]}{\partial \mathbf{C}} = -p\mathbf{C}^{-1} + 2\left(\frac{\partial \Psi}{\partial I_1} + I_1\frac{\partial \Psi}{\partial I_2}\right)\mathbf{I} - 2\frac{\partial \Psi}{\partial I_2}\mathbf{C} \,, \tag{3.10}$$

$$\boldsymbol{\sigma} = -p\mathbf{I} + 2\left(\frac{\partial \Psi}{\partial I_1} + I_1\frac{\partial \Psi}{\partial I_2}\right)\mathbf{b} - 2\frac{\partial \Psi}{\partial I_2}\mathbf{b}^2 \,. \tag{3.11}$$

3.2.4 Compressible hyperelasticity

A material which can experience volumen changes is said to be a compressible material. In numerical simulations, quasi-incompressible materials are usually treated with the same formulation as compressible ones to ensure an easier and faster convergence.

Most materials behave in a different way under bulk and shear deformations, so that it is convenient to split the strain energy function in the so-called volumetric and isochoric parts. In particular, $\mathbf{F}$ and $\mathbf{C}$ are decomposed into volume changing (dilatational) and volume preserving (distortional) parts:

$$\mathbf{F} = (J^{1/3}\mathbf{I})\,\bar{\mathbf{F}} = J^{1/3}\bar{\mathbf{F}}, \qquad \mathbf{C} = (J^{2/3}\mathbf{I})\,\bar{\mathbf{C}} = J^{2/3}\bar{\mathbf{C}}\,, \tag{3.12}$$

where $J^{1/3}\mathbf{I}$ and $J^{2/3}\mathbf{I}$ are associated with the change of volume, and $\bar{\mathbf{F}}$ and $\bar{\mathbf{C}} = \bar{\mathbf{F}}^T\bar{\mathbf{F}}$, called the modified deformation gradient tensor and modified right Cauchy-green tensor respectively, represent the distortion deformation. Then, it is possible to express the strain energy function with a decoupled representation:

$$\Psi(\mathbf{C}) = \Psi_{\text{vol}}(J) + \Psi_{\text{iso}}(\bar{\mathbf{C}})\,. \tag{3.13}$$

The multiplicative decomposition of tensor $\mathbf{F}$ is supported in the field of computational mechanics if working with quasi-incompressible (or slightly incompressible) materials to avoid numerical complications by treating separately the volumetric and isochoric parts. In case of using a standard displacement based method (Galerkin method) in which only the displacement field is discretized, numerical problems can arise if modelling nearly incompressible materials due to locking phenomena (in general, ill-conditioning of the stiffness matrix with over-stiffening of the system). Because of this, multi-field variational principles and a mixed finite element method (FEM) are used. In these methods, not only the displacement field is discretized, but also other fields like, for instance, the internal pressure or the volume ratio. The idea is to discretize variables in an independent way in order to achieve nonlocking and stable numerical solutions.

The second Piola-Kirchhoff stress tensor $\mathbf{S}$ can also be split from equation (3.7b):

$$\mathbf{S} = 2\frac{\partial\Psi_{\text{vol}}(J)}{\partial\mathbf{C}} + 2\frac{\partial\Psi_{\text{iso}}(\bar{\mathbf{C}})}{\partial\mathbf{C}} = \mathbf{S}_{\text{vol}} + \mathbf{S}_{\text{iso}}\,, \tag{3.14a}$$

$$\mathbf{S}_{\text{vol}} = Jp\mathbf{C}^{-1}, \qquad \mathbf{S}_{\text{iso}} = J^{-2/3}\left(\mathbb{I} - \frac{1}{3}\mathbf{C}^{-1}\otimes\mathbf{C}\right) : \bar{\mathbf{S}}\,, \tag{3.14b}$$

where $\mathbb{I}$ is the fourth-order unit tensor. The hydrostatic pressure p is defined as:

$$p = \frac{d\Psi_{\text{vol}}(J)}{dJ} \tag{3.15}$$

and the tensor $\bar{\mathbf{S}}$, called the fictitious second Piola-Kirchhoff stress tensor, as:

$$\bar{\mathbf{S}} = 2\frac{\partial \Psi_{\text{iso}}(\bar{\mathbf{C}})}{\partial \bar{\mathbf{C}}} \,. \tag{3.16}$$

It is important to remark that, unlike incompressible materials, in which the hydrostatic pressure is given by equilibrium equations and boundary conditions, in compressible materials the scalar function p is defined by a constitutive equation.

The Cauchy stress tensor is also split into the volumetric and isochoric parts, $\boldsymbol{\sigma}_{\text{vol}}$ y $\boldsymbol{\sigma}_{\text{iso}}$, in the following way:

$$\boldsymbol{\sigma}_{\text{vol}} = 2J^{-1}\mathbf{b}\frac{\partial \Psi_{\text{vol}}(J)}{\partial \mathbf{b}} = p\mathbf{I} \,, \tag{3.17a}$$

$$\boldsymbol{\sigma}_{\text{iso}} = 2J^{-1}\mathbf{b}\frac{\partial \Psi_{\text{iso}}(\bar{\mathbf{b}})}{\partial \mathbf{b}} = \left(\mathbb{I} - \frac{1}{3}\mathbf{I}\otimes\mathbf{I}\right) : \bar{\sigma} = \mathbb{P} : \bar{\boldsymbol{\sigma}} = \text{dev}\bar{\boldsymbol{\sigma}} \,, \tag{3.17b}$$

where $\mathbb{P} = \mathbb{I} - \frac{1}{3}\mathbf{I}\otimes\mathbf{I}$ is the projection tensor, a fourth order tensor which performs the transformation of a second order tensor into its deviatoric part. The fictitious Cauchy stress tensor, $\bar{\boldsymbol{\sigma}}$, is defined as:

$$\bar{\boldsymbol{\sigma}} = 2J^{-1}\frac{\partial \Psi_{\text{iso}}(\bar{\mathbf{b}})}{\partial \bar{\mathbf{b}}}\bar{\mathbf{b}} \,, \tag{3.18}$$

with $\bar{\mathbf{b}} = \bar{\mathbf{F}}\bar{\mathbf{F}}^T$ the modified left Cauchy-Green tensor. Finally, the decoupled strain energy function can be expressed as a function of the invariants of $\bar{\mathbf{C}}$ or $\bar{\mathbf{b}}$, for compressible isotropic hyperelastic materials, similarly to equation (3.6):

$$\Psi = \Psi_{\text{vol}}(J) + \Psi_{\text{iso}}[\bar{I}_1(\bar{\mathbf{C}}), \bar{I}_2(\bar{\mathbf{C}})] = \Psi_{\text{vol}}(J) + \Psi_{\text{iso}}[\bar{I}_1(\bar{\mathbf{b}}), \bar{I}_2(\bar{\mathbf{b}})] \,. \tag{3.19}$$

3.2.5 Hyperelastic models

Many hyperelastic models have been proposed in the literature, both for rubber-like materials and for biological materials. These models arise from the need to reproduce the behaviour of real materials. Normally, to characterise the mechanical behaviour of a given material, a set of experimental tests is carried out. Once the results are obtained, a model is needed to fit the results. The phenomenological approach proposes strain energy functions which try to fit the data in a purely mathematical way, that is to say, they do not take into account the internal structure of the material, they just treat it as a continuum. As a consequence, the material parameters which are present in these models do not usually have a physical meaning. This is a fast and easy procedure, but it loses touch with reality and physical sense. On the other hand, other

approaches try to model the inner structure to some extent, giving some physical meaning to the material parameters. The good point is that, theoretically, it is possible to obtain some of the parameters from the study of the material structure, being closer to reality and reducing the number of parameters which need to be fitted in a mathematical way. The problem is that normally it is a hard task to obtain such a model which really works.

Moreover, only one type of experimental test is generally fitted, for instance, a uniaxial tension test. This means that the computational model will behave as expected for this loading case, but not necessarily well for another type of load, shear stress for example. Many models fail to reproduce the behaviour of a material subjected to several loading conditions. Thus, it is important to know which material model is being used, how it behaves subjected to different loading conditions and which is the stress state the body is going to suffer in practice.

In this section, some strain energy functions will be presented, and in particular, those that were used in this work.

3.2.5.1 Incompressible models

Polynomial models. Probably the simplest model in the literature is the neo-Hookean model. The strain energy function of this material is:

$$\Psi = C_{10}(I_1 - 3) \, , \tag{3.20}$$

where C_{10} is a stress-like parameter. The simplicity of this model resides in its dependence on only one material parameter and the first invariant I_1. Due to this fact, it has been extensively used in the literature, for example in the simulation of the mechanical behaviour of the breast to predict deformations [18] or to simulate the behaviour of the ligaments of the knee [37]. This strain energy function is also used to model the behaviour of the isotropic matrix in the well known Holzapfel-Gasser-Ogden (HGO) fibre-reinforced model [38].

Another simple strain energy function, proposed at first by Mooney and reformulated by Rivlin, is the Mooney-Rivlin model:

$$\Psi = C_{10}(I_1 - 3) + C_{01}(I_2 - 3) \, . \tag{3.21}$$

Chen et al. [39] used this model to simulate the behaviour of the articular disc of the temporomandibular joint. In general, both of them belong to the family of the polynomial models. The polynomial strain energy functions have the following general form:

$$\Psi = \sum_{i+j=1}^{N} C_{ij}(I_1 - 3)^i (I_2 - 3)^j \ , \tag{3.22}$$

where C_{ij} are stress-like parameters. Thus, from equation (3.22), many different strain energy functions can be obtained varying the number of terms. In particular, the neo-Hookean and the Mooney-Rivlin models presented in equations (3.20) and (3.21) respectively, are particular cases of this polynomial function. In the case of the neo-Hookean model for only one term, and in the case of the Mooney-Rivlin model for $N = 1$. For example, Li et al. [40] used a 3 terms polynomial strain energy function to simulate the fibrocartilage of the human pubic symphysis.

Samani and Plewes [41] modelled the properties of the adipose tissue and the glandular tissue of the breast with a 5 terms polynomial strain energy function ($N = 2$).

$$\Psi = C_{10}(I_1 - 3) + C_{01}(I_2 - 3) + C_{11}(I_1 - 3)(I_2 - 3) + C_{20}(I_1 - 3)^2 + C_{02}(I_2 - 3)^2 \ . \tag{3.23}$$

Let us consider an isotropic incompressible hyperelastic material, whose behaviour is modelled by means of a polynomial function with $N = 2$, subjected to uniaxial tension in the z axis. This load case will be of interest in following sections, and that is the reason why the theoretical development is presented here. The Cauchy stress tensor in this case can be written:

$$\boldsymbol{\sigma} = \begin{bmatrix} 0 & 0 & 0 \\ 0 & 0 & 0 \\ 0 & 0 & \sigma^T_{z\,an} \end{bmatrix} \ . \tag{3.24a}$$

The aim is to obtain the analytical expression of $\sigma^T_{z\,an}$ as a function of the deformation. For uniaxial compression, the process is equivalent just by substituting $\sigma^C_{z\,an}$ for $\sigma^T_{z\,an}$. The subscript "an" stands for analytical solution. The deformation gradient tensor is given as a function of the principal stretches λ_a:

$$\mathbf{F} = \begin{bmatrix} \lambda_1 & 0 & 0 \\ 0 & \lambda_2 & 0 \\ 0 & 0 & \lambda_3 \end{bmatrix} \ . \tag{3.24b}$$

Using the incompressibility constraint, $J = 1$, and the symmetry of loads and displacement boundary conditions, which imply that the stretches in both axes x and y must be equal, $\lambda_1 = \lambda_2$, it is possible to obtain the relation between the principal stretches:

$$J = 1 = \det(\mathbf{F}) = \lambda_1\lambda_2\lambda_3 \ , \tag{3.24c}$$

If λ_3 is termed simply λ, equation (3.24c) implies:

$$\lambda_1 = \lambda_2 = \frac{1}{\sqrt{\lambda}} \ . \tag{3.24d}$$

Therefore, the deformation gradient tensor in (3.24b) has the form:

$$\mathbf{F} = \begin{bmatrix} \frac{1}{\sqrt{\lambda}} & 0 & 0 \\ 0 & \frac{1}{\sqrt{\lambda}} & 0 \\ 0 & 0 & \lambda \end{bmatrix} \tag{3.24e}$$

and the left Cauchy Green tensor $\mathbf{b}$:

$$\mathbf{b} = \begin{bmatrix} \frac{1}{\lambda} & 0 & 0 \\ 0 & \frac{1}{\lambda} & 0 \\ 0 & 0 & \lambda^2 \end{bmatrix} \ . \tag{3.24f}$$

Using equation (3.11) the boundary conditions yield:

$$\begin{aligned} \sigma^T_{y\,an} = &- p + 2\Big[C_{10} + C_{01}I_1 + C_{11}I_1\big(I_1 - 3\big) + C_{11}\big(I_2 - 3\big) + 2C_{20}\big(I_1 - 3\big) + \\ &+ 2C_{02}I_1\big(I_2 - 3\big)\Big]\frac{1}{\lambda} - 2\Big[C_{01} + C_{11}\big(I_1 - 3\big) + 2C_{02}\big(I_2 - 3\big)\Big]\frac{1}{\lambda^2} = 0 \ , \end{aligned} \tag{3.25a}$$

from which the hydrostatic pressure p can be worked out:

$$\begin{aligned} p = &\frac{2}{\lambda^4}\Bigg[2C_{02}(-1+\lambda)^2(1+2\lambda+\lambda^3+2\lambda^4) + \lambda\Bigg(\lambda\Big(C_{01} + 2C_{20} + C_{10}\lambda - \\ &- 3C_{20}\lambda + (C_{01} + C_{20})\lambda^3\Big) + C_{11}(-1+\lambda)^2(3+3\lambda+2\lambda^3+\lambda^4)\Bigg)\Bigg] \ . \end{aligned} \tag{3.25b}$$

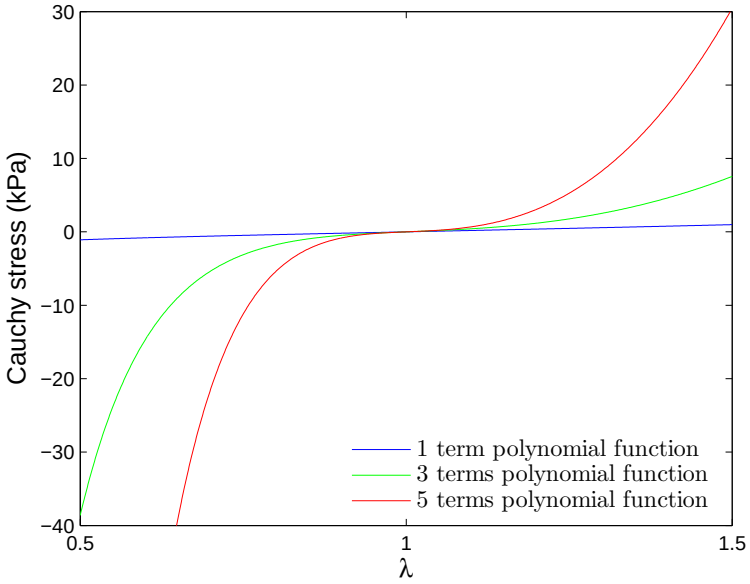

Figure 3.1: Stress-stretch curve for uniaxial tension-compression for the 1, 3 and 5 terms polynomial models with the parameters: $C_{10} = 0.3$ kPa, $C_{01} = 0.3$ kPa, $C_{11} = 2.25$ kPa, $C_{20} = 3.8$ kPa and $C_{02} = 4.72$ kPa. These constants were proposed by [41] for the breast adipose tissue.

Finally, the Cauchy stress tensor in z direction is calculated after substituting p:

$$\sigma^T_{z\,an} = 2C_{10}\left(\lambda^2 - \frac{1}{\lambda}\right) + 2C_{01}\left(\lambda - \frac{1}{\lambda^2}\right) + 6C_{11}\left(\lambda^3 - \lambda^2 - \lambda + \frac{1}{\lambda} + \frac{1}{\lambda^2} - \frac{1}{\lambda^3}\right) +$$

$$+ 4C_{20}\left(\lambda^4 - 3\lambda^2 + \lambda + \frac{3}{\lambda} - \frac{2}{\lambda^2}\right) + 4C_{02}\left(2\lambda^2 - 3\lambda - \frac{1}{\lambda} + \frac{3}{\lambda^2} - \frac{1}{\lambda^4}\right) . \tag{3.26}$$

The Cauchy stress for the neo-Hookean and Mooney-Rivlin materials, and in general, for any polynomial function with a number of terms less than 5, can be derived from equation (3.26) by cancelling the corresponding terms. For example, in the neo-Hookean model $C_{01} = C_{11} = C_{20} = C_{02} = 0$ and in the Mooney-Rivlin model $C_{11} = C_{20} = C_{02} = 0$.

In figure 3.1 an example of the Cauchy stress-stretch ($\sigma - \lambda$) curve in a uniaxial test is shown for the polynomial models with one (neo-Hookean), three and five terms. It can be noticed the different behaviour of the three models and how the curve becomes more markedly non-linear as the number of terms of the polynomial strain energy function increases, in compression ($\lambda < 1$) as well as in tension ($\lambda > 1$). In fact, for the stretch range presented in the graph and for the constants used, it is possible to notice that the behaviour of the neo-Hookean material is very close to linear. As more terms are added (3 and 5 terms polynomial functions) the curves become stiffer, more clearly in compression.

Another load case, also used later in this work, is a material subjected to a pure shear stress state. Let

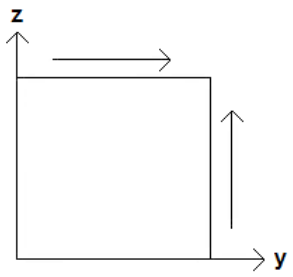

Figure 3.2: Pure shear stress state.

us consider an isotropic incompressible hyperelastic material, with its mechanical behaviour described by a polynomial strain energy function with $N = 2$ and with a stress state shown in (3.27a).

$$\boldsymbol{\sigma} = \begin{bmatrix} 0 & 0 & 0 \\ 0 & 0 & \sigma_{yz} \\ 0 & \sigma_{zy} & 0 \end{bmatrix} . \tag{3.27a}$$

The aim, as in the previous case, is to obtain the stresses as a function of deformation. However, implementing this stress state in a FE code causes some problems when the displacement boundary conditions are applied. The classical way of representing a pure shear stress state in linear elasticity theory is shown in figure 3.2. If the displacement boundary conditions are applied in this way in a large displacements and strains problem, other components of the stress tensor apart from σ_{yz} and σ_{zy} will appear. This problem is solved using the fact that this stress state can be expressed in the principal directions of the stress tensor (at 45^{o} from the y and z directions shown in figure 3.2) as a tension and a compression of the same magnitud, that is:

$$\boldsymbol{\sigma}_{ppl} = \boldsymbol{Q^T \sigma Q} = \begin{bmatrix} 0 & 0 & 0 \\ 0 & \sigma^S_{y\,an} & 0 \\ 0 & 0 & \sigma^S_{z\,an} \end{bmatrix} , \tag{3.27b}$$

where $\mathbf{Q}$ is a rotation matrix. Now, the displacement boundary conditions can be easily applied. In the linear elastic case, the behaviour of the material in compression and tension is equivalent, so that if $\sigma_{yz} = \sigma_{zy} = \sigma$, it turns out that $\sigma^S_{y\,an} = -\sigma^S_{z\,an} = \sigma$. In the following mathematical development, applied to a hyperelastic material subjected to large strains and displacements, the behaviour in compression and tension may be different, in contrast to the linear elastic case. Therefore it is not true in general that $\sigma^S_{y\,an} = -\sigma^S_{z\,an}$. Instead, the stress tensor is characterised by two different components. The aim is to obtain the stresses

as a function of deformation. To do that, the calculation of the deformation gradient is the starting point. Imposing zero displacements in x direction (perpendicular to the yz plane in figure 3.2), and keeping in mind that this is an incompressible material (equation (3.24c)), the cross-sectional area of the probe in the yz plane must remain constant during deformation. It can be proved that accomplishing these conditions and applying the tension in z direction and the compression in y direction, the tensor $\mathbf{F}$ is:

$$\mathbf{F} = \begin{bmatrix} 1 & 0 & 0 \\ 0 & 1/\lambda & 0 \\ 0 & 0 & \lambda \end{bmatrix} \tag{3.27c}$$

and the left Cauchy-Green tensor $\mathbf{b}$:

$$\mathbf{b} = \begin{bmatrix} \lambda^2 & 0 & 0 \\ 0 & \frac{1}{\lambda^2} & 0 \\ 0 & 0 & \lambda^2 \end{bmatrix} . \tag{3.27d}$$

Using equation (3.11) the boundary yield:

$$\begin{aligned} \sigma^S_{x\,an} = &- p + 2\Big[C_{10} - 6C_{20} + C_{01}\big(-1 + I_1\big) + \Big(2C_{20} + C_{11}\big(-4 + I_1\big)\Big)I_1 + \\ &+ 2C_{02}\big(-1 + I_1\big)\big(-3 + I_2\big) + C_{11}I_2\Big] = 0 \,, \end{aligned} \tag{3.28a}$$

from which the hydrostatic pressure p can be worked out:

$$\begin{aligned} p = &\frac{2}{\lambda^4}\Big(C_{11} + (C_{01} - C_{11} + 2C_{20})\lambda^2 + (C_{10} - 4C_{20})\lambda^4 + \\ &+ (C_{01} - C_{11} + 2C_{20})\lambda^6 + C_{11}\lambda^8 + 2C_{02}(-1 + \lambda^2)^2(1 + \lambda^4)\Big) \,. \end{aligned} \tag{3.28b}$$

Finally, the components of the Cauchy stress tensor, $\sigma^S_{y\,an}$ and $\sigma^S_{z\,an}$ can be expressed as:

$$\begin{aligned} \sigma^S_{y\,an} = &- \frac{2(-1 + \lambda^2)}{\lambda^4}\Big(C_{11} + 2C_{20} + (C_{10} - C_{11} - 4C_{20} + 2C_{02})\lambda^2 + \\ &+ (C_{01} - C_{11} + 2C_{20} - 4C_{02})\lambda^4 + (C_{11} + 2C_{02})\lambda^6\Big) \,, \end{aligned} \tag{3.29a}$$

$$\sigma^S_{z\,an} = \frac{2(-1+\lambda^2)}{\lambda^4}\Big(C_{11} + 2C_{02} + (C_{01} - C_{11} + 2C_{20} - 4C_{02})\lambda^2 + \\ + (C_{10} - C_{11} - 4C_{20} + 2C_{02})\lambda^4 + (C_{11} + 2C_{20})\lambda^6\Big) \,. \tag{3.29b}$$

In figure 3.3, an example of both components of the Cauchy stress tensor is shown for the polynomial models with one (neo-Hookean), three and five terms. As in the previous uniaxial example, it can be observed that the more terms the polynomial function has, the stiffer the response is. Again, the expression for the neo-Hookean and Mooney-Rivlin materials, and in general for any other polynomial model with less terms can be derived from equations (3.29a) and (3.29b), by cancelling the corresponding parameters: $C_{01} = C_{11} = C_{20} = C_{02} = 0$ for the neo-Hookean and $C_{11} = C_{20} = C_{02} = 0$ for the Mooney-Rivlin.

Rubin-Bodner model. The Rubin-Bodner model, later used in this work, was proposed by Rubin and Bodner for biological tissues [42]. Then it was used by Barbarino et al. [43] in a FE model of the face soft tissues. In particular, these authors used this strain energy function to model the skin and the muscles. They did not consider the transient and dissipative behaviour (viscoelastic), so that only the long term hyperelastic terms were included. The Rubin-Bodner strain energy function is:

$$\Psi = \frac{\mu_0}{2q}\left(e^{qg} - 1\right) \,, \tag{3.30}$$

with:

$$g = g_1 + g_2 = 2\, m_1\big(J - 1 - ln(J)\big) + (1-\omega)\, m_2\, (\bar{I}_1 - 3) \,, \tag{3.31}$$

where $\bar{I}_1$ is the modified first invariant, g_1 characterises the response of the fully elastic dilatation and g_2 the fully elastic distortion, m_1 and m_2 are material parameters and ω is an aging term.

3.2.5.2 Compressible and quasi-incompressible models

Analytically, the incompressibility condition is treated as explained in the previous sections. In the FEM, incompressibility can lead to several numerical problems due to the fact that the stiffness matrix becomes singular. To avoid these problems, materials are treated as quasi-incompressible, splitting the strain energy function in a volumetric and an isochoric part. But even using quasi-incompressibility, as explained in section 3.2.4, if a standard displacement based method is used, some numerical difficulties appear due to the fact that the stiffness matrix is almost singular because the effective bulk modulus is very big compared to the effective shear modulus. That depends on how strictly the condition is imposed, i.e., how close is

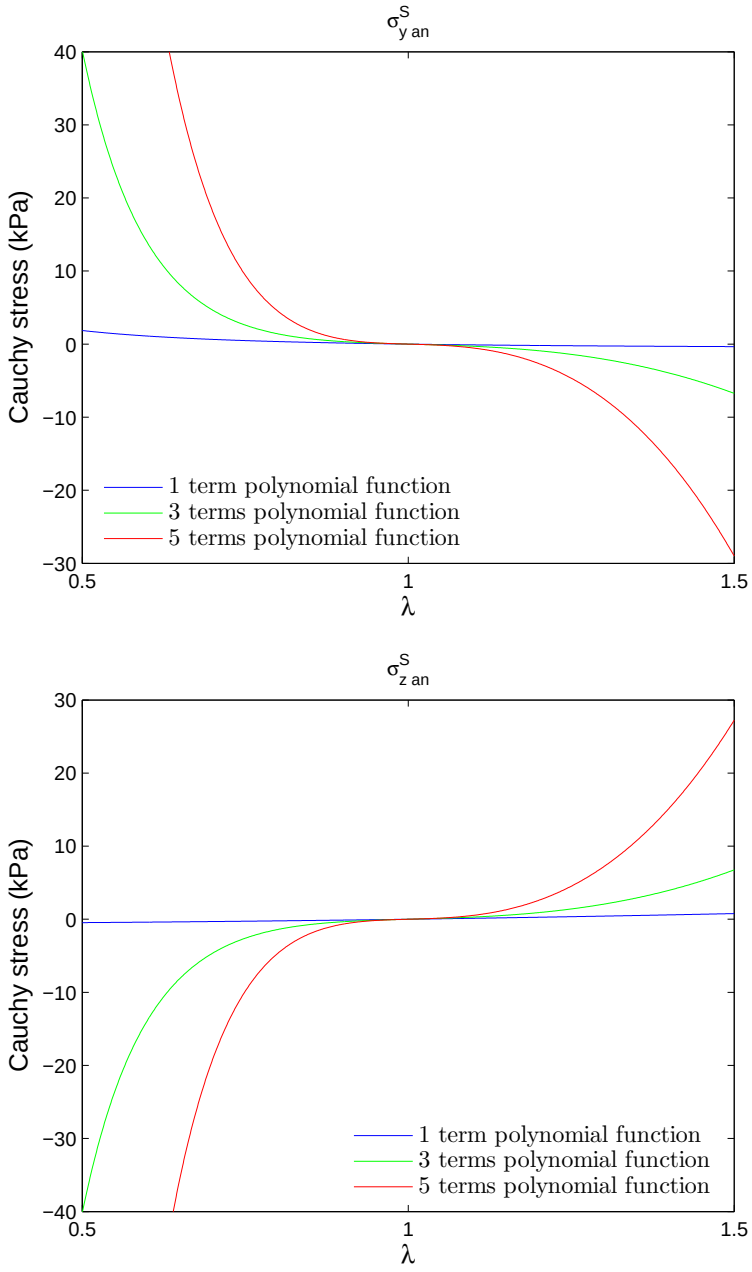

Figure 3.3: Stress-stretch curve for pure shear in principal directions for the 1, 3 and 5 terms polynomial models with the parameters: $C_{10} = 0.31$ kPa, $C_{01} = 0.3$ kPa, $C_{11} = 2.25$ kPa, $C_{20} = 3.8$ kPa and $C_{02} = 4.72$ kPa. These constants were proposed by [41] for the breast adipose tissue.

the material to an incompressible one. Another problem is that little displacements can produce important pressure variations. Unless reduced integration techniques are used, the stresses calculated at the Gauss integration points present large oscillations.

For example, the neo-Hookean strain energy function for a nearly incompressible material can be written:

$$\Psi = \Psi_{\text{iso}} + \Psi_{\text{vol}} = C_{10}(\bar{I}_1 - 3) + \frac{1}{D}(J-1)^2 \,. \tag{3.32}$$

The first term is the isochoric or distortional part which is function of the modified first invariant $\bar{I}_1$. The second term corresponds to the volumetric or dilatational part. The constant D determines the compressibility of the material. In the limit, if it equals zero, the material becomes totally incompressible. In practice, D is chosen small enough to ensure quasi-incompressibility, but no so small as to lead to numerical problems. A proper value of D depends on the model used and on the strictness desired for the incompressibility condition, but normal values are around 10^{-4}.

The Cauchy stress tensor is split into a volumetric part:

$$\boldsymbol{\sigma}_{\text{vol}} = p\mathbf{I} \,, \qquad \text{where} \qquad p = \frac{d\Psi_{\text{vol}}(J)}{dJ} = \frac{2}{D}(J-1) \,, \tag{3.33}$$

and an isochoric one:

$$\boldsymbol{\sigma}_{\text{iso}} = \frac{2}{J}\,\text{dev}\left(\frac{\partial \Psi_{\text{iso}}}{\partial \bar{\boldsymbol{b}}}\,\bar{\boldsymbol{b}}\right) \,, \tag{3.34}$$

where dev($\bullet$) denotes the deviatoric part of a tensor and in the case of the neo-Hookean model yields:

$$\boldsymbol{\sigma}_{\text{iso}} = \frac{2}{J}\,C_{10}\left(\bar{\boldsymbol{b}} - \frac{\bar{I}_1}{3}\boldsymbol{I}\right) \,. \tag{3.35}$$

Many functions can be used for the volumetric part of the strain energy function apart from that shown in equation (3.32). Another example commonly used is:

$$\Psi_{\text{vol}} = \frac{1}{D}\left(\frac{J^2-1}{2} - \ln J\right) \,, \tag{3.36}$$

leading to a volumetric part of the Cauchy stress tensor.

3.2.6 Elasticity tensors

The concept of linearization is of great importance in the numerical resolution of nonlinear problems in computational finite elasticity. The incremental/iterative techniques of Newton's type are used to solve the linearized problems. In practice, knowing this theory is key for the development of user defined materials in the available FE codes, as for example the UMAT subroutine in Abaqus. The elasticity tensor $\mathbb{C}$ measures

the variation of stress due to infinitesimal strain changes and is defined in material coordinates as:

$$\mathbb{C} = 2\frac{\partial \mathbf{S}(\mathbf{C})}{\partial \mathbf{C}} \qquad \text{or} \qquad C_{ABCD} = 2\frac{\partial S_{AB}}{\partial C_{CD}} \,, \tag{3.37}$$

with the symmetries (called minor symmetries):

$$C_{ABCD} = C_{BACD} = C_{ABDC} \,. \tag{3.38}$$

If a hyperelastic behaviour is assumed, according to equation (3.7b), the definition of the elasticity tensor in the material description is:

$$\mathbb{C} = 4\frac{\partial^2 \Psi(\mathbf{C})}{\partial \mathbf{C} \partial \mathbf{C}} \qquad \text{or} \qquad C_{ABCD} = 4\frac{\partial^2 \Psi}{\partial C_{AB} \partial C_{CD}} \,, \tag{3.39}$$

with the symmetries (called major symmetries):

$$\mathbb{C} = \mathbb{C}^T \qquad \text{or} \qquad C_{ABCD} = C_{CDAB} \,. \tag{3.40}$$

Equation (3.40) is a necessary and sufficient condition for a material to be hyperelastic. With the minor and major symmetries, $\mathbb{C}$ has only 21 independent componentes at each strain state. In the spatial description, $\mathbb{c}$ is defined as J^{-1} times the push forward of $\mathbb{C}$:

$$\mathbb{c} = J^{-1}\phi_*(\mathbb{C}) \qquad \text{or} \qquad c_{abcd} = J^{-1} F_{aA} F_{bB} F_{cC} F_{dD} C_{ABCD} \,. \tag{3.41}$$

Following the same procedure as in section 3.2.4 to decouple the strain energy function, the elasticity tensor can also be split as:

$$\mathbb{C} = \mathbb{C}_{\text{vol}} + \mathbb{C}_{\text{iso}} \,, \tag{3.42a}$$

where

$$\mathbb{C}_{\text{vol}} = 2\frac{\partial \mathbf{S}_{\text{vol}}}{\partial \mathbf{C}}, \qquad \mathbb{C}_{\text{iso}} = 2\frac{\partial \mathbf{S}_{\text{iso}}}{\partial \mathbf{C}} \,. \tag{3.42b}$$

$\mathbb{C}_{\text{vol}}$ and $\mathbb{C}_{\text{iso}}$ represent respectively the purely volumetric and purely isochoric contribution of the elasticity tensor. In the spatial description, the elasticity tensor can be written as:

$$\mathbb{c} = \mathbb{c}_{\text{vol}} + \mathbb{c}_{\text{iso}} \,, \tag{3.43}$$

with the following definitions:

$$J\,\mathbb{c}_{\text{vol}} = 4\mathbf{b}\frac{\partial^2\Psi_{\text{vol}}(J)}{\partial\mathbf{b}\partial\mathbf{b}}\mathbf{b} = J(\tilde{p}\mathbf{I}\otimes\mathbf{I} - 2p\mathbb{I})\;, \qquad \text{with} \quad \tilde{p} = p + J\frac{dp}{dJ}\;, \tag{3.44a}$$

$$J\,\mathbb{c}_{\text{iso}} = 4\mathbf{b}\frac{\partial^2\Psi_{\text{iso}}(\bar{\boldsymbol{b}})}{\partial\mathbf{b}\partial\mathbf{b}}\mathbf{b} = \mathbb{P} : \bar{\mathbb{c}}^* : \mathbb{P} + \frac{2}{3}\text{tr}(\bar{\boldsymbol{\tau}})\mathbb{P} - \frac{2}{3}(\mathbf{I}\otimes\boldsymbol{\tau}_{\text{iso}} + \boldsymbol{\tau}_{\text{iso}}\otimes\mathbf{I})\;, \tag{3.44b}$$

where $\mathbb{P} = \mathbb{I} - \frac{1}{3}\mathbf{I}\otimes\mathbf{I}$, is the spatial projection tensor, introduced previously, $\bar{\boldsymbol{\tau}} = J\bar{\boldsymbol{\sigma}}$ is the fictitious Kirchhoff stress tensor, $\boldsymbol{\tau}_{\text{iso}} = J\boldsymbol{\sigma}_{\text{iso}}$ is the isochoric part of the Kirchhoff stress tensor and:

$$\bar{\mathbb{c}}^* = 4\bar{\boldsymbol{b}}\frac{\partial^2\Psi_{\text{iso}}(\bar{\boldsymbol{b}})}{\partial\bar{\boldsymbol{b}}\partial\bar{\boldsymbol{b}}}\bar{\boldsymbol{b}} \tag{3.45}$$

is the fourth order fictitious elasticity tensor.

3.2.7 Fibre-reinforced materials

Many materials are composed of one or more families of fibres embedded in a matrix. In general, these materials are anisotropic if each family of fibres is oriented in a preferential direction. This type of material is called fibre-reinforced composite. The fibres are considered to be continuously distributed, so that it is possible to derive the constitutive equations based on the continuum approach. It is assumed that the anisotropy arises exclusively from the presence of fibres. If only one family of fibres exists, the material exhibits transversely isotropy. These materials are usually stiffer in the fibre direction than in the plane orthogonal to the fibres, where isotropy is attained.

3.2.7.1 One family of fibres

In a material reinforced with only one family of fibres oriented in a preferential direction, the stress at a material point depends on the deformation gradient $\mathbf{F}$ and on the fibre direction defined by the unit vector $\mathbf{a}_0$. If the body is deformed, the direction of the fibres changes and the new direction is defined by the unit vector $\mathbf{a}$. The stretch of the fibres, λ, can be calculated from the relation between the direction vectors in the reference and the current configurations:

$$\lambda\mathbf{a} = \mathbf{F}\boldsymbol{a}_0 \tag{3.46}$$

and knowing that $|\mathbf{a}| = 1$:

$$\lambda^2 = \boldsymbol{a}_0\boldsymbol{F}^T\mathbf{F}\boldsymbol{a}_0 = \boldsymbol{a}_0 \cdot \mathbf{C}\boldsymbol{a}_0\;. \tag{3.47}$$

If the material is assumed to be hyperelastic, the strain energy function must depend on the right Cauchy-Green tensor $\mathbf{C}$ and on the tensor product $\boldsymbol{a}_0 \otimes \boldsymbol{a}_0$:

$$\Psi = \Psi(\mathbf{C}, \boldsymbol{a}_0 \otimes \boldsymbol{a}_0) \, . \tag{3.48}$$

Two additional invariants, called pseudoinvariants of $\mathbf{C}$ and $\boldsymbol{a}_0 \otimes \boldsymbol{a}_0$, are defined to describe the properties of the fibres and its interaction with the surrounding matrix. Thus, I_4 and I_5 are defined as:

$$I_4 = \boldsymbol{a}_0 \cdot \mathbf{C}\boldsymbol{a}_0 = \lambda^2 \quad \text{and} \quad I_5 = \boldsymbol{a}_0 \cdot \boldsymbol{C}^2\boldsymbol{a}_0 \, . \tag{3.49}$$

Then, the strain energy function can be written as a function of the invariants and pseudoinvariants:

$$\Psi = \Psi\Big(I_1(\mathbf{C}), I_2(\mathbf{C}), I_3(\mathbf{C}), I_4(\mathbf{C}, \boldsymbol{a}_0), I_5(\mathbf{C}, \boldsymbol{a}_0)\Big) \, . \tag{3.50}$$

Thus, the Cauchy stress for a material with one family of fibres can be obtained using equations (3.7b) and (3.8), by extending them with the new pseudoinvariants:

$$\boldsymbol{\sigma} = 2J^{-1}\left[I_3\frac{\partial\Psi}{\partial I_3}\mathbf{I} + \left(\frac{\partial\Psi}{\partial I_1} + I_1\frac{\partial\Psi}{\partial I_2}\right)\mathbf{b} - \frac{\partial\Psi}{\partial I_2}\mathbf{b}^2 + I_4\frac{\partial\Psi}{\partial I_4}\mathbf{a}\otimes\mathbf{a} + I_4\frac{\partial\Psi}{\partial I_5}(\mathbf{a}\otimes\mathbf{ba} + \mathbf{ab}\otimes\mathbf{a})\right] . \tag{3.51}$$

3.2.7.2 Two families of fibres

In this case, it is also assumed that the fibres are continuously distributed. The stress at a material point depends on the deformation gradient $\mathbf{F}$ and on the preferential direction of both families of fibres. These directions are defined by the unit vectors $\mathbf{a}_0$ and $\mathbf{g}_0$ in the reference configuration, while in the current configuration, these directions are defined by the unit vectors $\mathbf{a}$ and $\mathbf{g}$ respectively.

If the material is assumed to be hyperelastic, the strain energy function must depend on the right Cauchy-Green tensor $\mathbf{C}$ and on the tensor products $\boldsymbol{a}_0 \otimes \boldsymbol{a}_0$ and $\boldsymbol{g}_0 \otimes \boldsymbol{g}_0$:

$$\Psi = \Psi(\mathbf{C}, \boldsymbol{a}_0 \otimes \boldsymbol{a}_0, \boldsymbol{g}_0 \otimes \boldsymbol{g}_0) \, . \tag{3.52}$$

Now, besides the pseudoinvariants shown in (3.49), another two invariants, I_6 and I_7, should be defined in the same way for the new family of fibres:

$$I_6 = \boldsymbol{g}_0 \cdot \mathbf{C}\boldsymbol{g}_0 \quad \text{and} \quad I_7 = \boldsymbol{g}_0 \cdot \boldsymbol{C}^2\boldsymbol{g}_0 \, . \tag{3.53}$$

Moreover, with two families of fibres, two more invariants need to be defined, which take into account the interaction between these two families:

$$I_8 = (\boldsymbol{a}_0 \cdot \boldsymbol{g}_0)\boldsymbol{a}_0 \cdot \mathbf{C}\boldsymbol{g}_0 \quad \text{and} \quad I_9 = (\boldsymbol{a}_0 \cdot \boldsymbol{g}_0)^2 \,. \tag{3.54}$$

The dot product $\boldsymbol{a}_0 \cdot \boldsymbol{g}_0$ is a geometrical constant, without any dependence on the deformations. Therefore, invariant I_9 is no longer considered.

Then, the strain energy function can be written as a function of the invariants and pseudoinvariants:

$$\Psi = \Psi\Big(I_1(\mathbf{C}), I_2(\mathbf{C}), I_3(\mathbf{C}), I_4(\mathbf{C}, \boldsymbol{a}_0), I_5(\mathbf{C}, \boldsymbol{a}_0), I_6(\mathbf{C}, \boldsymbol{g}_0), I_7(\mathbf{C}, \boldsymbol{g}_0), I_8(\mathbf{C}, \boldsymbol{a}_0, \boldsymbol{g}_0)\Big) \,. \tag{3.55}$$

Thus, the second Piola-Kirchhoff stress tensor for a material with two family of fibres can be obtained using equation (3.7b), and extending them with the new invariants:

$$\begin{aligned} S = 2\Bigg[&\left(\frac{\partial \Psi}{\partial I_1} + I_1 \frac{\partial \Psi}{\partial I_2}\right)\mathbf{I} - \frac{\partial \Psi}{\partial I_2}\mathbf{C} + I_3 \frac{\partial \Psi}{\partial I_3}\boldsymbol{C}^{-1} + \frac{\partial \Psi}{\partial I_4}\boldsymbol{a}_0 \otimes \boldsymbol{a}_0 + \frac{\partial \Psi}{\partial I_5}(\boldsymbol{a}_0 \otimes \mathbf{C}\boldsymbol{a}_0 + \boldsymbol{a}_0\mathbf{C} \otimes \boldsymbol{a}_0) + \\ &+ \frac{\partial \Psi}{\partial I_6}\boldsymbol{g}_0 \otimes \boldsymbol{g}_0 + \frac{\partial \Psi}{\partial I_7}(\boldsymbol{g}_0 \otimes \mathbf{C}\boldsymbol{g}_0 + \boldsymbol{g}_0\mathbf{C} \otimes \boldsymbol{g}_0) + \frac{1}{2}\frac{\partial \Psi}{\partial I_8}(\boldsymbol{a}_0 \cdot \boldsymbol{g}_0)(\boldsymbol{a}_0 \otimes \boldsymbol{g}_0 + \boldsymbol{g}_0 \otimes \boldsymbol{a}_0)\Bigg] \,. \end{aligned} \tag{3.56}$$

The Cauchy stress, σ, can be easily obtained from equation (3.56), using the well-known relation $\boldsymbol{\sigma} = J^{-1}\mathbf{F}\mathbf{S}\mathbf{F}^T$.

3.2.7.3 Fibre-reinforced models

Probably one of the most used models for fibre-reinforced materials is the well-known HGO model [38]. It was first developed for arterial tissue, but since its publication it has been widely used for many other biological materials. For instance, to model the trachea [44] or the knee ligaments [45]. The strain energy function, proposed for two families of fibres, is:

$$\bar{\Psi} = \frac{C_{10}}{2}(\bar{I}_1 - 3) + \frac{k_1}{2k_2}\sum_{i=4,6}\left(e^{k_2(\bar{I}_i - 1)^2} - 1\right) \,, \tag{3.57}$$

where $C_{10} > 0$ and $k_1 > 0$ are stress-like parameters and $k_2 > 0$ is a dimensionless parameter. The first part of the strain energy function, the one which depends on $\bar{I}_1$, is a neo-Hookean model representing the isotropic contribution of the matrix, whereas the second part, function of the modified invariants $\bar{I}_4$ and $\bar{I}_6$, represents the anisotropic contribution of the fibres, modelling the strong stiffening of the collagen fibres when stretched. Of course, it is possible to consider as many families of fibres as desired.

After this model, some variations have been proposed to improve it. It is the case of the Gasser-Ogden-Holzapfel (GOH) model [46]. It is very similar to the previous one, but modified to take into account the fibre dispersion. It has been extensively used in the literature for arteries and for other materials such as

the abdominal adipose tissue [47]. The proposed strain energy function is:

$$\bar{\Psi} = \frac{C_{10}}{2}(\bar{I}_1 - 3) + \frac{k_1}{2k_2} \sum_{i=4,6} \left(e^{k_2[\kappa \bar{I}_1 + (1-3\kappa)\bar{I}_i - 1]^2} - 1 \right) . \tag{3.58}$$

In the above equation, the parameters C_{10}, k_1 and k_2 have the same meaning that in the original model. The new parameter $\kappa \in [0, 1/3]$ accounts for the fibre dispersion. If its value is 0, the fibres are perfectly oriented in one direction without dispersion, whereas if its value is 1/3, the fibres are uniformly distributed in all directions and the material becomes isotropic.

3.3 Viscoelasticity

The majority of biological materials, and many other materials used in different applications, are characterised by constitutive equation which depends explicitly on time. If, besides, there is no damage, the behaviour is called viscoelasticity. The viscous part is responsible for the dependence on time (strain rate) and for the dissipation of energy during a loading cycle. Unlike elastic materials, viscoelastic ones exhibit hysteresis. The elastic part is responsible for the dependence on the strain and for finally recovering the initial state when all the loads are removed. Another feature of viscoelastic materials is the creep and stress relaxation phenomena. Creep is revealed when, after applying a constant stress, the material continues deforming beyond the onset of the stress. The stress relaxation is the opposite: the decrease in stress in a material subjected to a constant deformation. Theoretically, in a creep test (or in a stress relaxation test) the stress (deformation) is applied as a step function. In practice, it is impossible to apply a step-like load. Therefore, the step must be approximated by an initial ramp with a slope as steep as possible. In a creep test under a unit stress, the temporal evolution of strain is called creep function, $J(t)$. In a stress relaxation test under a unit strain, the temporal evolution of stress is known as relaxation function, $G(t)$.

3.3.1 Quasi-linear viscoelasticity

Quasi-linear viscoelasticity was first introduced by Fung [48] as a simplified way to deal with viscoelasticity. It allows characterizing the material behaviour as time dependent (viscoelasticity) and using a nonlinear stress-strain relationship. It assumes that the stress produced by a deformation step function can be written as:

$$\sigma(\lambda, t) = \overline{G}(t)\, T^e(\lambda) , \tag{3.59}$$

where λ is the stretch produced by the deformation and $\overline{G}(t)$ is the reduced relaxation function. This is a dimensionless function normalized such that $\overline{G}(0) = 1$. The function $T^e(\lambda)$, called the elastic response function, is expressed in the same units as the stress and represents the instantaneous stress which appears

in the material at the onset of the stretch.

Linearity is maintained as long as the Boltzmann's superposition principle is applied to give the stress evolution as:

$$\sigma(t) = \int_{-\infty}^{t} \overline{G}(t-\tau)\, \frac{dT^e[\lambda(\tau)]}{d\tau}\, d\tau\ . \tag{3.60}$$

Non-linearity is introduced in the formulation through the function $T^e(\lambda)$. This mixture of linear and non-linear formulations is what gives the name to the quasi-linear viscoelastic model. Considering that the material has initially no residual stresses or deformations:

$$\sigma(t) = \int_{0}^{t} \overline{G}(t-\tau)\, \frac{dT^e[\lambda(\tau)]}{d\tau}\, d\tau \qquad \forall \quad t \in [0,\infty)\ . \tag{3.61}$$

It is possible to apply the chain rule to simplify the above equation, for subsequent calculations, as will be seen in later chapters:

$$\sigma(t) = \int_{0}^{t} \overline{G}(t-\tau)\, \frac{dT^e(\lambda)}{d\lambda}\, \frac{d\lambda(\tau)}{d\tau}\, d\tau \qquad \forall \quad t \in [0,\infty)\ . \tag{3.62}$$

The elastic response function, $T^e(\lambda)$, can be derived from any strain energy function, like for example, the neo-Hookean or the Mooney-Rivlin, as the stress in a uniaxial test for a given stretch λ. The Prony series are commonly used for the relaxation function, $G(t)$:

$$G(t) = E_\infty + \sum_{i=1}^{n} E_i\, e^{-t/\tau_i}\ , \tag{3.63}$$

with n representing the Maxwell units in a generalised Maxwell model, E_i and τ_i are, respectively, the stiffness and the relaxation time of each unit.

The reduced relaxation function, $\overline{G}(t)$, is obtained from $G(t)$ by normalizing it such that $\overline{G}(0) = 1$. Thus, it is rewritten in terms of the Prony constants, g_i, as:

$$\overline{G}(t) = g_\infty + \sum_{i=1}^{n} g_i\, e^{-t/\tau_i}\ , \tag{3.64}$$

with

$$g_i = \frac{E_i}{E_\infty + \sum\limits_{i=1}^{n} E_i} \qquad \text{and} \qquad g_\infty + \sum_{i=1}^{n} g_i = 1\ . \tag{3.65}$$

Usually, the number of terms in the Prony series is fixed by the modeller a priori in order to obtain a good fit of the experimental data. In the fitting of experimental data with Prony series, it is important to take into account that different sets of τ_i and g_i can lead to equal goodness of fit, as shown by Lanczos [49].

This means that the solution fitted may be not unique and obviously this is not convenient for statistical purposes. Troyer et al. [50] demonstrated that fixing the time constants τ_i ensures that the mathematical form of equation (3.64) yields a unique solution, i.e, it is not possible to have two sets of g_i that fit the curve equally well. Because of this, it is a good practice to fix the values of τ_i beforehand and only fit the constants g_i.

3.3.2 Viscoelastic model with internal variables

The internal variables, often called hidden or history variables, are used to model materials which involve dissipation. Although these variables try to model a real characteristic of the material, they are not observable, therefore being treated in a purely phenomenological way. The thermodynamic state of a material depends on the deformation gradient, $\mathbf{F}$, its temperature and the internal variables. In this thesis, the temperature is assumed constant. The equations governing this behaviour are just briefly presented. For a deeper insight the reader is referred to the text of Holzapfel [36]. In contrast with the previously presented viscoelastic model, which is only valid for a uniaxial stress state, the viscoelastic model presented in this section is designed for a 3D stress state. However, for a uniaxial stress state under small strains and displacements, both models coincide.

The strain energy function, using the decoupling into the volumetric and isochoric parts, can be expressed as:

$$\Psi = \Psi^{\infty}_{\text{vol}}(J) + \Psi^{\infty}_{\text{iso}}(\bar{\mathbf{C}}) + \sum_{j=1}^{m} \Upsilon_j(\bar{\mathbf{C}}, \boldsymbol{\Gamma}_j) \,, \tag{3.66}$$

where $\Psi^{\infty}_{\text{vol}}$ and $\Psi^{\infty}_{\text{iso}}$ are respectively the volumetric and isochoric elastic response when time tends to infinity. The last term in equation (3.66) represents the non-equilibrium state and is called the dissipative potential. Tensors $\boldsymbol{\Gamma}_j$ determine the relaxation/creep behaviour, with $j = 1, ..., m$ the number of "viscoelastic processes" with their corresponding relaxation times τ_j, which play the same role as τ_i in the QLV model.

The second Piola-Kirchhoff stress tensor takes the form:

$$\mathbf{S} = \mathbf{S}^{\infty}_{\text{vol}} + \mathbf{S}^{\infty}_{\text{iso}} + \sum_{j=1}^{m} \mathbf{Q}_j \,, \tag{3.67}$$

with $\mathbf{Q}_j$ representing the non-equilibrium stresses, and $\mathbf{S}^{\infty}_{\text{vol}}$ and $\mathbf{S}^{\infty}_{\text{iso}}$ are respectively the fully elastic volumetric and isochoric contributions to the second Piola-Kirchhoff stress tensor. The evolution equations for these internal variables are taken, by analogy with the non-equilibrium stresses in a generalized Maxwell model, as:

$$\dot{\mathbf{Q}}_j + \frac{\mathbf{Q}_j}{\tau_j} = \dot{\mathbf{S}}_{\text{iso}\,j} \,, \tag{3.68}$$

where $\mathbf{S}_{\mathrm{iso}\,j}$ is the isochoric second Piola-Kirchhoff stress tensor which corresponds to the strain energy function $\Psi_{\mathrm{iso}\,j}$, responsible for the j relaxation process and defined in the subsequent equations. It is defined with the same structure of the right term of equation (3.14b) and equation (3.16):

$$\mathbf{S}_{\mathrm{iso}\,j} = J^{-2/3}\mathbb{P} : \bar{\mathbf{S}}_j, \qquad \bar{\mathbf{S}}_j = 2\frac{\partial \Psi_{\mathrm{iso}\,j}(\bar{\mathbf{C}})}{\partial \bar{\mathbf{C}}} \,, \tag{3.69}$$

being $\bar{\mathbf{S}}_j$ the fictitious second Piola-Kirchhoff stress. The solution of equations (3.68) for t $\in$ (0,T] is:

$$\mathbf{Q}_j = e^{-T/\tau_j}\mathbf{Q}_{j\,0^+} + \int_{t=0^+}^{t=T} e^{-(T-t)/\tau_j}\dot{\mathbf{S}}_{\mathrm{iso}\,j}(t)dt \,, \tag{3.70}$$

where $\mathbf{Q}_{j\,0^+}$ is the instantaneous response at the initial conditions. If the following assumption is made:

$$\Psi_{\mathrm{iso}\,j}(\bar{\mathbf{C}}) = \beta_j^{\infty}\Psi_{\mathrm{iso}}^{\infty}(\bar{\mathbf{C}}) \,, \tag{3.71}$$

the stress $\mathbf{S}_{\mathrm{iso}\,j}$ can be simplified as:

$$\mathbf{S}_{\mathrm{iso}\,j} = \beta_j^{\infty}\mathbf{S}_{\mathrm{iso}}^{\infty}(\bar{\mathbf{C}}) \,. \tag{3.72}$$

The β_j^{∞} constants are dimensionless strain energy factors, which make possible the simplification of the model through equations (3.71) and (3.72). These β_j^{∞} constants are equivalent to the g_i constants in the QLV model.

Chapter 4

Mechanical properties of breast tissues

4.1 Introduction

To develop a biomechanical FE model (and in general, any computational model) it is very important to characterise the behaviour of the materials which compose it, in order to obtain a reliable model. As seen in the previous chapter, the balance equations are valid for any material, but there are more unknowns than equations. So, it is necessary to add the constitutive equations of the material to solve the problem.

In this chapter, the experimental and computational procedures to estimate the mechanical properties of the tissues are presented in this introduction, along with the state of the art of the mechanical characterization of the tissues which compose the breast. Then, in section 4.2, a model for the mechanical behaviour of the mixture of fat and gland is included. This study was published in the article "J.L. Calvo-Gallego, J. Martínez-Reina, J. Domínguez. A polynomial hyperelastic model for the mixture of fat and glandular tissue in female breast. *International Journal for Numerical Methods in Biomedical Engineering* 2015; 31(9). doi: 10.1002/cnm.2723". Finally, the experimental tests carried out in this thesis to characterize the tissue are presented in section 4.3. A large part of the experimental procedure used in this section was published in the article "M.S. Commisso, J.L. Calvo-Gallego, J. Mayo, E. Tanaka, J. Martínez-Reina. Quasi-Linear Viscoelastic Model of the Articular Disc of the Temporomandibular Joint. *Experimental Mechanics* 2016; 56:1169-1177". Another part of the experimental procedure has been submitted as "J.L. Calvo-Gallego, M.S. Commisso, J. Domínguez, E. Tanaka, J. Martínez-Reina. Effect of freezing and storage time on the elastic and viscous properties of the disc of porcine temporomandibular joint" to the Journal of the Mechanical Behavior of Biomedical Materials.

4.1.1 Experimental estimation of properties

The most convenient way to determine the properties of a biological material is to carry out experimental tests. The final objective is to obtain a set of parameters which characterise a given strain energy function. This function represents the behaviour of the material and provides a mathematical framework to work with. Thus, the normal process is as follows: first, the tissue specimens are extracted from the donor (human or animal) and they are tested following a certain protocol; once the results of the tests are obtained, a strain energy function should be chosen; then the non-linear Continuum Mechanics equations are used to determine an analytical solution for the stress-strain relation of the performed test, which will be fitted to the experimental results. The choice of the strain energy function will depend on the shape of the experimental curve and on the results of the fitting algorithm. Normally, it is necessary to use several different functions, checking their goodness of fit to choose the best. The output of the fitting algorithm is a set of material parameters which defines the behaviour of the material together with the strain energy function used.

In the following, some parameters of the testing of living tissues and their influence on the results will be discussed.

4.1.1.1 Effect of freezing

In experimental tests of biological tissues, there are many things that should be taken into consideration. For instance, the tissues should be tested submerged in saline solution at 37°C, to maintain the physiological conditions of temperature and hydration, although some authors indicate that there is no difference between testing the specimens at 37°C or at room temperature [51].

A great debate still exists regarding the influence of freezing before testing on the mechanical properties of biological tissues and the influence of the time elapsed from the excision of the specimens to the test. Many authors claim that the cold storage causes changes in the mechanical properties of the tissues, as for example Linde and Sørensen [52], who analysed the effect of different storage methods on the elastic and viscoelastic properties of human trabecular bone under unconfined compression cyclic loading. They did not notice changes in stiffness but a significant change in viscoelastic properties. Clavert et al. [53] performed uniaxial tensile relaxation tests on human tendons (biceps brachii tendons) comparing the response obtained with immediate testing with that obtained after freezing at −30°C during 2 weeks, finding an altered ultimate tensile stress and Young's modulus. Kennedy et al. [54] carried out cyclic indentation tests on bovine articular cartilage, comparing a group tested fresh with specimens frozen at −20°C and −80°C. They checked that freezing decreased the stiffness. Chow and Zhang [55], who performed biaxial tensile tests on bovine aortic tissue stored at different temperatures and during intervals of different lengths, found several changes in the mechanical properties due to cold storage. Ternifi et al. [56] studied the influence of storage temperature on porcine kidney with shear wave elastography, concluding that freezing causes a decrease in

the shear modulus of the superficial zone but not in the central one.

Opposite to the previous studies, other authors state that freezing does not have any influence. For instance, Kiefer et al. [57], who performed indentation tests in bovine articular cartilage, concluded that the cryopreservation protocol used does not have any effect on its mechanical properties. Hongo et al. [58] obtained the same conclusion in porcine intervertebral discs, after conducting several types of test (lateral flexion, flexion-extension and rotation cycles) to analyse the effect of multiple freezing-thaw cycles. Van Haaren et al. [59] froze goat cortical bone during five different storage periods to study the effect on torsion, bending stiffness, strength and hardness. No significant differences were found. Nazarian et al. [60] carried out experimental tests on murine bone and stated that freezing does not change its mechanical properties. Szarko et al. [61] used indentation on bovine articular cartilage to check the influence of different storage temperatures. For $-20°$C and $-80°$C, they did not found alteration in the mechanical properties. Wex et al. [62] studied the mechanical properties of porcine liver tissue at different temperatures with shear relaxation and rheometry tests. No influence was noticed. Torimitsu et al. [63] froze cadaver skulls during different periods of time, concluding that it has little effect on the mechanical properties after conducting destructive 3-point bending tests. Wieding et al. [64], who performed destructive 4-point bending tests in ovine cortical bone using three different preservation techniques, did not find any difference in the elastic properties.

Obviously, the best option is testing the specimens submerged in saline solution at 37°C and as fresh as possible, trying to avoid freezing or any other preservation technique. In general, it is a good practice to avoid any procedure whose influence is not clear and could amplify the scatter of the results, but unfortunately, this is not always possible.

4.1.1.2 Zeroing the displacement

Another important point to consider is the definition of the zero displacement in the test. A wrong definition of this zero can produce errors in the characterisation of the mechanical behaviour of the tissue. For example, in a uniaxial compression test between two platens, if the upper platen is the movable one, while bringing the platens together before the experiment it is crucial to know where it should be stopped, which defines the zero of the displacement. Errors in this estimation may lead to a prestress if the platen has been moved too much towards the specimen or a shift in the measured displacement if the platen has been stopped too far away from the specimen. This error can have a big influence on the results, mainly in the toe region. Usually, the problem lies in the fact that the top surface of the specimen is not flat, which complicates the visual detection of contact. Moreover, since the contact cannot be considered as fully established when the platen just touches the upper part of this top surface, the platen must be positioned such that it is compressing a certain portion of the specimen. This occurs, for example, in the articular discs of the temporomandibular joint, which has a sloping top surface. With this type of specimens, some authors measure their height in several points to calculate a mean height. Then, they zero the displacement when the distance between the

platens is equal to the mean height [65]. In the specimens in which the top surface can be considered flat, the procedure is easier. Some authors move the upper platen until it comes into contact with the specimen, visually estimating this contact. Other authors lower the upper platen until it contacts with the specimen, determined from both visual inspection and from an initial increase in force (0.01N) [66].

In this thesis, the method to extract and prepare the specimens allowed obtaining them with the top and bottom surfaces plane and approximately parallel and, thus, for simplicity, the platen was positioned at the mean height of the specimen by visual inspection.

4.1.1.3 Scatter of the properties

A significant point to take into account too is the scatter in the properties of biological tissues. The same type of tissue in different individuals may not have the same behaviour. Even the comparison of the tissue in different regions of the same individual can lead to different properties. The general structure of a given healthy tissue is the same in every person, but the specific composition (relative quantities of the inner components) can vary, depending on many factors: life style, diet, weight, etc. For example, the bone mineral density is highly dependent on the physical activity [67]. In the same person, the structure of a tissue can be quite different across regions. For instance, it is known that the structure and composition of the articular cartilage depends on the depth [68, 69]. This variation in properties between individuals and across regions introduces an additional difficulty to characterise a given tissue. This makes necessary the use of statistical tools to overcome this trouble, assigning average properties which are able to represent the whole tissue.

4.1.2 Computational estimation of properties

Another way to characterise the behaviour of a biological material is a purely computational approach. It consists in knowing two different configurations of the body during the deformation process and simulating the transition from one to the other. To do that, it is necessary to choose a strain energy function beforehand and design an iterative process in which the material parameters of the strain energy function are changed in each iteration towards the optimisation. Finally, an optimum is reached if, starting from one configuration, the other configuration is reached (within a certain tolerance).

In general, the experimental approach is preferred because it provides more realistic properties of the tissue, though all the problems pointed out in the previous paragraphs and also all the approximations and errors that are usually committed while carrying out experimental tests must be kept in mind. The computational approach is easier from a practical point of view. It also tends to be more phenomenological, because it consists in matching two deformed shapes by taking into account a global behaviour. Moreover, the properties experimentally obtained are valid, in general, for any other situation, while those obtained

through numerical approximation are only valid, commonly, in this particular application.

4.1.3 Mechanical properties of breast tissues. State of the art

The material model chosen for the tissues is a key factor as said above, for its strong influence on the accuracy of the computational models [70, 71]. The breast is entirely composed of soft tissues which usually have a strong non-linear behaviour because of their internal structure and water content. Their behaviour is usually approximated as quasi-incompressible and hyperelastic. Depending on the importance of dynamic loads, viscoelastic effects should be added [72]. Moreover, depending on the internal microstructure, they can be considered as isotropic or anisotropic, for example, by modelling the collagen fibre directions [38].

Some information can be found in the literature about modelling the mechanical properties of fat and fibroglandular tissues. Most of the works modelled both tissues as isotropic and quasi-incompresible materials. Some considered the fat as anisotropic due to the connective tissue network inside the adipose tissue [7, 14], but no reliable work was found which experimentally obtained these anisotropic properties. Sarvazyan et al. [73] measured the Young's moduli of fat tissue, fibroglandular tissue and tumorous carcinoma. Krouskop et al. [74] obtained experimentally the elastic modulus of the breast tissue subjected to compression loading. Wellman [75] studied the non-linear behaviour of fat and glandular tissue and used exponential curves to describe the stress-strain relationship. Lorenzen et al. [76] determined the linear elastic properties of breast tissues by means of elastography, including breast tumours. Samani et al. [24] considered them as elastic and determined experimentally the Young's moduli of samples of both tissues. Some time later, Samani and Plewes [41] determined experimentally their elastic properties, but considering the materials as hyperelastic, with a five terms polynomial strain energy function. Other studies by Samani et al. [77, 51] and by O'Hagan and Samani [78, 79] have provided the properties of breast tissue with tumoral inclusions.

Other authors have tried to obtain the mechanical properties through numerical methods. Usually, they acquire Computed Tomography (CT) or MR images from the body in two different positions, for example, supine and standing up. Then, a FE model is constructed, and the constants of the strain energy function are determined by fitting the relative displacements between both positions. Pérez del Palomar et al. [18] fitted the constant of a neo-Hookean model for the tissue inside the breast with this technique (they did not differentiate between fat and glandula, considering them as a whole tissue). Rajagopal et al. [16, 17] also considered a unique neo-Hookean material and obtained the value of its constant starting from an unloaded configuration and reaching the prone position. Han et al. [7] obtained the properties of fat, glandula, muscle and tumour matching images in a mammographic compression of the breast and using a simple anisotropic model. Some time later, Han et al. [15] carried out a similar analysis, but using a neo-Hookean law and applying gravity loads in the prone position to reach the supine one instead of a compression. Gamage et al. [19] also simulated a change of position from prone to supine fitting a neo-Hookean model too.

In view of the above properties, linear elastic models were discarded in this work because the biological materials seem clearly nonlinear. If the deformation range is small, a linear elastic behaviour could be enough, but considering the large deformations produced in the breast, this type of material had to be discarded. Neo-Hookean models were also discarded. It is an easy model to use as it only has one parameter to fit, but it is clearly not enough to capture such a complex behaviour as this of the breast tissues. For this reason the model proposed by Samani and Plewes in 2004 [41] was initially implemented, and some other models were subsequently used.

The mechanical properties of fat in other parts of the body have been studied by some authors. For example, Sommer et al. [47] determined the mechanical properties of the human abdominal adipose tissue carrying out biaxial and shear tests. This material model was not initially used because the FE model was intended for a healthy breast, and therefore it was preferable to use properties obtained from the adipose tissue of the breast. Moreover, it is an anisotropic model with one family of fibres, but no information exists about the number of families of fibres and their orientation in the breast as far as the author knows. However, this model was finally used in this work to analyse the behaviour of the breast with an anisotropic model. The direction of the fibres was initially established as a hypothesis as will be seen in the next chapter.

4.1.4 Mechanical properties of skin. State of the art

The properties of skin have been studied in the literature more widely than those of fat and glandular tissue. The behaviour of skin is clearly nonlinear and anisotropic, and highly dependent on age [80, 81] and other variables, like for instance, hydration [82]. However, many authors made certain simplifications to model its behaviour. The literature about the mechanical properties of the skin is extensive but here, only those works dealing with the skin of the breast are presented, and some others which have been considered convenient. In the early 70's, Veronda and Westmann [83] performed tests on cat skin and determined its non-linear properties by fitting a custom-made strain energy function. Agache et al. [84] studied in vivo the viscoelasticity of the skin by means of a torque applied to the human forearm. Bischoff et al. [85] used an Arruda-Boyce strain energy function to fit experimental data by other authors. Gambarotta et al. [86] determined the in vivo mechanical properties of human skin. Pérez del Palomar et al. [18] covered their breast model with a layer of skin, modelled with a polynomial strain energy function fitted with the experimental results obtained by Gambarotta et al. [86]. The same did Lapuebla-Ferri [21] and Vavourakis et al. [23] in their models. Delalleau et al. [87] performed suction deformation tests on the forearm skin. They fitted a standard linear elastic model, a neo-Hookean model and a nonlinear one, characterised by two linear regions with different slopes. They concluded that the linear and neo-Hookean models cannot be used whereas the nonlinear one allows a good fit. Barbarino et al. [43] carried out experiments with a suction device to obtain the properties of the skin of the face. They used the model proposed by Rubin and Bodner

[42]. Annaidh et al. [88] studied the anisotropy of the human skin from the back, proving that its mechanical properties are dependent on the direction, but they did not propose any constitutive model. Sutradhar and Miller [89] determined the Young's modulus of the skin using a suction device. Khatam et al. [90] studied experimentally the deformations of the breast skin, but they did not propose any strain energy function. Some authors does not include the skin in their breast model, either because simplicity reasons or because they include it into a bulk material forming the breast [22, 16, 17, 19, 14, 4, 7].

In this thesis, the models proposed by Barbarino et al. [43] and Pérez del Palomar et al. [18] were used.

4.1.5 Mechanical properties of muscle. State of the art

In this study, the properties of muscles, although relevant, were not the most important ones. Muscle tissue is considerably stiffer than fat and glandula, so that its deformation under gravity forces is negligible. Moreover, it is important to note that in this work, while changing the position from supine to prone (or to standing up), the rest of the body should remain fixed, that is to say, there would be no relative movement between the arms and the trunk, so that only the breast would be free to move. In practice, it was difficult to ensure in the acquisition of images in supine and prone positions. Although it was intended to maintain the rest of the patient's body exactly in the same position relative to the trunk, there could be little variations. For instance, the angle between the arms and the trunk could be slightly different, so changing the position of the pectoral muscle and therefore of the breast tissues. The protocol applied during the image acquisition in this work tried to minimize these variations.

Due to the fact that muscles are not contracted during these movements, it was not necessary to consider an active-passive model of the muscle, but it was enough using a hyperelastic or even a linear elastic model. In the literature, some information about the elastic properties of the muscles can be found. Only the models which were used in this thesis are included here. For example, Barbarino et al. [43] obtained experimentally the properties of the muscle in the face, fitting a hyperelastic model proposed by Rubin and Bodner [42]. Ohl et al. [91] studied numerically the dynamics of a non-equilibrium bubble near some materials, included the muscles, modelling them as a linear elastic material with properties obtained experimentally on previous works.

4.1.6 Cooper's ligaments

Cooper's ligaments were not explicitly modelled in the present work for the reasons given next and, therefore, their properties were not needed. It is not easy to differentiate them in any medical image in order to construct a reliable model. Their structure, although qualitatively described by some authors using cadaveric dissections [92, 93, 94], has not been sufficiently described to allow an accurate modelling. Besides, these ligaments can play an important role in the mechanical behaviour of the breasts of young women, but

as women get older, ligaments become more and more slack and their role is less important [92, 95]. The reconstructive surgery is mainly applied in breasts of middle-aged to old women. Thus, the effect of Cooper's ligaments is not important, in a general basis. In chapter 5 it will be explained how the connective tissues network can be implicitly considered by using anisotropic models.

4.2 Model for the mixture of fat and glandular tissue

Computational models of the breast must face the problem of the complex distribution of tissues within the organ. The female breast is composed of various kinds of soft tissues, mainly fat, gland, Cooper's ligaments and skin. It is known that the fibroglandular tissue has a ramified distribution, starting from the nipple [96], but it is intermingled with the fat, thus, making the segmentation of both types of tissue from CT or MR images difficult in practice [97]. Moreover, Cooper's ligaments are difficult to distinguish even with advanced scanning techniques [98]. Therefore, building a computational model of the breast by distinguishing all the tissues is a hard task. Another difficulty is the fact that the volume fraction and the spatial distribution of each tissue vary much among women [18]. Because of this, most FE models of the breast do not distinguish the different tissues [18, 21, 99, 100, 17]. Instead, they model the breast as composed of a bulk material (a mixture of all tissues) covered with a thin layer of skin. The question addressed here is if that mixture of tissues is suitable for studying the breast, and which are the mechanical properties that reproduce the behaviour of the breast with the best accuracy, if possible, as a function of the fat volume ratio.

In the following, we will focus on the inner tissue of the breast, which, in a first approximation, will be modelled as a homogenized mixture of fat and fibroglandular tissue. The numerical method for homogenization of the mixture is based on the procedure proposed by Temizer and Zohdi [101]. The objective is to propose a mechanical model for the behaviour of that homogenized material, providing its properties as a function of the fat volume ratio, termed as f from now on. This is intended to simplify the computational models of the breast by suppressing the need for segmentation of fat and fibroglandular tissue in the breast. To achieve this objective, it is important to study how the distribution of both tissues affects the global behaviour of the breast. Thus, the mechanical behaviour of different mixtures of fat and fibroglandular tissue has been analysed as well as the effect of different proportions and distributions of tissues on the model parameters. All the conducted studies and simulations explained in the following sections have been organised in groups of experiments, with different objectives. For a better understanding a summary is presented in table 4.1.

Study	Objective	Type of computational model	Number of cases	Number of load cases in each case	Results
A	To fit a mechanical model of the homogenized tissue as a function of the fat content	Cubic model (8000 elements) with a uniform spatial random distribution of fat and glandula	16 cases (with different random distributions) per fat proportion (10, 30, 50, 70 and 90%)	3 load cases: uniaxial tension and compression and shear Total=16x5x3	Constants of the strain energy function used to model the homogenized tissue
B	To determine the influence of zones with higher concentration of one type of tissue	Same as in study A, but with different number of elements	2 cases: one with 1000 elements and another with 125 (50% of fat both). 16 cases (with different random distributions) per each one	3 load cases: uniaxial tension and compression and shear Total=16x2x3	Comparison with the constants obtained in study A
C	To determine the behaviour of the homogenized material in a simplified breast geometry	Spherical cap model	One model with the homogenized tissue and the other with a ramified distribution of fibroglandular tissue	3 cases per model, corresponding to prone, supine and standing up positions Total=2x3	Comparison of the displacements of both models
D	To determine the behaviour of the homogenized material in a simplified breast geometry with different boundary conditions	Spherical cap model	One model with the homogenized tissue and the other with a ramified distribution of fibroglandular tissue	3 cases per model, corresponding to prone, supine and standing up positions Total=2x3	Comparison of the displacements of both models

Table 4.1: Summary table of the conducted studies.

4.2.1 Study A

4.2.1.1 Methods

To determine the elastic properties of the homogenized material as a function of the fat volume ratio, a simple FE model has been built using Abaqus FEA®. The model consists in a cube with dimensions 1x1x1 mm^3 and meshed with 8000 type C3D8H elements (3D eight-noded hexahedral hybrid elements), 20 equally sized elements per edge.

The boundary conditions applied to the model depend on the load case considered: uniaxial tension, uniaxial compression or shear, and are explained below. In addition, displacement symmetry boundary conditions have been imposed in all cases in the $x = 0$, $y = 0$ and $z = 0$ faces of the cube (see figure 4.1). These symmetry conditions would be necessary in a homogeneous material to simulate a uniaxial stress state and were applied to the heterogeneous model for consistency of the homogenization procedure.

In tension, a uniform displacement in z direction has been applied to the $z = 1$ face of the cube, with no

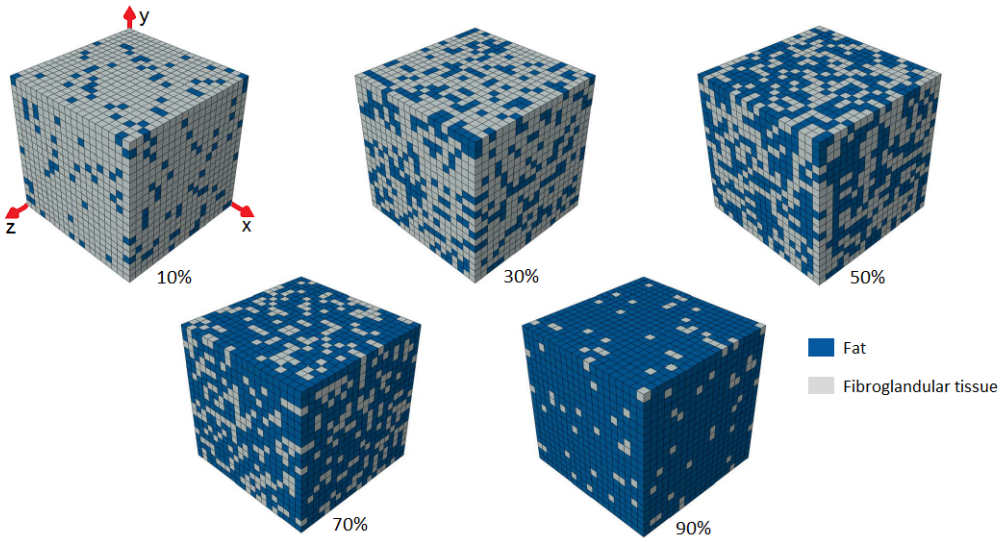

Figure 4.1: Cubic models with 10%, 30%, 50%, 70% and 90% of fat.

other restrictions. Since the behaviour is assumed incompressible, the deformation gradient tensor enforced is the one shown in equation (3.24e).

The stretch, λ, has been increased from 1 to 1.5. In compression, identical boundary conditions were applied, but now decreasing λ from 1 to 0.7. Finally, in the pure shear load case, uniform displacements were enforced in the y and z directions, such that the deformation gradient tensor is the one shown in equation (3.27c). The stretch, λ, has been increased from 1 to 1.5 in this case.

Next, material properties were assigned to each element, corresponding to fat or fibroglandular tissue. This assignment was random, with a uniform spatial distribution, that is, with no bias for any position within the cube, except for accomplishing a given fat proportion (in terms of volume ratio). This random distribution was obtained by numbering the elements of the mesh and assigning the fat properties to a series of elements obtained with the Matlab function *rand*. This function generates uniformly distributed pseudorandom numbers, which pass the required statistical tests of randomness and independence. The fat and fibroglandular tissue were assumed isotropic, hyperelastic and quasi-incompressible materials, and were modelled with a 5 terms polynomial strain energy function (equation (3.23)). The constants C_{ij} of the fat and fibroglandular tissues were taken from Samani and Plewes [41] and are shown in table 4.2, corresponding to the fat volume ratios $f = 0$ and $f = 1$.

Five fat volume ratios were tested: 10%, 30%, 50%, 70% and 90%. Sixteen cases with different random spatial distributions were studied for each fat volume ratio. Figure 4.1 shows one of the 16 cases for each fat volume ratio.

Each case was subjected separately to the three load cases (tension, compression and pure shear) by applying the corresponding displacement in N small increments. The evolution of Cauchy stresses during the load (σ^T_{zi} in tension, σ^C_{zi} in compression and σ^S_{yi} and σ^S_{zi} in pure shear, for $i = 1, ..., N$) was evaluated with

help of the FE solution, as usual in homogenization procedures. The nodal reaction forces in each direction and each face of the cube were retrieved from the FE solution. These nodal reaction forces were summed to obtain the total reaction forces, R_{ij}, in each direction i and each face j, and with them the components of the first Piola-Kirchhoff stress tensor, $P_{ij} = R_{ij}/A_0$, where A_0 is the area of the corresponding face in the initial configuration. Then, with the well-known relation $\boldsymbol{\sigma} = J^{-1}\boldsymbol{P}\boldsymbol{F}^T$, the effective Cauchy stress tensor was obtained. It is important to note that the stress states were not uniaxial in the heterogeneous models (or that corresponding to a pure shear state in that particular case). However, the stress components that violated the uniaxiality were negligible (two or three orders of magnitude lower than the uniaxial stress) as it is well-known from homogenization theory.

The homogenized tissue was assumed isotropic, hyperelastic and quasi-incompressible, and modelled with the same strain energy function as the fat and fibroglandular tissues (equation (3.23)).

The Cauchy stresses of the homogenized tissue can be represented analytically as a function of the constants C_{ij} and the stretch as follows. First, the analytical Cauchy stress tensor is given by equation (3.11). In uniaxial tension this tensor is as shown in equation (3.24a). The same applies for uniaxial compression, just substituting $\sigma^C_{z\,an}$ for $\sigma^T_{z\,an}$. In pure shear, this tensor is written in principal axes as presented in equation (3.27b). The subscript "an" stands for analytical solutions.

Calculating the $\mathbf{b}$ tensors (equations (3.24f) and (3.27d)) from the deformation gradient tensors of equations (3.24e) and (3.27c), and substituting for $\mathbf{b}$ in equation (3.11), the components $\sigma^T_{z\,an}$, $\sigma^S_{y\,an}$ and $\sigma^S_{z\,an}$ of the Cauchy stress tensor are obtained, whose expressions can be seen in equations (3.26) , (3.29a) and (3.29b) respectively.

The expression for $\sigma^C_{z\,an}$ is identical to that for $\sigma^T_{z\,an}$. A measure of the error produced in the estimation of the Cauchy stresses with this method can be represented by the squared error, SE, of the three load cases altogether:

$$SE(C_{10}, C_{01}, C_{11}, C_{20}, C_{02}) = \sum_{i=1}^{N}(\sigma^C_{zi} - \sigma^C_{z\,an})^2 + \sum_{i=1}^{N}(\sigma^T_{zi} - \sigma^T_{z\,an})^2 + \\ + \sum_{i=1}^{N}\left((\sigma^S_{yi} - \sigma^S_{y\,an})^2 + (\sigma^S_{zi} - \sigma^S_{z\,an})^2\right), \tag{4.1}$$

where N is the number of points used in each load case to compare the analytical and the FE solution.

The analytical stresses in equation (4.1) depend on the constants C_{ij} of the model, which can be fitted by minimizing SE in the least squares sense. With this procedure, a set of constants was estimated for each of the 16 random cases. Finally, the average constants of those 16 cases were obtained for each fat volume ratio.

Fat volume ratio		C_{10}	C_{01}	C_{11}	C_{20}	C_{02}	(10^{-4} MPa)	RMSE (kPa)
$f = 0$ (pure gland)		3.3	2.8	44.9	77.2	94.5	(A.Samani, 2004)	
$f = 0.1$	μ	3.2835	2.8271	42.5265	72.9896	89.2642		$3 \cdot 10^{-4}$
	σ	0.0074	0.0054	0.1206	0.0632	0.0521		
$f = 0.3$	μ	3.2453	2.8826	37.8507	64.6884	79.0541		$9 \cdot 10^{-4}$
	σ	0.0089	0.0064	0.1857	0.0832	0.0911		
$f = 0.5$	μ	3.2010	2.9331	33.3466	56.5675	69.2128		$7 \cdot 10^{-4}$
	σ	0.0166	0.0138	0.2114	0.1170	0.0911		
$f = 0.7$	μ	3.1738	2.9600	28.7921	48.8806	59.9891		$8 \cdot 10^{-4}$
	σ	0.0179	0.0136	0.2476	0.1341	0.1146		
$f = 0.9$	μ	3.1249	2.9899	24.5546	41.5000	51.2965		$3 \cdot 10^{-4}$
	σ	0.0059	0.0042	0.0967	0.0475	0.0428		
$f = 1$ (pure fat)		3.1	3.0	22.5	38.0	47.2	(A.Samani, 2004)	

Table 4.2: Mean, μ, and standard deviation, σ, obtained for each constant of the polynomial strain energy function. The fat volume ratio is termed as f.

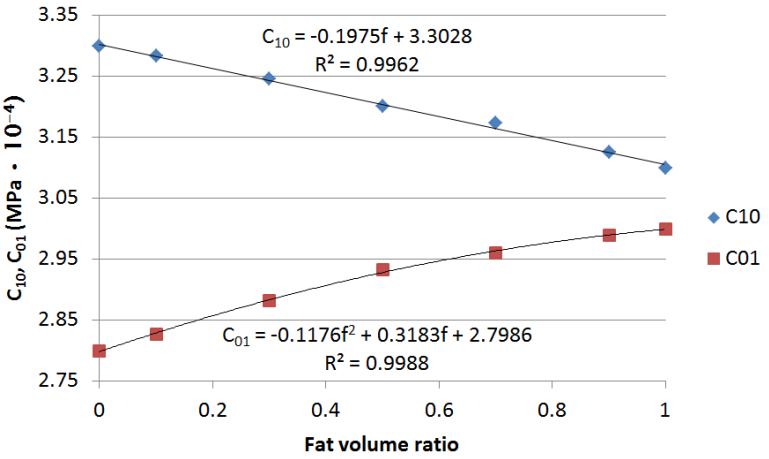

Figure 4.2: Correlations between C_{10} and C_{01} and fat volume ratio, f.

4.2.1.2 Results

The constants of the polynomial strain energy function were fitted for each of the 16 cases studied per fat volume ratio, by minimizing the SE given in equation (4.1). The mean and standard deviation for these constants were calculated for each fat volume ratio and are shown in table 4.2. The root-mean-squared errors (RMSE) for the 16 cases are also shown in table 4.2. Linear or quadratic regressions were selectively proposed between the 5 constants C_{ij} and f (see figures 4.2 and 4.3).

The small errors found in the least squares fitting of the constants with the three load cases applied (see table 4.2) show that the polynomial model is suitable to reproduce the behaviour of the homogenized tissue, provided that the individual compounds are well modelled with a polynomial model with the constants given by Samani and Plewes [41].

The mean values of the constants C_{ij} vary much with the fat content, confirming that the fat volume ratio

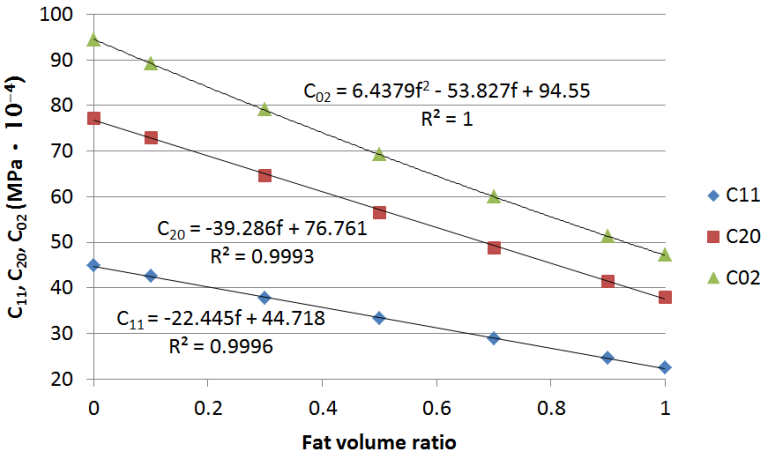

Figure 4.3: Correlations between C_{11}, C_{20} and C_{02} and fat volume ratio, f.

is a key factor in determining the properties of the composite tissue. In addition, the standard deviations are small, indicating that the distribution of fat is not so important, at least in the random distribution. A linear regression between the constants and the fat volume ratio fits quite well, except for C_{01} and C_{11}, for which a quadratic regression fits better.

In homogenization techniques, the application of displacement boundary conditions to obtain an average stress provides an upper bound of the effective stiffness. Alternatively, the application of traction boundary conditions to obtain an average displacement provides the lower bound. For this reason, three alternative loads were applied: constant tension, compression and pure shear stress in the corresponding faces of one model with 50% of fat proportion. The stretches, λ, were computed in this case, resulting in negligible differences of less than 0.03%.

4.2.2 Study B

4.2.2.1 Methods

After estimating the constants of the homogenized material for each fat volume ratio, other material distributions and geometries were simulated to test the behaviour of the homogenized material.

In study B, the same procedure followed in study A was conducted, but meshing the cube with less elements. By reducing the number of elements, it is more likely to have larger pieces of a single tissue. Such distribution would be closer to reality if both types of tissue were not as intermingled as in the model of study A. Then, the aim of the study B was to analyse the influence of these larger pieces of a single tissue in the overall behaviour of the homogenized material. Only the case of 50% fat volume ratio was analysed in this study. Two models, with 1000 and 125 elements, respectively, were tested and compared to the original model of 8000 elements (see figure 4.4). The selection of these element sizes (between 50 and 200 μm) is justified since a terminal duct lobular unit (TDLU) has an approximate diameter of 200-600 μm and the

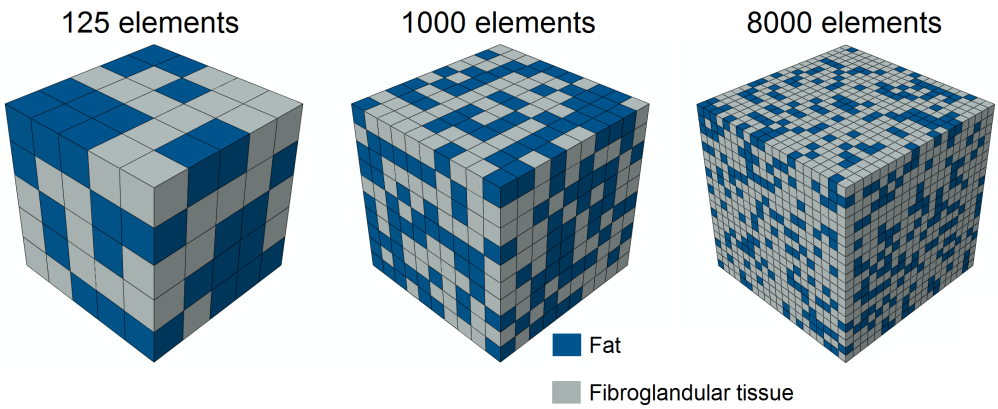

Figure 4.4: Cubic models with 125, 1000 and 8000 elements.

Number of elements	C_{10}	C_{01}	C_{11}	C_{20}	C_{02}	(10^{-4} MPa)
8000	3.2010	2.9331	33.3466	56.5675	69.2128	
1000	3.2056	2.9325	33.3109	56.4507	69.0912	
125	3.2007	2.9421	33.5065	56.4038	68.9541	

Table 4.3: Comparison between the uniform random distribution models with 8000, 1000 and 125 elements for $f = 0.5$.

little lactiferous ducts, which join those TDLUs, have an approximate diameter of 40-60 μm [27, 29]. During breastfeeding, these ducts increase their size, but that can be considered a marginal state of the female breast.

4.2.2.2 Results

A comparison of the random distribution models for different number of elements: 8000, 1000 and 125; was made for $f = 0.5$. The constants of the polynomial model obtained are shown in table 4.3.

The constants of the strain energy function are very similar in all cases, confirming that the homogenization is also valid in a breast in which larger pieces of a single tissue exist.

4.2.3 Study C

4.2.3.1 Methods

In study C, a simplified geometry of the tissue inside the breast, consisting in a spherical cap of 8 cm in radius and a height of 6 cm was built and meshed using 93312 type C3D8H elements. Two models were analysed for this geometry, one distinguishing between fat and fibroglandular tissue, named ramified model, and the other one without differentiation, i.e. using the homogenized material properties. The ramified model is shown in figure 4.5 and has 45.3% of fat. To construct this ramification, the point N1 (see figure 4.5) was established as the origin of a number of beams equally spaced over the spherical cap. The glandular tissue

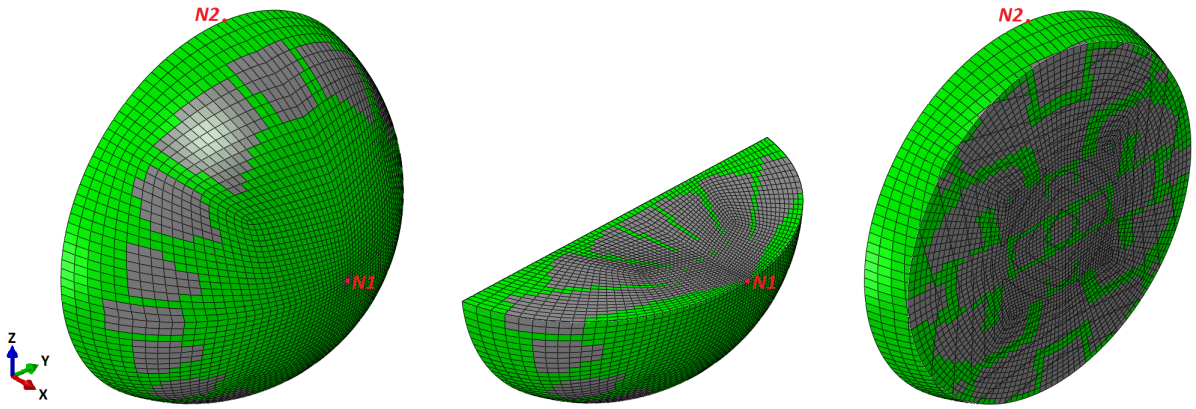

Figure 4.5: Ramified model.

was assigned to the elements within the beams, whose width was arbitrarily set, such that gland and fat were approximately divided in equal proportions.[1] This distribution tries to mimic, in a simplified manner, the ramified distribution of glandular tissue in an actual breast, in which the gland is more abundant near the nipple, where the lactiferous ducts converge. It must be clear that the intention of this study was not modelling an actual breast, in which case the skin (not included in this model) should be added and more complex boundaries conditions should be considered to model the interaction with the surrounding tissues and organs. The aim of study C was to compare the behaviour of both models (homogenized and ramified) under gravity loads, so to check the validity of the homogenization procedure when applied in a geometry similar to the actual one.

As boundary conditions, all the displacements were constrained in the back plane of the spherical cap, i.e. in the contact with the chest wall, like in other studies [18, 21]. Both models were subjected to gravity loads simulating three body positions: supine (gravity acting in the negative x direction of figure 4.5), prone (gravity acting in the positive x direction) and standing up (gravity acting in the negative z direction). The displacements of the nipple (point $N1$) in both models (ramified and homogenized) were compared for each load case.

The densities considered for fibroglandular and fat tissues were 1.04 g/cm^3 and 0.93 g/cm^3, respectively [102, 103, 104]. For the homogenized material, the density was calculated using the rule of mixtures.

4.2.3.2 Results

The results of the spherical cap geometry are presented here. The displacement of the nipple (node $N1$, see figure 4.5) in both models (ramified and homogenized) for the three body position simulated are compared in table 4.4. The relative difference between those displacements is also shown in the table.

The relative differences in displacement between both models (ramified and homogeneous), shown in

[1] The 50-50% is the most compromising proportion from the homogenization point of view. This homogenization procedure is more accurate as one constituent predominates and is exact for a 0-100% proportion, obviously.

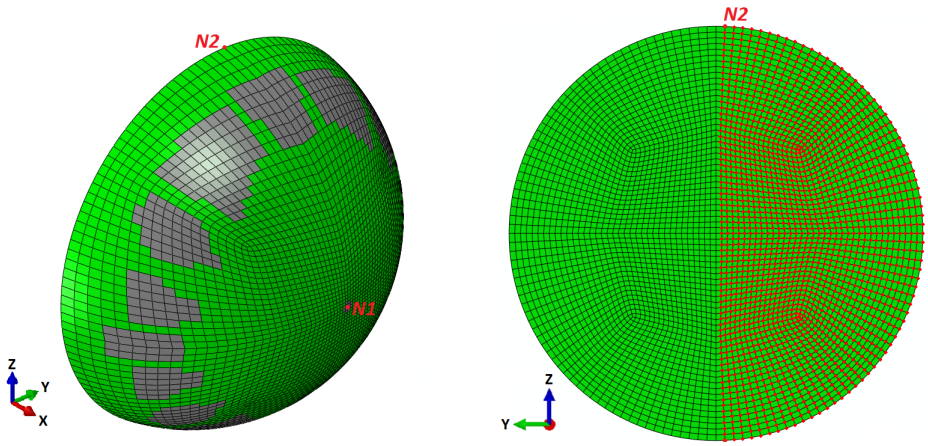

Figure 4.6: Boundary conditions of the back plane in study D.

table 4.4, are very small, thus confirming the validity of the homogenized model. Despite these good results, the magnitude of the displacements seems low compared to actual displacements in a real breast [19]. This is likely due to the simplistic boundary conditions imposed in the model (fixing the nodes in contact with the chest wall). The actual connection of the tissues is likely more flexible and makes those displacements to be larger. That is the reason why a second model with different boundary conditions (study D) was analysed.

4.2.4 Study D

4.2.4.1 Methods

Finally, in study D, the same procedure followed in study C (with the same models and materials) was conducted, but now changing the boundary conditions. In study C, all the displacements were constrained in the back plane of the spherical cap. In study D, the displacements were constrained in half of the back plane (in the right part of figure 4.6, the nodes that are highlighted in red color), while in the other half the nodes were connected with a certain stiffness to a rigid wall (the same stiffness in directions x, y and z). It is known that the connection between the breast and the chest is carried out through muscles and ligaments, and they have some flexibility. This precise configuration of dividing the breast in two halves was selected for producing a deformed shape that resembled the actual one more closely than that of the study C. To some extent, the rigid connection of the left part is mimicking the constraining effect of the sternum. The results shown here correspond to a stiffness of those connectors of 0.05 N/m, which was adjusted to produce a displacement of the nipple similar to the actual one. Anyhow, this study did not pursue a precise modelling of the boundary conditions of the breast, but studying the behaviour of the bulk material of the homogenized model in a more realistic scenario.

		Homogenized model	Ramified model	Relative difference
Spherical cap	Supine	1.83	1.85	0.86%
	Prone	2.02	2.04	0.83%
	Standing up	5.98	6.03	0.79%
Spherical cap with more flexible boundary conditions	Supine	17.665	17.591	0.42%
	Prone	13.491	13.463	0.2%
	Standing up	7.546	7.611	0.85%

Table 4.4: Modulus of the displacements (mm) of the nipple in the spherical cap geometry and in the spherical cap geometry with more flexible boundary conditions in both models and in the three body positions simulated. Relative difference between those displacements.

4.2.4.2 Results

The results of the spherical cap geometry with more flexible boundary conditions are presented here. The displacements of the nipple in both models for the three simulated body positions are compared in table 4.4. The relative difference between those displacements is also shown in the table.

As mentioned before, the intention was not modelling very precisely the actual boundary conditions of the breast, but checking if the behaviour of the bulk homogenized tissue is still valid with boundary conditions that produce a deformation state closer to the actual one. And so it is, given that in study D the displacements obtained with the homogenized model are very similar to those obtained with the ramified model.

4.2.5 Some remarks on the homogenized model

The usefulness of this homogenization study is linked to the availability of assessing the fat volume ratio within the breast in a straightforward way, at least approximately. Several techniques exist to measure that fat volume ratio, as has been stated in section 2.6. For some purposes, the aforementioned fat proportion categories (0-25%, 25-50%, 50-75%, 75-100%) can be enough in view of the variation of the material constants with the fat content. Therefore, a quick visual assessment of the fat volume ratio through mammography and the use of the proposed homogenized model can strongly simplify the problem of patient specific breast models.

The study has also some limitations. The interfaces between fat and gland have been modelled as a rigid union, i.e. the contact between both materials has not been taken into account. Moreover, the model depends on the suitability of the properties of fat and gland given by Samani and Plewes [41], which have been used to develop the present model. It is also important to note that the strain energy function used by these authors is not policonvex. However, this fact does not necessarily mean that this function should be ruled out, as explained in [105, 106, 107]. Finally, the homogenization procedure carried out here provides a material model which is adequate to simulate the bulk behaviour of the mixture of gland and fat, but it

would fail to describe the behaviour under very localized loads, like a needle insertion for example. In that case, the size of the needle could be of the same order of magnitude as that of the breast constituents. The structural organization of the tissues might play an important role and a microscopic model would be needed in such case.

4.3 Experimental characterisation of breast and abdominal tissues

Due to the scarce information that can be found in the literature about the mechanical properties of the adipose tissue in the breast as well as in the abdomen, experimental tests were carried out. Besides, these tests were motivated by the fact that, using the properties of fat provided in the literature to build a FE model of the breast, its behaviour is very far from the real behaviour of this organ, as will be seen later in the chapter devoted to numerical simulations. Indeed, the deformation seen in the model using the constants given by Samani and Plewes [41] is very low, indicating that the behaviour with such constants is much stiffer than the real one. Therefore, the suitability of the properties provided in the literature needs to be checked with care. Even less information exists about the properties of glandula, because samples are very difficult to be obtained. Due to the fact that the properties of glandula and fat are similar [41], that many authors model the breast with only one material, merging together adipose and glandular tissue [18, 21, 99, 100, 17], and that the homogenization procedure explained in section 4.2 seems to be adequate to model the mixture of adipose and glandular tissues, a unique material is going to be considered inside the breast.

4.3.1 Test protocol

4.3.1.1 Preparation of specimens

The adipose tissue samples were extracted from the breast and the abdomen of several patients subjected to a mastectomy surgery. The abdominal tissue used in the experiments was the portion of the abdomen which was not eventually used for the reconstruction (see figure 4.7). Therefore, its size depended on how the surgery was performed. In fact, it is not easy to acquire it because in many occasions there is not enough remaining tissue, or even the piece is so small that only a few specimens can be extracted from it, being useless to carry out subsequent statistical analyses. The breast tissue was usually obtained from the contralateral breast, when the doctors decided to apply a mastopexy to improve the shape and symmetry of both the healthy and reconstructed breasts (see figure 4.8). Normally, it is difficult to obtain large pieces of abdominal and breast fat from the same patient. The tissue was extracted from a total of four patients, with a mean and standard deviation age of 52.3 ± 6.9 years. The age of the patients ranged from 42 to 57 years.

Once the pieces were extracted in the surgery, they were introduced in a cool-box with ice to preserve

Figure 4.7: One of the pieces of abdominal fat from which specimens were extracted.

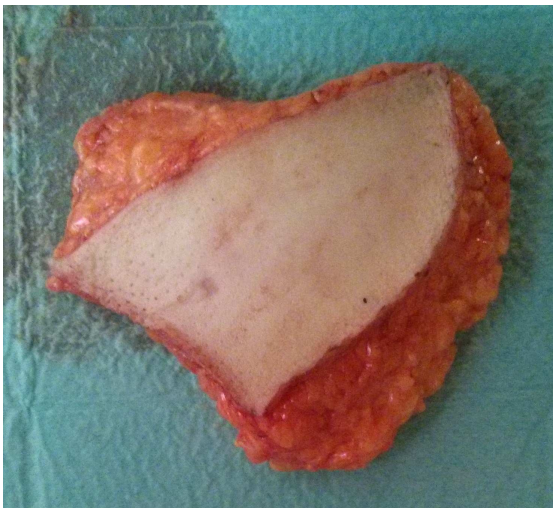

Figure 4.8: Breast fat sample.

them during transportation from the hospital to the Mechanical Engineering Laboratory. This was done shortly after excision (as soon as possible) to minimise the time the tissue was at room temperature. In the lab, the skin was removed from the piece by cutting a slice of tissue of approximately 5 mm in thickness. In the case of abdominal fat, the rest of the piece was divided in two slices of approximately equal size (superficial, underneath the skin; and deep, on top of the abdominal muscle), and each slice was, in turn, divided in two parts (medial and lateral). See figure 4.9 for a clear description of these divisions. The slices had a thickness ranging from 5 to 10 mm. This corresponded to the height of the tested specimens and was limited to that range to avoid slenderer specimens that could lead to buckling problems. This height is equal or lower than that used by Miller-Young et al. [66]. The division into lateral and medial parts was not performed in the smallest pieces. In the case of breast fat, only the division into superficial and deep slices could be done for size limitations. These divisions were intended to carry out statistical analysis to check if the mechanical properties of the fat are different depending on the region. All these cuts were made with a meat slicer machine and a sharp knife. It was important to make them while the tissue was cool, though

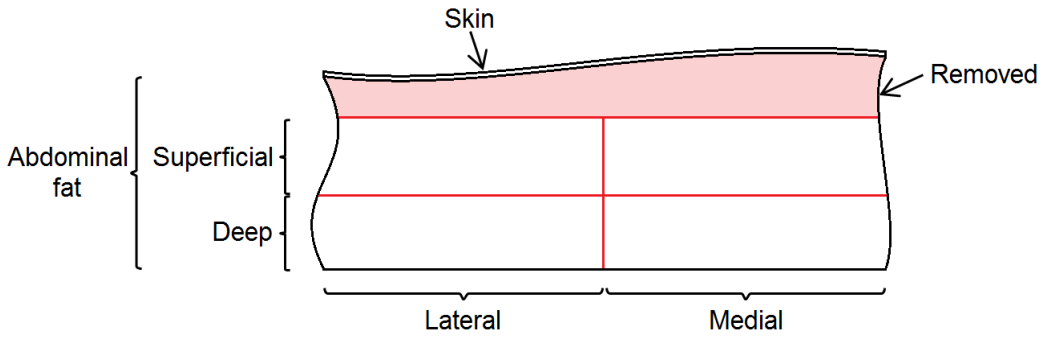

Figure 4.9: Diagram of the divisions in the sample.

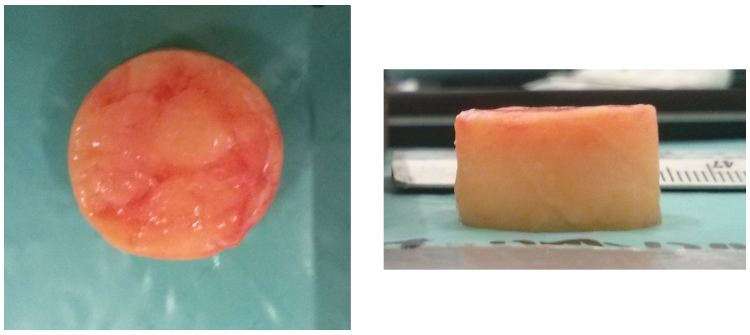

Figure 4.10: Cylindrical specimen, top and lateral views.

not completely frozen. If not, the fat is really soft and really difficult to cut in a proper way.

The reconstruction surgery with autologous tissue is quite long, so that the pieces could not be collected, transported to the lab, cut and tested in the same day of extraction. They were tested the days after, as soon as possible to reduce the time elapsed from excision to test. To avoid the degradation of the tissue, it was frozen. Each slice of tissue was wrapped in saline-soaked gauze, enveloped in a plastic film and introduced in hermetic vials to prevent dehydration and finally frozen at $-20°C$.

The tests were carried out in cylindrical specimens that were extracted from the slices with a hollow punch of 19mm of diameter. This needed to be done with the tissue frozen. Otherwise, the final shape of the specimens were irregular and far from cylindrical, because the tissue was largely deformed by the punch. Then the specimens needed to be extracted while the slice was still frozen. After that, the slice was returned to the freezer to prevent it from thawing. It is advisable to drive the punch into the tissue slowly, pushing with the hands. If this is done quickly, for example by hitting the punch with a hammer, the shape of the specimen is worse. A specimen with the final cylindrical shape can be seen in figure 4.10. Next, the specimen was submerged in saline solution at room temperature and allowed to thaw. Then, it was photographed with a rule next to it (to have a reference measurement) to measure its area through imaging techniques. It is important to make the photograph with the rule positioned at the height of top face of the specimen, in order to measure the true size of the specimen without perspective artifacts. It is also a good practice to

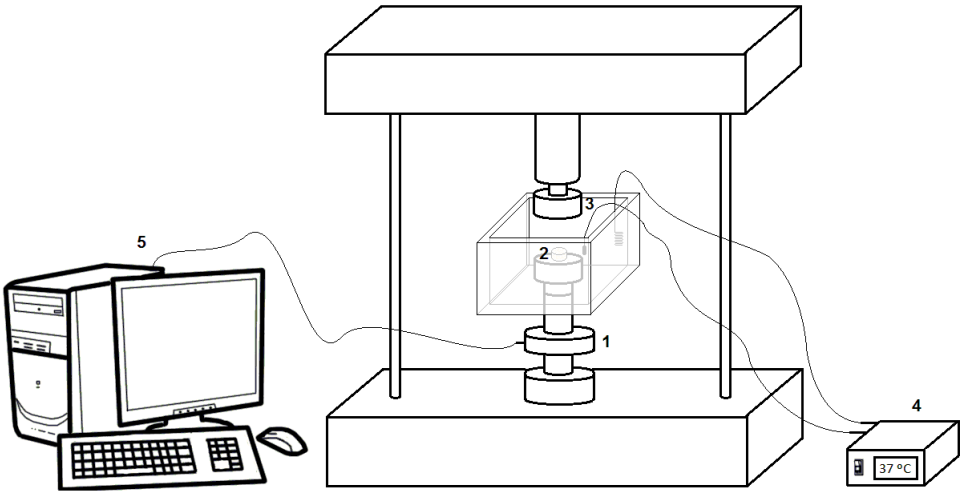

Figure 4.11: Scheme of the test. Remarked: (1) load cell, (2) sample, (3) upper platen, (4) temperature controller, (5) acquisition system.

take the photograph with the camera as far as possible from the specimen, to minimise likely optic errors.

4.3.1.2 Experimental setup

With the specimens prepared as explained before, the relaxation tests were carried out. The specimens were compressed between two platens, in a uniaxial compression test. To do this, a servo-hydraulic testing machine (858 Mini Bionix II, MTS, Eden Prairie, USA) was used together with ancillary equipment specially designed to perform the test under certain conditions of humidity and temperature. A scheme of the experimental setup can be seen in figure 4.11.

The experimental tests were carried out as follows. First, both platens of the testing machine were brought into contact to zero the displacement. Then, vaseline was spread on their surfaces to reduce friction (although this is probably not needed as the fat seemed to lubricate the platens itself). Once the specimen was thawed, it was placed in the center of the inferior platen of the testing machine. The specimen was not glued to the platen unlike in similar tests performed on articular discs in a previous study [65]. This was done to avoid any undesired effect of the boundary conditions. In all the conducted tests, the specimens remained within the platens, so that it was not necessary to glue them to prevent slipping. Next, a recipient was filled with saline solution (0.9% w/v of NaCl) at $37 \pm 1\,^{\circ}\mathrm{C}$ and the specimen remained submerged in it during the whole test. The temperature was controlled with a heater and a thermostat. After having zeroed the force, the upper platen was manually lowered, slowly approaching the sample, and visually positioned in contact with the top surface of the sample, as made in [66]. That served to measure the thickness of the specimen and to find the starting point of the test.

A preconditioning was applied to each sample: 20 cycles from 0% to 10% strain at 1 Hz, like in [108]. The preconditioning was followed by a ramp from 0% to ϵ strain, where ϵ was 40%, 50% or 60% depending on

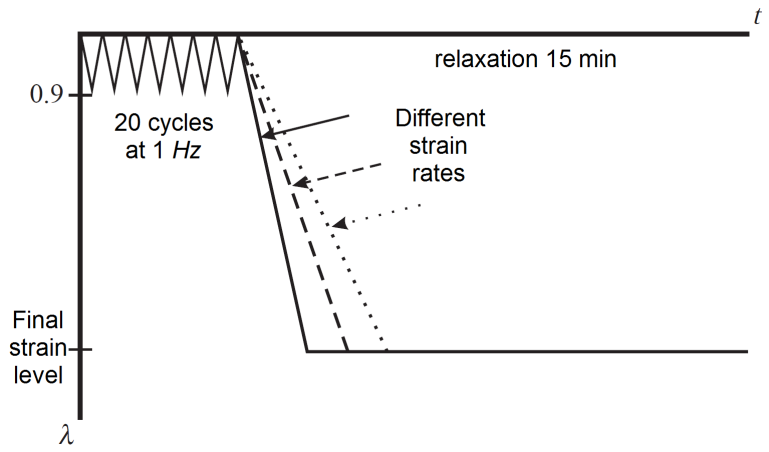

Figure 4.12: Scheme of the evolution of the stretch with time in the relaxation test.

the particular test, and this final strain was maintained for 15 min, allowing for stress relaxation (see figure 4.12). The strain level 50 % was the same used in [66], while 40 % and 60% were chosen below and above the level proposed by [66]. These three levels cover a wide enough range of strain to capture the behaviour of the tissue. Different strain rates of the loading ramp were tested: 50%, 60% and 70% /s. In [66], quasi-static compression was considered for strain rates in the range 0.01 - 0.1 % /s. Therefore, as a relaxation test instead of a quasi-static one is desired here, the chosen strain rates are 2 or 3 orders of magnitude higher, but not so high to have artifacts due to wave propagation [48, 109]. During the test, force and displacement of the upper platen were recorded. Later, they were converted into stress and stretch respectively.

4.3.2 Data fitting algorithm: QLV model

With the results obtained from the experimental tests, basically force and displacement, the mechanical properties of the tissue can be worked out by using a proper fitting algorithm. First, the QLV formulation proposed by Fung [48] and presented in section 3.3.1 was used to model the mechanical behaviour of the tissue. The QLV formulation has been widely used to model the behaviour of soft tissues [110, 111, 48, 112]. Moreover, it has been successfully used in our group to accurately describe the behaviour of the articular disc of the temporomandibular joint [65]. The advantage of this model is that it is possible to obtain both the viscoelastic and the elastic parts of the behaviour at the same time. The elastic part is extracted from the global equation by making time tend to infinity. For a general stretch history, $\lambda = \lambda(t)$, the temporal evolution of stress is given by equation (3.62). In this case, the stretch history is the relaxation test performed, which can be seen in figure 4.12: a ramp of finite strain rate followed by the stress relaxation. The preconditioning cycles were not considered in the fitting algorithm. The algorithm developed here to fit the experimental curve is able to consider the whole test, also taking into account the relaxation that takes place during the loading ramp. Therefore, the ramp does not need to be very fast to resemble an ideal

relaxation test (with a step strain). On the contrary, finite and moderate strain rates can be applied. This way, the waves propagated through the tissue for high strain rates are avoided.

A five terms Prony series (see equation (3.64)) was used for $\overline{G}(t)$, like in [113]. The relaxation time constants were taken in decades: $\tau_1 = 0.01$ s, $\tau_2 = 0.1$ s, $\tau_3 = 1$ s, $\tau_4 = 10$ s and $\tau_5 = 100$ s [114], fixed *a priori* to ensure the uniqueness of the fitted function $\overline{G}(t)$ [50].

The elastic response, $T^e(\lambda)$, provides the instantaneous stress response to the uniaxial stretch λ and is formulated here using incompressible hyperelastic models. Four strain energy functions were tried: a polynomial function with 5 terms[1], Ψ_{pol}; the first order Ogden model, Ψ_{Og}; the isotropic GOH model [46] (that is to say, making $\kappa = 1/3$ in equation (3.58)), Ψ_{GOH}; and a combination between a neo-Hookean model and an exponential one, Ψ_{exp}:

$$\Psi_{\text{pol}} = C_{10}(I_1-3) + C_{01}(I_2-3) + C_{11}(I_1-3)(I_2-3) + C_{20}(I_1-3)^2 + C_{02}(I_2-3)^2 \,, \tag{4.2a}$$

$$\Psi_{\text{Og}} = \frac{\mu}{\alpha}(\lambda_1^\alpha + \lambda_2^\alpha + \lambda_3^\alpha - 3) \,, \tag{4.2b}$$

$$\Psi_{\text{GOH}} = C_{10}(I_1-3) + \frac{k_1}{2\,k_2}\left[e^{k_2(I_1-3)^2} - 1\right] \,, \tag{4.2c}$$

$$\Psi_{\text{exp}} = C_{10}(I_1-3) + \frac{k_1}{k_2}\left[e^{k_2(I_1-3)} - 1\right] \,, \tag{4.2d}$$

where C_{ij}, μ and k_1 are stress-like parameters and α and k_2 are dimensionless parameters, as explained in section 3.2. With these strain energy functions the corresponding elastic response functions are:

$$\begin{aligned} T^e_{\text{pol}} =& 2C_{10}\left(\lambda^2 - \frac{1}{\lambda}\right) + 2C_{01}\left(\lambda - \frac{1}{\lambda^2}\right) + 6C_{11}\left(\lambda^3 - \lambda^2 - \lambda + \frac{1}{\lambda} + \frac{1}{\lambda^2} - \frac{1}{\lambda^3}\right) + \\ &+ 4C_{20}\left(\lambda^4 - 3\lambda^2 + \lambda + \frac{3}{\lambda} - \frac{2}{\lambda^2}\right) + 4C_{02}\left(2\lambda^2 - 3\lambda - \frac{1}{\lambda} + \frac{3}{\lambda^2} - \frac{1}{\lambda^4}\right) \,, \end{aligned} \tag{4.3a}$$

$$T^e_{\text{Og}} = \mu\left(\lambda^\alpha - \frac{1}{\lambda^{\frac{\alpha}{2}}}\right) \,, \tag{4.3b}$$

$$T^e_{\text{GOH}} = 2\left(C_{10} + k_1(\lambda^2 + \frac{2}{\lambda} - 3)\, e^{k_2\left(\lambda^2 + \frac{2}{\lambda} - 3\right)^2}\right)\left(\lambda^2 - \frac{1}{\lambda}\right) \,, \tag{4.3c}$$

$$T^e_{\text{exp}} = 2\left(C_{10} + k_1\, e^{k_2\left(\lambda^2 + \frac{2}{\lambda} - 3\right)^2}\right)\left(\lambda^2 - \frac{1}{\lambda}\right) \,. \tag{4.3d}$$

The experimental Cauchy stress was estimated from the applied force, $F(t)$, recorded during the test, by

[1] It includes any other polynomial function with less number of terms. For example, if the best fitting model is a neo-Hookean one, the fitting algorithm will make the other 4 constants equal to zero.

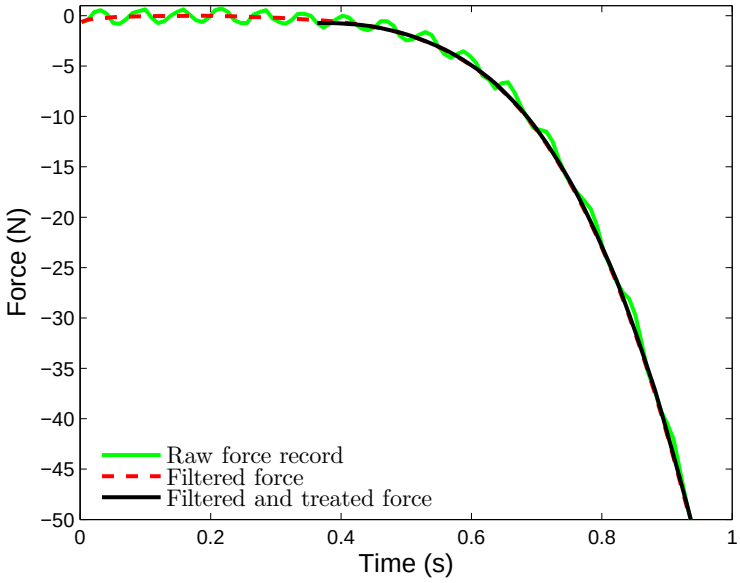

Figure 4.13: Comparison of the raw force record (green), the filtered record (red dashed) and the final record after treated with the proposed algorithm to eliminate the spurious toe region (black).

assuming uniaxial compression:

$$\overline{\sigma}(t) = \frac{F(t)\,\lambda(t)}{A_0}\,, \qquad \lambda(t) = 1 + \frac{u(t)}{L}\,, \tag{4.4}$$

where A_0 is the initial cross-sectional area of the sample, $u(t)$ the displacement of the upper platen, and L the initial thickness of the specimen.

The evolution of the force applied by the platen, $F(t)$, recorded during the loading ramp in one of the samples is shown in green in figure 4.13. The typical toe region of soft tissues is seen for small strains, together with some fluctuations due to the fact that the relative displacement was zeroed when the distance between the platens was equal to the sample's thickness. At that moment, the upper platen might not be in contact with whole top surface of the sample, resulting in a spurious toe region. To solve this problem, the signal was filtered using a moving average filter (red dashed line). Nonetheless, the initial slope of the filtered curve was still zero or even positive in some samples. This produced certain numerical problems in the fitting of the experimental stresses to the QLV model. For this reason, an algorithm was developed (see figure 4.14) to eliminate that spurious toe region.

In the first step, the algorithm takes into account all the points of the loading ramp and calculates a regression line of the $F - t$ curve. If the slope of this line is negative (numerically, this condition is imposed with a given tolerance), the algorithm continues. It eliminates the last point (the latest) and calculates the regression line again. The algorithm goes on until the slope turns positive. At this point, the time of the test is redefined, being $t' = 0$ the first point which has not been considered to calculate the regression line in

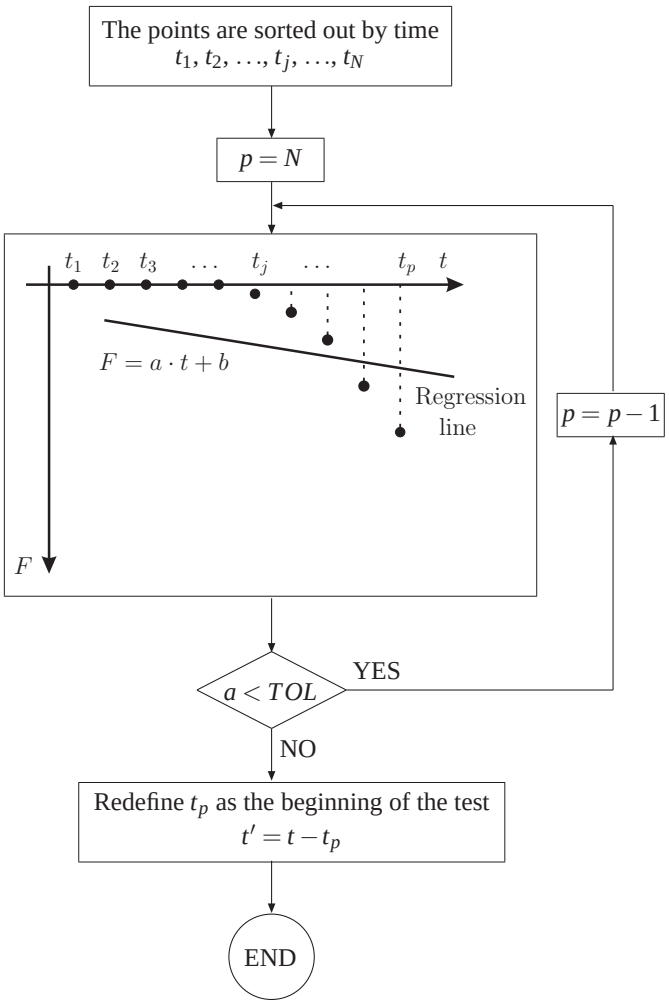

Figure 4.14: Algorithm proposed to eliminate the spurious toe region.

the last iteration of the algorithm. For a better understanding, see figure 4.14. The final force, after filtering and applying this algorithm, is shown in black in figure 4.13.

Once the raw stress record, $\overline{\sigma}$, was filtered and the spurious toe region removed, the resulting stress record, named here $\tilde{\sigma}$, was fitted to the analytical stress record, σ, given by equation (3.62) using a least squares method, that minimize the following quadratic error:

$$e = \sum_{i=1}^{N} \left(\tilde{\sigma}(t_i) - \sigma(t_i) \right)^2 , \tag{4.5}$$

where N is the total number of points recorded during the relaxation test and t_i is the instant of a certain point. This least squares method is sensitive to the initial guess in nonlinear problems like this, due to the fact that the minimum search can get stuck in a local minimum, not necessarily equal to the global minimum. For this reason, the optimisation was performed in two steps. First, a genetic algorithm was used to find a minimum of the quadratic error, e, which was used as the initial guess in the second step: the least squares optimisation. The genetic algorithm starts with a set of randomly selected potential minima, and makes them

evolve by iteratively applying a set of stochastic operators, known as selection, crossover and mutation. This guarantees that the minimum is searched in the entire domain, not only locally. However, genetic algorithms are heuristic methods and the minimum does not necessarily fulfill the optimality condition. This condition was met in the second step, which is a local search around the minimum found in the first step. The goodness of the least squares fitting was evaluated by means of the coefficient of variation, CV:

$$CV(\%) = \frac{\sqrt{\dfrac{\sum_{i=1}^{N}\left(\sigma(t_i) - \tilde{\sigma}(t_i)\right)^2}{N}}}{\mu_{\tilde{\sigma}}} \times 100\ , \tag{4.6}$$

where $\mu_{\tilde{\sigma}}$ is the average of the temporal record $\tilde{\sigma}(t)$.

The computation time is an important issue to take into account when the program must be run many times. The QLV fitting algorithm involves the calculation of several numeric integrals (see appendix A). If their calculation is placed inside the iteration loop, the integrals are evaluated in each step of the genetic algorithm or the least squares algorithm, slowing down considerably the fitting procedure. For this reason, the integrals were taken out from the iteration loop. They were calculated previously, just passing their values at each time point to the algorithm. For some strain energy functions, the integrals depend on a material parameter which is to be optimised too, so that it is not possible to pass the value of the integral into the algorithm a priori. To solve this problem, the integrals were precalculated for fixed values of the material parameter within a wide range (with a small increment between those values) and for each time point. This was the information passed to the algorithm. While iterating to find the optimum, the value of the integrals was obtained by interpolating between the two nearest values of the material parameter.

4.3.3 Data fitting algorithm: internal variables model

With the internal variables viscoelastic (IVV) model (described in section 3.3.2), the structure of the algorithm is the same as that presented in the previous section, except for the equations. Many authors have used this approach, or its extension to fibred materials presented in [115] to model different materials. The advantage of this model is that it is possible to obtain both the viscoelastic and the elastic part of the behaviour at the same time. When time tend to infinity, the non-equilibrium forces tends to zero, reaching the fully elastic response.

The Cauchy stress was obtained from equation (3.67), using the well known relation $\boldsymbol{\sigma} = J^{-1}\mathbf{F}\mathbf{S}\mathbf{F}^T$. For the non-equilibrium forces, $\mathbf{Q}_j$, 5 terms were selected by analogy with the previously presented viscoelastic model. That is to say, j varies from 1 to 5 in equation (3.67). As in the prior section, the relaxation time constants, τ_j, were fixed *a priori* to ensure the uniqueness of the fitted set of constants. They were also taken in decades: $\tau_1 = 0.01$ s, $\tau_2 = 0.1$ s, $\tau_3 = 1$ s, $\tau_4 = 10$ s and $\tau_5 = 100$ s.

The same four strain energy functions fitted with the QLV model were used with the IVV model. Knowing

the stretch history $\lambda = \lambda(t)$, shown graphically in figure 4.12, $\mathbf{S}^{\infty}_{\text{vol}}$ and $\mathbf{S}^{\infty}_{\text{iso}}$ can be calculated, and therefore $\mathbf{Q}_j$, as explained in section 3.3.2. The preconditioning cycles were not considered in the fitting algorithm either.

The treatment of the experimental stress, the fitting process and the evaluation of the goodness through the coefficient of variation were exactly the same as in the previous section. For the implementation of the equations, the update algorithm proposed in [38] has been followed. The key of this update algorithm is the numerical integration of the convolution integral showed in equation (3.70). Defining the time increment as $\Delta t = t_{n+1} - t_n$, the relevant quantities are iteratively updated at time t_{n+1} until the balance principles are satisfied. The second Piola-Kirchhoff stress tensor is given by:

$$\mathbf{S}_{n+1} = \left(\mathbf{S}^{\infty}_{\text{vol}} + \mathbf{S}^{\infty}_{\text{iso}} + \sum_{j=1}^{m} \mathbf{Q}_j \right) \Bigg|_{n+1} , \tag{4.7}$$

All the required strains at t_{n+1} are known and the stress contributions $\mathbf{S}^{\infty}_{\text{vol}}$ and $\mathbf{S}^{\infty}_{\text{iso}}$ can be determined through equation (3.14b) at t_{n+1}. To obtain the third term, $\sum_{j=1}^{m} \mathbf{Q}_{j\,n+1}$, the integral in

$$\mathbf{Q}_{j\,n+1} = e^{-t_{n+1}/\tau_j} \mathbf{Q}_{j\,0^+} + \int_{t=0^+}^{t=t_{n+1}} e^{-(t_{n+1}-t)/\tau_j} \dot{\mathbf{S}}_{\text{iso}\,j}(t)\, dt \, , \tag{4.8}$$

is split into:

$$\int_{t=0^+}^{t=t_{n+1}} (\bullet) dt = \int_{t=0^+}^{t=t_n} (\bullet) dt + \int_{t=t_n}^{t=t_{n+1}} (\bullet) dt \, . \tag{4.9}$$

Then, in order to simplify, the relation $\Delta t = t_{n+1} - t_n$ is applied to all the terms. For the first two terms, the property $e^{-(\Delta t+\beta)/\tau_j} = e^{-\Delta t/\tau_j}\ e^{-\beta/\tau_j}$ is used, and for the third term, the second-order mid-point rule is applied, i.e. t is approximated by $(t_{n+1} + t_n)/2$. Therefore, equation (4.8) is converted into:

$$\mathbf{Q}_{j\,n+1} = e^{-\Delta t/\tau_j} \left(e^{-t_n/\tau_j}\ \mathbf{Q}_{j\,0^+} + \int_{t=0^+}^{t=t_n} e^{-(t_n-t)/\tau_j}\ \dot{\mathbf{S}}_{\text{iso}\,j}(t)\ dt \right) + e^{-\Delta t/2\tau_j} \int_{t=t_n}^{t=t_{n+1}} \dot{\mathbf{S}}_{\text{iso}\,j}(t)\ dt \, . \tag{4.10}$$

Noting that the terms in parenthesis are $\mathbf{Q}_j$ at time t_n and solving the last integral recalling that $\dot{\mathbf{S}}_{\text{iso}\,j} = \beta^{\infty}_j \dot{\mathbf{S}}^{\infty}_{\text{iso}}$, the recurrence update formula for $\mathbf{Q}_j$ is obtained:

$$\mathbf{Q}_{j\,n+1} = e^{-\Delta t/\tau_j}\ \mathbf{Q}_{j\,n} + e^{-\Delta t/2\tau_j}\ \beta^{\infty}_j\ (\mathbf{S}^{\infty}_{\text{iso}\ n+1} - \mathbf{S}^{\infty}_{\text{iso}\ n}) \, . \tag{4.11}$$

Introducing equation (4.11) into equation (4.7), and using the well known relation $\boldsymbol{\sigma} = J^{-1}\mathbf{F}\mathbf{S}\mathbf{F}^T$, the analytical Cauchy stress needed for the fitting algorithm is obtained:

$$\boldsymbol{\sigma}_{n+1} = \boldsymbol{\sigma}^{\infty}_{\text{vol}\,n+1} + \boldsymbol{\sigma}^{\infty}_{\text{iso}\,n+1} +$$

$$+\sum_{j=1}^{m}\left(e^{-\Delta t/\tau_j}\ J^{-1}\mathbf{F}_{n+1}\mathbf{Q}_{j\,n}\mathbf{F}_{n+1}^{T}+e^{-\Delta t/2\tau_j}\ \beta_j^{\infty}\ (\boldsymbol{\sigma}_{\text{iso}\ n+1}^{\infty}-J^{-1}\mathbf{F}_{n+1}\mathbf{S}_{\text{iso}\ n}^{\infty}\mathbf{F}_{n+1}^{T})\right)\ . \tag{4.12}$$

4.3.4 Description of the experiments

Following the test protocol shown in section 4.3.1 and using the fitting algorithm proposed in sections 4.3.2 and 4.3.3, the viscoelastic properties of the abdominal and breast fat were determined. The information about the patients, the samples and the test conditions is summarised in table 4.5.

First, it is important to check which one of the four proposed strain energy functions fits best the experimental curves for each viscoelastic model. To do this, the mean CV was calculated for each group of specimens (sample division in table 4.5) and each strain energy function used. Then, the mean CV was calculated for each of the four strain energy functions and they were compared to determine which was the lowest CV and, therefore, the best model.

The validity of both, the QLV and the IVV models, must be verified once the most suitable model for the elastic response is selected. This must be done by checking if the material parameters are independent of the strain rate and the strain level of the relaxation test. To carry out this validation, in a given piece of tissue from the same patient, three specimen groups were extracted and each one was tested with a different strain rate. Then, in a piece of another patient, three more groups were extracted and each one tested with a different strain level. Choosing specimens from the same patient avoids the problem of inter-individuals differences, but increases the difficulty to obtain a suitable piece of tissue, due to the fact that its size must be large enough to host the sufficient number of specimens needed for statistical purposes. The strain rates selected were 50% /s, 60% /s and 70% /s and the strain levels, 40%, 50% and 60%.

If no difference exists between the material parameters obtained for the different strain levels and strain rates, that will mean that the model is valid to represent the behaviour of the adipose tissue. These two comparisons were carried out with statistical methods to compare the differences between groups. As there are multiple dependent variables but only one independent variable with several levels (the strain rate in one case and the strain level in the other comparison), the first choice was to perform a one-way multivariate analysis of variance (MANOVA) test. Of course, all the assumptions of MANOVA tests should be accomplished. If not, a non parametric MANOVA should be used instead.

After checking the validity of QLV and IVV models, they were compared in terms of goodness of fit. The one able to better reproduce the viscoelastic behaviour of the adipose tissue was chosen as the final model. Finally, using this model, some more comparisons were carried out to check if the adipose tissue has the same properties in different regions of the abdomen, and to investigate the differences between the adipose tissue of the abdomen and the breast.

Patient	Age	Extraction area	Sample division	Test strain rate	Test strain level	N° of specimens
A	42	Abdomen	Superficial	50% /s	50%	8
			Deep	50% /s	50%	10
B	55	Abdomen	Superficial-lateral	50% /s	50%	14
			Superficial-medial	50% /s	50%	26
			Deep-lateral	50% /s	50%	17
			Deep-medial	50% /s	50%	23
		Breast	Superficial	50% /s	50%	12
			Deep	50% /s	50%	14
C	55	Abdomen	Superficial-lateral	60% /s	40%	11
					50%	11
					60%	11
			Superficial-medial	60% /s	40%	12
					50%	12
					60%	10
			Deep-lateral	60% /s	40%	11
					50%	11
					60%	10
			Deep-medial	60% /s	40%	10
					50%	10
					60%	9
D	57	Abdomen	Superficial-lateral	50% /s	50%	13
				60% /s		12
				70% /s		12
			Superficial-medial	50% /s	50%	12
				60% /s		12
				70% /s		12
			Deep-lateral	50% /s	50%	11
				60% /s		11
				70% /s		11
			Deep-medial	50% /s	50%	11
				60% /s		10
				70% /s		11

Table 4.5: Information of patients and tissue extracted.

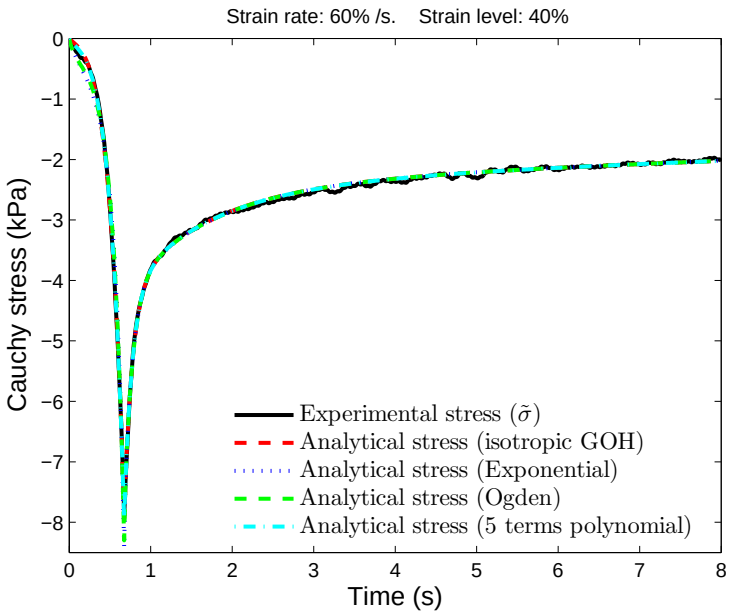

Figure 4.15: Example of an experimental stress record fitted with different hyperelastic models, for the QLV model.

4.3.5 Results

The results obtained in the experimental tests of abdominal and breast fat are presented in this section. Each specimen was tested and the results treated with the algorithm, obtaining the material parameters of the hyperelastic model used for T^e and the constants g_i of the Prony series in the case of the QLV model; and the material parameters of the hyperelastic model and the constants β_j^∞ in the case of the viscoelastic model with internal variables.

4.3.5.1 Goodness of fit of the hyperelastic models with the QLV model

Figure 4.15 compares a typical experimental stress record, $\tilde{\sigma}$, with the fitting curves for each one of the strain energy functions proposed. In figure 4.16 a detail of the loading ramp can be seen.

In these figures, it can be observed that the toe region of the experimental curve was not very wide in comparison with other tissues, as for example the articular discs of the temporomandibular joint [65]. The loading ramp applied to the tissue was quickly noticed by an increase in its stress state. The relaxation was very quick, with a high relaxation percentage occurring few seconds after the peak. Although it is not shown here, it could be observed that more than a 90% of the peak stress was relaxed after 15 minutes. Comparing these stress relaxation curves with those obtained by Miller-Young et al. [66] testing specimens of the human calcaneal fat pad in compression, the peak stress of the present work was of the same order of magnitude and in both, 75% of the stress was relaxed within the first minute.

The fitting was very accurate for all cases and quite similar for all the fitted hyperelastic models. In both figures 4.15 and 4.16, it can be noticed that the isotropic GOH and the 5 terms polynomial models

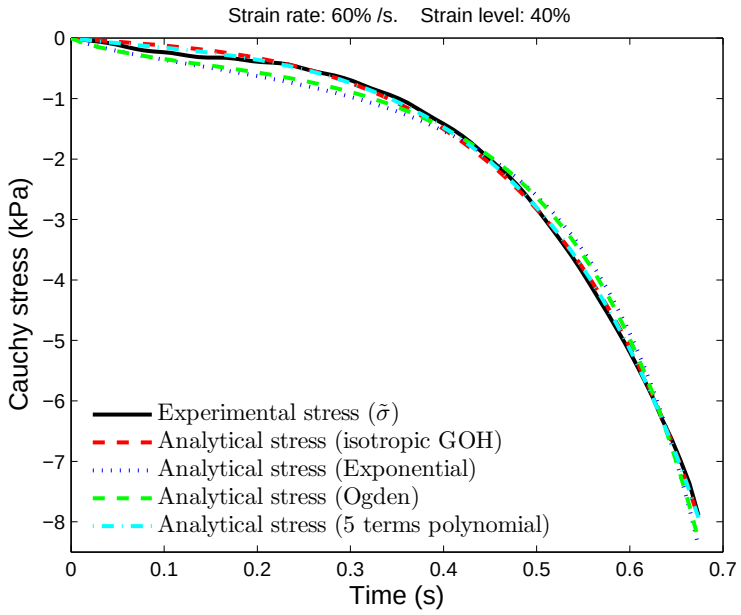

Figure 4.16: Detail of figure 4.15 to notice the loading ramp.

Patient	Extraction area	Model	Whole curve CV (%)	Loading ramp CV (%)
A	Abdomen	Exponential	4.13	18.27
		Ogden	4.15	18.09
		GOH	3.21	11.82
		Polynomial	3.05	10.89
B	Abdomen	Exponential	4.48	17.22
		Ogden	4.31	15.90
		GOH	3.26	8.58
		Polynomial	3.15	7.91
	Breast	Exponential	3.44	12.85
		Ogden	3.35	12.06
		GOH	2.65	6.83
		Polynomial	2.56	6.23
C	Abdomen	Exponential	4.95	21.46
		Ogden	4.96	21.22
		GOH	4.11	15.38
		Polynomial	3.86	14.13
D	Abdomen	Exponential	4.16	19.88
		Ogden	4.05	18.70
		GOH	3.06	11.49
		Polynomial	2.92	10.67

Table 4.6: Coefficient of variation for each patient and model, for the QLV model.

are closer to the experimental curve than the Ogden and exponential ones, although not too much. The average coefficient of variation, CV, for each patient and model is presented in table 4.6. The CV has been evaluated in the whole curve and in the loading ramp interval separately.

In view of table 4.6, it is clear that the best model is the polynomial one, closely followed by the GOH model, and a little bit farther by the Ogden and exponential models, in this order. However, the CV is very low for each patient and model. This fact means that the fitting was quite good in all cases.

However, due to the fact that the polynomial model has so many constants, in the results given by the fitting algorithm several constants from the total of five were zero for the majority of the specimens. Moreover, the constants equal to zero were not the same for all of the specimens. This means that a different model is being used to fit each specimen. For example, if constants C_{10}, C_{11} and C_{02} are zero, the strain energy function which is being fitted is:

$$\Psi = C_{01}(I_2 - 3) + C_{20}(I_2 - 3)^2 \,, \tag{4.13}$$

whereas if constants C_{01} and C_{20} are zero, the strain energy function which is being fitted is:

$$\Psi = C_{10}(I_1 - 3) + C_{11}(I_1 - 3)(I_2 - 3) + C_{02}(I_1 - 3)^2 \,. \tag{4.14}$$

Depending on the particular specimen, some constants are zero but not the same ones in all specimens. Then, if an average is calculated for each constant, a non zero mean value results. As a consequence, the whole material is represented by a 5 terms polynomial. But if the curve calculated with the mean constants is compared with the curves of each individual specimen, big differences can be found. This is because all the specimens have been fitted with a different strain energy function. From a physical point of view that does not make much sense. A specific material should be represented by a unique function. Also, neither equation (4.13) nor (4.14) correspond to well-known or widely used strain energy functions, which does not help to the choice of the 5 terms polynomial function as a suitable model for the fat.

With the GOH model, something similar occurs. In many specimens, the fitted constant k_2 was equal to zero. The main problem of $k_2 = 0$ is that it generates an indeterminate form (0/0) in the strain energy function. If the limit of the function when $k_2 \to 0$ is taken:

$$\lim_{k_2 \to 0} \frac{k_1}{2k_2} \left[e^{k_2 (I_1 - 3)^2} - 1 \right] = \frac{k_1}{2} (I_1 - 3)^2 \,. \tag{4.15}$$

Therefore, the GOH strain energy function (equation (4.2c)) would be in this case:

$$\Psi = C_{10}(I_1 - 3) + \frac{k_1}{2}(I_1 - 3)^2 \,, \tag{4.16}$$

Strain level	μ (kPa)	α	g_1	g_2	g_3	g_4	g_5	g_∞
40%	2.810 ± 2.608	11.919 ± 1.457	0.509 ± 0.262	0.342 ± 0.193	0.065 ± 0.033	0.028 ± 0.015	0.028 ± 0.016	0.028 ± 0.017
50%	8.757 ± 4.874	7.280 ± 1.229	0.606 ± 0.198	0.290 ± 0.175	0.045 ± 0.017	0.019 ± 0.007	0.021 ± 0.009	0.018 ± 0.008
60%	18.860 ± 16.274	5.048 ± 0.964	0.659 ± 0.175	0.249 ± 0.145	0.040 ± 0.016	0.018 ± 0.007	0.019 ± 0.007	0.014 ± 0.006

Table 4.7: Mean ± standard deviation of the QLV constants for the different groups, for patient C.

Strain rate	μ (kPa)	α	g_1	g_2	g_3	g_4	g_5	g_∞
50% /s	6.277 ± 4.076	8.504 ± 1.750	0.579 ± 0.215	0.290 ± 0.170	0.057 ± 0.027	0.027 ± 0.014	0.025 ± 0.013	0.020 ± 0.011
60% /s	8.536 ± 14.546	8.316 ± 1.953	0.610 ± 0.193	0.264 ± 0.139	0.054 ± 0.027	0.026 ± 0.014	0.025 ± 0.013	0.020 ± 0.011
70% /s	6.317 ± 4.343	8.564 ± 1.683	0.606 ± 0.173	0.263 ± 0.141	0.055 ± 0.022	0.029 ± 0.014	0.027 ± 0.011	0.020 ± 0.008

Table 4.8: Mean ± standard deviation of the QLV constants for the different groups, for patient D.

which is a particular case of the 5 terms polynomial strain energy function. This is the reason why the GOH and polynomial models perform very similarly when fitting the experimental curves. Therefore, the isotropic GOH model is not appropriate to model the fat either.

In conclusion, as some problems were found with these two models, the Ogden model was selected to represent the behaviour of the adipose tissue.

4.3.5.2 Validity of the QLV model

Once a suitable model has been selected to represent the behaviour of the adipose tissue, it has been used to check the validity of the QLV approach. As stated before, this must be done by checking if the fitted model constants are independent of the strain level and the strain rate. For that, the specimens extracted from patient C (to check the independence of the strain level) and those extracted from patient D (to check the independence of the strain rate) were used. The validity was proved only in the abdominal tissue, because it was difficult to obtain a large piece of breast fat to have enough specimens to test. Extracting the specimens from several patients was considered inadequate because differences between individuals could exist.

In table 4.7, for patient C, the mean and standard deviation for each strain level and each constant are presented. For patient D, the same is done in table 4.8. In both tables, it can be noticed the high values of the constants g_1 and g_2, which correspond to the relaxation times $\tau_1 = 0.01$ and $\tau_2 = 0.1$. These high values highlight the fast relaxation in the short-term.

To check if the material constants are independent of the strain level and the strain rate, a MANOVA

test was performed for each patient.

In the specimens extracted from patient D, the independent variable was the strain rate with three levels: 50% /s, 60% /s and 70% /s; and the dependent continuous variables (DVs) were the seven QLV constants: μ, α, g_1, g_2, g_3, g_4 and g_5. The material parameter g_∞ was not included in the statistical analysis because it is a linear combination of the rest of constants g_i, due to the normalization condition of $\overline{G}(t)$:

$$\overline{G}(0) = 1 = g_\infty + \sum_{i=1}^{5} g_i \ . \tag{4.17}$$

Before applying a MANOVA, some assumptions needed to be checked. First, multinormality was checked for each independent group using the test developed by Cardoso de Oliveira and Ferreira [116]. This test was not significant for the 50% /s group ($p = .098$) and 60% /s group ($p = .160$), but significant for the 70% /s group ($p < .001$) and, thus, multinormality was violated, making it necessary to perform a non-parametric MANOVA (NMANOVA).

The seven variables were compared in the NMANOVA: μ, α, g_1, g_2, g_3, g_4 and g_5. The NMANOVA test performed in this thesis is a multivariate extension of the Kruskal-Wallis test, developed by Katz and McSweeney [117]. No significant differences were found for the three groups compared ($p = .819$). Some authors state that MANOVA is indicated if the dependent variables are correlated, but not so strongly that multicollinearity exists [118, 119]. As this is not the case for all the variables in this study, the statistical analysis was repeated after eliminating the correlated variables, just to be sure of the correctness of the previous conclusion. Constants g_1 and g_2 were strongly correlated and the same occurred to g_3, g_4 and g_5 (Spearman $|R| > .86$ in both cases). Thus, they could be regarded as the same variable for statistical purposes. Then, the analysis was repeated with 4 DVs: μ, α, g_1 and g_3. The conclusion was the same: there were no statistical differences. Therefore, the material constants could be considered independent of the strain rate.

In the specimens extracted from patient C, the independent variable was the strain level with three levels: 40%, 50% and 60%; and the dependent continuous variables (DVs) were the seven QLV constants: μ, α, g_1, g_2, g_3, g_4 and g_5. The material parameter g_∞ was not included either.

Multinormality was checked for each independent group. This test was significant for the three groups: 40% ($p < .001$), 50% ($p = .018$) and 60% ($p = .020$) and, thus, multinormality was violated, making it necessary to perform a NMANOVA.

The seven variables were compared in the NMANOVA: μ, α, g_1, g_2, g_3, g_4 and g_5 with the test developed by Katz and McSweeney [117]. Significant differences were found ($p < .001$). Afterwards, post-hoc tests were carried out to detect the origin of these differences. To do so, the proposal by Katz and McSweeney [117] was followed again. Significant differences were found for μ (between 40% and the other two groups, $p < .001$), α (between all groups, $p < .001$), g_1 (between 40% and 60%, $p = .038$), g_3 (between 40% and

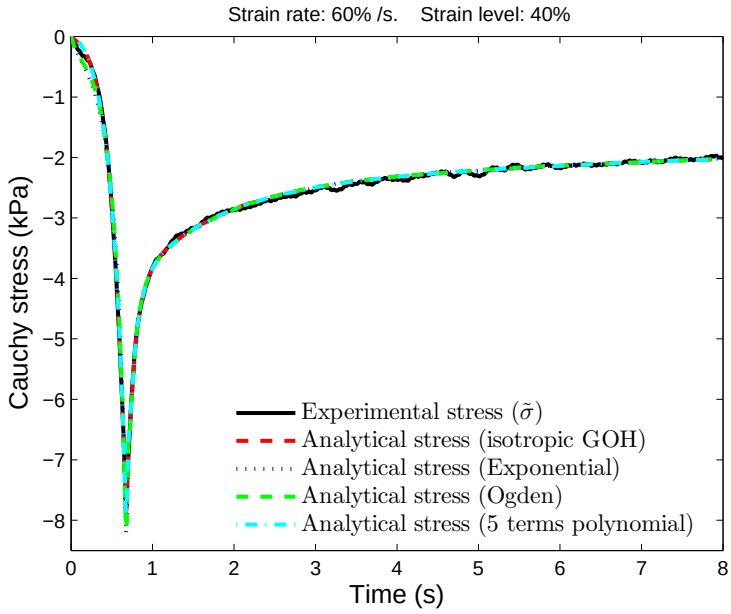

Figure 4.17: Example of an experimental stress record fitted with different hyperelastic models, for the IVV model.

60%, $p < .001$) and g_4 (between 40% and 60%, $p = .018$). As in the previous case, the statistical analysis was repeated after eliminating the correlated variables, just to be sure of the correctness of the previous conclusion. In this case, μ and α were strongly correlated, and the same occurred to g_1 and g_2; and to g_3, g_4 and g_5 (Spearman $|R| > .80$ in all cases). Therefore, the analysis was repeated with 3 DVs: μ, g_1 and g_3. The conclusion was the same: there were statistical differences ($p < .001$). As a consequence, the material constants are not independent of the strain level.

With these statistical results, it can be concluded that the QLV model is not suitable to model the adipose tissue, due to the fact that the independence of the model with the strain level cannot be ensured. Moreover, the assumption of the multiplicative decomposition of the stress into a function which only depends on time and another one which only depends on strain (equation (3.59)) is not valid, due to the fact that $\bar{G}(t)$, by definition, can not depend on the strain level.

4.3.5.3 Goodness of fit of the hyperelastic models with the IVV model

Figure 4.17 compares a typical experimental stress record, $\tilde{\sigma}$, with the fitting curves for each one of the strain energy functions proposed. In figure 4.18 a detail of the loading ramp can be seen. The experimental curve shown in the figures is the same one shown in figures 4.15 and 4.16.

As in the QLV model, it can be seen that the fitting is very accurate for all cases and quite similar for all the fitted hyperelastic models. In both figures 4.17 and 4.18, it can be noticed that the isotropic GOH and the 5 terms polynomial models are closer to the experimental curve than the Ogden and exponential ones, although not too much. The goodness of fit is slightly better than with the QLV model for all the

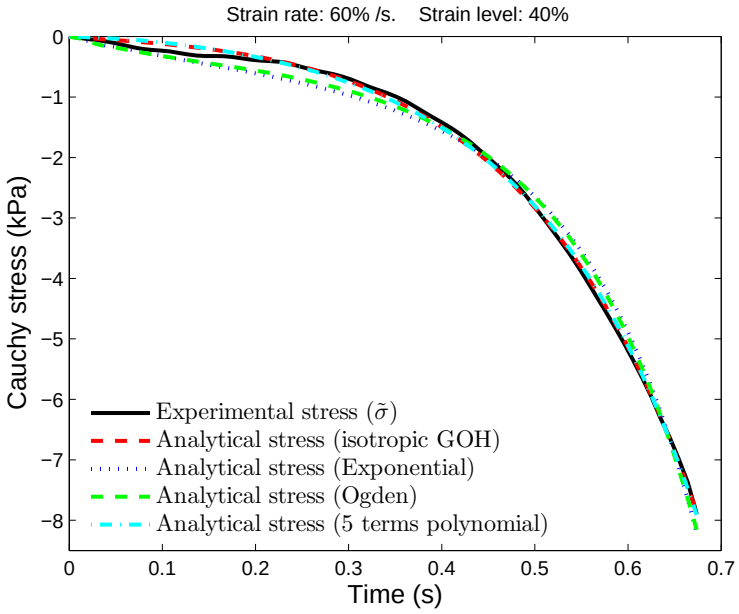

Figure 4.18: Detail of figure 4.17 to appreciate the loading ramp.

hyperelastic strain energy functions tried, except for the polynomial model, in which case it is slightly worse, although that is difficult to notice with the naked eye. It can be noticed by looking at the average coefficient of variation, CV, which is presented for each patient and model in table 4.6, for the QLV model, and in table 4.9, for the IVV model. The CV has been evaluated again in the whole curve and in the loading ramp interval separately.

Looking at table 4.9, it is clear that the best model is the GOH model, closely followed by the polynomial one, and a little bit farther, by the Ogden and exponential models, in this order. However, the CV is very low for each patient and model. This fact means that the fitting was quite good in all cases.

As in the previous QLV model, the use of the polynomial and the GOH strain energy functions lead to many constants equal to zero, causing the same problems discussed in section 4.3.5.1. Therefore, the Ogden model was selected to represent the behaviour of the adipose tissue, as done with the QLV model.

4.3.5.4 Validity of the IVV model

Once a suitable model has been selected to represent the behaviour of the adipose tissue, it has been used to check the validity of the IVV approach. As stated before, this must be done by checking if the fitted model constants are independent of the strain level and the strain rate. For that, the specimens extracted from patient C and those extracted from patient D were used, as in the validation of the QLV model.

In table 4.10, for patient C, the mean and standard deviation for each strain level and each constant are presented. For patient D, the same is done in table 4.11. It can be noticed how the values of the variables β_j^∞ decrease as j increases. That is to say, the highest β_j^∞ correspond to the lowest relaxation times τ_j.

Patient	Extraction area	Model	Whole curve CV (%)	Loading ramp CV (%)
A	Abdomen	Exponential	3.79	16.30
		Ogden	3.86	16.39
		GOH	3.16	11.54
		Polynomial	3.18	11.88
B	Abdomen	Exponential	4.12	15.00
		Ogden	4.05	14.23
		GOH	3.27	8.65
		Polynomial	3.38	9.58
	Breast	Exponential	3.18	10.73
		Ogden	3.17	10.47
		GOH	2.70	6.78
		Polynomial	2.72	6.95
C	Abdomen	Exponential	4.50	18.84
		Ogden	4.56	18.95
		GOH	3.98	14.69
		Polynomial	4.01	14.93
D	Abdomen	Exponential	3.81	17.66
		Ogden	3.77	16.99
		GOH	3.04	11.36
		Polynomial	3.14	12.27

Table 4.9: Coefficient of variation for each patient, for the IVV model.

Strain level	$\boldsymbol{\mu}$ (kPa)	$\boldsymbol{\alpha}$	$\boldsymbol{\beta_1^\infty}$	$\boldsymbol{\beta_2^\infty}$	$\boldsymbol{\beta_3^\infty}$	$\boldsymbol{\beta_4^\infty}$	$\boldsymbol{\beta_5^\infty}$
40%	0.063 ± 0.040	11.481 ± 1.676	93.284 ± 57.32	12.269 ± 5.702	3.632 ± 1.078	1.601 ± 0.502	1.597 ± 0.472
50%	0.190 ± 0.125	6.632 ± 1.369	103.973 ± 73.506	13.002 ± 6.436	3.579 ± 1.161	1.635 ± 0.569	1.800 ± 0.610
60%	0.545 ± 1.316	4.381 ± 1.421	96.235 ± 51.204	13.242 ± 6.136	3.820 ± 0.776	1.938 ± 0.454	2.030 ± 0.349

Table 4.10: Mean ± standard deviation of the IVV constants for the different groups, for patient C.

Strain rate	$\boldsymbol{\mu}$ (kPa)	$\boldsymbol{\alpha}$	$\boldsymbol{\beta_1^\infty}$	$\boldsymbol{\beta_2^\infty}$	$\boldsymbol{\beta_3^\infty}$	$\boldsymbol{\beta_4^\infty}$	$\boldsymbol{\beta_5^\infty}$
50% /s	0.121 ± 0.068	8.165 ± 2.006	84.956 ± 61.953	15.444 ± 7.511	4.278 ± 1.479	2.151 ± 0.715	1.980 ± 0.455
60% /s	0.156 ± 0.198	8.111 ± 2.160	82.744 ± 59.015	15.055 ± 7.816	4.096 ± 1.195	2.077 ± 0.556	2.008 ± 0.410
70% /s	0.130 ± 0.069	8.249 ± 1.893	83.547 ± 81.419	13.209 ± 6.727	4.159 ± 1.602	2.281 ± 1.058	2.114 ± 0.544

Table 4.11: Mean ± standard deviation of the IVV constants for the different groups, for patient D.

This way, the fast relaxation observed in the experimental curves is being modelled.

To check if the material constants are independent of the strain level and the strain rate, a MANOVA test was performed for each patient.

In the specimens extracted from patient D, the categorical independent variable was the strain rate with three levels: 50% /s, 60% /s and 70% /s; and the dependent continuous variables (DVs) were the seven constants of the IVV model: μ, α, β_1^∞, β_2^∞, β_3^∞, β_4^∞ and β_5^∞.

The assumptions of MANOVA needed to be checked. First, multinormality was checked for each independent group using the test developed by Cardoso de Oliveira and Ferreira [116]. This test was not significant for the 50% /s group ($p = .534$) and 70% /s group ($p = .205$), but significant for the 60% /s group ($p = .003$) and, thus, multinormality was violated, making it necessary to perform a non-parametric MANOVA (NMANOVA).

The seven variables compared in the NMANOVA were: μ, α, β_1^∞, β_2^∞, β_3^∞, β_4^∞ and β_5^∞. The NMANOVA developed by Katz and McSweeney [117] showed no significant differences for the three groups compared ($p = .314$). The correlation between the dependent variables was checked, but they were not highly correlated.

In the specimens extracted from patient C, the independent variable was the strain level with three levels: 40%, 50% and 60%; and the dependent continuous variables (DVs) were the seven IVV constants: μ, α, β_1^∞, β_2^∞, β_3^∞, β_4^∞ and β_5^∞.

Multinormality was checked with the Cardoso de Oliveira and Ferreira's test [116] for the three groups, which was not significant for the 50% ($p = .061$) and 60% ($p = .380$) groups, but significant for the 40% group ($p = .029$). Thus, multinormality was violated, making it necessary to perform a NMANOVA.

The Katz and McSweeney's test showed significant differences between the groups ($p < .001$). Afterwards, post-hoc tests were carried out to detect the origin of these differences. To do so, the post-hoc test proposed by Katz and McSweeney was followed again. Significant differences were found for μ (between 40% and the other two groups, $p < .001$), α (between 40% and the other two groups, $p < .001$, and between 50% and 60%, $p = .003$), β_4^∞ (between 40% and 60%, $p = .004$, and between 50% and 60%, $p = .028$) and β_5^∞ (between 40% and 60%, $p < .001$). The statistical analysis was repeated after eliminating the correlated variables, just to be sure of the correctness of the previous conclusion in case of collinearity [118, 119]. In this case, μ and α were strongly correlated, and the same occurred to β_3^∞ and β_4^∞. Therefore, the analysis was repeated with 5 DVs: μ, β_1^∞, β_2^∞, β_3^∞ and β_5^∞. The conclusion was the same: there were statistical differences ($p < .001$). As a consequence, the material constants are not independent of the strain level.

With these statistical results, it can be concluded that the IVV model is not suitable to model the adipose tissue, due to the fact that the independence of the model with the strain level cannot be ensured.

4.3.5.5 Discussion

With the results obtained in the previous sections, it can be concluded that neither the QLV nor the IVV models are suitable to model the viscoelastic behaviour of the adipose tissue. Both are independent of the strain rate, but dependent of the strain level. However, these models could be valid in certain applications in which the stress level is not widely varied. Between the two models, the IVV one was finally selected because of its better goodness of fit, as can be seen by comparing the CVs of both models. Therefore, the IVV model with an Ogden strain energy function was the choice made here to characterise the viscoelastic behaviour of the human adipose tissue.

In the following sections, the adipose tissue from different anatomical regions is compared. As the strain level and the strain rate are the same for all the subsequent tests, the model can be considered valid to carry out this regional comparison.

4.3.5.6 Comparison between the abdominal fat for different individuals

The objective of this comparison was to check if the mechanical properties of the abdominal adipose tissue are different between individuals. This study did not seek to be fully comprehensive or to establish final conclusions, as more patients would be needed for this. Obtaining the properties of the abdominal adipose tissue for different individuals as a function of several parameters would be very interesting, but a larger sample size would also be needed. Therefore, the aim here was to conclude whether differences between individuals were suspected, in order to recommend the extraction of the specimens from the same patient if avoiding the inter-individual effects is desired for the subsequent comparisons. In this thesis in particular, the specimens were always extracted from the same patient for each individual comparison, not to introduce an additional scatter which might alter the results. With the present comparison, the adequateness of this decision was checked and the convenience of continuing doing so in the further experimental tests.

The specimens extracted from patients A and B were used (see table 4.5), grouped in deep and superficial adipose tissue for both patients. All the specimens were tested under the same conditions: strain level equal to 50% and strain rate equal to 50% /s. The model used to fit the mechanical behaviour is the IVV model with the Ogden strain energy function for the elastic response. As discussed previously, although it has been proved that this is not a suitable model for the global behaviour of the adipose tissue, it accurately fits the experimental tests (better that the QLV model) and due to the fact that all the specimens were tested under the same conditions, that model has been considered adequate to carry out the comparison. In table 4.12, the mean and standard deviation for the constants of the IVV model for each group of abdominal adipose tissue are presented.

Patient	Area	μ (kPa)	α	β_1^∞	β_2^∞	β_3^∞	β_4^∞	β_5^∞
A	Superficial	0.121 ± 0.101	8.744 ± 2.406	90.877 ± 57.008	12.721 ± 2.927	4.160 ± 0.636	2.345 ± 0.523	2.131 ± 0.459
	Deep	0.123 ± 0.028	7.215 ± 1.233	113.999 ± 61.016	16.097 ± 8.853	4.730 ± 1.412	2.194 ± 0.658	2.356 ± 0.891
B	Superficial	0.071 ± 0.050	8.992 ± 1.582	91.383 ± 41.541	13.189 ± 4.655	4.048 ± 1.312	2.104 ± 0.749	1.888 ± 0.517
	Deep	0.062 ± 0.036	8.290 ± 1.075	128.283 ± 77.469	17.861 ± 7.272	3.908 ± 0.969	1.593 ± 0.365	1.572 ± 0.325

Table 4.12: Mean ± standard deviation of constants of the IVV model for the superficial and deep layers abdominal adipose tissue, for patients A and B.

A MANOVA was carried out to search for differences. The independent variable had 4 levels: superficial abdominal fat of patient A, deep abdominal fat of patient A, superficial abdominal fat of patient B and deep abdominal fat of patient B; and the DVs were the seven constants from the IVV model: μ, α, β_1^∞, β_2^∞, β_3^∞, β_4^∞ and β_5^∞.

The assumptions of MANOVA needed to be checked. First, multinormality was checked for each group using the test developed by Cardoso de Oliveira and Ferreira. This test was not significant for all the groups: superficial-patient A ($p = 1$), deep-patient A ($p = 0.497$), superficial-patient B ($p = 0.058$) and deep-patient B ($p = 0.091$). Additionally, to check the normality, individual Kolmogorov-Smirnov (K-S) tests were carried out for each of the dependent variables in each group, concluding that each distribution could be considered as normal. Another assumption needed to be accomplished to perform a MANOVA is the homogeneity of the covariance matrix. To test that, a Box's M test was conducted. It was significant ($p < .001$), therefore rejecting the null hypothesis of homogeneity and making it necessary to perform a non-parametric MANOVA (NMANOVA).

The seven variables were compared in the NMANOVA: μ, α, β_1^∞, β_2^∞, β_3^∞, β_4^∞ and β_5^∞. Significant differences were found ($p < .001$) between the four groups using the Katz and McSweeney's test. Afterwards, the Katz and McSweeney's post-hoc tests were carried out to detect the origin of the differences between patients A and B. Significant differences were found for μ (between the deep fat of patient A and the superficial fat of patient B, $p = 0.008$, and between the deep fat of patient A and the deep fat of patient B, $p = 0.002$), β_4^∞ (between the superficial fat of patient A and the deep fat of patient B, $p = 0.031$) and β_5^∞ (between the deep fat of patient A and the deep fat of patient B, $p = 0.023$). MANOVA is indicated if the dependent variables are correlated, but not so strongly that multicollinearity exists. In this case β_4^∞ and β_5^∞ were strongly correlated (Spearman $R = .83$). Therefore the analysis was repeated considering 6 DVs: μ, α, β_1^∞, β_2^∞, β_3^∞ and β_4^∞. The conclusion was the same: there are significant statistical differences ($p < .001$).

In figure 4.19 two curves are drawn for each of the four anatomical regions. These curves are the lowest and the highest experimental curves from the total of each group, in terms of the peak reached for the

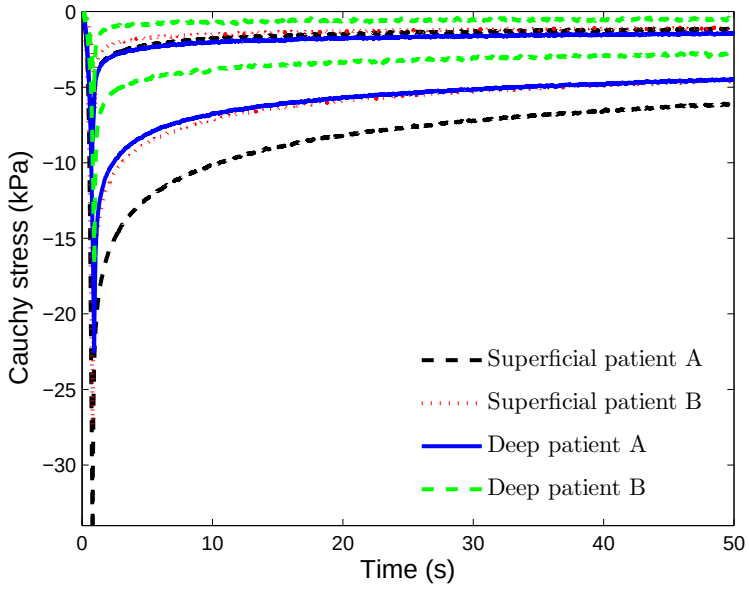

Figure 4.19: Comparison between the experimental curves for the abdominal adipose tissue for different individuals.

Cauchy stress, i.e., the rest of experimental curves in each group lie between these two curves. It can be observed that the highest curves (those corresponding to the smallest peak of compression Cauchy stress) are more similar to each other than the lowest curves for the four groups. The difference detected with the statistical analysis between the superficial abdominal fat of patient A (black curves) and the deep fat of patient B (green curves) is clear in view of figure 4.19, because the ranges are very different. The same occurred (slightly less marked) with the difference between the deep abdominal adipose tissue of patient A (blue curves) and B (green curves).

The difference between the deep layer of fat of patient A (blue curves) and the superficial fat of patient B (red curves) is difficult to notice in the graph, as the range seems to be similar. However, the peak of the curves of the superficial abdominal adipose tissue of patient B are smaller. Most of those specimens lie in the region enclosed by the deep fat of patient B (green curves). The difference between these two groups was detected in the constant μ, therefore influencing the peak stress. This supports the results obtained with the statistical procedure.

In view of the results of the statistical analysis, inter-individual differences are suspected both in the elastic and viscous constants, though they cannot be confirmed with such a small sample. For this reason it seemed a correct decision to extract the specimens from the same individual in the previous statistical analyses (validity of the QLV and IVV models), and indicating that the same must be done for the following comparisons in this thesis.

Area	μ (kPa)	α	β_1^∞	β_2^∞	β_3^∞	β_4^∞	β_5^∞
Superficial breast	0.068 ± 0.044	9.169 ± 1.036	69.793 ± 31.821	21.646 ± 5.716	5.933 ± 1.784	3.513 ± 1.215	2.926 ± 0.792
Deep breast	0.068 ± 0.032	8.065 ± 1.249	90.533 ± 63.971	15.516 ± 5.351	3.813 ± 1.323	1.951 ± 0.849	1.691 ± 0.807
Superficial-lateral abdomen	0.084 ± 0.069	8.810 ± 1.372	73.697 ± 27.216	16.278 ± 5.107	5.201 ± 1.525	2.779 ± 0.821	2.208 ± 0.611
Superficial-medial abdomen	0.066 ± 0.034	9.052 ± 1.685	103.158 ± 45.338	11.327 ± 3.388	3.430 ± 0.516	1.756 ± 0.355	1.726 ± 0.360
Deep-lateral abdomen	0.059 ± 0.025	8.191 ± 1.326	145.958 ± 99.222	19.868 ± 9.030	3.992 ± 1.162	1.571 ± 0.395	1.579 ± 0.288
Deep-medial abdomen	0.061 ± 0.042	8.376 ± 0.896	114.278 ± 57.308	16.806 ± 5.310	3.836 ± 0.845	1.570 ± 0.299	1.541 ± 0.340

Table 4.13: Mean ± standard deviation of constants of the IVV model for the different breast and abdominal areas of the patient B.

4.3.5.7 Comparison between areas of the abdominal and breast fat

The objective of this study is to check if the mechanical properties of different regions of the breast and abdominal adipose tissue are different for the same patient. For that purpose the specimens extracted from patient B were used (see table 4.5). Those specimens were grouped in six regions in total, corresponding to different anatomical areas. Four regions were considered for the abdominal fat: superficial-lateral, superficial-medial, deep-lateral and deep-medial (see figure 4.9). In the case of the breast fat, it was not possible to divide the complete extracted sample in more regions because of its size, thus two groups were considered: superficial and deep. All the specimens were tested under the same conditions: strain level equal to 50% and strain rate equal to 50% /s. The model used to fit the mechanical behaviour is the IVV model with the Ogden strain energy function for the elastic response which, as discussed previously, fits the experimental tests quite accurately. In table 4.13, the mean and standard deviation for the constants of the IVV model for each area of the breast and abdominal adipose tissue are presented.

To check the regional dependence of the material constants for the abdominal and breast adipose tissue, a MANOVA test was used. The independent variable was the extraction area with six levels: superficial breast, deep breast, superficial-lateral abdomen, superficial-medial abdomen, deep-lateral abdomen and deep-medial abdomen; and the DVs were the seven constants obtained from the fitting of the IVV model: μ, α, β_1^∞, β_2^∞, β_3^∞, β_4^∞ and β_5^∞.

Multinormality was checked using the Cardoso de Oliveira and Ferreira's test. This test was not significant for all the groups: superficial breast ($p = 0.779$), deep breast ($p = 0.931$), superficial-lateral abdomen ($p = 0.751$), superficial-medial abdomen ($p = 0.860$), deep-lateral abdomen ($p = 0.220$) and deep-medial abdomen ($p = 0.843$), so that the sample could be considered as multinormally distributed. Additionally,

individual Kolmogorov-Smirnov (K-S) tests were carried out for each of the dependent variables in each group, concluding that each distribution could be considered as normal. A Box's M test was conducted to check the homogeneity of the covariance matrix. It was significant ($p < .001$), therefore being necessary to perform a non-parametric MANOVA (NMANOVA).

The seven variables compared in the NMANOVA were: μ, α, β_1^∞, β_2^∞, β_3^∞, β_4^∞ and β_5^∞. Significant differences were found between the five groups compared using the Katz and McSweeney's test ($p < .001$). Afterwards, the Katz and McSweeney's post-hoc tests were carried out to detect the origin of these differences. Significant differences were found for β_2^∞ (between the superficial breast and the superficial-medial abdomen, $p = .001$, and between the deep-lateral and the superficial-medial abdomen, $p = .003$), β_3^∞ (between the superficial breast and the superficial-medial abdomen, $p = .006$), β_4^∞ (between the superficial breast and the deep-medial abdomen, $p = .002$; between the superficial breast and the deep-lateral abdomen, $p = .004$; between the superficial breast and the superficial-medial abdomen, $p = .042$; between the deep-medial abdomen and the superficial-lateral abdomen, $p = .015$; and between the deep-lateral abdomen and the superficial-lateral abdomen, $p = .032$) and β_5^∞ (between the superficial breast and the deep-medial abdomen, $p < .001$, and between the superficial breast and the deep-lateral abdomen, $p = .013$). In this case, β_3^∞, β_4^∞ and β_5^∞ were strongly correlated (Spearman $R > .82$) and could be regarded as the same variable from a statistical point of view. Therefore the test was repeated considering only β_4^∞ from these three variables, to check the correctness of the previous conclusion. The result could be maintained ($p < .001$). The p-values of the post-hoc comparisons are summarized in table 4.14, showing the lowest p-value of the seven dependent variables in each cell and highlighting in bold typeface the significant ones ($p < .05$). Many p-values are equal to one because the Bonferroni correction was used for the comparisons and all the values which were higher than one due to this correction has been set equal to one.

As a consequence, it can be stated that there are differences between the mechanical properties of the superficial breast and three groups of the abdomen: superficial-medial, deep-medial and deep-lateral. However, there are no differences with the superficial lateral one and with the deep layer of the breast fat. No differences were detected between the deep breast and the rest of the groups either. These conclusions have a high relevance for the breast reconstruction surgery with abdominal adipose tissue. The breast adipose tissue could be regarded as a unique tissue from the mechanical point of view. Thus for the breast reconstruction surgery, the deep breast fat can be replaced by any part of the abdomen, as no significant differences exist in the mechanical properties. However, the superficial breast fat should be replaced by the superficial lateral region of the abdomen. It must be clearly stated that autologous breast implants are usually made of a single piece of abdominal fat tissue and that taking two pieces from different parts of the abdomen imply surgical difficulties that could preclude its practical application. For that reason, the most advisable protocol would be to use a flap extracted from the superficial lateral area of the abdomen to replace the whole breast.

	Superficial breast	Deep breast	Superficial-lateral abdomen	Superficial-medial abdomen	Deep-lateral abdomen	Deep-medial abdomen
Superficial breast		$p = .111$	$p = 1$	$\mathbf{p = .001}$	$\mathbf{p = .004}$	$\mathbf{p < .001}$
Deep breast			$p = 1$	$p = 1$	$p = 1$	$p = 1$
Superficial-lateral abdomen				$p = .069$	$\mathbf{p = .032}$	$\mathbf{p = .015}$
Superficial-medial abdomen					$\mathbf{p = .032}$	$p = .192$
Deep-lateral abdomen						$p = 1$
Deep-medial abdomen						

Table 4.14: P-values of the post-hoc comparisons, showing the lowest p-value of the seven dependent variables in each cell and highlighting in bold typeface the significant ones ($p < .05$).

Also important although with less clinical relevance are the differences found between regions of the abdominal adipose tissue. It seems that no differences exist in the mechanical properties between both regions of the superficial layer, between both parts of the deep layer and between both parts of the medial regions. However, differences between the deep and superficial layers were founded, that is to say, the mechanical properties of the abdominal adipose tissue seem to change with the depth. This fact is in accordance with other authors' findings [47] who suspected it, although they did not proved it.

In addition, all the differences were detected in the constants which control the stress relaxation. Apparently the elastic constants were the same for the whole adipose tissue in the abdomen and breast, but the viscous constants were not. This implies that the behaviour under static loading can be consider equivalent, but not under dynamic loading.

In figure 4.20, as previously, the lowest and the highest experimental curves, in terms of the peak Cauchy stress, are drawn for the superficial breast fat and the three abdominal groups with which differences were found. The difference between the superficial breast fat and both deep regions of the abdomen is clear in view of the different ranges they have. The difference between the superficial breast and the superficial-medial abdomen is not easily seen with the naked eye. For practical reasons, the whole set of experimental curves could not be shown, but their general trend is as follows. Most of the specimens of the superficial-medial abdomen lie in the region enclosed by the curves of the deep layers of the abdomen. Moreover, most of the specimens of the superficial breast fat lie closer to its lowest limit than to the highest one, which could explain the origin of the differences found with the statistical analysis.

In figure 4.21, a figure similar to the previous one is presented, but now for the four abdominal groups. The differences between both deep groups and the superficial-lateral one seems to be justified by the differences

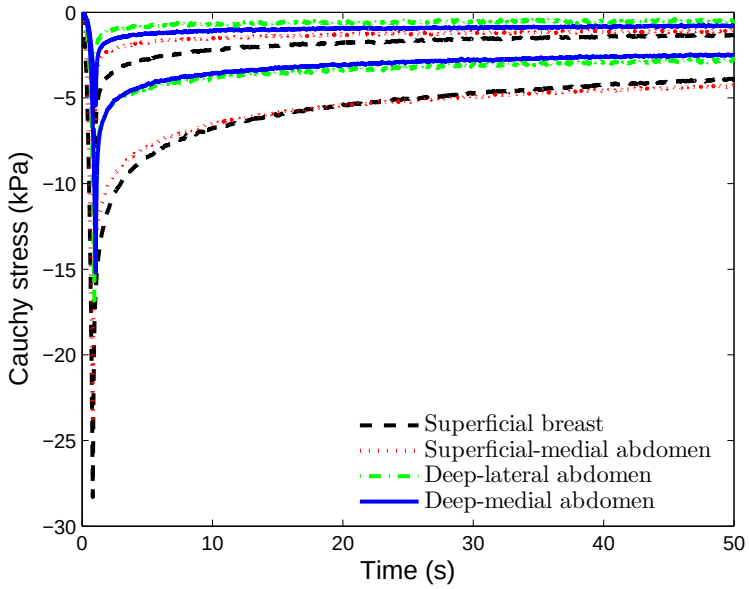

Figure 4.20: Comparison between the experimental curves for the superficial breast and the three abdominal groups with which differences were found.

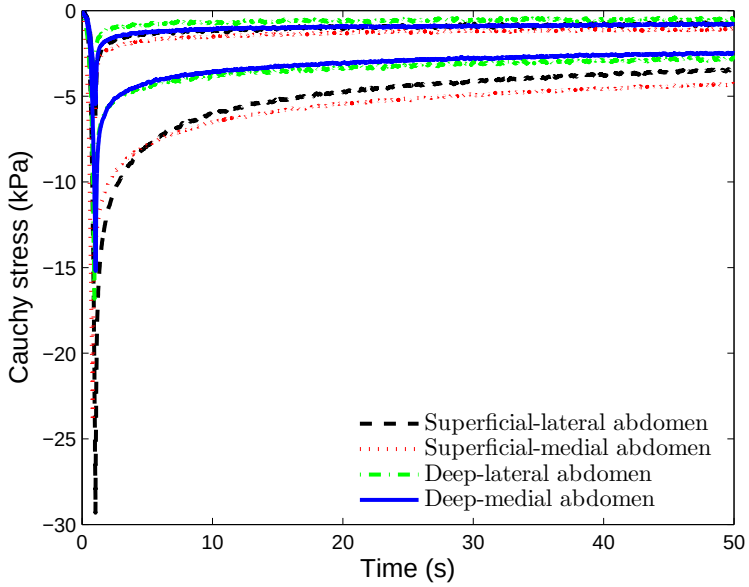

Figure 4.21: Comparison between the experimental curves for the four abdominal groups.

in the ranges. For the difference between the deep-lateral and superficial medial regions, although the ranges seem different, it is important to recall from the analysis of the previous figure that most of the specimens for the superficial-medial part lie in the region enclosed by the curves of the deep layers of abdominal fat. Therefore, no difference seems to be noticeable with the naked eye. If the curves for the specimens of both groups are studied in detail, it seems that they do not follow the same tendency in some areas. This could mean that the relaxation was different during the experimental test.

It is important to note that this study should be broaden to a larger number of patients, to increase the certainty of the above conclusions.

4.3.6 Comparison between the Samani's constants and the ones obtained here

In this section, the constants given by Samani for the breast adipose tissue [41], which are the unique ones for breast fat in the literature, are compared with those obtained in this work.

Here, the experimental tests were carried out on human adipose tissue mainly because of two reasons. First, because little information exists in the literature about the properties of this tissue, and even less about the breast and abdominal fat in particular. But also due to the fact that the FE models that used the experimental constants provided by Samani resulted very stiff compared with reality, as will be seen later in this document (chapter 5). When gravity loads were applied, the model was almost not deformed. That was actually the reason to carry out the previous experimental tests: to be sure of the goodness of the constants provided by Samani.

Here, the viscoelastic properties of the adipose tissue have been obtained. To be able to do a comparison with the information given by Samani, only the elastic part has been taken into account. Of course, the constants compared in this section are those corresponding to the fitting of the IVV model with the Ogden strain energy function for the elastic behaviour, as this was the finally selected model. Moreover, as Samani did experiments in the breast tissue, only our results for the breast have been compared. In figures 4.22 and 4.23, the stress-stretch curve of a uniaxial test simulated in a material with a behaviour described by the polynomial model and Samani's constants is compared with that simulated in a material having the behaviour fitted in the previous sections, both for the superficial and deep layers of the breast respectively. As can be seen in both figures, the difference between both models is very noticeable, even for small stretches. The behaviour with the Samani's model is much stiffer.

As will be seen later, after noticing that the FE model behaved much stiffer than in the reality, another set of simulations were conducted by dividing Samani's constants by some factors (10,100...) to analyse the effect of the softening of the tissues. Then, another curve is added to figures 4.22 and 4.23 in which the same curve is plotted but with Samani's constants divided by 100. As can be seen, the latter curve is very similar to that using the constants obtained in this thesis. In section 5.6.6, the constants will be compared

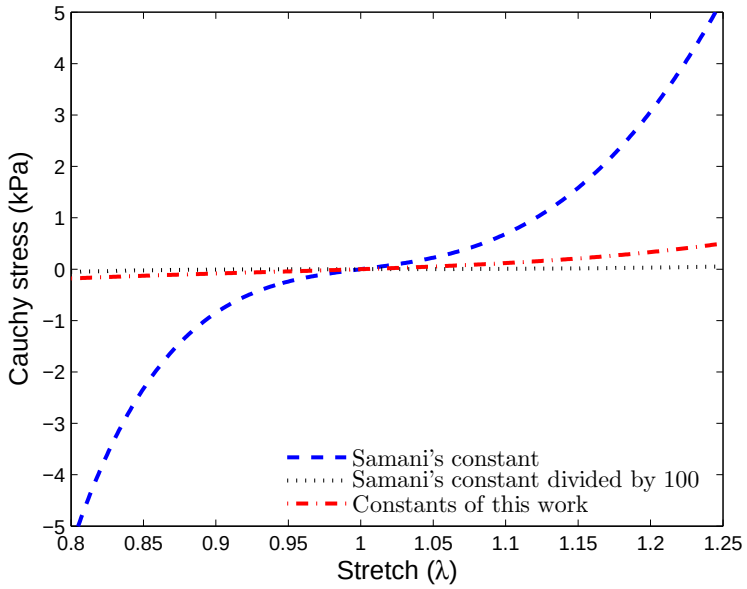

Figure 4.22: Comparison between the elastic constants given by Samani for the breast fat and the ones calculated in this work for the superficial layer.

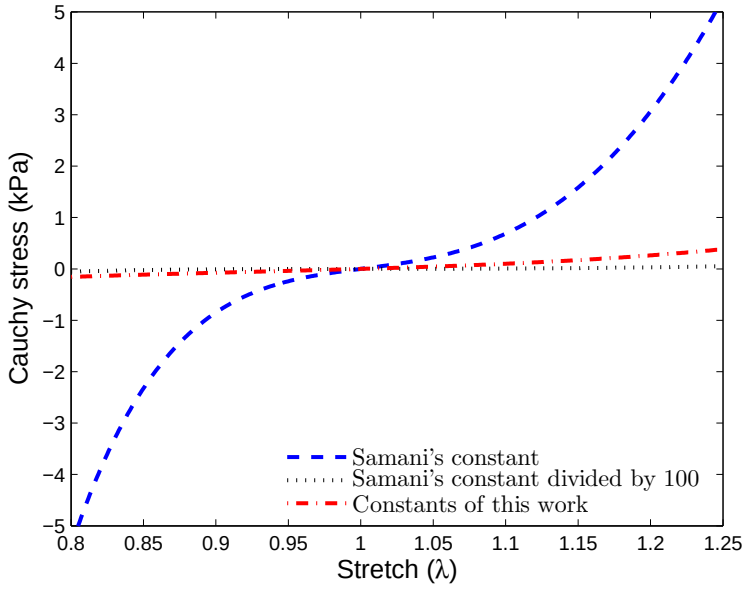

Figure 4.23: Comparison between the elastic constants given by Samani for the breast fat and the ones calculated in this work for the deep layer.

in a FE model of the breast. Therefore, and based on our experimental results and on the computational work, it seems that the constants provided by Samani do not match very well to the real behaviour of the breast adipose tissue.

Chapter 5

Finite element models of the breast

5.1 Introduction

The cooperation between medicine and biomechanics has emerged as a major issue which can be very useful to widen the knowledge and drive the research. In particular, the FE models of biological systems have been widely used for many years and have proved to be very useful in many applications. Although it is quite complicated to model the behaviour of biological tissues, their interactions and functions, many advances have been carried out and a lot of help has been provided to clinicians in many fields.

As stated in the introduction of this thesis, the motivation of this work is to shed light on the modelling of the behaviour of the healthy breast, because, to the best of the author's knowledge, nobody has been able to simulate the natural movement of the breast, i.e., its global behaviour.

Many breast FE models exist for different applications. Mainly, they are devoted to simulate mammographic compression, gravity loading or to match different medical images, as mammography and MRI. Azar et al. [3] constructed a FE model to predict the location of a tumour when the breast is compressed between two plates. They tested the model comparing the estimated location of the tumour with real MR images. In the same year, Samani et al. [5] made a model, also for compression between two plates, validating it with a phantom and finally with a real breast with the aid of MRI. Schnabel et al. [8] presented a method to validate nonrigid image registration using FE models. For many years, Ruiter el al. [9, 10] and Hopp et al. [11, 12, 13] have been working to develop medical image registration algorithms, using FE models of the breast to simulate breast mammographic compression. Pathmanathan et al. [6] built a breast FE model and obtained an undeformed configuration and a breast compression, but they did not compare the numerical results with experimental ones. Rajagopal et al. [16, 17] developed a subject-specific breast model subjected to gravity, using cubic-Hermite basis functions to generate the geometry. They identified the reference state as the breast immersed in water. Considering the breast composed of only one material, and modelling it

with a neo-Hookean strain energy function, they fitted its material parameter to simulate the prone position. Pérez del Palomar et al. [18] constructed a FE model to simulate the change in position between supine and standing up. They measured the distances between some characteristic points in the model and compared them with the real ones. Lapuebla-Ferri [21] presented a model to simulate a prosthesis insertion for augmentation mammoplasty. The deformed shape of the FE model was compared with the real shape. Han et al [7] built a FE model for mammary compression between two plates and firstly compared different solvers. Finally, they compared the results between four different material characteristics: isotropic-anisotropic and homogeneous-heterogeneous. Gamage et al. [19] built a model to simulate the position change from prone to supine with heterogeneous FE models. They compared the results with the homogeneous models. Zain-Ul-Abdein et al. [20] constructed a FE model, starting from a reference position, that was the breast immersed in water. Then, they applied gravity loads to simulate the upright position and compared it with a real image through the distance between some points. Mertzanidou et al. [14] presented a framework for MRI to X-ray mammography registration, i.e., using a compression simulation. They optimised both material and pose parameters simultaneously during registration. Han et al. [15] proposed a hybrid nonlinear biomechanical model based registration method. It combined a biomechanical FE modelling with image registration techniques. The FE model gave a plausible deformation which was used to initialize the registration. Pianigiani et al. [4] developed a subject-specific breast model based on anthropometric measurements. They validated the model by comparing it with reality in a craniocaudal compression. Then, they simulated 3 different loading conditions, used 3 different materials and compared the displacement of a tumour inclusion between them.

Some authors have worked trying to determine the reference state of the breast, i.e., the geometry of the breast if it were not subjected to any load. Rajagopal et al. [22] proposed an inverse method to obtain this unloaded configuration from a deformed state. They validated this method comparing the computed reference state in two problems: the analytic solution of pressure inflation and axial extension of a thick-walled cylinder and the experimental results of a silicon gel sample subjected to gravity loads. In the same year, Rajagopal et al. [16] identified the reference state as that where the breast is immersed in water. However, the density of the breast tissues is not equal to the water density and therefore the gravity is not completely cancelled. Moreover, their assumption does not take into account the possible prestress of the skin and breast tissues. Zain-Ul-Abdein et al. [20] considered also this situation as the reference state. Vavourakis et al. [23] recently proposed a displacement-pressure formulation to obtain the unloaded configuration of soft tissues and applied it to the breast. Other authors, such as Riveros et al. [120], have published methods to obtain the reference state which can be applied to the breast, though they were initially applied to other tissues.

All these models can be used for the application they were designed for (with better or worse results

depending on the particular model), but when they are used to simulate a different scenario, they normally do not work. Pérez del Palomar [18] and Zain-Ul-Abdein et al. [20] validated their models measuring the distance between some points of the mesh. But simply looking at the deformed shape of the models with the naked eye, it is clear that they are far from the real deformation. Many authors validated their models using a compression test and comparing the deformed shapes with a real image [3, 24, 7, 14, 4], but these deformations were obtained by imposing displacements in the contact between the breast and the plates and considering the materials as incompressible. Therefore, it was quite foreseeable that the deformed configurations were similar to reality, but not necessarily the stresses.

As stated previously, our aim was to simulate the change of position from supine to prone and estimate the deformed shape of the breast due to the action of gravity loads. The initial objective was to simulate the behaviour under any change of position of the body, but to simplify the problem, only the supine-prone change was chosen because it is considered as the most complex, due to the great deformations which are produced. For that purpose, a FE model of a female breast was constructed and its deformed shape after applying gravity was compared with superficial 3D scan images taken from the same individual that the FE model. Using the material properties and boundary conditions provided in the literature, the behaviour of the breast was quite far from the real one. That could mean that those properties and boundary conditions existing in the literature might be useful for a limited number of applications, but not to reproduce the real breast behaviour in a large deformations problem like this. Therefore, this thesis intends to provide more information to comprehend the way the breast deforms under loading. Once the FE model was built, simple boundary conditions and material models were initially tried. Then, they were changed to study their influence and to approach a more realistic deformation.

This chapter is structured so that the different models are presented following the real timeline, explaining the improvement provided by each model, and why the next model was built. First, it will be explained how the FE model was constructed and the possible boundary conditions applied as well as some other information needed to understand the whole process.

5.2 FE model construction

The FE model was constructed from CT images taken from a 48 years old female patient at the *Virgen del Rocío* Hospital before surgery for breast reconstruction. The resolution of these images is worse than that of MR images, so hindering the differentiation of soft tissues. However, the protocol of this hospital dictates the use of that imaging technique, which was therefore the only one available. The CT images were taken in supine position, so that this was the initial position of the FE model.

The CT study consisted of 120 images with a resolution of 0.87 x 0.87 x 5 mm. The patient stretched her arms over her head (aligned with the trunk) and kept them extended during acquisition. A sample image of

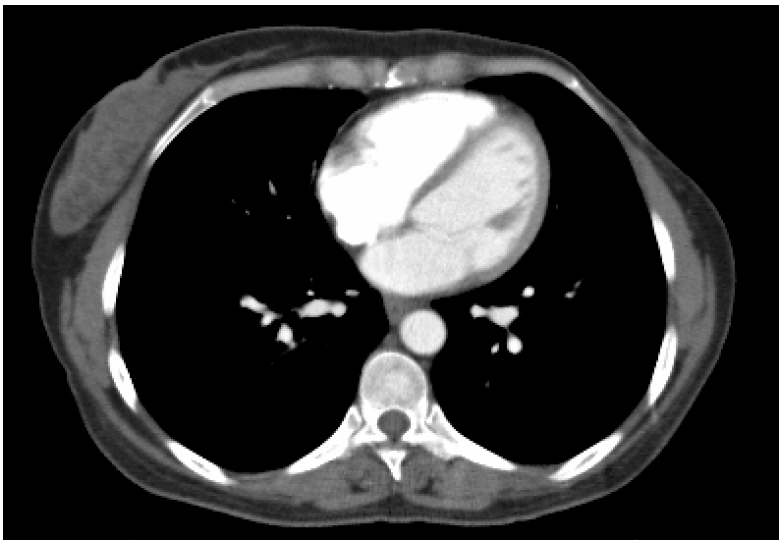

Figure 5.1: Sample image of the CT with the original resolution (0.87 x 0.87 mm in the transverse plane) viewed in craniocaudal direction from bottom to top.

the original CT can be seen in figure 5.1. In it, the spine can be seen at the bottom of the image, the heart in the center-right part and the right breast is observed on the left. The left breast is not present because the CT was taken after a mastectomy surgery of this breast. The Simpleware software was used to process the images in order to build the FE model. In particular, the ScanIP and ScanFE modules were used. With the first one, the CT images were processed and the tissues segmented. Then, the file was exported to ScanFE, where the parameters to build the FE model were set, and finally the input file (.inp) generated for the simulation software Abaqus. The process is detailed next.

First, the CT images were imported with the ScanIP module. This software works with voxels, whose dimensions correspond to the resolution of the images and from which the elements of the FE model were generated. As the initial resolution was 0.87 x 0.87 x 5 mm, the voxels had one dimension considerably larger than the others. To improve the aspect ratio of the voxels, the images needed to be resampled to convert the voxels into cubes. Another issue to take into account was that the smaller the voxels were, the higher the number of elements would be, so increasing the computation time. Therefore, it was important to reach a compromise between computation time and resolution of the model. A mesh convergence analysis was carried out to determine a mesh density which accomplished this compromise solution. At first, the images were resampled to a resolution of 0.87 x 0.87 x 0.87 mm (only changing in the craniocaudal direction), but the number of elements of the so generated FE model was too high to get reasonable computation times. Then, the images were resampled to a new resolution of 2.1 x 2.1 x 2.1 mm, using a linear interpolation of the grey level. In figure 5.2, the same slice of figure 5.1 is shown but now with the new resolution. As can be noticed the resolution is worse, mainly in the boundaries, but even the details are conserved, being this resample adequate given that a smoothing operation would be carried out afterwards to improve the

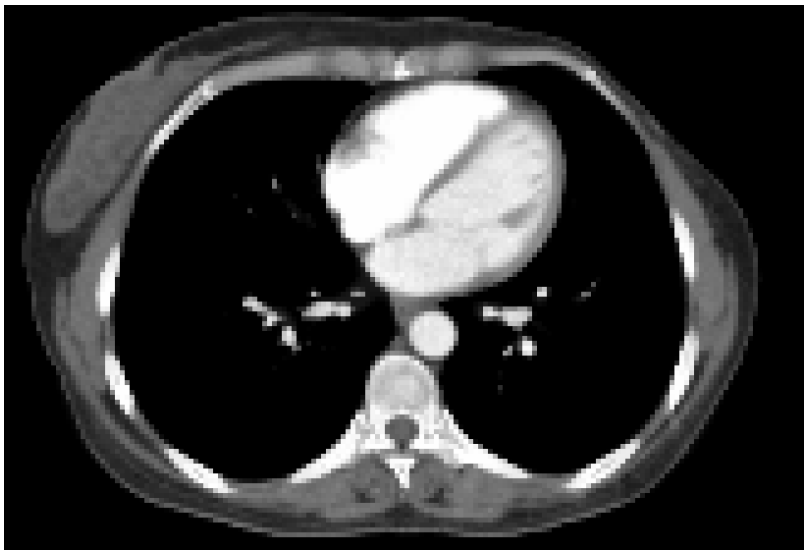

Figure 5.2: Resampled image of the CT (2.1 x 2.1 mm resolution in the transverse plane).

surfaces.

As only one breast was modelled (the right one in this case) and no other parts of the body, the images were cropped in order to reduce the size of the model, and as a consequence, the number of elements, which is key in the computation time. Superiorly, the model was trimmed approximately at the height of the clavicle, and inferiorly below the inframammary fold. Medially, it was cut in the middle of the sternum (sagittal plane) and laterally by the coronal plane (see figure 5.3).

The segmentation process started with an automatic segmentation with grey level thresholds. Then, a manual segmentation was performed to improve the automatic one and reduce errors. All the internal organs were removed (e.g. the heart or the lungs) and only the bones (ribs and sternum), muscle, skin and mammary tissue were left. Finally, a smoothing process with a recursive gaussian filter was carried out to smooth the boundaries. In figure 5.4 the result of the segmentation is shown. The bones appear in red color, the muscles in green and the fat in pink. The area shown in blue color was the brighter area and corresponds to the mammary gland, which is intermingled with adipose tissue. It was not possible to differentiate the fat from the glandular tissue in the CT image, so that both tissues had to be treated jointly. The properties of this mixture were calculated with the homogenized model presented in section 4.2, considering a 50% of fat, as estimated by the surgeons. It was not possible to differentiate the skin either, so it will be created later as a membrane covering the breast.

This segmentation was then exported to the ScanFE module. The bones were assumed rigid and not included in the FE model. They were only segmented to locate the area in contact with the muscle, which was fixed in the FE model. Linear tetrahedral elements were selected to mesh the model and after meshing an additional smoothing was performed on the surface. Finally, the program generated an Abaqus input file. The skin was created by superimposing membrane elements on the exterior face of the adipose tissue

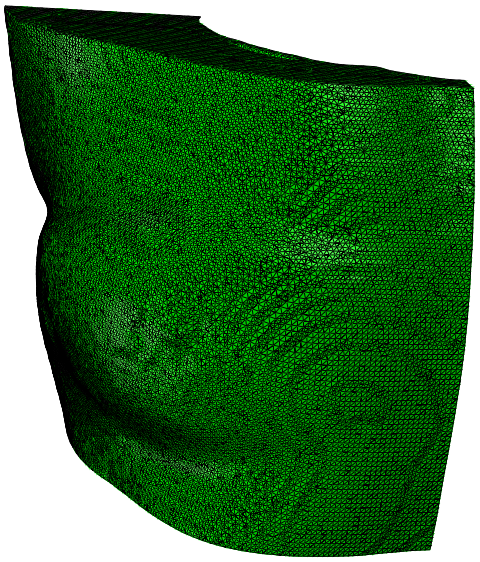

Figure 5.3: Breast model with 937517 elements, viewed from the front.

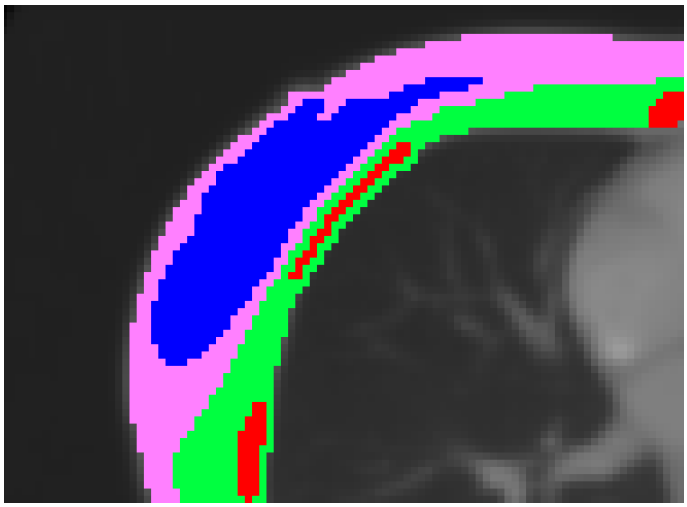

Figure 5.4: Segmentation of the tissues in the CT images (2.1 x 2.1 mm resolution in the transverse plane).

elements.

The FE model finally comprised 186303 nodes and 937517 elements: 29726 of skin, 346510 of muscle, 428397 of adipose tissue and 132884 of the fat-gland mixture. C3D4H elements (3D four-noded tetrahedral hybrid elements) were selected for all the tissues except for the skin, modelled with M3D3 elements (3D three-noded membrane elements). The final model is shown in figure 5.3.

The time needed to solve this model under gravity loads was considerably high. A convergence analysis was carried out to find a compromise between computation time and accuracy of the solution. Five models with less elements were built in the same way described before. Convergence was evaluated by comparing the displacement of a point of the model which is located in the region of maximum displacements. In figure 5.5, the displacement of this node and CPU time are plotted against the number of nodes.

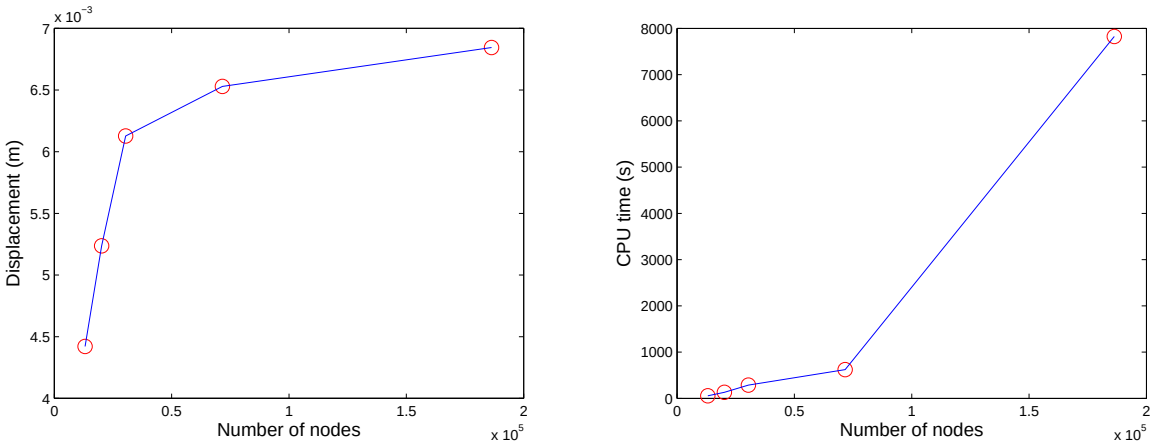

Figure 5.5: Convergence analysis. Number of nodes vs. displacement and CPU time.

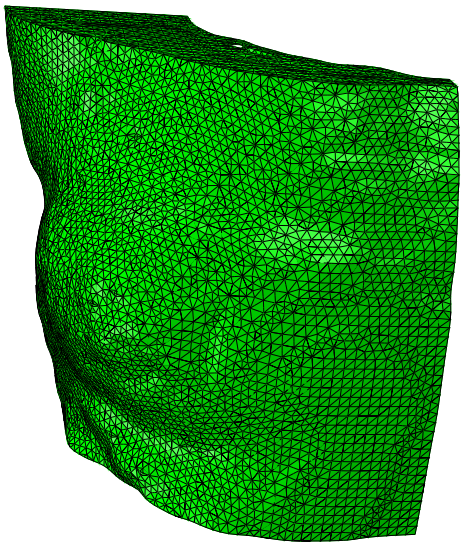

Figure 5.6: Breast model with 152407 elements.

The model with 30403 nodes (the one which appears in the middle of the graphs shown in figure 5.5) was finally selected because the computation time was greatly reduced compared with the model presented before (the one with the highest number of nodes), and the accuracy was reasonably maintained. For this model, shown in figure 5.6, the resolution of the CT images was 4.2 x 4.2 x 4.2 mm (see figure 5.7). Comparing the CT images from which this model was generated with the original CT, it can be seen that the resolution is considerably worse, but the main features are conserved and only the surfaces are slightly blurry. The model had 30403 nodes and 152407 elements: 7396 of skin, 58643 of muscle, 64866 of adipose tissue and 21502 of the fat-gland mixture.

In many simulations carried out in this thesis, the breast was subjected to large deformations. As a result, several elements of the mesh were highly distorted. In those cases, the convergence with the model presented before was difficult because there were some bad shaped elements in the area where the adipose

Figure 5.7: Resampled image of the CT (4.2 x 4.2 mm resolution in the transverse plane).

tissue, the fat-gland mixture and the muscle were close to each other. The Simpleware software was not able to generate good quality elements in these areas where different surfaces came together. Moreover, some simulations were carried out with a contact surface between the muscle and the breast tissues, which requires a sufficiently smoothed surface. The above model did not accomplish this requirement, as it was not specifically designed for this. To solve these problems, another model was created, with approximately the same mesh density, by joining the adipose tissue and the fat-gland mixture in one single material. As only one material existed, the elements near the interface between the mixture and the muscle became better shaped and produced less convergency problems. The performance of this model was compared with the previous described model, checking that the displacements were practically the same.

This model had a total of 31669 nodes and 138229 elements: 7234 of skin, 63147 of muscle and 67848 of the fat-gland material. The properties of this mixture were calculated with the homogenized model presented in section 4.2, considering a 80% of fat. This rough fat proportion was estimated knowing the volumen ratio between the pure adipose tissue and the fat-gland mixture of the previous model, and that this previous mixture had a 50% of fat as estimated by surgeons. The number of elements was slightly reduced compared with the previous model, mainly because a lot of elements were needed to delimit the surface between the adipose tissue and the mixture of fat and gland in the old model.

The densities considered for fibroglandular and fat tissues were 1.04 g/cm^3 and 0.93 g/cm^3, respectively [102, 103, 104]. For the homogenized material, the density was calculated using the rule of mixtures. The density for the skin was taken as 1.1 g/cm^3 [121] and its thickness as 1.61 mm [122, 123, 124]. The density of the muscle was taken as 1.0597 g/cm^3 [125].

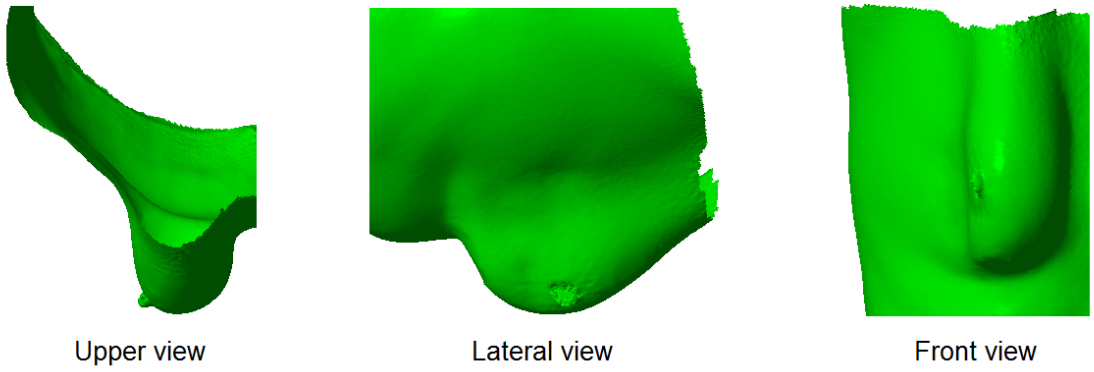

Figure 5.8: Superficial 3D scan of the breast in prone position.

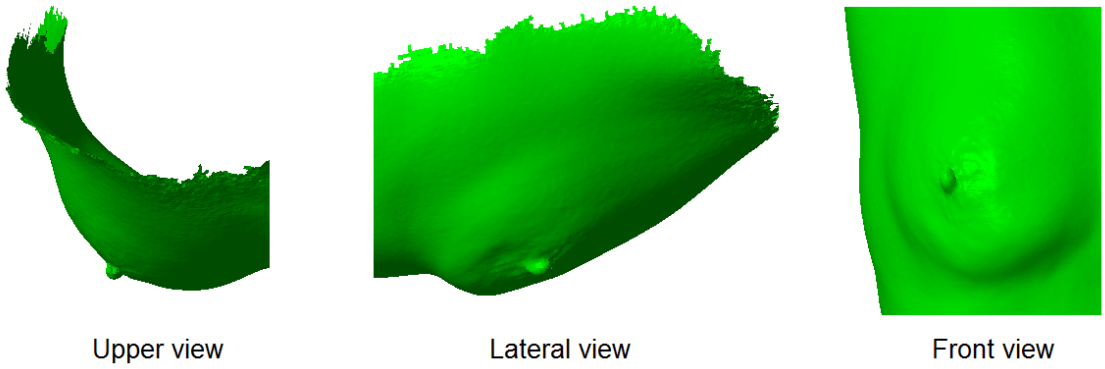

Figure 5.9: Superficial 3D scan of the breast in standing up position.

5.3 Superficial 3D scan images

To check the correct behaviour of the FE model, it was validated using superficial 3D scan images, by comparing the deformed shape of the breast. As said before, the simulated case was a change of position between supine and prone. The CT images used to build the FE model were taken in supine position, and applying gravity loads, the prone position was obtained. Therefore, a superficial 3D scan image was also taken in this prone position, to obtain the real deformation of the breast. This scan image was taken with the arms stretched over the patient's head (aligned with the trunk), just like the CT images. Thus, the muscles are supposedly not activated between both positions, being possible to model them as a hyperelastic material without considering the active force. In figure 5.8 the 3D scan image in prone position can be seen from different points of view. A superficial 3D scan image was also taken in standing position. Different views of it are shown in figure 5.9.

To compare the superficial 3D scan with the deformed FE model, the external surface of this model and the 3D scan were superimposed. In the majority of the cases, a simple comparison with the naked eye was enough to evaluate if the simulated deformation was similar to reality or not. Nonetheless, to evaluate quantitatively the goodness of the simulation, the distance between both surfaces in anteroposterior direction

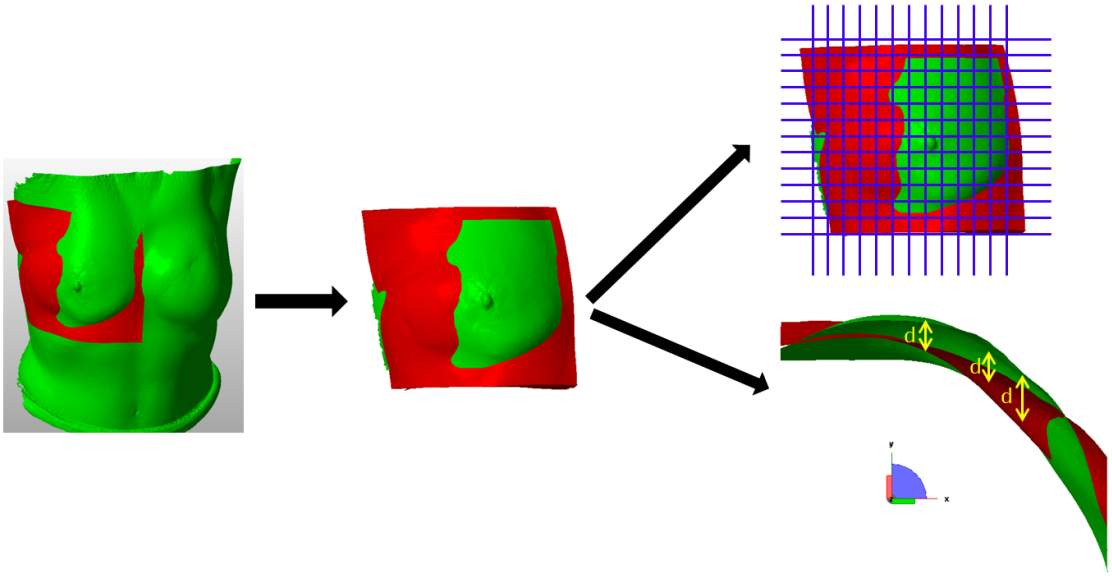

Figure 5.10: Scheme of the method to evaluate the accuracy of the deformed model.

was measured in a grid of 140 points, as can be seen in the scheme of figure 5.10. A mean absolute error and a mean relative error (relative to the real displacement) were assessed between both configurations.

5.4 Boundary conditions

In the process followed to build the breast model, this was cut off from the rest of the body, so generating 4 boundaries: upper, lower, medial and lateral (see figure 5.11), being therefore necessary to impose boundary conditions in these limits. In this section, the anatomical conditions which actually exist in these boundaries of the breast model are explained for each tissue (except for the gland, which is inside), as well as how they were finally modelled. Nonetheless, some of these boundaries were changed through the simulations of this chapter to analyze their influence. Moreover, the interactions between the different tissues are also presented.

5.4.1 Adipose tissue

The adipose tissue (in yellow in figure 5.11) is rigidly bonded to the skin, as could be checked in the breast and abdomen samples extracted and tested in section 4.3, and to the glandular tissue, and so was the connection between these tissues modelled. Between the adipose tissue and the muscle, at the back of the breast, there is a layer called the retromammary space, made of loose connective tissue, anteriorly covered by the deep layer of the superficial fascia and posteriorly covered by the pectoralis fascia. It allows some degree of movement of the breast over the chest wall [94]. There is no consensus on how loose or rigid this connection is and no data on this issue was found in the literature either. Therefore, several solutions were

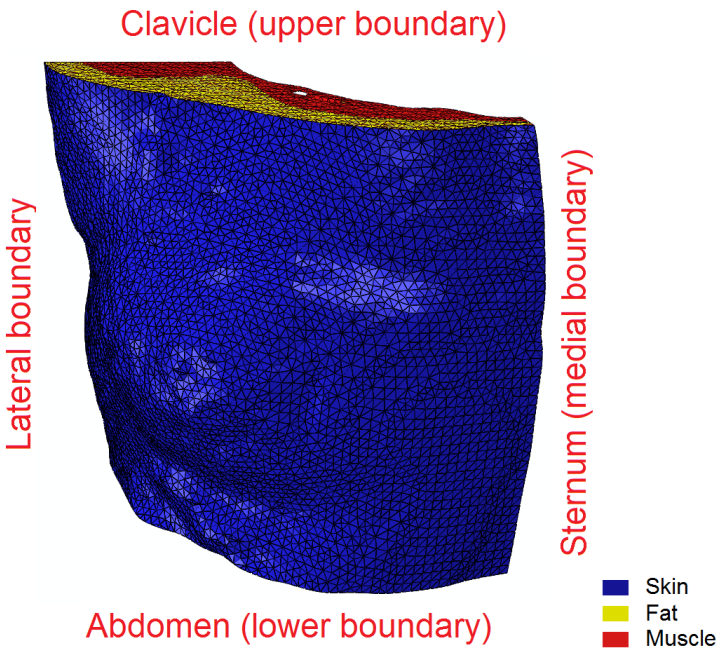

Figure 5.11: Boundaries produced by the cut of the model from the rest of the body.

tried to model the interaction between muscle and fat: free, fixed, spring connection and different contact surface options. The precise conditions will be specified in the corresponding section.

The four boundaries generated by the separation of the model from the rest of the body (see figure 5.11) are complex too. The medial one, attached to the sternum, can be considered as fixed because it is very thin and close to the bone. Moreover, the symmetry with respect to the sagittal plane restrains its movement in the mediolateral direction. The other three cut boundaries are connected to the rest of the tissues of the body, and it is difficult to determine exactly how the behaviour of these areas is. It was modelled with several conditions to study which was the closest to the real behaviour.

5.4.2 Muscle

The pectoral muscles are inserted to the ribs, the sternum, the humerus, the scapula and the clavicle by means of tendons. They are strongly joined to these bones so that, in the model, the nodes of the muscles which are in contact with the bones were considered as fixed, restraining all their degrees of freedom. That included all the connections to the ribs, the upper boundary of the muscle, which corresponds to its connection to the clavicle, and the medial-superior boundary, with the insertion to the sternum (see figure 5.11). For the medial-inferior, lower and lateral boundaries, the nodes were also considered fixed, due to the fact that the pectoral muscles are joined to other big groups of muscles and that makes a strong bond. Moreover, as explained in the previous section, the change between supine and prone position was performed without the contraction of the muscles, so that the muscular structure was quite fixed. Although these conditions were used in the subsequent models on a general basis, in the first ones, some other boundary conditions were

tried to analyse their influence.

In the model, the muscle was only in contact with the adipose tissue, and the modelling of this interaction was explained above.

5.4.3 Glandular tissue

The glandular tissue was considered as rigidly bonded to the fat over its contact surface. It has no contact with the rest of the tissues, except for a small area in which it is connected to the skin (near the nipple area) and here it was considered rigidly bonded too. In the FE model in which the glandular tissue and the fat were modelled jointly, the boundary conditions of this mixture were equivalent to those of the adipose tissue, explained above.

In figure 5.11, the glandular tissue is not shown because it is inside the model, surrounded by fat and skin. Therefore, this tissue is not involved in the four cut boundaries.

5.4.4 Skin

As said above, the skin is closely bonded to the adipose tissue and, thus, it was modelled as perfectly bonded. With respect to the four cut boundaries, the skin of the model is connected to the rest of the skin and therefore, some kind of elastic bound must exist. In the medial boundary (in the sternum), the skin can be considered fixed mainly because it is very close to the bone and its movement is limited, due to the symmetry with respect to the sagittal plane. In the other three boundaries, different conditions were tested: fixed, totally free and an intermediate situation with springs, so simulating the effect of the rest of the skin. The precise conditions will be specified in the corresponding section.

5.5 Material models used

All the tissues were considered near-incompressible, hyperelastic and isotropic (except for sections 5.6.12 and 5.6.13.3, in which a fibred model was used). In table 5.1, a summary of the the material models used through this chapter is presented. A short name is given to each in order to simplify their reference through the subsequent sections.

The original constants of some material models were divided by certain factors in this thesis, as will be seen later. This change is denoted with a subscript in the name of the model, indicating the factor which divides the original constants. Moreover, when the homogenized model presented in section 4.2 was used, a superscript indicates the fat percentage considered. For example, the H^{50}_{100} material model is the homogenized model with a 50% of fat, with the constants divided by a factor of 100.

Name	Material model	Taken from	Strain energy function	Tissue	Original material constants
BM	Rubin-Bodner	Barbarino et al. [43]	$\Psi = \frac{\mu_0}{2q}\,(e^{qg}-1)$, $g = 2\,m_1\big(J-1-ln(J)\big)+(1-\omega)\,m_2\,(\bar{I}_1-3)$	Muscle	$\mu_0 = 3.7$ MPa, $q = 25$, $m_1 = 595$, $m_2 = 2.16\cdot 10^{-3}$, $\omega = 0$
Ohl	Linear elastic	Ohl et al. [91]		Muscle	$E = 790$ kPa, $\nu = 0.45$
S_f	5 terms polynomial	Samani et al. [41]	$\Psi = C_{10}(I_1-3)+C_{01}(I_2-3)+C_{11}(I_1-3)(I_2-3)+C_{20}(I_1-3)^2+C_{02}(I_2-3)^2$	Fat	$C_{10} = 310$, $C_{01} = 300$, $C_{11} = 2250$, $C_{20} = 3800$, $C_{02} = 4720$ (Pa)
TT	First order Ogden	Model proposed in this thesis, section 4.3	$\Psi = \frac{\mu}{\alpha}(\lambda_1^\alpha+\lambda_2^\alpha+\lambda_3^\alpha-3)$	Fat	$\mu = 67.869$ (Pa), $\alpha = 8.575$
H_f^p	5 terms polynomial	Homogenized model proposed in section 4.2	$\Psi = C_{10}(I_1-3)+C_{01}(I_2-3)+C_{11}(I_1-3)(I_2-3)+C_{20}(I_1-3)^2+C_{02}(I_2-3)^2$	Mixture fat-gland	Function of p (see section 4.2)
BS	Rubin-Bodner	Barbarino et al. [43]	$\Psi = \frac{\mu_0}{2q}\,(e^{qg}-1)$, $g = 2\,m_1\big(J-1-ln(J)\big)+(1-\omega)\,m_2\,(\bar{I}_1-3)$	Skin	$\mu_0 = 1.7$ MPa, $q = 36$, $m_1 = 1294$, $m_2 = 8\cdot 10^{-4}$, $\omega = 0.9$
PP	5 terms polynomial	Pérez del Palomar et al. [18]	$\Psi = C_{10}(I_1-3)+C_{01}(I_2-3)+C_{11}(I_1-3)(I_2-3)+C_{20}(I_1-3)^2+C_{02}(I_2-3)^2$	Skin	$C_{10} = 31$, $C_{01} = 30$, $C_{11} = 22.5$, $C_{20} = 50$, $C_{02} = 60$ (Pa)
GOH	Gasser-Ogden-Holzapfel	Gasser et al. [46]	$\Psi = \frac{C_{10}}{2}(I_1-3)+\frac{k_1}{2k_2}\left(e^{k_2[\kappa\bar{I}_1+(1-3\kappa)\bar{I}_4-1]^2}-1\right)$	Mixture fat-gland	$C_{10} = 300$ Pa, $k_1 = 1700$ Pa, $k_2 = 15.4$, $\kappa = 0.13$

Table 5.1: Summary of the material models used in chapter 5. The subscript f stands for the factor dividing the original constants. The superscript p stands for the percentage of fat considered.

5.6 FE Models

In this section, the different FE models which have been built are presented. Their advantages or problems are discussed and the subsequent modification introduced to each model will be justified in terms of improvement of the deformed shape compared with the 3D scan image. Only those models which are useful to understand the process followed during the development of this thesis are presented. Many other models, checks, attempts and convergence tests carried out are not included. In tables 5.2, 5.3 and 5.4, a summary of the FE simulations presented in this work is included.

5.6.1 Muscle fixed to the ribs and sternum, without skin.

The first model was made with the simplest configuration. Thus, like in other breast models in the literature, all the materials were considered bonded to the surrounding tissues in the contact between each other, and their properties were taken from the literature. Only those nodes of the muscle in contact with the ribs and sternum were fixed, the rest were considered free to move. The skin was not modelled in these first models to analyse separately the behaviour of the other tissues.

For the muscle, the BM model, presented in table 5.1, was used. The values of the constants are also shown in table 5.1. A UHYPER subroutine was programmed to implement the Rubin and Bodner model, as it is not included as a material model in Abaqus. The properties of the muscle are not the most influential ones, due to the fact that it is much stiffer than the breast tissues and that it is not much deformed with the position change. For the adipose tissue, the S_1 model was used, i.e., with the original properties, shown

Section	Skin	Breast tissues	Muscle	Boundary conditions	Other
5.6.1	No	Fat (S_1) and fat-gland mixture (H_1^p)	BM	Contact muscle-ribs/sternum fixed	Supine-prone simulation, with 3 proportions for the fat-gland mixture (30%, 40% and 50% of fat) Supine-standing up simulation, with 3 proportions for the fat-gland mixture (30%, 40% and 50% of fat)
5.6.2	BS. Membrane	Fat (S_1) and fat-gland mixture (H_1^{50})	BM	Contact muscle-ribs/sternum fixed	
5.6.3	BS. Membrane	Fat (S_1) and fat-gland mixture (H_1^{50})	BM	Contact muscle-ribs/sternum fixed. Perimeter of muscle fixed	
5.6.4	BS. Membrane	Fat (S_j) and fat-gland mixture (H_j^{50})	BM	Contact muscle-ribs/sternum fixed. Perimeter of muscle fixed. Fat fixed in medial and lateral boundaries	2 simulations using S_{100} - H_{100}^{50} and S_{200} - H_{200}^{50}
	BS. 3D solid	Fat (S_{200}) and fat-gland mixture (H_{200}^{50})	BM	Contact muscle-ribs/sternum fixed. Perimeter of muscle fixed. Fat fixed in medial and lateral boundaries	
	No	Fat (S_{200}) and fat-gland mixture (H_{200}^{50})	BM	Contact muscle-ribs/sternum fixed. Perimeter of muscle fixed. Fat fixed in medial and lateral boundaries	
5.6.5	No	Fat (S_j) and fat-gland mixture (H_j^{50})	BM	Contact muscle-ribs/sternum fixed. Perimeter of muscle fixed. Fat fixed in medial and lateral boundaries	5 simulations using S_{200} - H_{200}^{50}, S_{400} - H_{400}^{50}, S_{800} - H_{800}^{50}, S_{1600} - H_{1600}^{50} and S_{4000} - H_{4000}^{50}
5.6.6	BS. Membrane	Fat (S_j) and fat-gland mixture (H_j^{50})	BM	Contact muscle-ribs/sternum fixed. Perimeter of muscle fixed. Fat fixed in medial and lateral boundaries	2 simulations using S_1 - H_1^{50} and S_{100} - H_{100}^{50}
		Fat (TT)	BM	Contact muscle-ribs/sternum fixed. Perimeter of muscle fixed. Fat fixed in medial and lateral boundaries	
5.6.7	BS. Membrane	Fat (S_1) and fat-gland mixture (H_1^{50})	BM	Contact muscle-ribs/sternum fixed. Perimeter of muscle fixed	Thin layer of tissue between muscle and breast tissues (neo-Hookean). 3 simulations varying C_1
5.6.8	BS. Membrane	Fat (S_j) and fat-gland mixture (H_j^{50})	No	Perimeter of skin fixed	4 simulations using S_{10} - H_{10}^{50}, S_{100} - H_{100}^{50}, S_{400} - H_{400}^{50} and S_{2000} - H_{2000}^{50}
5.6.9	BS. Membrane	Fat (S_{100}) and fat-gland mixture (H_{100}^{50})	BM	Contact muscle-ribs/sternum fixed. Perimeter of muscle and skin fixed. Spring connection muscle-breast tissues	Several spring stiffness and distributions
5.6.10	PP. Membrane	Fat (S_{100}) and fat-gland mixture (H_{100}^{50})	No	Perimeter of skin fixed. Fat fixed in medial boundary	
	BS. Membrane	Fat (S_{100}) and fat-gland mixture (H_{100}^{50})	No	Perimeter of skin fixed. Fat fixed in medial boundary	3 simulations changing μ_0 and 6 varying q
				Lateral and medial boundaries of skin fixed. In upper and lower boundaries, displacements constrained in craniocaudal direction. Fat fixed in medial boundary	3 simulations varying q, 4 varying m_1 and 3 changing m_2

Table 5.2: Summary of the FE simulations presented in this work, ordered by section.

Section	Skin	Breast tissues	Muscle	Boundary conditions	Other
5.6.11.1	PP. Membrane	Unique, fat-gland mixture (H_j^{80})	Ohl	Contact in the whole surface muscle-breast tissues. Contact muscle-ribs/sternum fixed. Perimeter of muscle fixed. Breast tissues fixed in sternum. In upper and lower boundaries of skin, displacements in medial-lateral and anteroposterior directions allowed, but not in craniocaudal	3 simulations using H_{10}^{80}, H_{100}^{80} and H_{1000}^{80}
				Contact in the whole surface muscle-breast tissues. Contact muscle-ribs/sternum fixed. Perimeter of muscle fixed. Breast tissues fixed in sternum	2 simulations using H_{100}^{80} and H_{1000}^{80}
5.6.11.2	PP. Membrane	Unique, fat-gland mixture (H_{1000}^{80})	Ohl	Contact in the whole surface muscle-breast tissues. Contact muscle-ribs/sternum fixed. Perimeter of muscle fixed. Breast tissues fixed in sternum. In the lower boundary of skin, displacements constrained in craniocaudal direction. Springs in the lateral boundary of skin	Simulations with several spring stiffness
				Contact in the whole surface between muscle-breast tissues. Contact muscle-ribs/sternum fixed. Perimeter of muscle fixed. Breast tissues fixed in sternum. In the lower boundary of skin, displacements constrained in craniocaudal direction. Springs in the lateral and upper boundaries of skin	Simulations with several spring stiffness
5.6.11.3	PP. Membrane	Unique, fat-gland mixture (H_1^{80})	Ohl	Contact surface muscle-breast tissues in a stripe of the lateral boundary. Contact muscle-ribs/sternum fixed. Perimeter of muscle fixed. Breast tissues fixed in sternum. In upper and lower boundaries of skin, displacements in craniocaudal direction constrained	
5.6.11.4	PP. Membrane	Unique, fat-gland mixture (H_j^{80})	Ohl	Contact surface muscle-breast tissues in a stripe of the lateral, upper and lower boundaries. Contact muscle-ribs/sternum fixed. Perimeter of muscle fixed. Breast tissues fixed in sternum. In upper and lower boundaries of skin, displacements in craniocaudal direction constrained	3 simulations using H_1^{80}, H_{10}^{80} and H_{100}^{80}
		Unique, fat-gland mixture (H_{100}^{80})	Ohl	Contact surface muscle-breast tissues in a stripe of the lateral, upper and lower boundaries. Contact muscle-ribs/sternum fixed. Perimeter of muscle fixed. Breast tissues fixed in sternum. In upper and lower boundaries of skin, displacements in craniocaudal direction constrained. Springs in the lateral and upper boundaries of skin	Simulations with several spring stiffness
				Contact surface muscle-breast tissues in a stripe of the lateral, upper and lower boundaries. Contact muscle-ribs/sternum fixed. Perimeter of muscle fixed. Breast tissues fixed in sternum. In upper and lower boundaries of skin, displacements in craniocaudal direction constrained. Springs in the lateral and upper boundaries of skin, and in the whole contact muscle-breast tissues	Simulations with several spring stiffness

Table 5.3: Summary of the FE simulations presented in this work, ordered by section.

Section	Skin	Breast tissues	Muscle	Boundary conditions	Other
5.6.12	PP. Membrane	Unique. GOH	Ohl	Contact in the whole surface muscle-breast tissues. Contact muscle-ribs/sternum fixed. Perimeter of muscle fixed. Breast tissues fixed in sternum	Fibres: anteroposterior direction, with dispersion. 2 simulations changing C_{10}
				Contact in the whole surface muscle-breast tissues. Contact muscle-ribs/sternum fixed. Perimeter of muscle fixed. Breast tissues fixed in sternum. In upper and lower boundaries of skin, displacements in craniocaudal direction constrained	Fibres: anteroposterior direction, without dispersion. 5 simulations changing C_{10}
				Contact in the whole surface muscle-breast tissues. Contact muscle-ribs/sternum fixed. Perimeter of muscle fixed. Breast tissues fixed in sternum. In upper and lower boundaries of skin, displacements in craniocaudal direction constrained. Springs in the lateral boundary of skin	Fibres: anteroposterior direction, without dispersion. Simulations with several spring stiffness
5.6.13.1	BS. Membrane	Fat (S_{1600}) and fat-gland mixture (H^{50}_{1600})	BM	Contact muscle-ribs/sternum fixed. Perimeter of muscle fixed. Breast tissues fixed in medial and lateral boundaries	2 simulations with different skin prestress
		Fat (S_{4000}) and fat-gland mixture (H^{50}_{4000})	BM	Contact muscle-ribs/sternum fixed. Perimeter of muscle fixed. Breast tissues fixed in medial, lateral and upper boundaries	2 simulations with different skin prestress
		Fat (S_{100}) and fat-gland mixture (H^{50}_{100})	BM	Contact muscle-ribs/sternum fixed. Perimeter of muscle and skin fixed. Breast tissues fixed in medial boundary. In upper and lower boundaries, displacements in craniocaudal direction constrained. No connection muscle-breast tissues	Prestress only in half of the skin. 10 simulations with different skin prestress
5.6.13.2	BS. Membrane	Unique, fat-gland mixture (H^{80}_{1})	BM	Contact muscle-ribs/sternum fixed. Perimeter of muscle fixed. Breast tissues fixed in medial boundary	4 simulations using H^{80}_{1}, H^{80}_{100}, H^{80}_{500} and H^{80}_{1000}
				Contact muscle-ribs/sternum fixed. Perimeter of muscle fixed. Breast tissues fixed in medial boundary. In upper and lower boundaries, displacements in craniocaudal direction constrained. No connection muscle-breast tissues	4 simulations using H^{80}_{1}, H^{80}_{5}, H^{80}_{10} and H^{80}_{100}
5.6.13.3	BS. Membrane	Unique. GOH	BM	Contact muscle-ribs/sternum fixed. Perimeter of muscle fixed. Breast tissues fixed in medial and lateral boundaries. In upper and lower boundaries, displacements in craniocaudal direction constrained	Fibres aligned with the maximum principal Cauchy stress direction

Table 5.4: Summary of the FE simulations presented in this work, ordered by section.

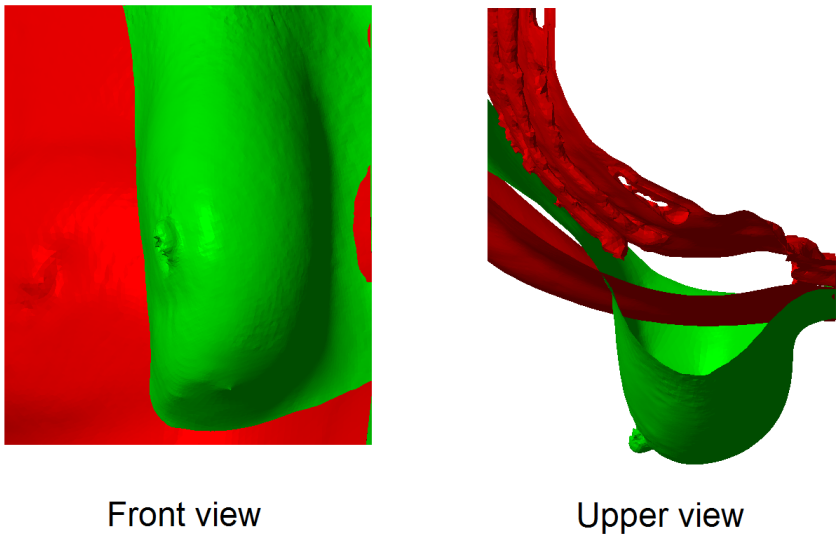

Figure 5.12: Deformed shape of the model for a 50% fat proportion superimposed with the real deformation in prone position, presented in section 5.6.1.

in table 5.1. For the mixture of gland and fat, the H_1^{30}, H_1^{40} and H_1^{50} models were used (see table 5.1). As estimated by the surgeons who treated the patient under study, her breast had about 50% of fat. Then 3 different fat percentages were tried for the mixture: 30%, 40% and 50%. The constants of the 5 terms polynomial model for each fat proportion are shown in table 5.5.

Fat proportion	C_{10}	C_{01}	C_{11}	C_{20}	C_{02}	(Pa)
30%	324.53	288.26	3785.07	6468.84	7905.41	
40%	322.38	290.71	3574.00	6104.66	7404.93	
50%	320.10	293.31	3334.66	5656.75	6921.28	

Table 5.5: Values for the mixture of fat and gland, obtained from section 4.2.

Two static analyses were run using Abaqus Standard to simulate the change from supine to prone and standing up positions. The only applied load was the gravity. As the initial model was built in supine position, the gravity was applied twice in posteroanterior direction to obtain the prone deformed shape. In the first step to "eliminate" the gravity[1] and in the second step to simulate it in prone position. In the case of the standing up position, the gravity was first applied in posteroanterior direction to estimate the unloaded configuration, and then applied again in craniocaudal direction to obtain the standing up deformed shape. The accuracy of the deformation was evaluated quantitatively as explained in section 5.3.

In figure 5.12 the deformed shape in prone position is shown in red superimposed with the real deformation (shown in green in the figure). Table 5.6 shows the mean absolute and mean relative errors for each fat

[1]The deformed shape of this first step could be thus considered a reference configuration (unloaded). This is not exactly true because this configuration is actually loaded (gravity in posteroanterior direction) and therefore it is not stress free. The problem comes from the fact that the model was built in supine position and therefore there were no loads or stresses in the model in this configuration, but in reality, this is a loaded state. This will be discussed later on (see section 5.6.13.2).

	30% fat	40% fat	50% fat
Mean absolute error	23.8 ± 13.9 mm	23.6 ± 14.4 mm	24.8 ± 15.3 mm
Mean relative error	86.2%	85.5%	89.8%

Table 5.6: Quantitative comparison between the deformed shape of the model (presented in section 5.6.1) and the real deformation in prone position.

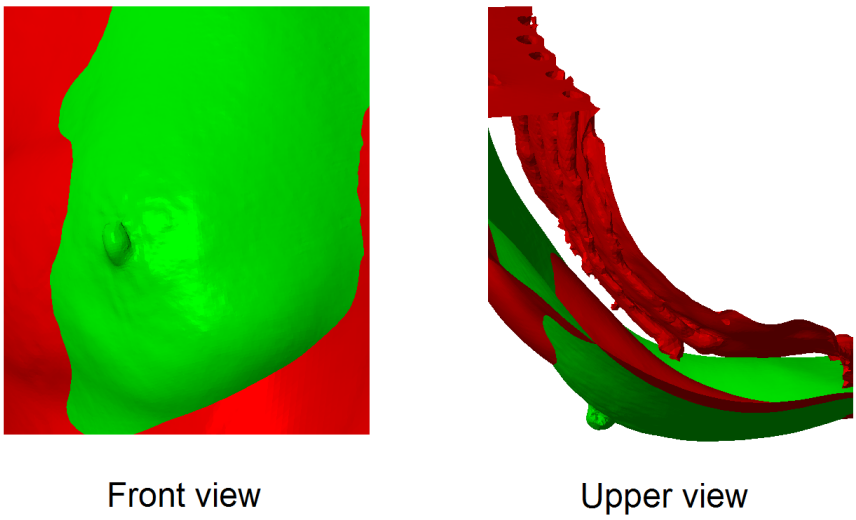

Figure 5.13: Deformed shape of the model for a 50% fat proportion superimposed with the real deformation in standing up position, presented in section 5.6.1.

proportion. Figure 5.13 presents the deformed shape in standing up position (in red) together with the real deformation (in green). In table 5.7 the mean absolute and mean relative errors are shown for each fat proportion. The errors were computed as explained before and depicted in figure 5.10.

As can be noticed in figure 5.12, the simulated deformation was very far from the real deformation. To be precise, the model was almost not deformed, indicating that the behaviour was much stiffer than in reality. The errors in table 5.6 clearly show that the model behaviour was not correct in this case. Moreover the fat proportion had little influence, in the specified range and with the H_1^p models.

In figure 5.13, corresponding to the standing up position, the simulated deformation was very far from the real one, and the model was almost not deformed, as in the previous simulation. However, it seemed that the deformed shape of the model was closer to reality than in the previous simulation. In view of table 5.7, it can be seen that the mean absolute error was lower than in the prone case, but only because the

	30% fat	40% fat	50% fat
Mean absolute error	5.8 ± 3.1 mm	5.4 ± 3.1 mm	5.3 ± 3.1 mm
Mean relative error	90.6%	84.4%	82.8%

Table 5.7: Quantitative comparison between the deformed shape of the model (presented in section 5.6.1) and the real deformation in standing up position.

displacements were smaller. If the relative errors are compared, the percentages are of the same order of magnitude.

The standing up simulation was carried out to check if the unrealistic deformed shape obtained for the prone position was related only with the change of position from supine to prone, or on the contrary, it was an inherent problem associated with the model itself. The results indicated that the simulated position was not the problem and that the discrepancies may arise from different reasons, but the model was much stiffer than the real breast and one of these reasons could be that the original Samani's properties, used for the fat and from which the H_1^p models were obtained, were inadequate. Given that the relative errors were similar in both positions and it was easier to check visually whether the prone position was correct, in the subsequent simulations this was the simulated position and the visual check was the preferred option to evaluate the accuracy of the simulated deformed shape.

5.6.2 Muscle fixed to the ribs and sternum, with skin

The model presented in the previous section (with the H_1^{50} model for the fat-gland mixture) was run without the skin to analyse the behaviour of the other tissues. But, obviously, the skin should be included in the model as it is in the reality. The inclusion of the skin is the only difference with the model of the previous section. The skin was generated by selecting the outer faces of the tetrahedral elements and superimposing membrane elements over those faces such that both types of elements shared the outer nodes. The BS model was used for the skin with the material constants shown in table 5.1. As can be seen in the deformed shape of figure 5.14, the deformation was very small. The displacements were measured and compared with the previous model and were even smaller, as expected, since the addition of the skin made the model stiffer, obviously. Nonetheless, the skin was kept in the model from this point on (except for section 5.6.5).

5.6.3 All the boundaries of the muscle fixed, with skin

In the previous models, even though the displacements were small and the global behaviour very stiff, the muscle was deformed in a non anatomical way in certain areas of the boundaries, being quite separated from its true position. For example, in the medial-inferior area, corresponding to the part below the sternum, as shown in figure 5.15. In the lateral boundary of the model, the same occurred. This strange deformations may be due to the lack of restrictions in the boundaries of the muscle, which were considered free to move, while in reality the pectoral muscles are joined to other big groups of muscles creating a strong bond.

To avoid this separation of the muscle from its true position (e.g., from the sternum, as seen in figure 5.15), the muscle was also considered fixed in the whole perimeter of the model. The rest of parameters remained unchanged from the previous sections. The deformed shape is compared with that of section 5.6.2 in figure 5.16. It can be seen that they are almost identical except for the area close to the sternum and the

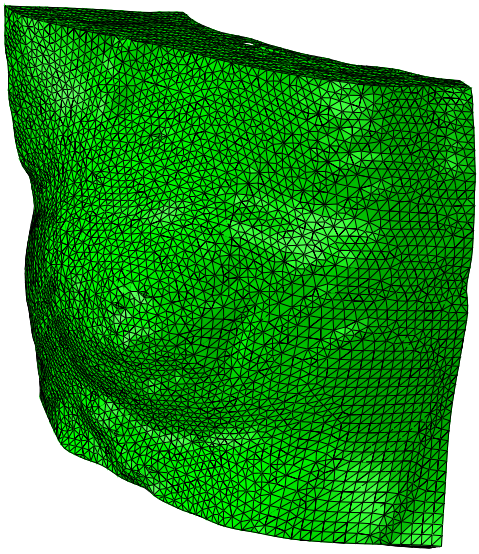

Figure 5.14: Deformed shape of the model with skin in prone position, presented in section 5.6.2.

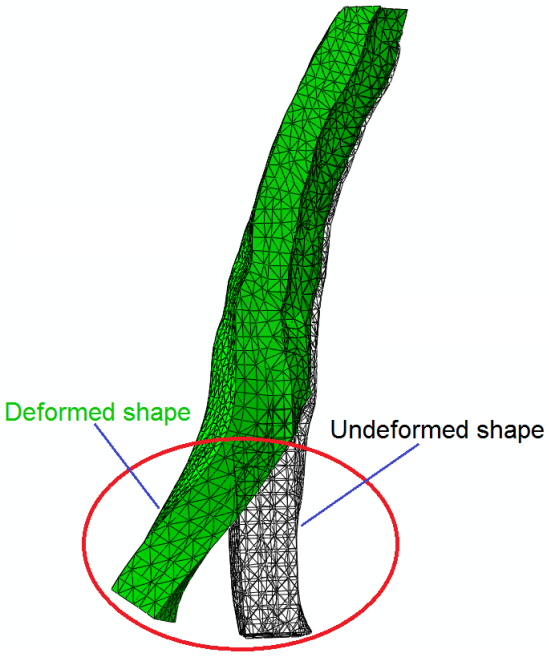

Figure 5.15: Deformed and undeformed shapes of the model with skin in prone position, presented in section 5.6.2. Lateral view of the sternum.

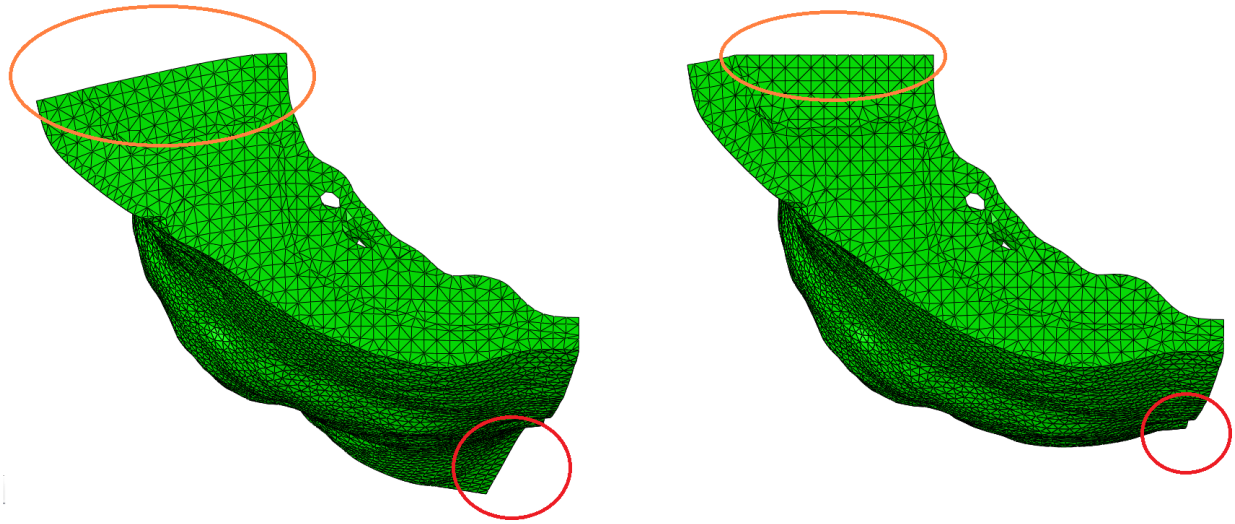

Figure 5.16: Left: model with the muscle fixed only in the contact with ribs and sternum, presented in section 5.6.2. Right: model with the muscle fixed in the whole perimeter of the model, presented in section 5.6.3. Upper view.

lateral boundary.

These strange deformations of the muscle were eliminated but, as expected, the model was slightly stiffer than the previous ones, because of the new boundary conditions imposed.

5.6.4 Sensitivity of the model to the stiffness of the fat-gland properties, with skin

In the true deformation of the breast, the soft tissues are displaced towards the axilla in supine position, whereas in prone position they move closer to the sternum. After realizing in the previous models that they were much stiffer than the reality, even without skin and with different boundary conditions, a sensitivity analysis was performed on the elastic properties assumed for the fat and glandular tissues. For this purpose, the material parameters of the strain energy function were divided by certain factors to analyse their effect on the deformed shape.

Apart from dividing the material constants by a certain factor, some new boundary conditions were added to this set of simulations, to bring the behaviour of the model closer to reality. The adipose tissue was fixed in the medial (sternum) and lateral boundaries. In the sternum, it was fixed because in previous simulations, as well as in reality, it was checked that the displacement of this area was negligible. Regarding the lateral boundary, it was observed that if the adipose tissue was free, the skin of this boundary dropped excessively and rotated in an incorrect direction, while in the true deformation the skin remained near the chest, as can be noticed in figure 5.8. Probably, this deformation would be constrained by the rest of the skin, not included in the model. For the moment, the traction that the skin outside the model is exerting

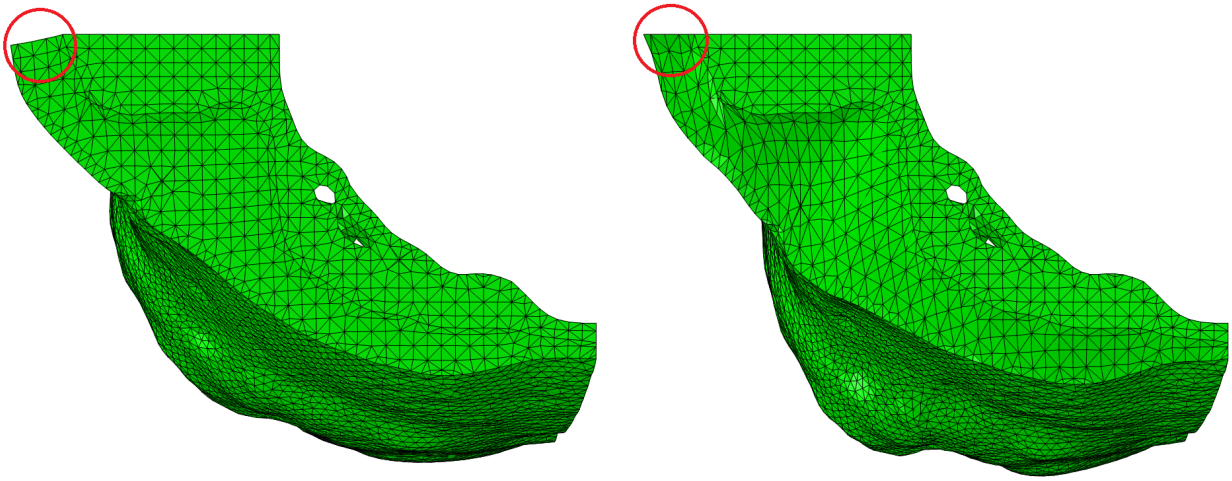

Figure 5.17: Left: model with the S_1 material model for the fat and the H_1^{50} for the fat-gland mixture. Right: model with with the S_{100} material model for the fat and the H_{100}^{50} for the fat-gland mixture. Upper view. Section 5.6.4

to the skin included in it is not considered and fixing the lateral boundary of the adipose tissue was enough to prevent this strange deformation. As can be seen in figure 5.17 (upper left), this new boundary did not have much influence on the global deformation of the model.

Two models were built, with the S_{100} and S_{200} material models for the fat, together with the H_{100}^{50} and H_{200}^{50}, respectively, for the mixture of fat-gland. For both cases, the BM material model was used for the muscle and the BS for the skin, as in the model of the previous section. The model with the constants divided by 200 was also run without skin and with the skin modelled as a solid layer (not as a membrane like previously).

The deformed shape of the model with the S_{100} and H_{100}^{50} material models is shown in figure 5.17, compared with the model using S_1 and H_1^{50}. The deformation in the new model (right) was larger, although not too much compared with the old one (left), even though the constants were divided by 100. Moreover, comparing the deformed shape with the real deformation, it was still quite far.

The model with the S_{200} and H_{200}^{50} constants did not converge, neither with the skin modelled as a membrane, nor as a solid layer. However, it converged without skin. The simulation with the skin as a membrane stopped when only a 1.5 % of the total load was applied. The non convergence was motivated by a certain region of the skin where it was buckling. The less rigid the breast tissues are, the higher the difference of stiffness between the skin and the rest of the model is and, therefore, the less support the breast tissues give to prevent the buckling of the skin membrane when a little compression appears.

For the previous reason, two tests were done. First, running the model with the skin modelled as a solid layer, to check if the convergence problem was related with the membrane, and running the model without skin, to check whether the issue was the skin itself. First, the skin was modelled with C3D6H

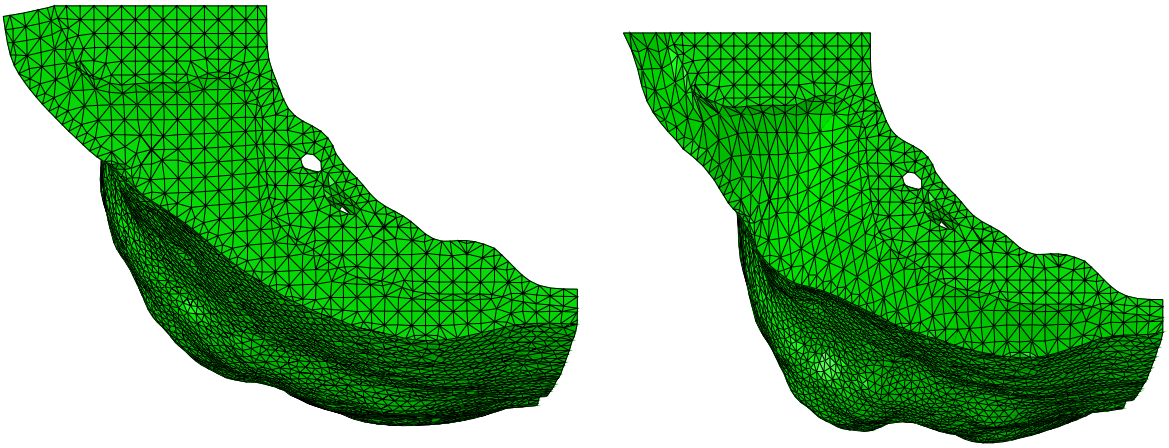

Figure 5.18: Left: model with the the S_1 material model for the fat and the H_1^{50} for the fat-gland mixture. Right: model without skin, with the S_{200} material model for the fat and the H_{200}^{50} for the fat-gland mixture. Upper view. Section 5.6.5.

solid elements, generated by duplicating the nodes of the membrane elements in the direction of the outer normal to the surface. The new nodes were created such that the thickness of the skin was the same as in the membrane model. This simulation stopped because of convergence problems too, so discarding the membrane modelling of the skin as the source of the problem. Second, the skin was eliminated from the model, allowing the completion of the simulation without convergence problems and confirming that they were derived from instability issues.

Other approaches were tried to avoid the convergence problem[1]: applying the load in very small steps, applying the gravity to different groups of elements at different times to stretch the skin, pre-deforming the skin to avoid compressions, using only displacement boundary conditions and then changing to load boundary conditions, etc. None of them was useful to overcome the convergence problem and, eventually, not including the prestress of the skin was identified as the possible cause of the convergence error. This prestress of the skin will be studied in section 5.6.13.1.

5.6.5 Sensitivity of the model to the stiffness of the fat-gland properties, without skin

The sensitivity analysis was performed on the elastic properties assumed for the breast tissues, dividing the material parameters by some factors, in a model without skin, given that in the previous section it was shown that convergence problems appeared in the model with skin. The exclusion of the skin is therefore the only difference with the previous model. Models with the constants divided by 200, 400, 800, 1600 and 4000 were analysed, i.e, the S_{200}, S_{400}, S_{800}, S_{1600} and S_{4000} material models were used for the fat together with H_{200}^{50}, H_{400}^{50}, H_{800}^{50}, H_{1600}^{50} and H_{4000}^{50} for the mixture fat-gland, respectively.

[1]Knowing that in hyperelastic materials, the final stress-strain state is independent of the path followed to reach it.

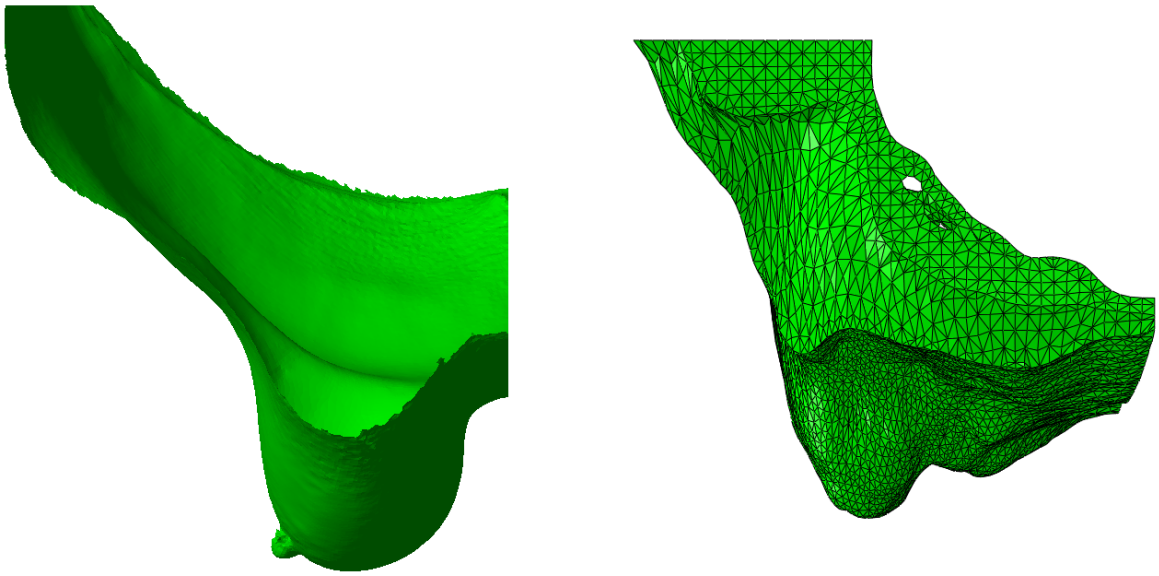

Figure 5.19: Left: 3D scan image in prone position. Right: model without skin, with the S_{1600} material model for the fat and the H^{50}_{1600} for the fat-gland mixture. Upper view. Section 5.6.5.

In figure 5.18, the deformed shape with the constants divided by 200 is shown (right) together with the model with the original constants (left). The deformed shape of the model with the material parameters divided by 1600 is compared in figure 5.19 with the superficial 3D scan image, while the model using S_{4000} and H^{50}_{4000} is shown in figure 5.20. The models with the S_{400}-H^{50}_{400} and S_{800}-H^{50}_{800} material models are not shown, because they follow the same tendency as those in figures 5.18, 5.19 and 5.20.

In view of figure 5.18, and comparing it with figure 5.17, the deformation was slightly larger, but the difference is really hard to see with the naked eye. Moreover, this result indicates that the skin did not have a big influence on the behaviour in this model (though, it surely does in the real breast, where it plays an important mechanical role).

In figure 5.19, the deformed shape of the model with the S_{1600} and H^{50}_{1600} material models is compared with the superficial 3D scan image in prone position. As can be seen, both deformed shapes are very different. In reality, the breast tissue is forming only one bulge, near the sternum, whereas in the model, there were two bulges, and the lowest one was quite far from the sternum.

These existence of two bulges and their separation from the sternum were even more noticeable in the model using the S_{4000} and H^{50}_{4000} material models, due to the fact that the materials were more flexible. On the left part of figure 5.20, the deformed shape is shown. The same model was run but allowing the movement of the lateral boundary of the adipose tissue, to analyze whether this condition permitted the tissue to move closer to the sternum. But, as can be seen in figure 5.20, where both models are compared, the only difference in the deformation was found at the lateral boundary (upper left corner). This conclusion was also reached in the previous section, but here this boundary condition was checked again with a more

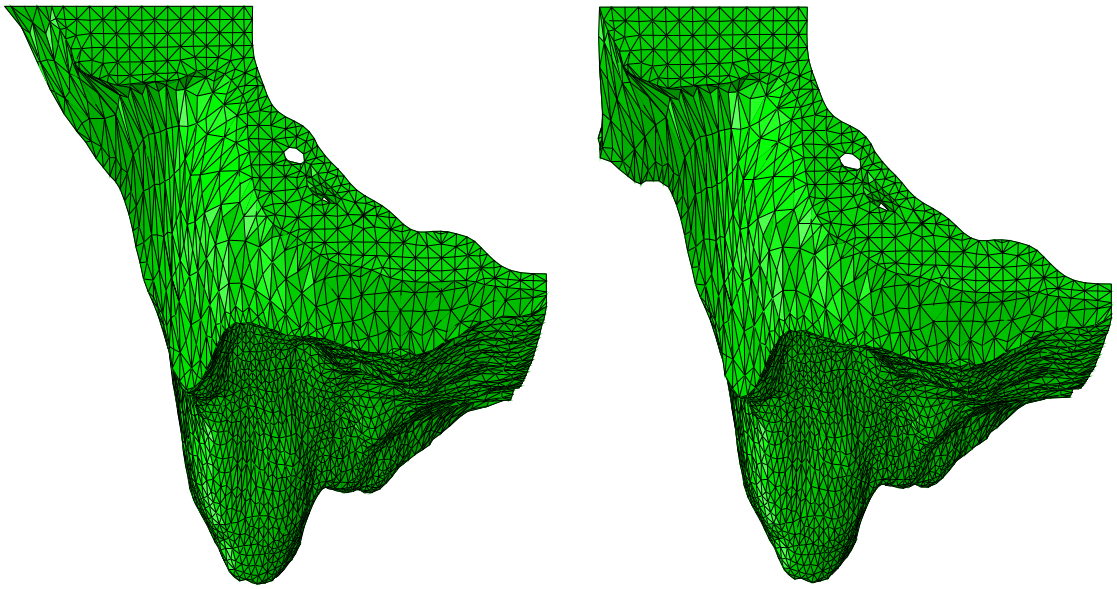

Figure 5.20: Model without skin, with the S_{4000} material model for the fat and the H^{50}_{4000} for the fat-gland mixture. Left: lateral boundary fixed. Right: lateral boundary free to move. Upper view. Section 5.6.5.

flexible model.

The deformed shapes presented in this section indicated that a decrease of the stiffness of the tissues allowed a larger deformation, but the deformed shape was still far from the reality. This might indicate that the problems were not only related with the stiffness of the breast tissues, but also with the boundary conditions or the interaction between those tissues.

5.6.6 Comparison between the material models based on Samani's constants and the one obtained in this thesis

The S_j and H^{50}_j material models, based on the constants provided by Samani [41], and the TT material model, obtained in this thesis for the breast fat, were compared in a FE breast model under gravity loads to simulate the change from supine to prone position. The boundary conditions of the model presented in section 5.6.4 were used, i.e., muscle fixed in the contact with the ribs and in the four cut boundaries and breast tissues fixed in the medial and lateral boundaries. The muscle was modelled with the BM model and the skin included using the BS material model. Three FE models were compared, only differing in the material model used for the fat and gland tissues: S_1-H^{50}_1, S_{100}-H^{50}_{100} and TT. In the first two FE models, the adipose tissue and the fat-gland mixture were considered separately. In the last one, based on the viscoelastic properties of the breast adipose tissue determined in section 4.3, the breast was considered as only composed of fat, because no experimental tests were carried out on glandular tissue. As viscoelastic effects were not needed in this simulation, given that only the static deformed shape was compared, only the elastic part was used, i.e., a first order Ogden material model. The mean of the constants for the superficial

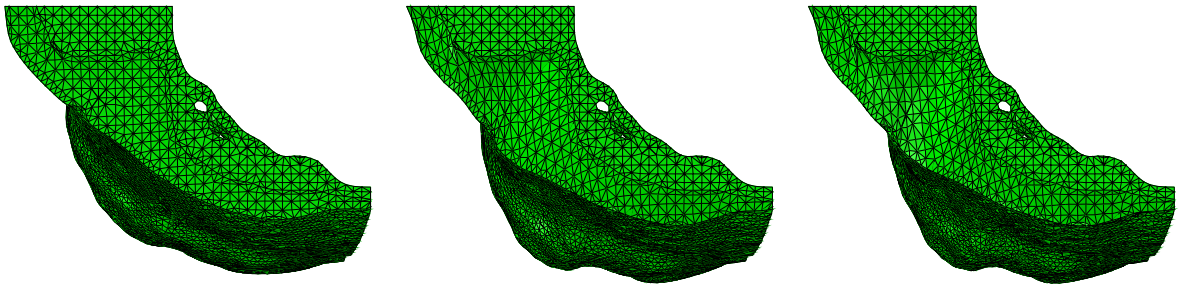

Figure 5.21: Left: model with S_1-H_1^{50}. Centre: model with S_{100}-H_{100}^{50}. Right: model with TT. Upper view. Section 5.6.6.

and deep breast fat layers were used and are shown in table 5.1.

In figure 5.21, the deformed shapes of the three models are shown together. As can be seen, the deformations in the model with the TT material model were larger than in the model with S_1. It can be also noticed that the deformed shapes of the S_{100}-H_{100}^{50} and TT models are very similar.

Using the model and the constants for the breast adipose tissue obtained in this work, the breast deformed to a great extent, but the shape was not similar to the real one yet. Actually, the deformation was almost the same as that obtained with the S_{100} and H_{100}^{50} material models. From these results and with those obtained in previous sections, it seemed clear that the behaviour of the model was far from reality and the cause was not the material model or the stiffness of the tissues. This conclusion suggested that the problem might be related with the boundary conditions or with the interaction between the breast tissues. Therefore, in the following sections, the material models based on Samani's constant were used and not that obtained in this work, to be able to compare with previous models without changing more factors.

5.6.7 Tissue layer in the interface between the muscle and breast tissues

As concluded in previous sections, the FE models presented so far did not behave as reality, and this was not caused by the material model used or the stiffness of the tissues. To check this conclusion, other models were also constructed with different material models, like neo-Hookean or linear elastic ones, varying their material constants, with and without skin. Even models in which the muscle was eliminated and the adipose tissue fixed in the contact surface with the muscle were studied. But the model showed to be unable to simulate the deformation of the breast in the correct way, i.e., forming a unique bulge near the sternum and with the rest of the skin close, almost adhered, to the chest. So, a different approach was tried.

In the previous models, the breast tissues were fixed to the muscle. Since most of this tissue was near the axilla in supine position (i.e., in the initial configuration of the FE model), when the gravity was applied in posteroanterior direction, the tissues went down but hardly moved in mediolateral direction. Thus, a bulge was formed near the axilla. The system behaved like a spring, which went down without any lateral

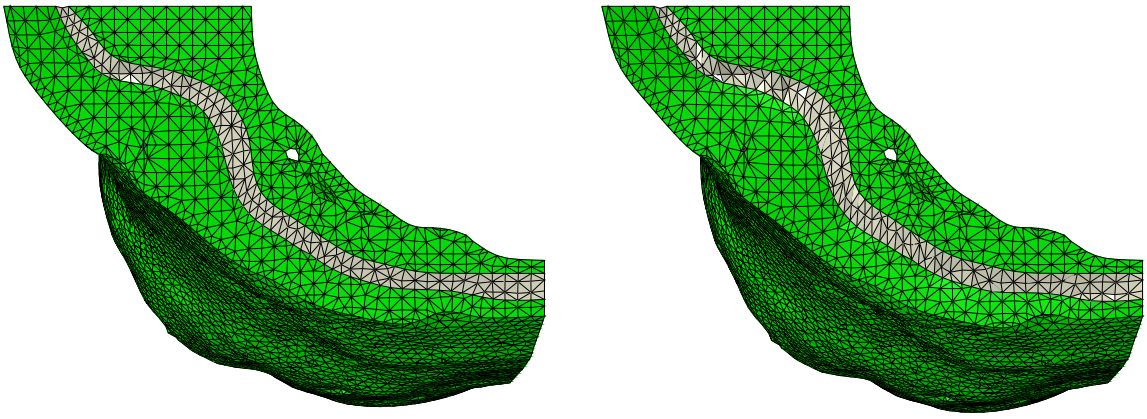

Figure 5.22: Models with the retromammary space (in grey) as a tissue layer. Left: $C_1 = 310$ Pa. Right: $C_1 = 100$ Pa. Upper view. Section 5.6.7.

movement. However, in the real breast this lateral displacement is actually produced. The connection between the breast and the muscle must allow a certain movement, due to the retromammary space, located between the pectoralis fascia and the deep layer of the superficial fascia (that posteriorly covers the breast), which is a space filled with loose connective tissue. There are also suspensory ligaments between both fascial layers, but modelling them was almost impossible because of several reasons: they are not clearly seen in any medical image, their properties are unknown and extracting them to carry out experimental tests is difficult, because the surgeons are not able to distinguish them with certainty.

To model the retrommamary space, a thin layer was created between the muscle and the breast tissue, by selecting the first row of elements of both tissues which were in contact. Only the nodes of the medial boundary were fixed. For the behaviour of the retrommmary space layer, a neo-Hookean material model was used. The constant of the neo-Hookean model was initially set equal to the first constant of the adipose tissue (the constant C_{10} of the 5 terms polynomial strain energy function S_1), i.e., $C_1 = 310$ Pa. Thus, the behaviour of the retromammary space was slightly more flexible as that of the adipose tissue, as only one term was considered from the total of five of the strain energy function of the fat. Two more values of C_1 were used: 100 and 10 Pa. The rest of boundary conditions and materials remained like in the previous models (for the fat, the S_1 material model was used, and for the fat-gland mixture, the H_1^{50}).

In figure 5.22, the deformed shape of the simulations corresponding to $C_1 = 310$ Pa and $C_1 = 100$ Pa are shown. As can be seen, the retromammary layer (in grey) was more deformed than the rest of the tissue, but the deformed shape was not substantially improved respect to the previous models. The simulation converged for these values of the neo-Hookean constant, but as the material became more flexible, in particular $C_1 = 10$

Pa, some convergence problems arose[1]. The layer of material was very thin and when large deformations were produced, some elements became very distorted. This model simply represent a transition to the following models, but its performance was the same as in the previous simulations, because there was nothing in the model that allowed the lateral movement of the breast.

5.6.8 Complete lack of connection between the muscle and the breast tissues

The connection between the muscle and the breast tissues can play an important role in the behaviour of the breast. In the previous models both tissues were rigidly bonded. In this section the other extreme case was studied: muscle and breast tissues were not bonded and no restriction or connection existed between both tissues. This approach has a severe limitation: a separation of the surfaces of both tissues, which were initially in contact, would create a void which would be hard to explain from a physiological point of view. Therefore, it only makes sense as another extreme situation in which the retromammary space was filled with a material of null (or almost zero) stiffness. As the change of position from supine to prone was simulated, the role of the muscles had no influence on the results and they were eliminated from the model. The boundaries of the skin were then fixed, to support the weight of the breast tissues. The BS material model was used to characterise its behaviour.

Four models with different material constants for the adipose tissue and the fat-gland mixture were used to study the evolution of the deformed shape: S_{10}-H^{50}_{10}, S_{100}-H^{50}_{100}, S_{400}-H^{50}_{400} and S_{2000}-H^{50}_{2000}.

The deformed shape of the model using S_{10}-H^{50}_{10} is shown in figure 5.23 (right), next to the 3D scan image (left). They are not superimposed for clarity. In figure 5.24 the models using S_{100}-H^{50}_{100} and S_{2000}-H^{50}_{2000} are shown together. The model using S_{400} for the fat and H^{50}_{400} for the fat-gland mixture is not shown, because it followed the same tendency as the shown models.

As can be seen in figure 5.23, the displacements of the model using the S_{10} material model for the adipose tissue and the H^{50}_{10} for the fat-gland mixture were larger than in the reality. In fact, the breast behaved similarly as a balloon filled with a fluid, hanging from the boundaries and forming only one bulge. In the real breast, the tissues are displaced near the sternum, forming one bulge, wide in craniocaudal direction and narrow in mediolateral direction. Moreover, the skin is not separated from the chest until the bulge is formed near the sternum, causing two pronounced changes in the curvature, responsible for its particular shape. These differences with reality can be observed in figure 5.23. In the deformed shape of the model, these two areas with different curvatures did not appear, because the breast tissues were completely separated from the muscle. Moreover, the lowest point of the deformed shape was far from the sternum, because there

[1]To try to overcome the difficulties generated by the distortion of the elements, the capabilities of the adaptive mesh in Abaqus Standard were explored. However, it is not possible to use adaptive mesh with tetrahedral elements in Abaqus Standard. Besides, it is indicated for wear and ablation processes, not for large deformation ones. In Abaqus Explicit it is not possible to use the adaptive mesh either. All the tetrahedral and hexahedral elements are full integrated or reduced integrated with hourglass control, and adaptive mesh does not support full integration or hourglass control elements. Then, the adaptive mesh procedure was abandoned.

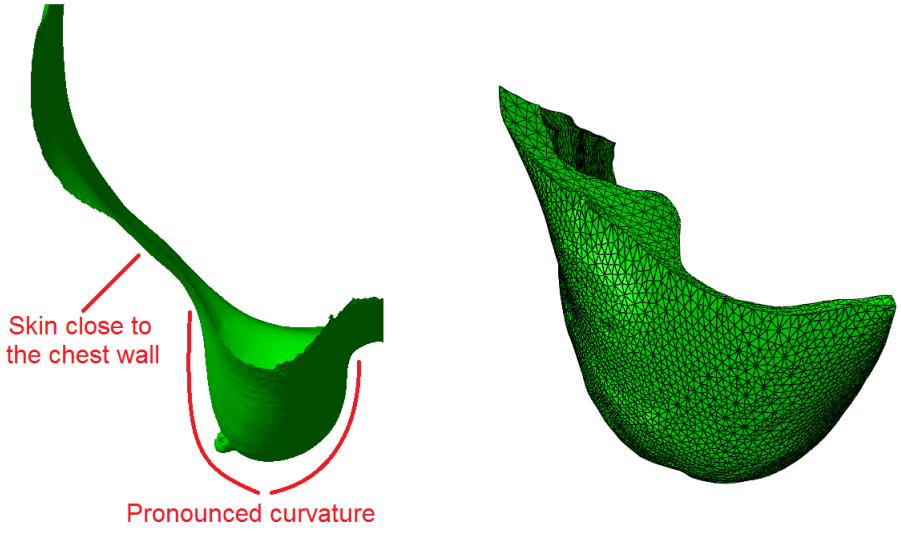

Figure 5.23: Model without connection between the muscle and breast tissues. Left: 3D scan of the breast in prone position, highlighting the differences between the real breast and the FE simulated deformed shape. Right: model using S_{10} for the adipose tissue and H_{10}^{50} for the fat-gland mixture. Upper view. Section 5.6.8.

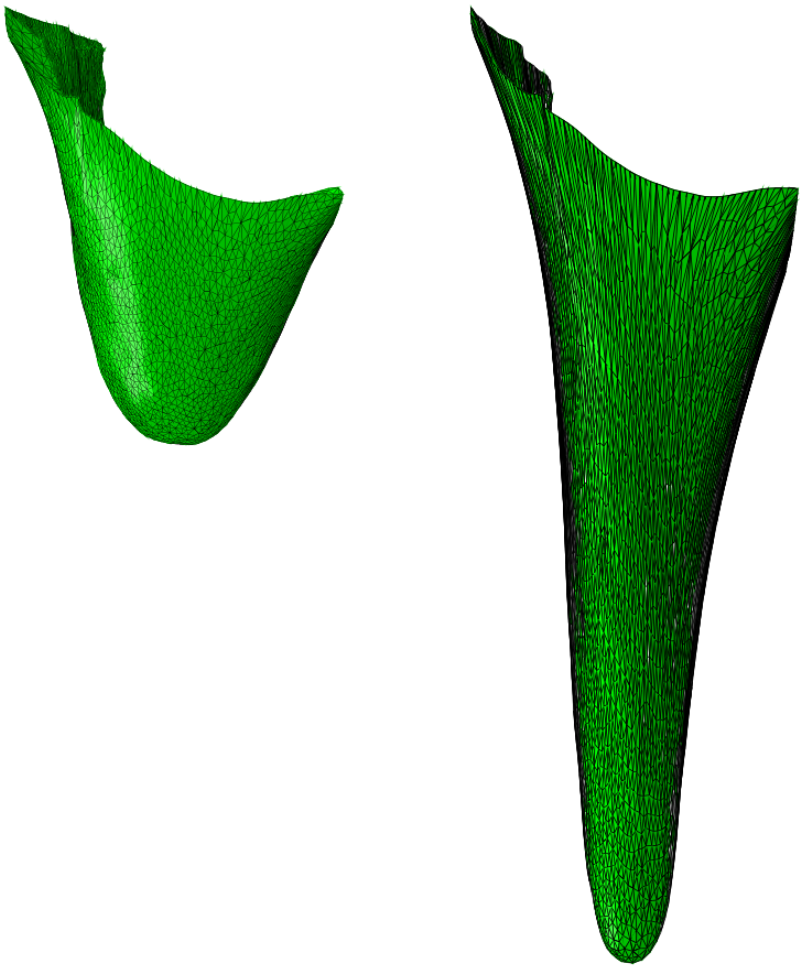

Figure 5.24: Model without connection between the muscle and breast tissues. Left: S_{100} and H_{100}^{50}. Right: S_{2000} and H_{2000}^{50}. Upper view. Section 5.6.8.

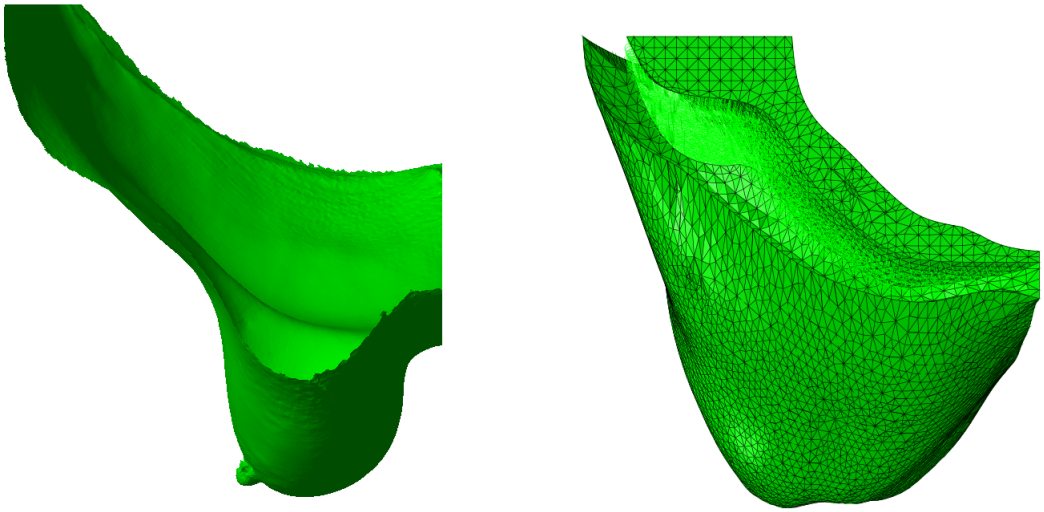

Figure 5.25: Left: 3D scan of the breast in prone position. Right: model with springs connecting the muscle with the breast tissues. Upper view. Section 5.6.9.

was nothing in the breast model that could cause the breast to come closer to the sternum.

In figure 5.24, it is clearly seen that the deformation and displacements in the right-hand side model were really enormous, even compared with the left-hand side model, which also presented larger displacements than the reality. The simulation with this so flexible material was done to analyze the evolution of the deformed shape as the stiffness was lowered.

In view of these results, it was concluded that the boundary conditions cannot be so flexible, and that there must be something in the breast which avoids these large deformations. In section 5.6.6, it was seen that the S_{100} and H^{50}_{100} material models should be used in the FE breast model to obtain a similar behaviour to that using the material model experimentally obtained in this thesis. With the boundary conditions simulated here, using S_{10} and H^{50}_{10} (stiffer than S_{100} and H^{50}_{100}) the deformations in the model were larger than those in the reality. Therefore, it seemed that the issue was more related to the boundary conditions than to the material properties of the tissues.

5.6.9 Spring connection between the muscle and the breast tissues

In the previous section, the displacements of the breast model were larger than those of the real organ for the reference material constants (S_{100} and H^{50}_{100}). Next, a model with a spring connection between the muscle and breast tissues was built to reproduce an intermediate situation and so to mimic a structure of loose connective tissue or weak ligaments. Therefore, in this model the muscle is included again using the BM material model, fixing the nodes in contact with the ribs and those of the four cut boundaries. The muscle and breast tissues were not bonded, but each node of the muscle surface was connected by a linear spring with the facing node of the posterior breast surface (one to one correspondence), producing a force

proportional to the distance between both nodes [1]. The skin was modelled with the BS material and fixed in the four boundaries again. For the fat, the S_{100} material model was used and for the mixture of fat and gland, the H^{50}_{100}. The stiffness of the springs was set equal to 0.1 N/m, with a density of 7.5 springs/cm^2, which results in an equivalent stiffness of $7.5 \cdot 10^{-3}$ N/cm/cm^2. This value is not based on the literature, but taken to obtain approximately the same displacement in anteroposterior direction as this of the 3D scan image of the real breast in prone position. The resulting deformed shape is shown in figure 5.25. Again, it was not satisfactory.

Another models with springs were tried, dividing the whole surface in four areas (upper-medial, upper-lateral, lower-medial and lower-lateral) of approximately equal size. A different stiffness was assigned to the springs of each area. Different combinations of stiffness were tried (ranging from 0.01 to 1 N/m). The objective was to simulate a situation in which the stiffness of the retrommary space was different, depending on the region. The results improved, but they were not satisfactory yet and the number of variables that should be adjusted were increased. Obviously, dividing the surface in enough zones with springs with different stiffness, and even also dividing the breast tissues in areas with different properties, it would be possible to reproduce the shape of the breast. Nevertheless, the number of variables needed to be adjusted would be very large and the process would completely lose the physical sense. The breast behaviour would be totally faked.

5.6.10 Analysis of the influence of the skin properties

In this section, the influence of the skin properties in the behaviour of the breast model is studied. The FE model without any connection between the muscle and the breast was used, because the properties of the skin played a crucial role in it. Therefore, the muscle was not included. For the breast tissues, the model S_{100} for the adipose tissue and the H^{50}_{100} for the mixture of fat and gland were used. They were fixed only in the medial boundary.

5.6.10.1 Comparison of two material models of the skin

First, two different material models of the skin were compared: the BS model used in the previous simulations, and the PP model used by several authors [18, 21, 23] to cover the breast. The skin was fixed in its four boundaries.

Figure 5.26 compares the deformed shapes of both models. They were practically equal (being the PP model slightly stiffer), indicating that both models behave similarly under the simulated conditions. Therefore, the BS model was selected to complete the rest of the study.

[1] Opposite to other options in which the spring force is proportional to the distance in a certain direction

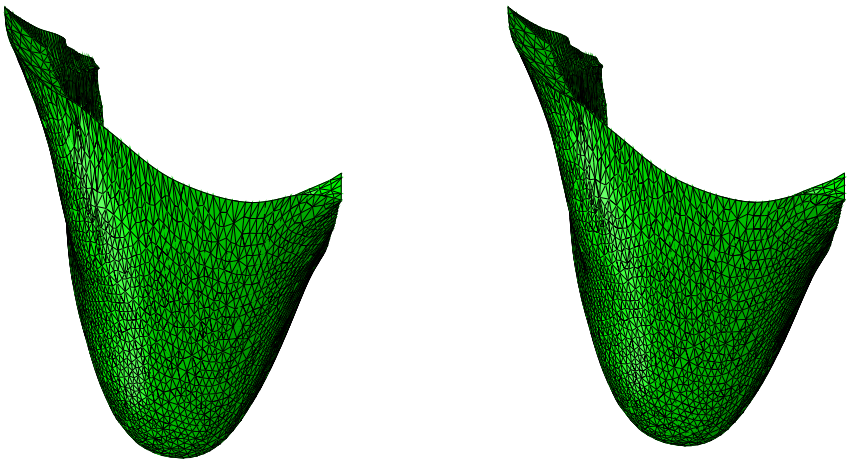

Figure 5.26: Model without connection between the muscle and breast tissues and material models S_{100} and H^{50}_{100}. Left: Rubin-Bodner model for the skin. Right: polynomial model for the skin. Upper view. Section 5.6.10.

5.6.10.2 Sensitivity analysis of the Rubin and Bodner's material constants

A sensitivity analysis of the FE model to the values of the material constants of the BS material model was carried out. This model, as seen in section 3.2.5.1, depends on five material constants. The original values provided by Barbarino et al. [43] for the skin are included in table 5.1. Each constant was varied at a time *ceteris paribus*. The sensitivity analysis was only conducted for the first four constants. The last one, ω, is age related and was maintained with its original value. Moreover, as it multiplies m_2 in equation (3.31), both variables can be considered together for the purpose of this analysis.

Analysis of μ_0

The values tested for μ_0 were: 1.7 (initial), 17 and 85 MPa. In these simulations, the four boundaries of the skin were fixed. In figure 5.27 the deformed shapes of the three models with different values of μ_0 are compared. As can be seen, the model became stiffer as the constant μ_0 increased, reducing the maximum displacement, though with no effect on the global shape of the breast since all the nodes were proportionally displaced. Moreover, it can be seen that μ_0 needs to be considerably varied to notice changes in the deformed shape.

Analysis of q

Here, two boundary conditions were changed with respect to the previous simulations. In the real breast (figure 5.9, lateral and front views) the tissue moves towards the sternum forming a bulge which extends along the sternum in craniocaudal direction, while in the model there was a minimum in the center of the

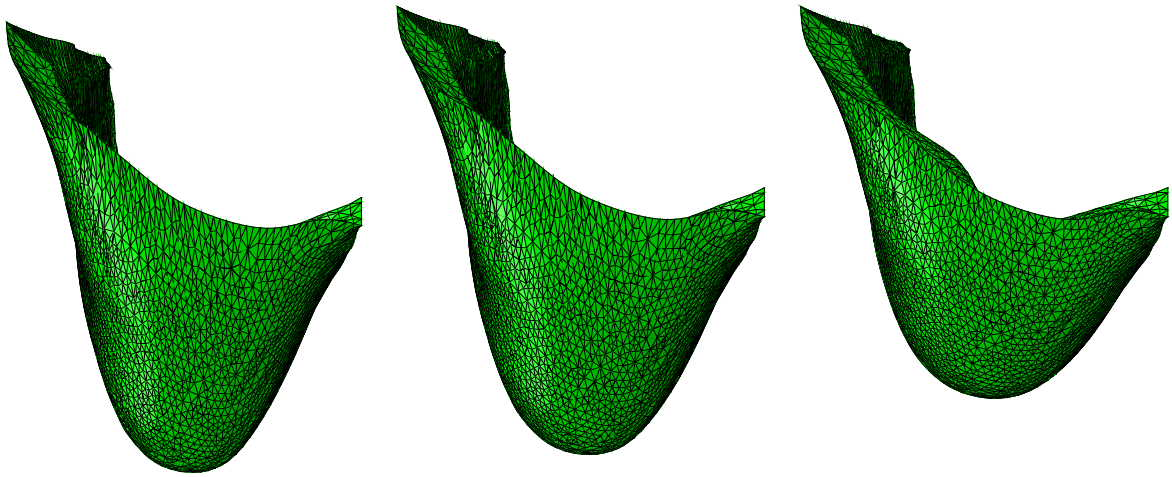

Figure 5.27: Left: Original properties of the skin ($\mu_0 = 1.7$). Centre: $\mu_0 = 17$. Right: $\mu_0 = 85$. Upper view. Section 5.6.10.

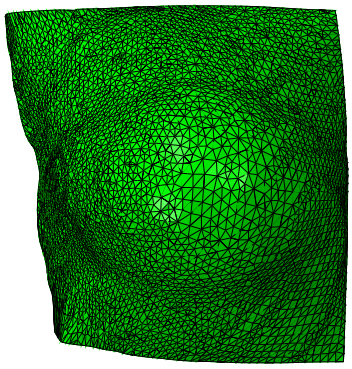

Figure 5.28: Front view of the model without connection between the muscle and the breast tissues. Section 5.6.10.

space delimited by the four line boundaries (as shown in figure 5.28). Therefore, in the new model, the upper (clavicle) and lower (closer to the abdomen) boundary conditions of the skin were changed: the displacements in the mediolateral and the anteroposterior directions were allowed, but not in the craniocaudal direction. That is to say, the nodes at the boundaries can only move within the plane of figure 5.27. The objective was to test the behaviour of the skin with a less constrained movement in these directions, allowing the displacement of the breast tissues towards the sternum.

First the simulations were run with the same boundary conditions as in the previous section (analysis of μ_0), i.e., with the four skin boundaries fixed. The values tested for q were: 36 (initial), 360, 3600, 36000, 360000 and 600000. Then, both boundary conditions explained in the above paragraph, upper and lower, were changed for three values of q: 36, 36000 and 600000. The effect of the change of boundary conditions was also analysed.

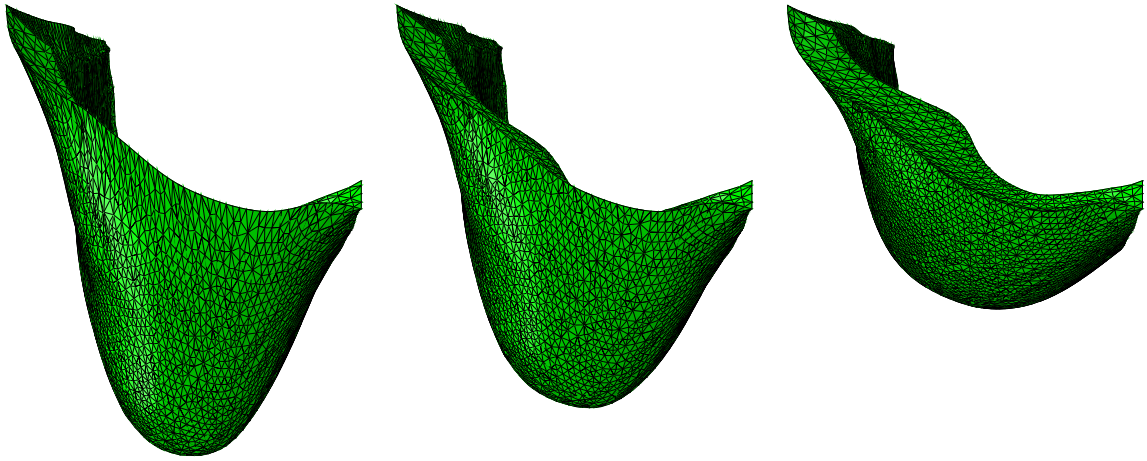

Figure 5.29: Four boundaries of skin fixed. Left: Original properties of the skin ($q = 36$). Centre: $q = 36000$. Right: $q = 600000$. Upper view. Section 5.6.10.

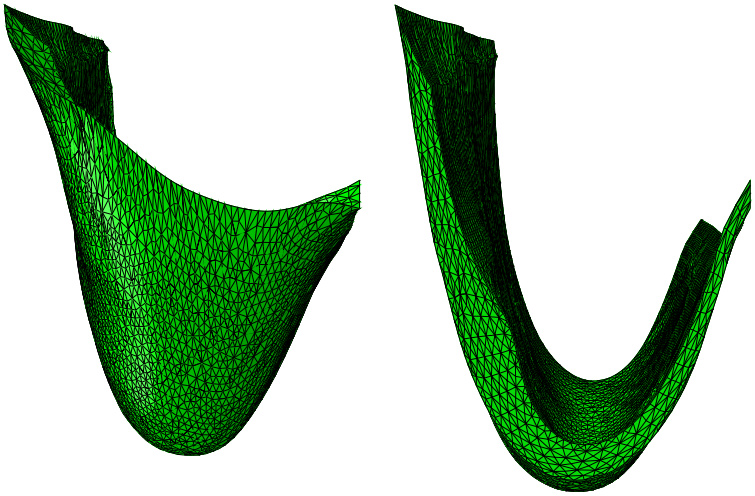

Figure 5.30: Comparison of boundary conditions for the original properties of the skin. Left: four boundaries fixed. Right: upper and lower boundaries changed. Upper view. Section 5.6.10.

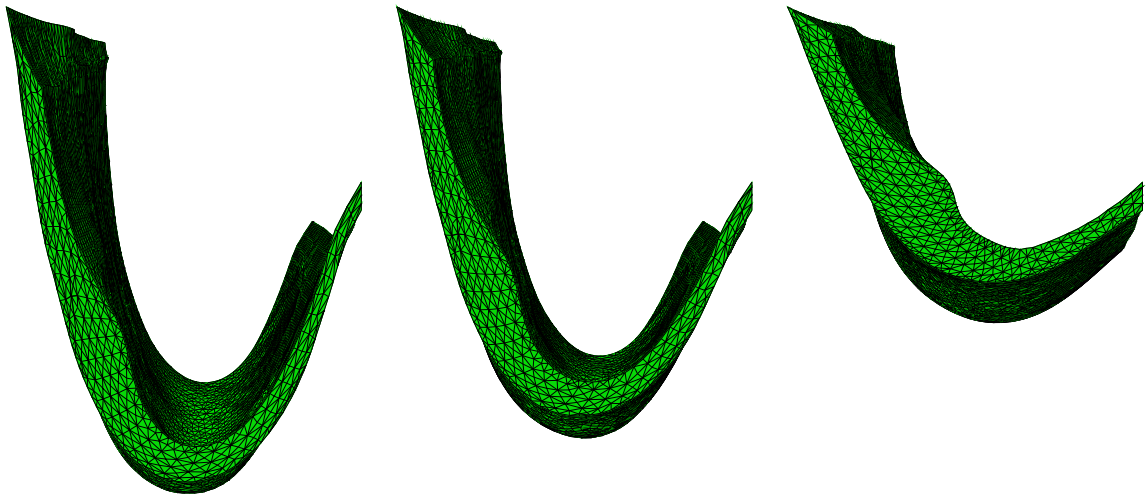

Figure 5.31: Upper and lower boundaries changed. Left: Original properties of the skin ($q = 36$). Centre: $q = 36000$. Right: $q = 600000$. Upper view. Section 5.6.10.

In figure 5.29, the deformed shapes of three models (without changing the boundary conditions with respect to the previous simulations) with different values of q are compared: 36 (original value), 36000 and 600000. The rest of the models are not shown because they followed the same tendency and did not provide additional information to the deformed shapes shown in figure 5.29. The model was stiffer and the displacements smaller as the constant q increased, and the deformed shape had its lowest point located more or less in the center of the model and without the pronounced curvatures seen in the real breast.

In figure 5.30, both models for the original properties of the skin but changing the boundary conditions are compared. As can be seen, the effect on the deformed shape in craniocaudal direction was very important, because the upper and lower boundaries of the skin were released in mediolateral and anteroposterior direction in the model shown on the right-hand side. Seeing the model from an upper view, with these new boundary conditions, the shape of the breast was more similar to the reality in craniocaudal direction. Nonetheless, if the model is seen from a lateral view, both upper (sternum) and lower (abdominal) boundaries became excessively separated from the chest wall. Moreover, the displacement of the model was slightly larger in anteroposterior direction, but the lowest point remained far from the sternum (approximately at the same distance that in the model with the four boundaries of the skin fixed) and the pronounced curvatures were not produced.

In figure 5.31 the deformed shapes (changing both new boundary conditions) for three values of q are compared: 36 (original value), 36000 and 600000. Similarly to figure 5.29, the model was stiffer as the constant q increased. Comparing the models with different boundary conditions for the same value of q (figures 5.29 and 5.31), the maximum displacements in anteroposterior direction were slightly higher when the upper and lower boundaries were released.

Analysis of m_1

The values tested for m_1 were: 1294 (initial), 129.4, 12940 and 129400. The effect of varying the parameter m_1 is shown in figure 5.32 (the case $m_1 = 12940$ is not shown, as it did not provide additional information to the other images). Comparing the simulation for $m_1 = 129.4$ and $m_1 = 129400$, the deformed shape was approximately the same. The variation of this parameter within that range did not affect much the global behaviour. In the strain energy function (recall equations (3.30) and (3.31)), this parameter multiplies the terms which forces the incompressibility. Thus, as the skin is being modelled as incompressible, this term should be approximately zero and, therefore, the variations of m_1 has a very small effect on the behaviour.

Analysis of m_2

Finally the values tested for m_2 were: 0.0008 (initial), 0.00008 and 0.008. The effect of varying the

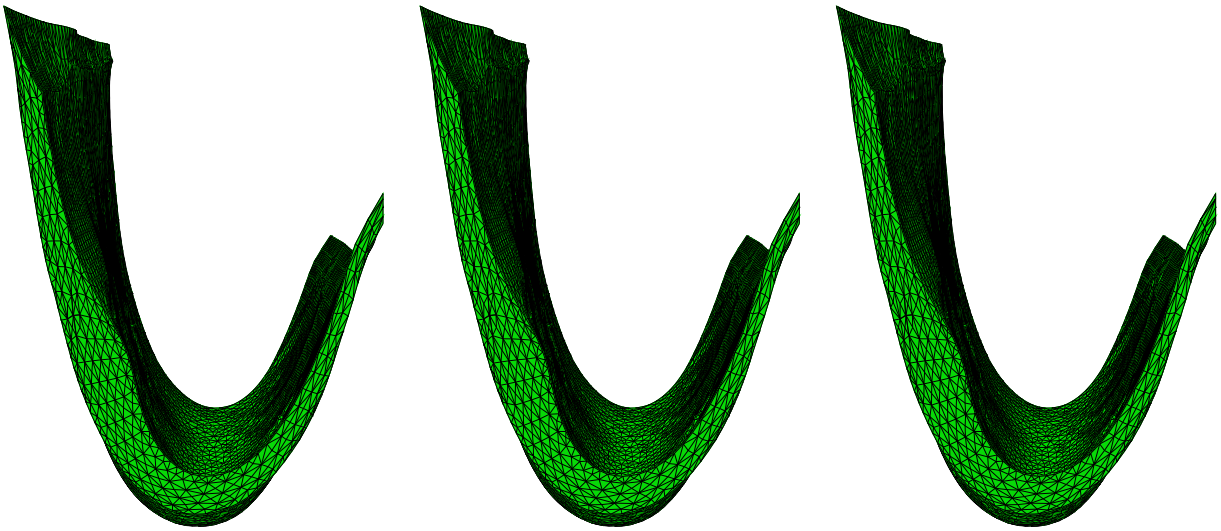

Figure 5.32: Left: Original properties of the skin ($m_1 = 1294$). Centre: $m_1 = 129.4$. Right: $m_1 = 129400$. Upper view. Section 5.6.10.

parameter m_2 is shown in figure 5.33. As can be noticed, the deformation did not vary much. Similarly to the case of m_1, in the strain energy function (recall equations (3.30) and (3.31)) m_2 multiplies the term $(1-\omega)$ being $\omega = 0.9$ as proposed by Barbarino et al. [43]. Moreover, the original value of m_2 is very small. Because of this two reasons, the effect of m_2 on the behaviour is noticeable but low.

5.6.11 Contact surface between the muscle and the breast tissues

The previous models presented in this chapter failed mimicking the real behaviour of the breast. On the one hand, in the FE models with a rigid bond between the muscle and breast tissues, the latter were not displaced to the sternum and the deformations using the material properties provided by the literature were very small. Making the tissues more flexible did not solve the problem and even created a new one, because two bulges appeared in the model. On the other hand, when the muscle and the breast tissues were not bonded, the deformed shape was more similar to the real one, but the tissues were far from the sternum and the two areas with different curvatures (see figure 5.23) could not be distinguished.

Based on the anatomy, the experimental observation and all the simulations carried out, the deformation of the real breast in prone position seemed to be caused by a sliding of the breast tissues over the muscle. The retromammary space located between both tissues is formed by loose connective tissue, ligaments and a fascial structure. Therefore, it is possible that this anatomical structure allows a finite sliding between the two types of tissues over their contact surface. For this reason, a model with a contact interaction between the muscle and the breast tissues was built.

The contact was modelled with a finite sliding contact formulation, surface to surface, without friction and with no separation, forcing both surfaces to remain in contact. A different FE model to the one used in the

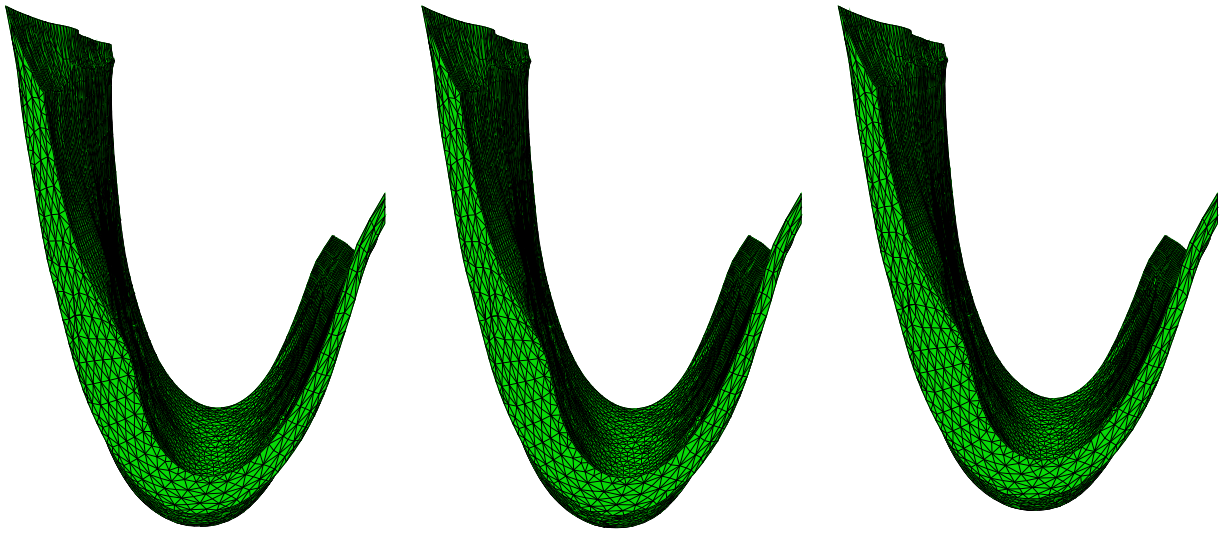

Figure 5.33: Left: Original properties of the skin ($m_2 = 0.0008$). Centre: $m_2 = 0.00008$. Right: $m_2 = 0.008$. Upper view. Section 5.6.10.

previous sections was used for these simulations, the last one presented in section 5.2, with 138229 elements. It is important to note that this model is the first one in which the adipose tissue and the fat-gland mixture were considered as a unique material (a total fat-glad mixture), modelled with the H_j^{80} material model. This model was constructed to smooth the surface between the muscle and the breast tissue, because the previous model did not converge under gravity loads (even in incremental load analyses for low percentages of the applied gravity), as the surface was not smooth enough. Three different types of contact were simulated: 1) with the whole surface between muscle and fat-gland mixture in contact, 2) with only the lateral line (the boundary line) of the fat-gland mixture enforced to glide on the muscle and 3) with the lateral, upper, and lower boundary lines of the fat-gland mixture enforced to glide on the muscle. Therefore, in the last two contact interactions, the rest of the surface of the fat-gland mixture can lose contact from the muscle, except for the lines in which the no separation contact is modelled.

The simulations were carried out with Abaqus Explicit, because the surfaces did not present a regular shape even after smoothing, thus making difficult the convergence with Abaqus Standard. With Standard, the simulations neither were successfully finished nor were aborted with a substantial percentage of the gravity load applied, even after trying different combinations of parameters of the contact formulation.

In Abaqus Explicit only dynamic simulations are allowed. As the deformed shape under static conditions was desired, some simplifications were implemented to obtain it: the load was applied slowly, damping was added in order to reduce the oscillations around the static deformation and the simulation time was long enough to allow time for the model to tend to the static deformed situation.

In the previous models used in Abaqus Standard, the skin and the muscle tissues were modelled with a Rubin and Bodner strain energy function by means of a user subroutine (UHYPER). But, in Abaqus Explicit,

this subroutine cannot be used and an alternative was implemented. Due to the fact that the behaviour of the muscle did not play an important role in the problem, as seen in all the previous simulations, a linear elastic model taken from Ohl et al. [91] was assumed with the constants shown in table 5.1. For the skin, the PP material model presented in table 5.1 was used. In the following subsections, the models with a contact surface are presented.

5.6.11.1 Contact in the whole surface between the muscle and the breast tissues

This subsection presents several models in which the whole interface between the muscle and the breast tissues was considered as a contact surface (without separation between both surfaces).

For these models, the muscle was fixed in the four cut boundaries and in the contact with the ribs. The fat-gland mixture was only fixed in the medial boundary (sternum) and totally free to move in the other three boundaries. The properties of the fat-gland mixture, as explained in section 5.2, were estimated with the homogenized model presented in section 4.2, considering a 80% of fat. Here, the H^{80}_{10}, H^{80}_{100} and H^{80}_{1000} material models were used. The skin was fixed in the sternum, totally free to move in the lateral boundary, and only the movement in craniocaudal direction was constrained in the upper and lower boundaries (clavicle and abdomen), as explained in the previous section. For clarity, these boundary conditions will be referred to as BC1 through this subsection.

The models with the constants divided by 100 and 1000 were also simulated changing some boundary conditions of the skin. The upper and lower boundaries were totally free, without any constraint in their movements. These boundary conditions will be referred to as BC2.

In figure 5.34, the deformed shape of the models with the BC1 boundary conditions and the H^{80}_{100} and H^{80}_{1000} materials are shown together with the 3D scan image in prone position (the model using H^{80}_{10} is not included as it did not provide additional information to the deformed shapes shown). In figure 5.35, the same deformed shapes are presented, but with the BC2 boundary conditions.

As can be seen in figure 5.34, the model using H^{80}_{1000} is more similar to the real deformation than the previous models without the contact surface, presented from section 5.6.1 to 5.6.10. The lower region of the model was displaced a similar quantity that in the reality, though it is quite different since the bulge is not as close to the sternum as the 3D scan. Besides, there is a marked peak which is not in the real deformation and, in general, the external surface of the model is more abrupt than in the reality. Nonetheless, the solution was considerably improved.

Comparing figures 5.34 and 5.35, the displacements were slightly larger and more towards the sternum in the simulation with free upper and lower boundaries (BC2), but not too much. Besides, the surface was smoother, though without a great difference.

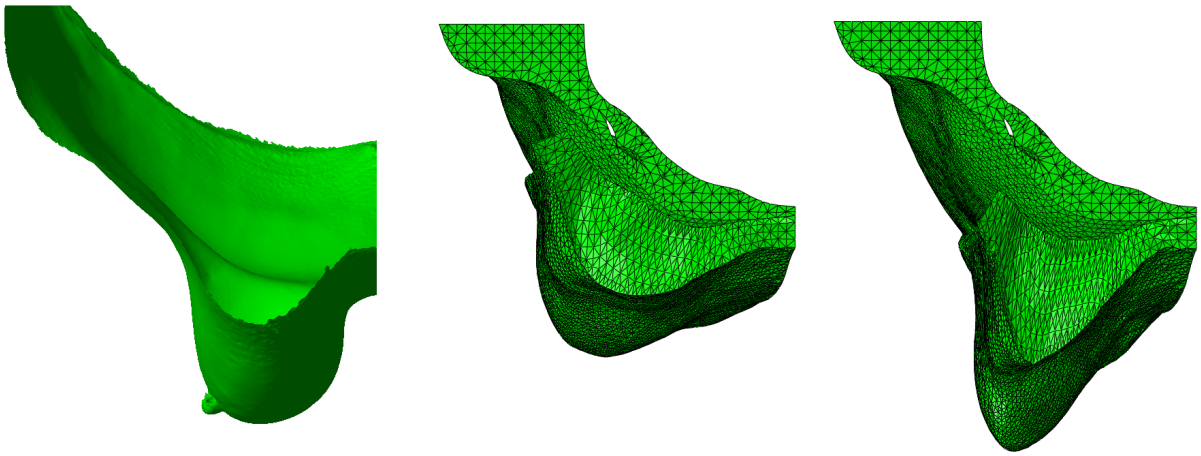

Figure 5.34: Contact surface between the muscle and breast tissues. BC1 boundary conditions. Left: 3D scan in prone position. Centre: H^{80}_{100}. Right: H^{80}_{1000}. Upper view. Section 5.6.11.1.

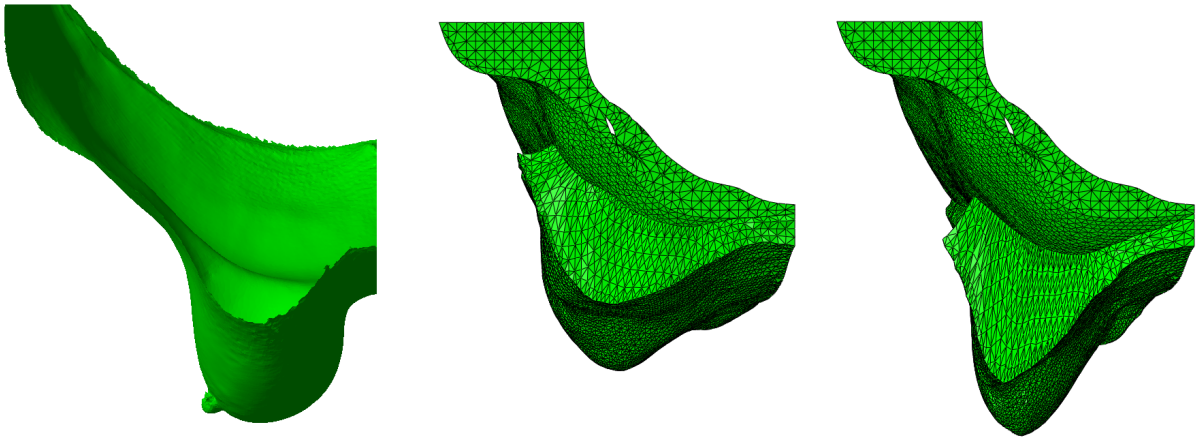

Figure 5.35: Contact surface between the muscle and breast tissues. BC2 boundary conditions. Left: 3D scan in prone position. Centre: H^{80}_{100}. Right: H^{80}_{1000}. Upper view. Section 5.6.11.1.

5.6.11.2 Contact in the whole surface between the muscle and the breast tissues, with springs

As the skin is actually not free but connected with the rest of the skin of the body, a variation of the previous model was built, with the H^{80}_{1000} material model and modifying the boundary conditions at the skin. Springs were included at the boundaries to simulate the effect of the rest of the skin, not included in the model. Each node of the boundary was duplicated, defining the springs between both nodes. The new ones were fixed and the force exerted by the springs was proportional to the distance between both nodes. The previous models can be seen as a particular case where the stiffness of these springs are zero. In the lower boundary, the movement in craniocaudal direction was constrained again, because it was proved in the previous sections that the nodes at this boundary did not move much in that direction. The rest of the boundary conditions of the model remained equal.

Two models were built: 1) with springs both in the lateral (5 N/m for all the springs, with a density of 2.82 springs/cm, resulting in an equivalente stiffness of 14.1 N/m/cm) and upper (5 N/m for all the springs,

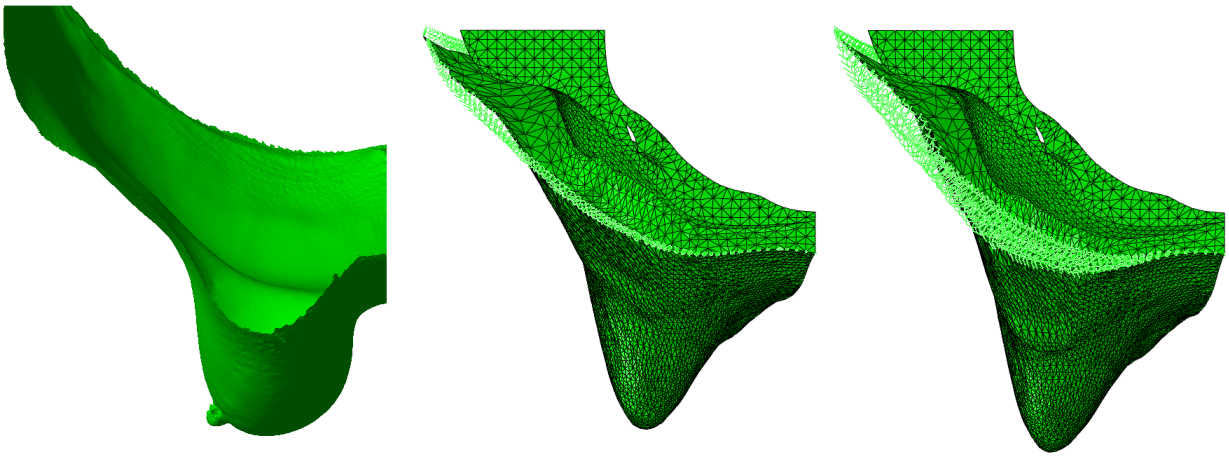

Figure 5.36: Contact surface between the muscle and breast tissues and boundaries with springs. Left: 3D scan in prone position. Centre: springs with the same stiffness. Right: different values for the stiffness. Upper view. Section 5.6.11.2.

with a density of 3.16 springs/cm, resulting in an equivalente stiffness of 15.7 N/m/cm) boundaries and 2) with springs both in the lateral (same stiffness as in case 1) and upper (1 N/m for all the springs, with a density of 3.16 springs/cm, resulting in an equivalente stiffness of 3.16 N/m/cm) boundaries. These stiffness values were not based in any physical property (nothing was found in the literature to model the effect of the rest of the skin), but in the results of several numerical tests to produce the most similar deformed shape to reality.

In figure 5.36, the deformed shape of models 1 and 2 presented in the above paragraph are shown and compared with the 3D scan image. In view of the obtained results, the external surface was smoother than in the models without springs. These springs increased the traction of the skin, which influenced on the final deformed shape of the breast, but the tissues remained separated from the sternum. Comparing both models 1 and 2, the deformed shapes are similar, although a larger deformation was produced when the upper springs were less stiff.

5.6.11.3 Contact in the lateral boundary

In this subsection, the model was modified so that the contact without separation between both surfaces was only enforced between the muscle and a narrow stripe in the lateral boundary. For the fat-gland mixture, the H_1^{80} model was used. For the rest of the tissues, the material models are the same that in the previous section. For the boundary conditions, the muscle was fixed in its 4 cut boundaries and in the ribs, and the fat-gland mixture was fixed in the sternum. The skin was also fixed in the sternum and the movements in the craniocaudal direction were constrained in the upper and lower boundaries. No springs were used, to analyse the effect of this new contact condition. The result is shown and compared with the real deformed shape in figure 5.37.

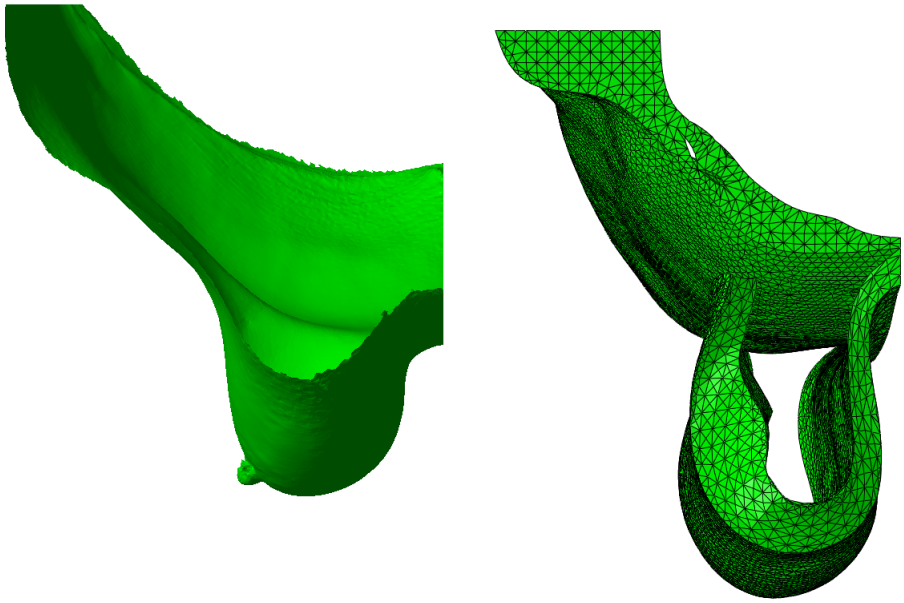

Figure 5.37: Contact surface between the muscle and breast tissues only in the lateral boundary. Left: 3D scan in prone position. Right: FE model. Section 5.6.11.3.

The deformed shape was qualitatively similar to the real breast. The breast tissues moved closer to the sternum and both pronounced curvatures appeared. Moreover, the external surface was quite smooth and the rest of the skin would remain attached to the chest wall. However, the breast fell more than the real one[1], and the deformed shape is a bit unrealistic. The clavicle and abdominal boundaries were separated from the chest wall (in anteroposterior direction), and this is not realistic. The next models are intended to overcome these problems.

5.6.11.4 Contact in the upper, lower and lateral boundaries

The contact surface of the model was modified adding to the areas with no separation contact (the lateral boundary) the upper and lower boundaries, to overcome the problems found in the previous section. That is to say, three narrow stripes in the lateral, upper and lower boundaries were enforced to slip over the muscle surface. The rest of boundary conditions remained like in the previous model. Three properties for the fat-gland mixture were used: H_1^{80}, H_{10}^{80} and H_{100}^{80}.

The model using H_{100}^{80} was also studied adding springs with two different configurations: 1) in each node of the upper (1 N/m for all the springs, with a density of 3.16 springs/cm, resulting in an equivalente stiffness of 3.16 N/m/cm) and lateral boundaries (1 N/m for all the springs, with a density of 2.82 springs/cm, resulting in an equivalente stiffness of 2.82 N/m/cm), to model the effect of the rest of the skin, not included in the model, and also in the whole surface of the muscle (0.1 N/m for all the springs, with a density of 7.69 springs/cm^2, resulting in an equivalente stiffness of $7.69 \cdot 10^{-3}$ N/cm/cm^2), linking each node to the corresponding one in the fat-gland mixture (to mimic a structure of loose connective tissue or weak

[1]Remember that in this model, the H_1^{80} material model was used, which imply an overestimation of the stiffness.

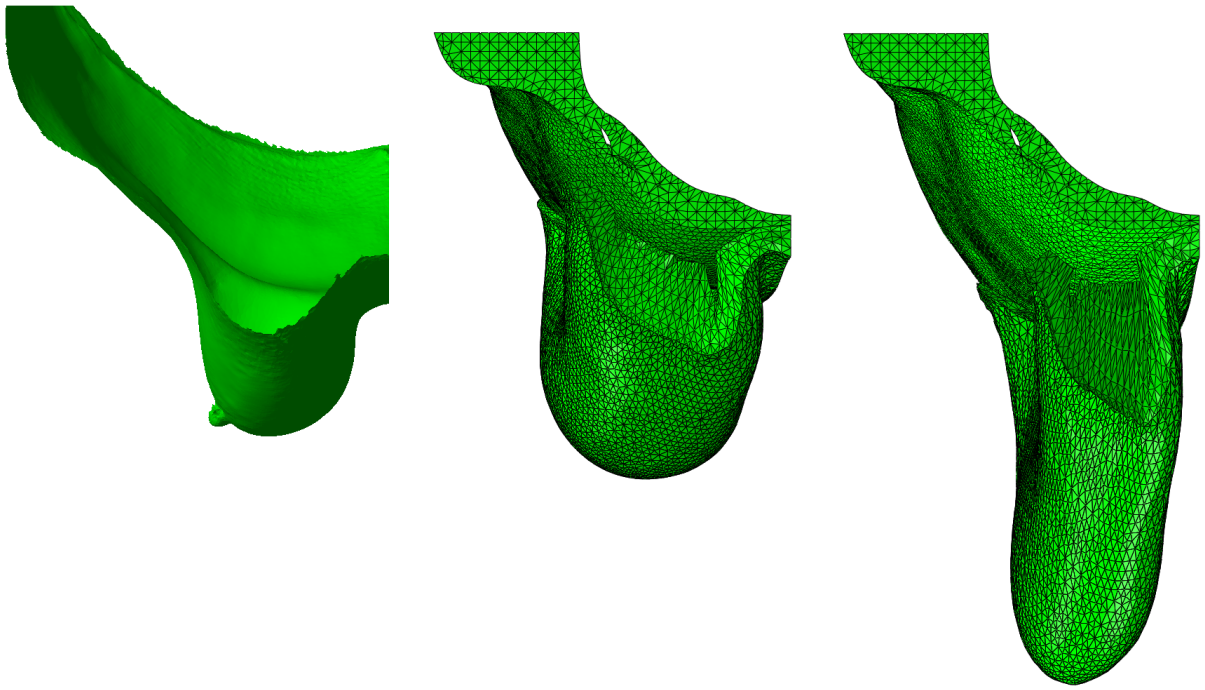

Figure 5.38: Contact surface between the muscle and fat-gland mixture along the boundary. Left: 3D scan in prone position. Centre: H_{10}^{80}. Right: H_{100}^{80}. Upper view. Section 5.6.11.4.

ligaments), and 2) equal to the previous one, just making the stiffness of the springs in the lateral boundary almost zero. The values of the spring stiffness were taken to obtain a similar displacement in anteroposterior direction to the 3D scan image.

The results without springs are shown in figure 5.38 (the model using H_1^{80} is not included as it did not provide additional information to the shown deformed shapes). In figure 5.39 both configurations with springs are shown. In the center the case 1, and at the right-hand side the case 2.

As can be seen in figure 5.38, the problems found at the boundaries in the previous section were more or less solved, but the deformed shape was worse. In the case using H_{100}^{80}, the displacements were excessively large. In the case using H_{10}^{80}, the displacements were similar in anteroposterior direction, but the bulge was wider and not as close to the sternum as in the previous section.

In figure 5.39, the springs added in these upper and lateral boundaries and also in the whole surface of the muscle can be seen. In the upper and lateral boundaries, they did not introduce an important change in the deformed shape. The springs in the whole surface of the muscle changed considerably the deformed shape, but not in the correct way. The breast remained far away from the sternum.

The deformed shapes resulting from the models presented in this section are the closest ones to the true deformed shape of the breast in prone position which have been obtained in this thesis with isotropic material models. In the following sections, anisotropic models will be used and other factors influencing the breast deformed shape will be studied, such as skin prestress.

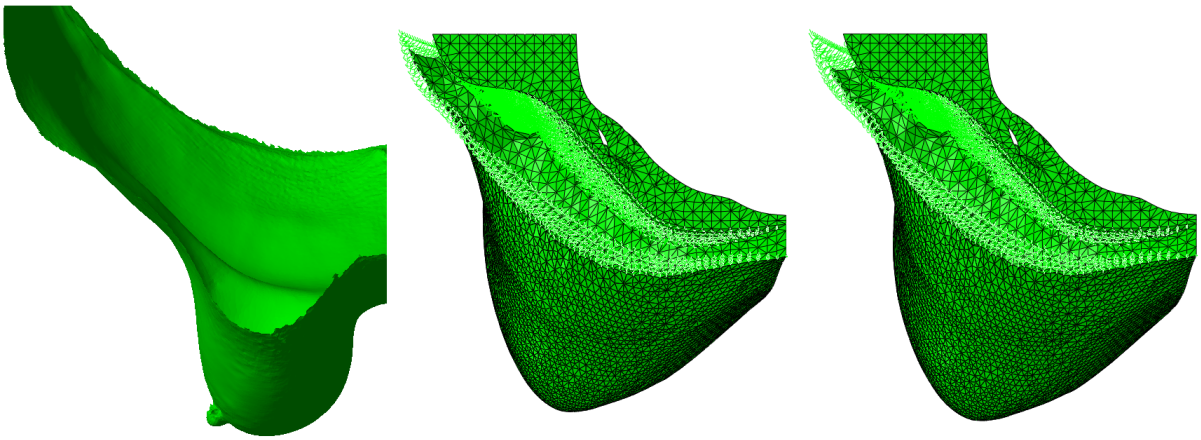

Figure 5.39: Model with contact surface between the muscle and fat-gland mixture along the boundaries and springs. Left: 3D scan in prone position. Centre: lateral boundary spring stiffness = 0.1 N/m. Right: lateral boundary spring stiffness ≈ 0 N/m. Upper view. Section 5.6.11.4.

5.6.12 Model with anisotropic properties for the breast tissues

In this section, a fibre reinforced anisotropic model was used to model the breast tissue. The fat is formed by adipocytes surrounded by collagen fibres [27]. No information was found in the literature showing that these collagen fibres are aligned in a preferential direction. However, taking into account that the human body always tends to optimize its structure to bear the loads in the most efficient way, it can be hypothesized that the fibres have a preferential direction. Moreover, the glandular tissue is composed of conducts oriented towards the nipple and Copper's ligaments connects the anterior and posterior faces of the breast, both structures having a similar direction and therefore supporting the hypothesis of the existence of a fibre principal direction.

Therefore, a new FE model was built using a Gasser-Ogden-Holzapfel (GOH) material model (presented in section 3.2.7) for the breast tissue. The fibres were oriented in anteroposterior direction. In the simulations carried out previously, the problem was that the breast tissue did not move close enough to the sternum. Then, the anteroposterior direction in the breast tissues might be more rigid than the mediolateral one. This fact also supported the idea of orienting the fibres in this direction. Although the GOH model was explained in section 3.2.7, here it is reminded for clarity. The strain energy function for one family of fibres is:

$$\bar{\Psi} = \frac{C_{10}}{2}(\bar{I}_1 - 3) + \frac{k_1}{2k_2}\left(e^{k_2[\kappa\bar{I}_1 + (1-3\kappa)\bar{I}_4 - 1]^2} - 1\right) . \tag{5.1}$$

where $c > 0$ and $k_1 > 0$ are stress-like parameters and $k_2 > 0$ is a dimensionless parameter. The parameter $\kappa \in [0, 1/3]$ accounts for the fibre dispersion. If its value is 0, the fibres are perfectly oriented in one direction without dispersion, whereas if its value is 1/3, the fibres are uniformly distributed in all directions and the material becomes isotropic. The first part of the strain energy function, the one which depends on $\bar{I}_1$, is a neo-Hookean model representing the isotropic contribution of the matrix, whereas the second part,

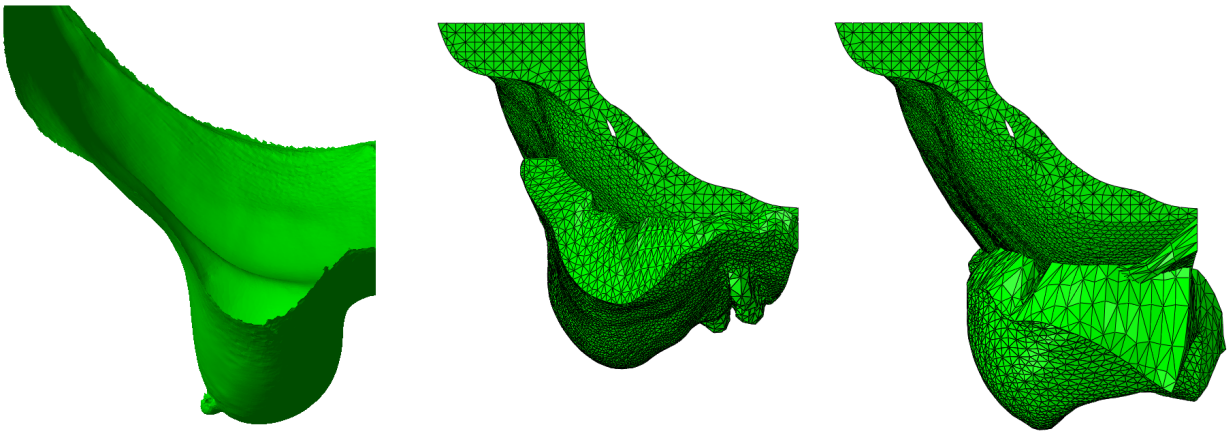

Figure 5.40: Model with contact surface between the muscle and breast tissue, this last one modelled with the *GOH* model, with fibres in anteroposterior direction and with dispersion. Left: 3D scan in prone position. Centre: $C_{10} = 300$ Pa. Right: $C_{10} = 1$ Pa. Upper view. Section 5.6.12.

function of the modified invariant $\bar{I}_4$, represents the anisotropic contribution of the fibres, modelling the strong stiffening of the collagen fibres when stretched. The preferential direction of the family of fibres is defined by the unit vectors $\mathbf{a}_0$, with respect to the material configuration.

The material constants of the model were taken from [47] and shown in table 5.1 as *GOH* model. Two cases were studied in Abaqus Explicit:

- With fibre dispersion ($\kappa = 0.13$): the parameter C_{10} is related to the stiffness of the matrix where the fibers are embedded. The values 300 (original) and 1 Pa were used for the constant. The muscle was fixed in its four cut boundaries and in the contact with the ribs. The breast tissue and the skin were fixed only in the sternum, being the rest of the boundaries free to move. The whole surface between the muscle and the breast tissue was modelled as a contact surface, not allowing the separation between both surfaces.

- Without fibre dispersion ($\kappa = 0$): the parameter C_{10} was also varied: 600, 400, 200, 100 and 20 Pa. k_1 was changed with respecto to the original value, to allow a higher deformation ($k_1 = 850$ Pa). The boundary conditions are the same as in the previous case with fibre dispersion, except for the upper and lower boundaries (clavicle and abdomen) of the skin, which were not totally free to move in these simulations. More precisely, the movement in craniocaudal direction was constrained.

In figure 5.40 two deformed shapes of the model with fibre dispersion, for C_{10} equal to 300 and 1 Pa, are shown and compared with the 3D scan image in prone position. In figure 5.41 the deformed shape of the model without fibre dispersion is shown, for the values of C_{10} 600 and 200 Pa. In figure 5.43, the upper and front views of the deformed shape of the model without fibre dispersion is shown for $C_{10} = 100$ Pa. The models for the other values of C_{10} are not shown because they do not provide additional information to that presented in the previous figures.

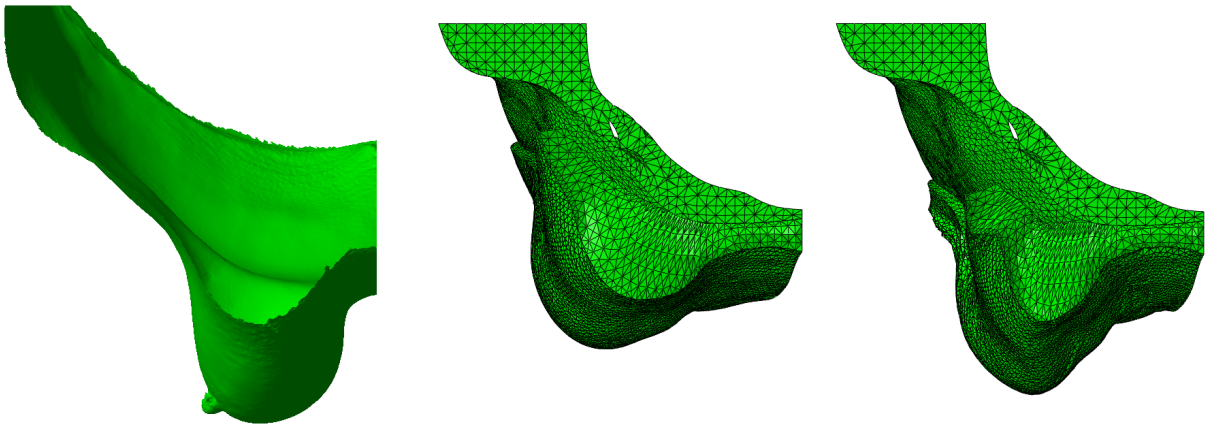

Figure 5.41: Model with contact surface between the muscle and breast tissue, this last one modelled with the *GOH* model, with fibres in anteroposterior direction, without dispersion. Left: 3D scan in prone position. Centre: $C_{10} = 600$ Pa. Right: $C_{10} = 200$ Pa. Upper view. Section 5.6.12.

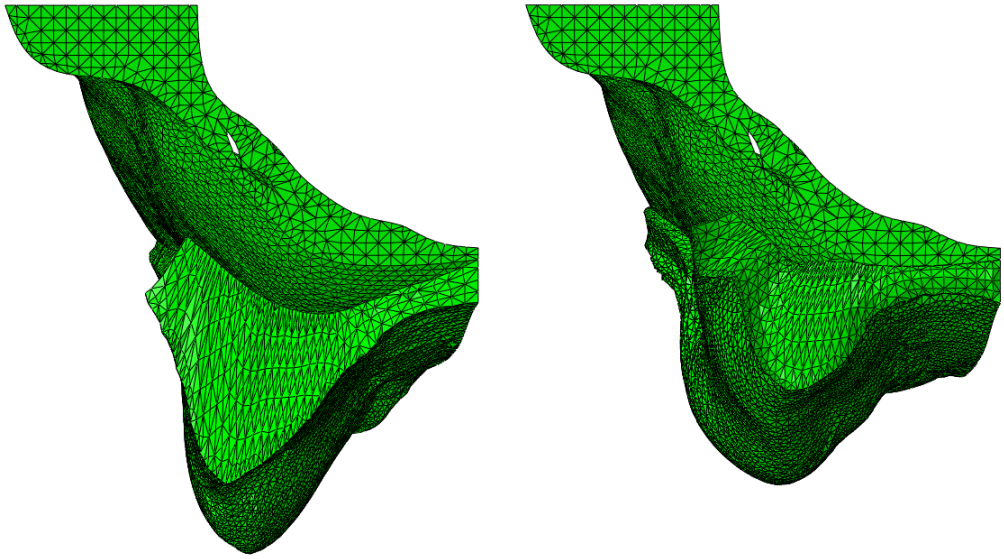

Figure 5.42: Model with contact surface between the muscle and breast tissue. Left: isotropic model for the breast tissues. Right: anisotropic model for the breast tissues. Upper view. Section 5.6.12.

As can be seen in figure 5.40, the deformed shape is quite unrealistic, specially in the case with $C_{10} = 1$Pa (right) and likely due to numerical problems.

The same simulations were conducted but without fibre dispersion. The objective was to check if the resulting deformed shape is more realistic without fibre dispersion. The deformations were normal, as can be seen in figure 5.41, and thus the fibre dispersion was thought to be responsible for the numerical problems. In figure 5.42, the deformed shape on the right-hand side of figure 5.41 is compared with the deformed shape of the model with a contact surface between the muscle and the breast tissues, but with the latter modelled as isotropic (the same model presented in section 5.6.11.1 in figure 5.35). It can be seen that the displacement of the anisotropic model in anteroposterior direction is smaller, but in mediolateral direction is even larger. Besides, the lowest point of the breast was not as markedly abrupt as in the previous cases

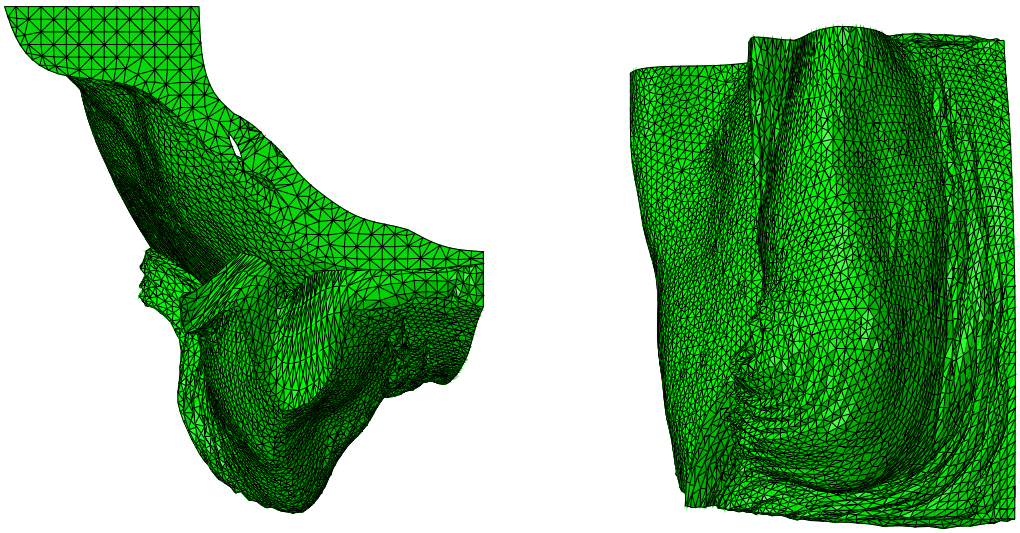

Figure 5.43: Model with contact surface between the muscle and breast tissue and $C_{10} = 100$ Pa. Left: upper view. Right: front view. Section 5.6.12.

with an isotropic material. Therefore, the material was assumed slightly more flexible, to try to reproduce a closer deformation to the real one, more displaced to the sternum and with a slightly larger displacement in anteroposterior direction.

For $C_{10} = 100$ Pa, the simulation converged but the deformed shape had many wrinkles as can be seen in figure 5.6.12, mainly in the front view. The simulation did not converge for $C_{10} = 20$ Pa. To solve the convergence issue, some solutions were tried: changing some parameters, as the ones which control the damping, and adding springs with different stiffness (0.05 and 0.1 N/m) in the boundary to stabilize the movement, but the convergence was not reached with these strategies.

5.6.13 Other models

This section presents the results of some simulations carried out with other models. These models are not less important than the rest. The reason why they are presented apart is that they do not fit well in the time line which has been followed during this chapter and it was preferred to explain them separately.

5.6.13.1 Skin prestress

The skin prestress was first studied because of two reasons. The first one is that it really exists in the skin of the body as will be discussed later on. Moreover, when convergence problems arose due to skin compression (section 5.6.4), the skin prestress was thought to play an important role in the simulations. The skin can experience unstable behaviours such as buckling under compression, in the body and particularly in the breast (for example if one pinches a piece of skin between the fingers), but at least in the organ studied

here, that is not a normal situation. However, a certain compression appeared in the simulations. This compression could actually be a reduction of its tension if the skin was prestressed enough.

The second reason is that it was also known that the initial configuration of the model in supine position is not a stress free state and that, maybe, it had an important influence on the results of the FE model, but this last point will be explained better in section 5.6.13.2.

Some information can be found in the literature about skin prestress in the human body, and particularly in the breast. However, the majority of the articles focus on Langer's lines, their distribution and the magnitude of the skin retraction when cut [126, 127, 128, 129], but few give a quantitative value of the prestress. Moreover, the values differ quite much among the different authors. For example, Alexander and Cook [130] used a suction device to investigate the prestress of the skin in the back. They found that this prestress was between 5.6 and 24.8 kPa. Flynn et al. [131] did experimental tests in the forearm and fitted them with FE analyses, determining that the prestress was in the range between 28 and 92 kPa. In the same year, Flynn et al. [132] did more experiments with the same procedure, but giving a different range for the prestress, now between 1.1 and 7.6 kPa. Diridollou et al. [133] did also experimental tests in the skin of the forearm, estimating an average prestress of 13.5 kPa. Therefore, it is clear that the prestress is a real characteristic of the skin, but its real magnitude is not known with certainty.

Uniform prestress

As presented in section 5.6.4, the convergence problems due to compression in the skin appeared when a model with the following conditions was simulated: muscle fixed in the four cut boundaries and in its contact with the ribs, breast tissue and skin fixed in the medial (sternum) and lateral boundary, muscle and breast tissues rigidly bonded and using the S_f material model for the fat and the H_f^{50} model for the fat-gland mixture, with $f > 100$. For the skin and the muscle, the BS and BM models were used respectively. Lets us recall (see section 5.6.4) that the same model without skin converged without problems. For example, in figure 5.44 on the left-hand side, the model without skin and with the S_{1600} material model for the fat and the H_{1600}^{50} for the fat-gland mixture is shown again. For this reason, this model, now with skin, was used to study the skin prestress and the convergence. The prestresses were applied in an equibiaxial way, i.e., the same magnitude was applied in two perpendicular directions of the membrane elements of the skin, creating a uniform prestress.

With the S_{1600} and H_{1600}^{50} material models, prestresses of 100 and 150 Pa were introduced in the model before the gravity loads were applied. With the S_{4000} and H_{4000}^{50}, skin prestresses of 150 and 1250 Pa were studied. The boundary conditions of the skin were changed in these simulations, now fixing the upper and lower boundaries, to avoid the release of the pretension in craniocaudal direction.

In figure 5.44, the deformed shape using the S_{1600} and H_{1600}^{50} material models and a prestress of 150 Pa

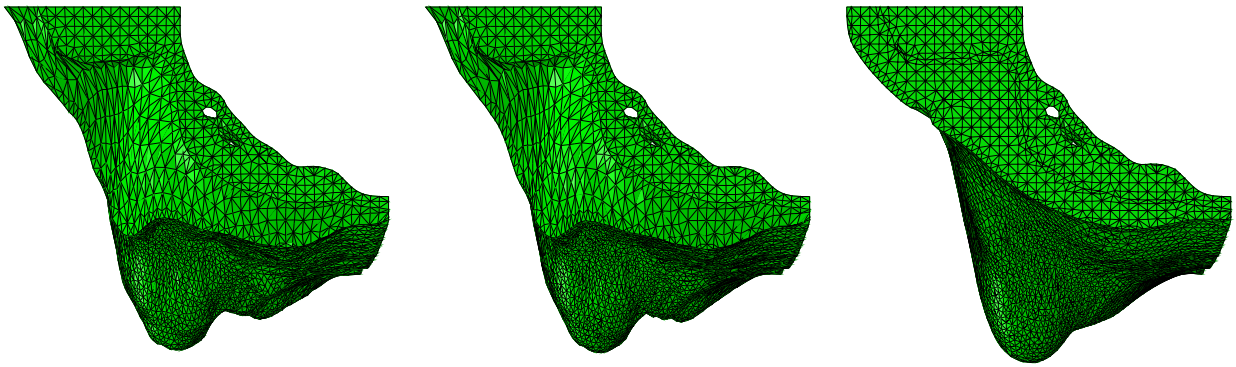

Figure 5.44: Analysis of the effect of skin prestress. Left: S_{1600} and H^{50}_{1600}, without skin. Centre: S_{1600} and H^{50}_{1600}, with skin prestress (150 Pa). Right: S_{4000} and H^{50}_{4000}, with skin prestress (1250 Pa). Section 5.6.13.1.

is shown in the center. On the right-hand side, the model with S_{4000} and H^{50}_{4000} and a prestress of 1250 Pa is included. On the left-hand side, the deformed shape of the model without skin and with the S_{1600} and H^{50}_{1600} models presented in section 5.6.4 is added to compare the results with those simulated in this section.

The model using S_{1600} and H^{50}_{1600} and a uniform prestress of 100 Pa did not converge but few steps remained to complete the simulation (90% of the gravity applied). The prestress was not enough to avoid the compression in the skin. With 150 Pa of prestress, the simulation converged. Comparing the deformed shape of this model (in the centre of figure 5.44) with the left one in the figure, it can be seen that the deformation is almost the same. Therefore, the model without skin, and the one with a small skin prestress behaved similarly. Moreover, the prestress was able to overcome the convergence problem. In most of the areas of the model with skin prestress the surface was smoother, and the lowest point of the deformed shape slightly shifted towards the sternum, though not much. Besides, the displacement in anteroposterior direction was slightly larger, which at first seemed to be strange. The reason was that, as the skin was not fixed in the upper and lower boundaries, the prestress in craniocaudal direction could be relaxed, concentrating the breast tissue near the center and therefore producing a lower peak of the deformed shape. This boundary condition was not changed at first to allow a direct comparison with the previous model (on the left), but it was changed in the next model.

The constants were divided by 4000 in the next simulations to allow a higher displacement in anteroposterior direction. Using 150 Pa of prestress, the simulation did not converge (it reached approximately the 50% of the applied load). With 1250 Pa, the simulation converged. Due to the fact that the tissues were more flexible in these simulations, a higher prestress was needed. As can be seen in figure 5.44 on the right, the effect of the new boundary conditions is clear, maintaining fixed the skin in the upper and lower boundaries. As noticed, the displacements in anteroposterior direction were similar compared with the other two models. However, the surface was smoother and the deformation near the boundaries was more normal.

Different prestresses in two regions of the skin

Additionally, another model was built differentiating two areas of the skin separated by a central line along the craniocaudal direction, i.e., a half near the sternum (medial) and a half near the axilla (lateral). The objective was to analyse the effect of having different prestresses in each area. In the real breast, in supine position (initial configuration) the skin would be stretched due to the weight of the breast tissues. Moreover, the tension in the skin would not be uniform, as each portion of skin is not bearing the same load. For example, the skin near the sternum would have a higher prestress, whereas the skin near the axilla would be almost unloaded. This effect was modelled assigning a different prestress in different areas of the skin. So, the lateral half was not prestressed, while the medial one was. In these simulations, the muscle was fixed in the four cut boundaries and in its contact with the ribs and the skin was also fixed in the four boundaries. For the breast, besides fixing it in the medial boundary, the displacements in craniocaudal direction were also constrained in the upper and lower boundaries. The breast tissues and the muscle were not bonded in these simulations. For the breast tissues properties, the S_{100} material model was used for the fat and the H^{50}_{100} for the fat-gland mixture. The simulations were done using prestresses from 0 to 15 kPa.

In figure 5.45, three deformed shapes are shown, with different prestress in the medial and lateral halves, corresponding to prestresses of 0, 500 and 5000 Pa. The rest of the prestresses below 5000 Pa are not included because they did not provide additional information to the shown deformed shapes. It can be seen that the skin prestress had an influence on the maximum displacements, and that as it increased, the breast tissues were slightly displaced to the sternum, although it is difficult to notice this effect with the naked eye. It is important to note that the magnitude of the prestress was considerably high compared to the low effect which it caused in the lateral movement of the tissues. For higher values, 10000 and 15000 Pa, the simulations did not converge due to element distortion.

In conclusion, the prestress solved the convergence problem and had an effect on the deformed shape, but not important enough to obtain a deformation similar to the real one.

5.6.13.2 Pullback algorithm

The FE models presented in this thesis were built from CT images taken in supine position, which was considered the initial configuration. Many authors who work with FE biomechanical models consider the medical images as the initial configuration, that is, stress free, although obviously it is not. In the case of the breast in the supine position, stresses and strains exist because the gravity is acting in this position, and they may play and important role in the subsequent simulations. Therefore, it would be good to calculate a reference state for the breast in which no external loads are applied. In this particular case, the objective was to "eliminate" the gravity from the model in supine position. Starting from this reference configuration and applying the gravity in different directions, the prone, supine and standing up positions would be obtained.

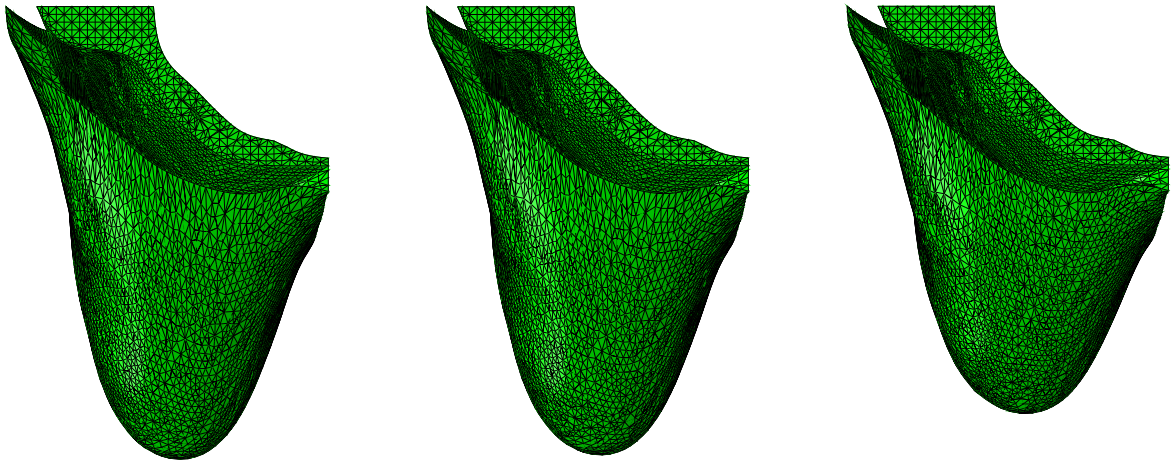

Figure 5.45: Analysis of the effects of different skin prestresses as a function of the region. Left: prestress = 0 Pa. Centre: prestress = 500 Pa. Right: prestress = 5000 Pa. Section 5.6.13.1.

In the previous simulations carried out in this thesis, the prone position was obtained applying twice the gravity in posteroanterior direction. With the first gravity load applied, it was intended to obtain a reference configuration, but it was not stress free. The approach presented in this section is closer to reality.

To calculate the reference configuration of the breast, the algorithm proposed by Riveros et al. [120] was used. This is an iterative algorithm in which the reference configuration is updated in each step. It stops when, after applying the exiting loads to the updated reference configuration, the geometry of the medical images is obtained. In this particular case, it stopped upon the application of the gravity loads to the reference configuration, when the deformed shape in supine position, that taken from the medical images, was obtained (of course, with a given tolerance). The steps of the algorithm in the case of the breast are explained, although the reader is referred to Riveros et al. [120] for a deeper insight in the algorithm.

The position of the nodes of the FE model mesh is called X in a general basis. X_{image} represents the configuration of the medical images. The objective is to obtain X_{ref}, a mesh such that when the gravity loads are applied, the configuration X_{image} is obtained. The reference configuration is updated in each step, X^k_{ref}.

1. The reference configuration (configuration "without gravity") is initialized with the supine position configuration.

$$X^0_{ref} = X_{image} \ .$$

2. Gravity is applied in anteroposterior direction to the reference configuration of the $(k-1)$ iteration, X^{k-1}_{ref}, to obtain the corresponding deformed configuration X^k_{def}.

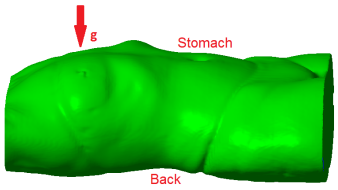

Figure 5.46: Scheme of the gravity load application.

3. Once the simulation is finished, the error is compared with the tolerance in each node i of the FE mesh.

$$|X_{image} - X^k_{def}| < tol \ .$$

4. If the previous condition is not accomplished for every node, the reference configuration is updated.

$$X^k_{ref} = X^{k-1}_{ref} + (X_{image} - X^k_{def}) \ .$$

5. Steps 2, 3 and 4 are repeated until condition 3 is fulfilled for every node.

6. If condition 3 is fulfilled, X^k_{ref} is taken as X_{ref}.

To implement this algorithm, a Fortran script was written. This script called Abaqus to run the simulations, extracted the results, checked the condition to finish the loop and made the calculations of step 4. Abaqus Standard was used in these simulations. Once X_{ref} was obtained, gravity was applied in posteroanterior direction to simulate the prone position.

First, the pullback algorithm was used in the model in which the muscle and the breast tissue were rigidly bonded. The muscle was fixed in the four cut boundaries and in the contact with the ribs, and the breast tissue and the skin were fixed in the sternum. For the skin, the BS model was used, and for the muscle, the BM model. For the adipose tissue, the S_1, S_{100}, S_{500} and S_{1000} material models were used and for the mixture of fat-gland, the H^{50}_1, H^{50}_{100}, H^{50}_{500} and H^{50}_{1000}.

Then, the algorithm was applied to the model with no connection between the muscle and the breast tissue. The muscle was fixed in its four cut boundaries and in the contact with the ribs. The skin and the breast tissue were fixed in the sternum, and their displacements in the upper and lower boundaries were constrained in the craniocaudal direction. For the skin, the BS model was used, and for the muscle, the BM model. The S_1 and H^{50}_1 models were used for the fat and fat-gland mixture respectively.

The results of the pullback algorithm for the model with the muscle and breast tissues rigidly bonded and the original Samani's properties are presented in figure 5.47. On the left-hand side, the reference configuration is shown, i.e., the configuration "without gravity" which was obtained after applying the pullback algorithm. In the center, the prone position obtained starting from this reference configuration is attached. Finally on the right-hand side, the prone position obtained without the pullback algorithm (that is to say, applying

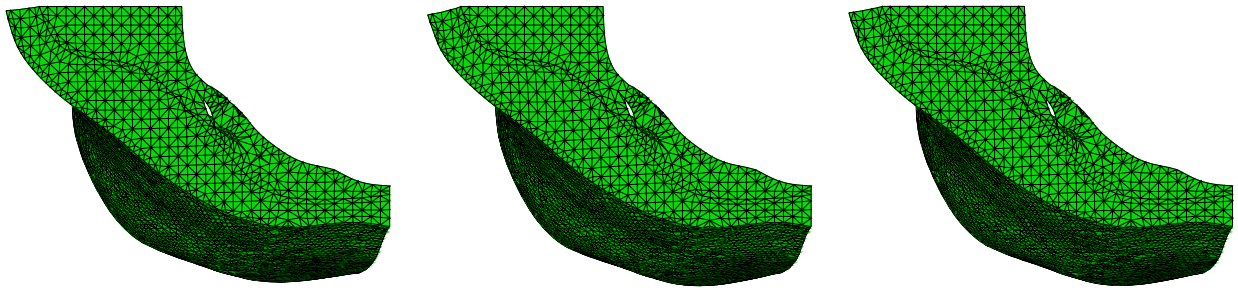

Figure 5.47: Comparison of using or not using the pullback algorithm. Left: reference configuration ("without gravity"). Centre: deformed shape in prone position using the pullback algorithm. Right: idem not using the pullback algorithm. Upper view. Section 5.6.13.2.

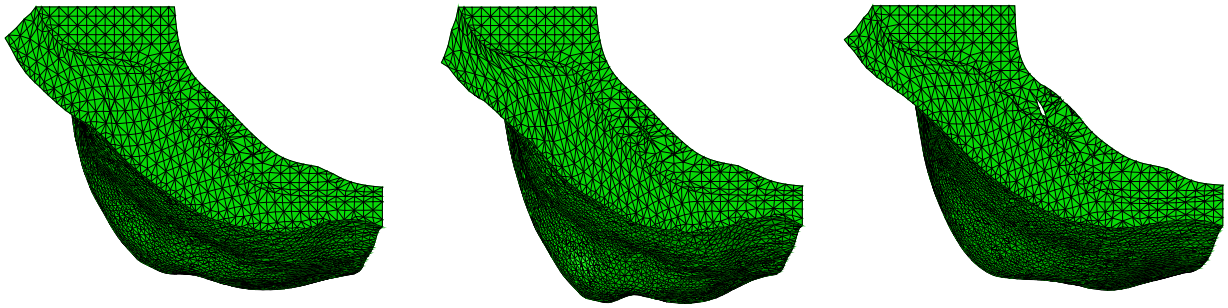

Figure 5.48: Comparison of using or not using the pullback algorithm, with S_{100}-H^{50}_{100}. Left: reference configuration ("without gravity"). Centre: deformed shape in prone position using the pullback algorithm. Right: idem without using the pullback algorithm. Upper view. Section 5.6.13.2.

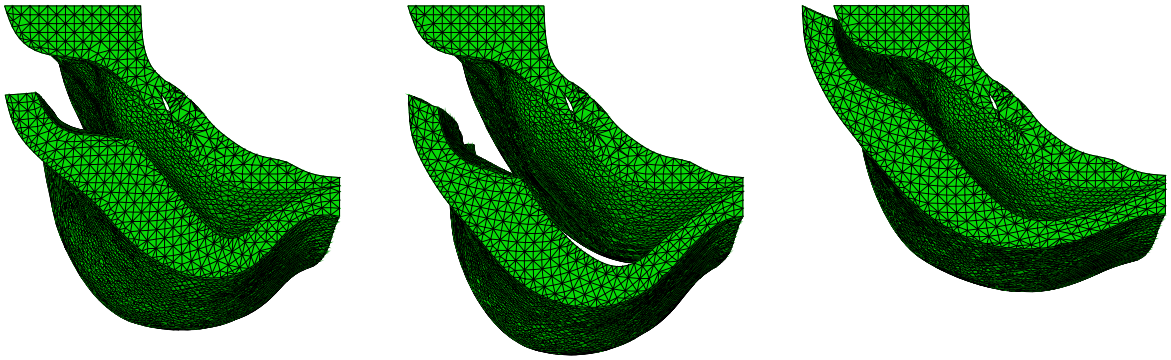

Figure 5.49: Comparison of using or not using the pullback algorithm, without connection between the muscle and the breast tissue. Left: reference configuration ("without gravity"). Centre: deformed shape in prone position using the pullback algorithm. Right: idem using the pullback algorithm. Upper view. Section 5.6.13.2.

twice the gravity to the initial model in supine position, as in the previous simulations in this thesis) is shown. The results for S_{100}-H^{50}_{100} are presented in figure 5.48.

The results for the model with no connection between the muscle and the breast tissues are shown in figure 5.49. As in the previous figures, the reference configuration is shown on the left-hand side. In the center, the prone position using the pullback algorithm is included, and on the right-hand side, the prone position obtained without the algorithm is presented.

In figure 5.47, comparing both models in prone position, the displacements were larger in the model using the pullback algorithm, although, due to the high stiffness of the model, it was difficult to notice the difference with the naked eye.

Comparing both models in prone position in figure 5.48, it is clearly seen that in the deformed shape obtained using the pullback algorithm the displacements were larger in general and in particular the lateral movement. That means that the pullback algorithm produces a deformed shape closer to reality, with the same material, properties and boundary conditions.

The process was repeated with the constants divided by 500 and 1000, to check what happened with a more flexible model, but the algorithm did not converge due to bad shaped or even zero volume elements appearing while updating the reference configuration during the iterative process.

Regarding the models without connection between the muscle and the breast tissues, compared in figure 5.49, it can be noticed that in the new model (center) the breast tissue shifted more in anteroposterior direction and to the sternum that in the model without the pullback algorithm, therefore improving the results. However, the lateral boundary became very separated from the muscle surface, as can be seen in figure 5.49, and this is not very realistic.

Using a model with a contact surface between the breast tissue and the muscle together with the pullback algorithm was not possible. In the first step of the algorithm, both surfaces were in contact. However, when the reference configuration was updated, the surfaces became separated, which in this type of model was not possible because both tissues were supposed to remain in contact.

5.6.13.3 Fibre direction calculation

As it was explained in section 5.6.12, a correct modelling of the breast tissue could need allowing for a fibred model. However, as stated in that section, no information was found in the literature about the preferential direction of the fibres in the adipose tissue in general, and in particular in the breast. Here, a method was proposed to estimate the preferential directions of fibres in the adipose tissue based on the works of some authors who observed how living tissues are remodelled to adapt its microstructure in the most efficient way from a mechanical point of view [46, 134, 135, 136]. In particular, tissues reinforced with collagen fibers are thought to have the fibres oriented in the direction in which the tissue is withstanding the largest tensile stress. In this manner, the mechanical properties of collagen fibres are exploited in the most efficient way.

It has been proposed that the preferential direction of the fibres is the direction of the maximum principal stress [134, 135, 137]. The question is which position of the body should be considered to calculate those principal stresses. Since during most of the time, the women's trunk is in vertical direction, the standing up position was selected.

To do that, the GOH model was used. Although the model is explained in section 3.2.7, here it is reminded. The strain energy function for one family of fibres is:

$$\bar{\Psi} = \frac{C_{10}}{2}(\bar{I}_1 - 3) + \frac{k_1}{2k_2}\left(e^{k_2[\kappa \bar{I}_1 + (1-3\kappa)\bar{I}_4 - 1]^2} - 1\right) . \tag{5.2}$$

where $c > 0$ and $k_1 > 0$ are stress-like parameters and $k_2 > 0$ is a dimensionless parameter. The parameter $\kappa \in [0, 1/3]$ accounts for the fibre dispersion. If its value is 0, the fibres are perfectly oriented in one direction without dispersion, whereas if its value is 1/3, the fibres are uniformly distributed in all directions and the material becomes isotropic. The first part of the strain energy function, the one which depends on $\bar{I}_1$, is a neo-Hookean model representing the isotropic contribution of the matrix, whereas the second part, function of the modified invariant $\bar{I}_4$, represents the anisotropic contribution of the fibres, modelling the strong stiffening of the collagen fibres when stretched. The preferential direction of the family of fibres is defined by the unit vectors $\mathbf{a}_0$, with respect to the material configuration.

The GOH model was implemented in Abaqus using a UMAT. Inside this subroutine, the behaviour of the material was defined and also the maximum principal Cauchy stress direction was calculated and the fibres of the model were reoriented to coincide with this previously calculated direction. The material parameters for the model are presented in table 5.1.

An algorithm was designed to determine the final fibre direction.

1. In the first step, the fat-gland mixture is assumed isotropic ($\kappa = 1/3$). Gravity loads are applied in standing up position and the principal Cauchy stresses are calculated for each element of the model. They are named such that:

$$\sigma_1 > \sigma_2 > \sigma_3 \qquad\qquad \sigma_1 = \sigma_{max} \tag{5.3}$$

   The maximum principal Cauchy stress direction, referred to the material configuration, is defined as $\boldsymbol{a}_0^0$.

2. For the step k, the fat-gland mixture is considered anisotropic and the fibre direction is initially defined as the maximum principal Cauchy stress direction calculated in the previous step, $\boldsymbol{a}_0^{(k-1)}$.

3. Gravity loads are applied and $\boldsymbol{a}_0^k$ is recalculated for each element. In case $\sigma_1 \approx \sigma_2 > 0$, $\boldsymbol{a}_0^k = \boldsymbol{a}_0^{(k-1)}$. This last condition is imposed because if an element is subjected to a biaxial tension stress state, the algorithm can get stuck in an infinite loop where the fibre direction is continuously switching between both principal directions.

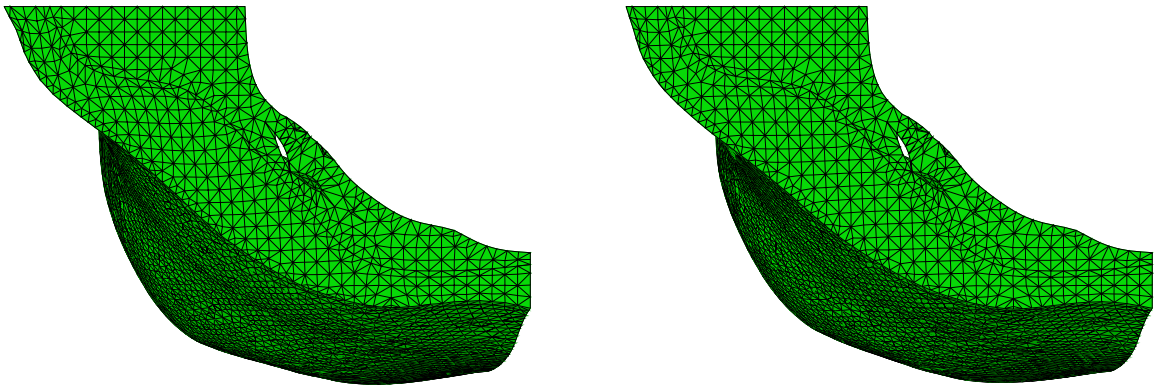

Figure 5.50: Left: Deformed shape in prone position with the fat-gland mixture considered isotropic, upper view. Right: Deformed shape in prone position at the end of the fibre direction calculation algorithm, upper view. Section 5.6.13.3.

4. In each element of the model, the following dot product is calculated:

$$\boldsymbol{a}_0^{(k-1)} \cdot \boldsymbol{a}_0^k = \cos\left(\boldsymbol{a}_0^{(k-1)}, \boldsymbol{a}_0^k\right) . \tag{5.4}$$

   If $\cos\left(\boldsymbol{a}_0^{(k-1)}, \boldsymbol{a}_0^k\right) > 1 - \epsilon$, with $\epsilon \ll 1$ a predefined tolerance, it would mean that the orientation vector is almost the same that in the previous step and the algorithm has converged.

5. Steps 2, 3 and 4 are repeated until condition 4 is fulfilled for every element.

The algorithm was applied to a model in which the muscle and the breast tissue were rigidly bonded. The muscle was fixed in the four cut boundaries and in the contact with the ribs, and the breast tissue and the skin were fixed in the medial and lateral boundaries. In the upper an lower boundaries, only the displacement in craniocaudal direction were constrained. For the skin, the BS model was used, and for the muscle, the BM model. For the mixture of fat-gland, the GOH model was used with the properties showed in table 5.1.

In figure 5.50 at the left-hand side, the deformed shape of the model is shown at the end of the first step of the algorithm, i.e, with the fat-gland mixture considered isotropic. At the right-hand side, the deformed shape of the model at the end of the fibre direction calculation algorithm is presented. In this case, 7 iterations were needed to reach the convergence (the average change in direction in the last step with respect to the previous one was 0.72°.)

As can be seen, the deformed shapes are quite similar. The reason is that the fibre direction did not change much between them. Moreover, the model is behaving quite stiffly, making more difficult to detect differences with the naked eye. The average change in direction between both situations (first and last step of the algorithm) was 16.41°.

The algorithm worked well, and it will be very useful to improve the solution when a FE model able to

approximately reproduce the behaviour of the breast is obtained.

Chapter 6

Closure

6.1 Summary and conclusions

In this work, a contribution to the knowledge of the biomechanics of the breast has been made. None of the previous works in the literature were completely valid to simulate the real movement of the breast and little knowledge existed about many factors which play an important role in the behaviour of the breast. This thesis has addressed this field in detail and provided the path that must be followed in future computational and experimental studies about the breast. Many possibilities have been discarded shedding light on the way the development of the FE model of the breast should be carried out. Moreover, the difficult interaction between the adipose tissue and the pectoral muscle has been pointed out as key in the process.

Concerning the experimental work, an ample set of relaxation tests has been done in human adipose tissue, in the abdomen and in the breast. Different patients and areas have been tested. Two different viscoelastic models (with several hyperelastic strain energy functions) were adjusted to the experimental tests, providing very good results. For both viscoelastic models, the independency of their constants with respect to the strain rate was proved, although the independency with respect to the strain level was not accomplished. That means that it is not possible to define a unique set of constants for the adipose tissue with these two models. Probably the tissue was experiencing some degradation (damage) during the tests at the different strain levels, making the constants dependent on it. This damage should be studied more carefully and a damage model should be used in case the degradation was confirmed. In spite of this fact, for a certain strain level, both models are valid, being the internal variables viscoelastic (IVV) model, with an Ogden strain energy function, the formulation that adjusted the experimental results more accurately.

Several comparisons have been made to analyse the differences between the mechanical behaviour of the adipose tissue of different areas and individuals. The mechanical behaviour of different individuals' abdominal fat was compared. Inter-individual differences were found in both, the elastic and the viscous

constants, confirming that it was a correct decision to extract the specimens from the same individual in the subsequent statistical analyses, for example, to check the validity of the QLV and IVV models or to compare the adipose tissue from different anatomical regions. It is therefore advisable to extract the specimens from the same patient if avoiding the inter-individual effects is desired. In the comparison of the mechanical properties of the adipose tissue of several regions of the abdomen and the breast, differences were found between the superficial breast and three groups of the abdomen: superficial-medial, deep-medial and deep-lateral. However, there are no differences with the superficial lateral group. No differences were detected between the deep breast and the rest of the groups either. These conclusions have a high relevance for the breast reconstruction surgery with autologous abdominal tissue. The breast adipose tissue can be considered as a unique tissue from the mechanical point of view. Moreover, in the breast reconstruction surgery, the deep breast fat can be replaced by any part of the abdomen, since no significant differences exist in the mechanical properties. However, the superficial breast fat should be replaced, if possible, by the superficial lateral region of the abdomen. Also important although with less clinical relevance are the differences found between regions of the abdominal adipose tissue. It seems that no differences exist in the mechanical properties between both regions of the superficial layer, between both parts of the deep layer and between both parts of the medial regions. However, differences between the deep and superficial layers were found, that is to say, the mechanical properties of the abdominal adipose tissue seem to change with the depth.

Comparing the elastic part of the final model presented here for the breast adipose tissue with the Samani's constants (which are the only ones found in the literature for the breast fat), it can be seen that the behaviour modelled with the Samani's constants is much stiffer than that measured experimentally in this thesis. Also supported by the results obtained in the FE models, it seems that the constants provided by Samani do not correspond to the real behaviour of the breast adipose tissue.

Regarding the computational work, several models, boundary conditions and strain energy functions for different materials have been tried. The estimation of the deformed shape of the breast when the body changes from supine to prone position has been improved much from the initial models, although some issues need to be solved yet to improve the models and finally obtain a deformation which can be considered valid. It has been found that none of the material models and boundary conditions proposed in the literature produce reasonable results. In particular, they yield an excessively stiff behaviour.

The interaction between the muscle and the breast tissue has been detected to play a key role in the deformation of the breast. The properties of the muscle are not determinant, as the muscle is not activated during the change of position modelled here and, moreover, it is stiffer than the rest of the involved tissues. Of course, if an activity in which the dynamics matter, like running, is under study, the role of the muscle can change. The skin properties can be important in the global behaviour because it is the tissue which

surrounds the organ. In general, a deeper knowledge about the mechanical properties of the materials is needed. Normally, these properties have been determined in the literature with one "simple" experimental test, whereas the deformation in the breast is not simple whatsoever and quite different from the experimental test which was carried out. This can lead to wrong results when using these mechanical properties in a computational model. In addition, more studies are needed about the internal structure of the tissues and their connections.

6.2 Original contributions

The main contributions of this thesis, both in the experimental and computational fields, are briefly summarized in the following points:

- Optimisation of the experimental procedure, reducing its size and improving the temperature control and the setup, with respect to the previous setup that existed in the research group. This previous setup was considerably big and heavy, even causing problems in the load cell due to bending stresses. The temperature control was also very big and less accurate.

- Fitting algorithm performed in two steps, the first one consisting in a genetic algorithm to search for the initial guess of the second step, a least square optimisation. This way, the dependence of the least squares fitting on the initial guess is avoided. If the first step is not run, the final solution depends on the initial guess and therefore, the algorithm can stop in a local minimum and not in the global one.

- High reduction of the computation time of the QLV fitting algorithm by precalculating the integrals.

- Algorithm to eliminate the spurious toe region of the experimental tests.

- Experimental obtention of the viscoelastic properties of the human abdominal and breast adipose tissue.

- Investigation of the differences between the mechanical properties of the adipose tissue in several anatomical regions.

- Advances in the FE modelling of a female healthy breast.

- Algorithm to find the most probable direction of the fibres inside the breast tissues.

- Advances in the definition of a correct unloaded configuration of the healthy breast.

6.3 Limitations

6.3.1 Experimental work

In the experimental work carried out in this thesis, a larger number of patients would have been needed to draw the statistical conclusions with more certainty. The differences between patients were studied with two patients and the differences between anatomical regions of the same patient were studied in one patient. It would have been better to have more patients to check the conclusions obtained in this thesis in more cases. Besides, it would have been interesting to have enough patients to obtain the mean properties for the adipose tissue in the global population and to study if they are function of weight, body mass index or a similar parameter. The problem is that a large number of patients would be needed for this, considering that inter-individual differences may exist.

Moreover, the used viscoelastic models and strain energy functions were not able to represent the global behaviour of the adipose tissue. The independence of the strain rate was accomplished, but the independence of the strain level was not. Probably the tissue was experiencing some degradation (damage) during the tests at the different strain levels. This damage should be studied more carefully and a damage model should be used in case that the degradation was confirmed. It was not possible to carry out the experimental tests at lower strain levels because the produced forces would have been much smaller and the available load cell in the laboratory would have been unable to measure them.

6.3.2 Computational work

The homogenization procedure for the fat-gland mixture carried out in section 4.2 provides an appropriate material model for the simulation of the bulk behaviour, but it would fail to describe the behaviour under localized loads like a needle insertion. In that case, the microstructure of the tissues might play an important role because the size of the needle could be of the same order of magnitude as that of the breast constituents. Moreover, the contact between the adipose and gland tissue has not been taken into account, the interfaces have been modelled as a rigid union. It is also important to note that the model depends on the suitability of the properties of fat and gland given by Samani and Plewes [41]. Finally, the strain energy function used by these authors is not policonvex. However, this fact does not necessarily mean that this function should be ruled out, as explained in [105, 106, 107].

In the simulations of the change of position from supine to prone, apart from the normal sources of error in this type of analysis, there are another possible errors beyond the control of the author. Firstly, the CT images were taken some months before the superficial 3D scan images. In fact, the CT was done before the reconstruction surgery of the patient, and the 3D scan after it. Therefore, as a long time passed, it is possible that the woman suffered some changes between both dates, which can have a big influence on the analysis

presented here. This is even more probable taking into account that a surgery took place in the meantime. For instance, her weight could have changed, varying the amount of adipose tissue in the healthy breast. The ideal scenario would have been to take both images the same day, one after the other. Apparently, it was not possible to do so because of incompatibility of hospital protocols.

Another possible source of error is the corporal position when taking the images. Both the CT and the superficial 3D scan were taken with the patient's arms stretched over her head (aligned with the trunk) and kept extended during acquisition. But if the position is not exactly the same, e.g. the arms are not completely extended or a little bit lower in one of the images, the muscle structure and the location of each tissue can vary in a significant way.

Finally, it is important to say that it was not possible to obtain an accurate deformed shape of the breast. One possible cause could be the definition of the contact model or the boundary conditions which can have a big influence on the behaviour of the breast model. Maybe they are not similar enough to the reality to obtain an accurate deformed shape. Another possible cause is the use of the C3D4H elements instead of the C3D8H ones, which in general are more appropriate.

6.4 Future work

Regarding the experimental work, more experimental tests on breast adipose tissue are planned to be made. The aim is to be able to determine if there are significant differences between the breast fat of different individuals. Besides these planned tests, the histological structure of the abdominal and breast fat should be studied, to try to link the differences which have been found to a difference in the internal structure of the tissue. Moreover, to improve the characterisation of the adipose tissue, its structure should be studied in more detail, trying to change from the current phenomenological approach to a more mechanistic modelling of the tissue. To do that, it would be interesting to study if a preferential direction exist in the connective tissue in order to use an anisotropic model based on measurable parameters. Until having this knowledge of the real structure, any used model would be phenomenological, even if biaxial tests were carried out to adjust its behaviour. This part can only be partially done in our group, because we do not have yet the needed facilities. Experimental tests on the mammary gland should be tried, but unfortunately it exclusively depends on the availability of this tissue. Its obtention is difficult because it is not usually extracted or removed, except for a mastectomy and here the tissue is needed afterwards to carry out anatomical pathology exams.

A new viscoelastic model, able to represent the whole behaviour of the adipose tissue, is needed. The models used here were able to fit quite accurately the experimental curves, but they failed to provide a unique set of constants for different testing conditions. If the models which can be found in the literature are not useful, a new viscoelasticity model should be developed.

Regarding the anatomy of the breast, of course related to the development of a FE model, it would be

advisable to widen the knowledge about the distribution and structure of the suspensory ligaments of the breast. Moreover, the experimental characterisation of their properties would be necessary, as well as any equivalent model to mimic their behaviour. In the same vein, the retromammary space should be studied. How the breast is connected to the muscle, which movements this layer allows and how much it can move are questions that should be answered to be able to develop a correct model of the global behaviour of the breast. All of this work is intended to be done in our group with the collaboration of the *Virgen del Rocío* Hospital in the near future.

Regarding the FE model itself, more studies will be carried out following the idea of a flexible connection between the muscle and the breast. In general, the FE studies will continue, improving them until the deformed configuration is accurate enough, comparing it with the 3D scan images.

It is necessary to continue working in the pull-back algorithm to try to improve its performance adapting it to the particular breast geometry and problems. It has a solid physical meaning: the stress state of the breast in supine position cannot be a zero stress state. In particular, it is very interesting its application to the model in which a no separation surface contact is defined between the muscle and the breast tissues. Abaqus Explicit will be used to try to overcome the convergence problems encountered with Abaqus Standard.

In the same vein, the fibre orientation algorithm should be applied too if the existence of clearly oriented fibres is demonstrated through histological inspection. It is also a physically based idea, as the body always try to optimize the behaviour of the tissues. Therefore, it seems reasonable to orient the fibres in the most efficient direction, i.e. the direction in which the principal stresses are larger, taking into account the position in which the woman spends more time.

Appendix A

Integrals for the QLV fitting algorithm

In this appendix, the complete procedure to obtain the analytical stress in the QLV approach for each of the four strain energy function used in this work is presented. This mathematical procedure starts from the equations introduced in section 3.3.1, which are reminded here, and then it is particularized for each strain energy function. Thus, recall that the stress produced by a deformation step function can be written as:

$$\sigma(\lambda, t) = \overline{G}(t)\, T^e(\lambda)\ . \tag{A.1}$$

Applying the Boltzmann's superposition principle and the chain rule, and considering that the material has initially no residual stresses or deformations:

$$\sigma(t) = \int_0^t \overline{G}(t-\tau)\, \frac{dT^e(\lambda)}{d\lambda}\, \frac{d\lambda(\tau)}{d\tau}\, d\tau \qquad \forall \quad t \in [0, \infty)\ . \tag{A.2}$$

The elastic response function, $T^e(\lambda)$, can be derived from any strain energy function as the stress in a uniaxial test for a given stretch λ. A five terms Prony series was used for the reduced relaxation function, $\overline{G}(t)$:

$$\overline{G}(t) = g_\infty + \sum_{i=1}^{5} g_i\, e^{-t/\tau_i}\ . \tag{A.3}$$

The evolution of λ with time in a test is shown in figure A.1. As the stretch is maintained from time t_0 to the end of the test, the term $d\lambda(\tau)/d\tau$ in equation (A.2) vanishes in this interval. Therefore, equation (A.2) can be simplified as:

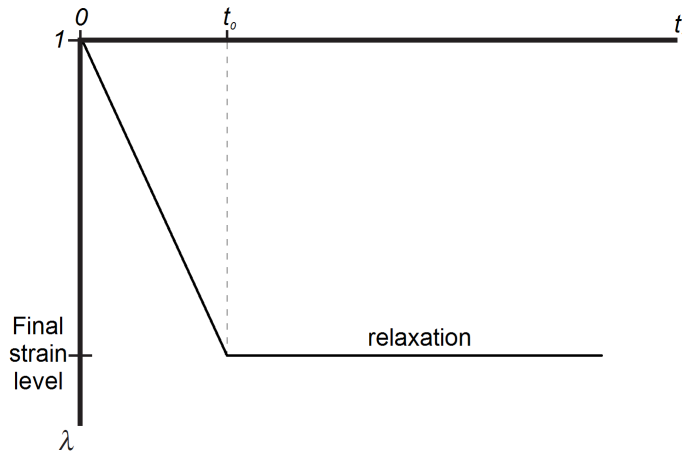

Figure A.1: Evolution of the stretch with time in the relaxation test.

$$\sigma(t) = \int_0^{t_0} \overline{G}(t-\tau)\, \frac{dT^e(\lambda)}{d\lambda}\, \frac{d\lambda(\tau)}{d\tau}\, d\tau \qquad \forall \quad t \in [t_0, \infty)\ . \tag{A.4}$$

From time 0 to t_0, the stretch λ can be expressed in terms of the deformation rate v (in mm/s) as:

$$\lambda(\tau) = 1 + \frac{v}{L}\tau\ , \tag{A.5}$$

with L the initial thickness of the specimen. If equation (A.5) is written in terms of the strain rate v_ε:

$$\lambda(\tau) = 1 + v_\varepsilon \tau\ . \tag{A.6}$$

Therefore, $d\lambda(\tau)/d\tau = v_\varepsilon$ and equation (A.4) can be rewritten as:

$$\sigma(t) = v_\varepsilon \int_0^{t_0} \overline{G}(t-\tau)\, \frac{dT^e(\lambda)}{d\lambda}\, d\tau \qquad \forall \quad t \in [t_0, \infty) \tag{A.7}$$

and introducing equation (A.3) into (A.7):

$$\sigma(t) = v_\varepsilon \int_0^{t_0} \left(g_\infty + \sum_{i=1}^{5} g_i\, e^{-(t-\tau)/\tau_i} \right) \frac{dT^e(\lambda)}{d\lambda}\, d\tau\ , \tag{A.8}$$

$$\sigma(t) = v_\varepsilon\, g_\infty \int_0^{t_0} \frac{dT^e(\lambda)}{d\lambda}\, d\tau\ + v_\varepsilon \sum_{i=1}^{5} \left(g_i\, e^{-t/\tau_i} \int_0^{t_0} e^{\tau/\tau_i}\, \frac{dT^e(\lambda)}{d\lambda}\, d\tau \right)\ . \tag{A.9}$$

Knowing that $dT^e(\lambda)/d\lambda$ depends on λ, and therefore on τ (equation (A.6)), equation (A.9) can be written as:

$$\sigma(t) = v_\varepsilon \sum_{j=1}^{n} \left(g_\infty\, I_{\infty,\,j} + \sum_{i=1}^{5} \left(g_i\, e^{-t/\tau_i}\, I_{i,\,j} \right) \right)\ , \tag{A.10}$$

being n the number of simple terms of $dT^e(\lambda)/d\lambda$ (addends), $I_{\infty,\,j}$ each of the individual integrals multiplied by g_∞ and $I_{i\,j}$ each of the individual integrals multiplied by g_i.

In the following sections, equation (A.10) is particularized for each strain energy function through the definition of $dT^e(\lambda)/d\lambda$ and the integrals will be given.

A.1 Polynomial strain energy function with five terms

For the polynomial strain energy function with five terms, the elastic response function $T^e(\lambda)$ is:

$$T^e_{\text{pol}} = 2C_{10}\left(\lambda^2 - \frac{1}{\lambda}\right) + 2C_{01}\left(\lambda - \frac{1}{\lambda^2}\right) + 6C_{11}\left(\lambda^3 - \lambda^2 - \lambda + \frac{1}{\lambda} + \frac{1}{\lambda^2} - \frac{1}{\lambda^3}\right) + \\ +4C_{20}\left(\lambda^4 - 3\lambda^2 + \lambda + \frac{3}{\lambda} - \frac{2}{\lambda^2}\right) + 4C_{02}\left(2\lambda^2 - 3\lambda - \frac{1}{\lambda} + \frac{3}{\lambda^2} - \frac{1}{\lambda^4}\right), \tag{A.11}$$

and its derivative with respect to λ:

$$\frac{dT^e_{\text{pol}}(\lambda)}{d\lambda} = 2C_{10}\left(2\lambda + \frac{1}{\lambda^2}\right) + 2C_{01}\left(1 + \frac{2}{\lambda^3}\right) + 6C_{11}\left(3\lambda^2 - 2\lambda - 1 - \frac{1}{\lambda^2} - \frac{2}{\lambda^3} + \frac{3}{\lambda^4}\right) + \\ +4C_{20}\left(4\lambda^3 - 6\lambda + 1 - \frac{3}{\lambda^2} + \frac{4}{\lambda^3}\right) + 4C_{02}\left(4\lambda - 3 + \frac{1}{\lambda^2} - \frac{6}{\lambda^3} + \frac{4}{\lambda^5}\right). \tag{A.12}$$

In this case, as equation (A.12) has 20 terms, i.e. $n = 20$, there is a total of 120 integrals in equation (A.10), 20 related to g_∞ and 20 to each g_i. Therefore, only 40 integrals have to be solved from the total of 120, as the rest are obtained just changing i from 1 to 5. Most of these 40 integrals can be directly solved because they have a closed-form solution. However 10 of them, shown below, need to be numerically solved:

$$I_{i,\,2} = \int_0^{t_0} e^{\tau/\tau_i}\, 2C_{10}\frac{1}{\lambda^2}\, d\tau = 2C_{10}\int_0^{t_0} e^{\tau/\tau_i}\frac{1}{(1+v_\varepsilon\tau)^2}\, d\tau = 2C_{10}\, I^{num}_{i,\,1}, \tag{A.13}$$

$$I_{i,\,4} = \int_0^{t_0} e^{\tau/\tau_i}\, 4C_{01}\frac{1}{\lambda^3}\, d\tau = 4C_{01}\int_0^{t_0} e^{\tau/\tau_i}\frac{1}{(1+v_\varepsilon\tau)^3}\, d\tau = 4C_{01}\, I^{num}_{i,\,2}, \tag{A.14}$$

$$I_{i,\,8} = -\int_0^{t_0} e^{\tau/\tau_i}\, 6C_{11}\frac{1}{\lambda^2}\, d\tau = -6C_{11}\int_0^{t_0} e^{\tau/\tau_i}\frac{1}{(1+v_\varepsilon\tau)^2}\, d\tau = -6C_{11}\, I^{num}_{i,\,1}, \tag{A.15}$$

$$I_{i,\,9} = -\int_0^{t_0} e^{\tau/\tau_i}\, 12C_{11}\frac{1}{\lambda^3}\, d\tau = -12C_{11}\int_0^{t_0} e^{\tau/\tau_i}\frac{1}{(1+v_\varepsilon\tau)^3}\, d\tau = -12C_{11}\, I^{num}_{i,\,2}, \tag{A.16}$$

$$I_{i,\,10} = \int_0^{t_0} e^{\tau/\tau_i}\, 18C_{11}\frac{1}{\lambda^4}\, d\tau = 18C_{11}\int_0^{t_0} e^{\tau/\tau_i}\frac{1}{(1+v_\varepsilon\tau)^4}\, d\tau = 18C_{11}\, I^{num}_{i,\,3}, \tag{A.17}$$

$$I_{i,\,14} = -\int_0^{t_0} e^{\tau/\tau_i}\; 12C_{11}\frac{1}{\lambda^2}\; d\tau = -12C_{11}\int_0^{t_0} e^{\tau/\tau_i}\frac{1}{(1+v_\varepsilon\tau)^2}\; d\tau = -12C_{11}\; I_{i,\,1}^{num}\;, \tag{A.18}$$

$$I_{i,\,15} = \int_0^{t_0} e^{\tau/\tau_i}\; 16C_{20}\frac{1}{\lambda^3}\; d\tau = 16C_{20}\int_0^{t_0} e^{\tau/\tau_i}\frac{1}{(1+v_\varepsilon\tau)^3}\; d\tau = 16C_{20}\; I_{i,\,2}^{num}\;, \tag{A.19}$$

$$I_{i,\,18} = \int_0^{t_0} e^{\tau/\tau_i}\; 4C_{02}\frac{1}{\lambda^2}\; d\tau = 4C_{02}\int_0^{t_0} e^{\tau/\tau_i}\frac{1}{(1+v_\varepsilon\tau)^2}\; d\tau = 4C_{02}\; I_{i,\,1}^{num}\;, \tag{A.20}$$

$$I_{i,\,19} = -\int_0^{t_0} e^{\tau/\tau_i}\; 24C_{02}\frac{1}{\lambda^3}\; d\tau = -24C_{02}\int_0^{t_0} e^{\tau/\tau_i}\frac{1}{(1+v_\varepsilon\tau)^3}\; d\tau = -24C_{02}\; I_{i,\,2}^{num}\;, \tag{A.21}$$

$$I_{i,\,20} = \int_0^{t_0} e^{\tau/\tau_i}\; 16C_{02}\frac{1}{\lambda^5}\; d\tau = 16C_{02}\int_0^{t_0} e^{\tau/\tau_i}\frac{1}{(1+v_\varepsilon\tau)^5}\; d\tau = 16C_{02}\; I_{i,\,4}^{num}\;. \tag{A.22}$$

In the above equations, $I_{i,\,k}^{num}$ with $k = 1, 2, 3, 4$, denotes the integrals which finally have to be solved numerically. As can be seen, although 10 integrals have been shown, finally they lead to these four integrals.

A.2 First order Ogden strain energy function

For the first order Ogden strain energy function, the elastic response function $T^e(\lambda)$ is:

$$T_{\mathrm{Og}}^e = \mu\;\left(\lambda^\alpha - \frac{1}{\lambda^{\alpha/2}}\right)\;, \tag{A.23}$$

and its derivative with respect to λ:

$$\frac{dT_{\mathrm{Og}}^e(\lambda)}{d\lambda} = \mu\;\alpha\;\left(\lambda^{\alpha-1} + \frac{1}{2}\;\frac{1}{\lambda^{\alpha/2+1}}\right)\;. \tag{A.24}$$

In this case, as equation (A.24) has only 2 terms, i.e. $n = 2$, there is a total of 12 integrals in equation (A.10), 2 related to g_∞ and 10 to each g_i. Therefore, only 4 integrals have to be solved from the total of 12, as the rest are obtained just changing i from 1 to 5. Then, 2 can be directly solved because they have a closed-form solution and the other 2, shown below, need to be numerically solved:

$$I_{i,\,1} = \int_0^{t_0} e^{\tau/\tau_i}\;\mu\alpha\;\lambda^{\alpha-1}\; d\tau = \mu\alpha\int_0^{t_0} e^{\tau/\tau_i}\;(1+v_\varepsilon\tau)^{\alpha-1}\; d\tau\;, \tag{A.25}$$

$$I_{i,\,2} = \int_0^{t_0} e^{\tau/\tau_i}\;\frac{\mu\alpha}{2}\;\frac{1}{\lambda^{\alpha/2+1}}\; d\tau = \frac{\mu\alpha}{2}\int_0^{t_0} e^{\tau/\tau_i}\;\frac{1}{(1+v_\varepsilon\tau)^{\alpha/2+1}}\; d\tau\;. \tag{A.26}$$

A.3 Isotropic GOH strain energy function

For the isotropic GOH strain energy function, the elastic response function $T^e(\lambda)$ is:

$$T^e_{\mathrm{GOH}} = 2\,\left(C_{10} + k_1\left(\lambda^2 + \frac{2}{\lambda} - 3\right)\,e^{k_2(\lambda^2+\frac{2}{\lambda}-3)^2}\right)\,\left(\lambda^2 - \frac{1}{\lambda}\right)\,, \tag{A.27}$$

and its derivative with respect to λ:

$$\begin{aligned}\frac{dT^e_{\mathrm{GOH}}(\lambda)}{d\lambda} &= 2C_{10}\,\left(2\lambda + \frac{1}{\lambda^2}\right) + 2k_1\,e^{k_2(\lambda^2+\frac{2}{\lambda}-3)^2}\,\left(4\lambda^3 - 6\lambda - \frac{3}{\lambda^2} + \frac{4}{\lambda^3} + 1 + \right.\\ &\left. +2k_2\,\left(2\lambda^7 - 12\lambda^5 + 4\lambda^4 + 18\lambda^3 - 6\lambda - 36 + \frac{36}{\lambda} - \frac{8}{\lambda^2} + \frac{18}{\lambda^3} - \frac{24}{\lambda^4} + \frac{8}{\lambda^5}\right)\right)\,.\end{aligned} \tag{A.28}$$

In this case, as equation (A.28) has 18 terms, i.e. $n = 18$, there is a total of 108 integrals in equation (A.10), 18 related to g_∞ and 18 to each g_i. Therefore, only 36 integrals have to be solved from the total of 108, as the rest are obtained just changing i from 1 to 5. Only 3 of these integrals can be directly solved because they have a closed-form solution. The rest, 33, shown below, need to be numerically solved:

$$I_{\infty,\,3} = \int_0^{t_0} 2k_1\,e^{k_2(\lambda^2+\frac{2}{\lambda}-3)^2}\,4\lambda^3\,d\tau = 8k_1\int_0^{t_0} e^{k_2\left((1+v_\varepsilon\tau)^2+\frac{2}{(1+v_\varepsilon\tau)}-3\right)^2}\,(1+v_\varepsilon\tau)^3\,d\tau = 8k_1\,I^{num}_{\infty,\,1}\,, \tag{A.29}$$

$$\begin{aligned}I_{\infty,\,4} &= -\int_0^{t_0} 2k_1\,e^{k_2(\lambda^2+\frac{2}{\lambda}-3)^2}\,6\lambda\,d\tau = -12k_1\int_0^{t_0} e^{k_2\left((1+v_\varepsilon\tau)^2+\frac{2}{(1+v_\varepsilon\tau)}-3\right)^2}\,(1+v_\varepsilon\tau)\,d\tau = \\ &= -12k_1\,I^{num}_{\infty,\,2}\,,\end{aligned} \tag{A.30}$$

$$\begin{aligned}I_{\infty,\,5} &= -\int_0^{t_0} 2k_1\,e^{k_2(\lambda^2+\frac{2}{\lambda}-3)^2}\,\frac{3}{\lambda^2}\,d\tau = -6k_1\int_0^{t_0} e^{k_2\left((1+v_\varepsilon\tau)^2+\frac{2}{(1+v_\varepsilon\tau)}-3\right)^2}\,\frac{1}{(1+v_\varepsilon\tau)^2}\,d\tau = \\ &= -6k_1\,I^{num}_{\infty,\,3}\,,\end{aligned} \tag{A.31}$$

$$I_{\infty,\,6} = \int_0^{t_0} 2k_1\,e^{k_2(\lambda^2+\frac{2}{\lambda}-3)^2}\,\frac{4}{\lambda^3}\,d\tau = 8k_1\int_0^{t_0} e^{k_2\left((1+v_\varepsilon\tau)^2+\frac{2}{(1+v_\varepsilon\tau)}-3\right)^2}\,\frac{1}{(1+v_\varepsilon\tau)^3}\,d\tau = 8k_1\,I^{num}_{\infty,\,4}\,, \tag{A.32}$$

$$I_{\infty,\,7} = \int_0^{t_0} 2k_1\,e^{k_2(\lambda^2+\frac{2}{\lambda}-3)^2}\,d\tau = 2k_1\int_0^{t_0} e^{k_2\left((1+v_\varepsilon\tau)^2+\frac{2}{(1+v_\varepsilon\tau)}-3\right)^2}\,d\tau = 2k_1\,I^{num}_{\infty,\,5}\,, \tag{A.33}$$

$$I_{\infty,\,8} = \int_0^{t_0} 2k_1\ 2k_2\ e^{k_2(\lambda^2+\frac{2}{\lambda}-3)^2}\ 2\lambda^7\ d\tau = 8k_1\ k_2\ \int_0^{t_0} e^{k_2\left((1+v_\varepsilon\tau)^2+\frac{2}{(1+v_\varepsilon\tau)}-3\right)^2}\ (1+v_\varepsilon\tau)^7\ d\tau =$$
$$= 8k_1\ k_2\ I^{num}_{\infty,\,6}\ , \tag{A.34}$$

$$I_{\infty,\,9} = -\int_0^{t_0} 2k_1\ 2k_2\ e^{k_2(\lambda^2+\frac{2}{\lambda}-3)^2}\ 12\lambda^5\ d\tau =$$
$$= -48k_1\ k_2\ \int_0^{t_0} e^{k_2\left((1+v_\varepsilon\tau)^2+\frac{2}{(1+v_\varepsilon\tau)}-3\right)^2}\ (1+v_\varepsilon\tau)^5\ d\tau = -48k_1\ k_2\ I^{num}_{\infty,\,7}\ , \tag{A.35}$$

$$I_{\infty,\,10} = \int_0^{t_0} 2k_1\ 2k_2\ e^{k_2(\lambda^2+\frac{2}{\lambda}-3)^2}\ 4\lambda^4\ d\tau =$$
$$= 16k_1\ k_2\ \int_0^{t_0} e^{k_2\left((1+v_\varepsilon\tau)^2+\frac{2}{(1+v_\varepsilon\tau)}-3\right)^2}\ (1+v_\varepsilon\tau)^4\ d\tau = 16k_1\ k_2\ I^{num}_{\infty,\,8}\ , \tag{A.36}$$

$$I_{\infty,\,11} = \int_0^{t_0} 2k_1\ 2k_2\ e^{k_2(\lambda^2+\frac{2}{\lambda}-3)^2}\ 18\lambda^3\ d\tau =$$
$$= 72k_1\ k_2\ \int_0^{t_0} e^{k_2\left((1+v_\varepsilon\tau)^2+\frac{2}{(1+v_\varepsilon\tau)}-3\right)^2}\ (1+v_\varepsilon\tau)^3\ d\tau = 72k_1\ k_2\ I^{num}_{\infty,\,1}\ , \tag{A.37}$$

$$I_{\infty,\,12} = -\int_0^{t_0} 2k_1\ 2k_2\ e^{k_2(\lambda^2+\frac{2}{\lambda}-3)^2}\ 6\lambda\ d\tau =$$
$$= -24k_1\ k_2\ \int_0^{t_0} e^{k_2\left((1+v_\varepsilon\tau)^2+\frac{2}{(1+v_\varepsilon\tau)}-3\right)^2}\ (1+v_\varepsilon\tau)\ d\tau = -24k_1\ k_2\ I^{num}_{\infty,\,2}\ , \tag{A.38}$$

$$I_{\infty,\,13} = -\int_0^{t_0} 2k_1\ 2k_2\ e^{k_2(\lambda^2+\frac{2}{\lambda}-3)^2}\ 36\ d\tau =$$
$$= -144k_1\ k_2\ \int_0^{t_0} e^{k_2\left((1+v_\varepsilon\tau)^2+\frac{2}{(1+v_\varepsilon\tau)}-3\right)^2}\ d\tau = -144k_1\ k_2\ I^{num}_{\infty,\,5}\ , \tag{A.39}$$

$$I_{\infty,\,14} = \int_0^{t_0} 2k_1\ 2k_2\ e^{k_2(\lambda^2+\frac{2}{\lambda}-3)^2}\ \frac{36}{\lambda}\ d\tau =$$
$$= 144k_1\ k_2\ \int_0^{t_0} e^{k_2\left((1+v_\varepsilon\tau)^2+\frac{2}{(1+v_\varepsilon\tau)}-3\right)^2}\ \frac{1}{(1+v_\varepsilon\tau)}\ d\tau = 144k_1\ k_2\ I^{num}_{\infty,\,9}\ , \tag{A.40}$$

$$I_{\infty,\,15} = -\int_0^{t_0} 2k_1\ 2k_2\ e^{k_2(\lambda^2+\frac{2}{\lambda}-3)^2}\ \frac{8}{\lambda^2}\ d\tau =$$
$$= -32k_1\ k_2\ \int_0^{t_0} e^{k_2\left((1+v_\varepsilon\tau)^2+\frac{2}{(1+v_\varepsilon\tau)}-3\right)^2}\ \frac{1}{(1+v_\varepsilon\tau)^2}\ d\tau = -32k_1\ k_2\ I^{num}_{\infty,\,3}\ , \tag{A.41}$$

$$I_{\infty,\,16} = \int_0^{t_0} 2k_1\; 2k_2\; e^{k_2(\lambda^2+\frac{2}{\lambda}-3)^2}\; \frac{18}{\lambda^3}\; d\tau = \\ = 72k_1\; k_2\; \int_0^{t_0} e^{k_2\left((1+v_\varepsilon\tau)^2+\frac{2}{(1+v_\varepsilon\tau)}-3\right)^2}\; \frac{1}{(1+v_\varepsilon\tau)^3}\; d\tau = 72k_1\; k_2\; I^{num}_{\infty,\,4}\;, \tag{A.42}$$

$$I_{\infty,\,17} = -\int_0^{t_0} 2k_1\; 2k_2\; e^{k_2(\lambda^2+\frac{2}{\lambda}-3)^2}\; \frac{24}{\lambda^4}\; d\tau = \\ = -96k_1\; k_2\; \int_0^{t_0} e^{k_2\left((1+v_\varepsilon\tau)^2+\frac{2}{(1+v_\varepsilon\tau)}-3\right)^2}\; \frac{1}{(1+v_\varepsilon\tau)^4}\; d\tau = -96k_1\; k_2\; I^{num}_{\infty,\,10}\;, \tag{A.43}$$

$$I_{\infty,\,18} = \int_0^{t_0} 2k_1\; 2k_2\; e^{k_2(\lambda^2+\frac{2}{\lambda}-3)^2}\; \frac{8}{\lambda^5}\; d\tau = \\ = 32k_1\; k_2\; \int_0^{t_0} e^{k_2\left((1+v_\varepsilon\tau)^2+\frac{2}{(1+v_\varepsilon\tau)}-3\right)^2}\; \frac{1}{(1+v_\varepsilon\tau)^5}\; d\tau = 32k_1\; k_2\; I^{num}_{\infty,\,11}\;, \tag{A.44}$$

$$I_{i,\,2} = \int_0^{t_0} e^{\tau/\tau_i}\; 2C_{10}\; \frac{1}{\lambda^2}\; d\tau = 2C_{10}\; \int_0^{t_0} e^{\tau/\tau_i}\; \frac{1}{(1+v_\varepsilon\tau)^2}\; d\tau = 2C_{10}\; I^{num}_{i,\,1}\;, \tag{A.45}$$

$$I_{i,\,3} = \int_0^{t_0} e^{\tau/\tau_i}\; 2k_1\; e^{k_2(\lambda^2+\frac{2}{\lambda}-3)^2}\; 4\lambda^3\; d\tau = \\ = 8k_1\; \int_0^{t_0} e^{\tau/\tau_i} e^{k_2\left((1+v_\varepsilon\tau)^2+\frac{2}{(1+v_\varepsilon\tau)}-3\right)^2}\; (1+v_\varepsilon\tau)^3\; d\tau = 8k_1\; I^{num}_{i,\,2}\;, \tag{A.46}$$

$$I_{i,\,4} = -\int_0^{t_0} e^{\tau/\tau_i}\; 2k_1\; e^{k_2(\lambda^2+\frac{2}{\lambda}-3)^2}\; 6\lambda\; d\tau = \\ = -12k_1\; \int_0^{t_0} e^{\tau/\tau_i} e^{k_2\left((1+v_\varepsilon\tau)^2+\frac{2}{(1+v_\varepsilon\tau)}-3\right)^2}\; (1+v_\varepsilon\tau)\; d\tau = -12k_1\; I^{num}_{i,\,3}\;, \tag{A.47}$$

$$I_{i,\,5} = -\int_0^{t_0} e^{\tau/\tau_i}\; 2k_1\; e^{k_2(\lambda^2+\frac{2}{\lambda}-3)^2}\; \frac{3}{\lambda^2}\; d\tau = \\ = -6k_1 \int_0^{t_0} e^{\tau/\tau_i}\; e^{k_2\left((1+v_\varepsilon\tau)^2+\frac{2}{(1+v_\varepsilon\tau)}-3\right)^2}\; \frac{1}{(1+v_\varepsilon\tau)^2}\; d\tau = -6k_1\; I^{num}_{i,\,4}\;, \tag{A.48}$$

$$I_{i,\,6} = \int_0^{t_0} e^{\tau/\tau_i}\; 2k_1\; e^{k_2(\lambda^2+\frac{2}{\lambda}-3)^2}\; \frac{4}{\lambda^3}\; d\tau = \\ = 8k_1 \int_0^{t_0} e^{\tau/\tau_i}\; e^{k_2\left((1+v_\varepsilon\tau)^2+\frac{2}{(1+v_\varepsilon\tau)}-3\right)^2}\; \frac{1}{(1+v_\varepsilon\tau)^3}\; d\tau = 8k_1\; I^{num}_{i,\,5}\;, \tag{A.49}$$

$$I_{i,\,7} = \int_0^{t_0} e^{\tau/\tau_i}\; 2k_1\; e^{k_2(\lambda^2+\frac{2}{\lambda}-3)^2}\; d\tau = 2k_1 \int_0^{t_0} e^{\tau/\tau_i}\; e^{k_2\left((1+v_\varepsilon\tau)^2+\frac{2}{(1+v_\varepsilon\tau)}-3\right)^2}\; d\tau = 2k_1\; I^{num}_{i,\,6}\;, \tag{A.50}$$

$$I_{i,\,8} = \int_0^{t_0} e^{\tau/\tau_i}\; 2k_1\; 2k_2\; e^{k_2(\lambda^2+\frac{2}{\lambda}-3)^2}\; 2\lambda^7\; d\tau =$$
$$= 8k_1\; k_2\; \int_0^{t_0} e^{\tau/\tau_i}\; e^{k_2\left((1+v_\varepsilon\tau)^2+\frac{2}{(1+v_\varepsilon\tau)}-3\right)^2}\; (1+v_\varepsilon\tau)^7\; d\tau = 8k_1\; k_2\; I_{i,\,7}^{num}\;, \tag{A.51}$$

$$I_{i,\,9} = -\int_0^{t_0} e^{\tau/\tau_i}\; 2k_1\; 2k_2\; e^{k_2(\lambda^2+\frac{2}{\lambda}-3)^2}\; 12\lambda^5\; d\tau =$$
$$= -48k_1\; k_2\; \int_0^{t_0} e^{\tau/\tau_i}\; e^{k_2\left((1+v_\varepsilon\tau)^2+\frac{2}{(1+v_\varepsilon\tau)}-3\right)^2}\; (1+v_\varepsilon\tau)^5\; d\tau = -48k_1\; k_2\; I_{i,\,8}^{num}\;, \tag{A.52}$$

$$I_{i,\,10} = \int_0^{t_0} e^{\tau/\tau_i}\; 2k_1\; 2k_2\; e^{k_2(\lambda^2+\frac{2}{\lambda}-3)^2}\; 4\lambda^4\; d\tau =$$
$$= 16k_1\; k_2\; \int_0^{t_0} e^{\tau/\tau_i}\; e^{k_2\left((1+v_\varepsilon\tau)^2+\frac{2}{(1+v_\varepsilon\tau)}-3\right)^2}\; (1+v_\varepsilon\tau)^4\; d\tau = 16k_1\; k_2\; I_{i,\,9}^{num}\;, \tag{A.53}$$

$$I_{i,\,11} = \int_0^{t_0} e^{\tau/\tau_i}\; 2k_1\; 2k_2\; e^{k_2(\lambda^2+\frac{2}{\lambda}-3)^2}\; 18\lambda^3\; d\tau =$$
$$= 72k_1\; k_2\; \int_0^{t_0} e^{\tau/\tau_i}\; e^{k_2\left((1+v_\varepsilon\tau)^2+\frac{2}{(1+v_\varepsilon\tau)}-3\right)^2}\; (1+v_\varepsilon\tau)^3\; d\tau = 72k_1\; k_2\; I_{i,\,2}^{num}\;, \tag{A.54}$$

$$I_{i,\,12} = -\int_0^{t_0} e^{\tau/\tau_i}\; 2k_1\; 2k_2\; e^{k_2(\lambda^2+\frac{2}{\lambda}-3)^2}\; 6\lambda\; d\tau =$$
$$= -24k_1\; k_2\; \int_0^{t_0} e^{\tau/\tau_i}\; e^{k_2\left((1+v_\varepsilon\tau)^2+\frac{2}{(1+v_\varepsilon\tau)}-3\right)^2}\; (1+v_\varepsilon\tau)\; d\tau = -24k_1\; k_2\; I_{i,\,3}^{num}\;, \tag{A.55}$$

$$I_{i,\,13} = -\int_0^{t_0} e^{\tau/\tau_i}\; 2k_1\; 2k_2\; e^{k_2(\lambda^2+\frac{2}{\lambda}-3)^2}\; 36\; d\tau =$$
$$= -144k_1\; k_2\; \int_0^{t_0} e^{\tau/\tau_i}\; e^{k_2\left((1+v_\varepsilon\tau)^2+\frac{2}{(1+v_\varepsilon\tau)}-3\right)^2}\; d\tau = -144k_1\; k_2\; I_{i,\,6}^{num}\;, \tag{A.56}$$

$$I_{i,\,14} = \int_0^{t_0} e^{\tau/\tau_i}\; 2k_1\; 2k_2\; e^{k_2(\lambda^2+\frac{2}{\lambda}-3)^2}\; \frac{36}{\lambda}\; d\tau =$$
$$= 144k_1\; k_2\; \int_0^{t_0} e^{\tau/\tau_i}\; e^{k_2\left((1+v_\varepsilon\tau)^2+\frac{2}{(1+v_\varepsilon\tau)}-3\right)^2}\; \frac{1}{(1+v_\varepsilon\tau)}\; d\tau = 144k_1\; k_2\; I_{i,\,10}^{num}\;, \tag{A.57}$$

$$I_{i,\,15} = -\int_0^{t_0} e^{\tau/\tau_i}\; 2k_1\; 2k_2\; e^{k_2(\lambda^2+\frac{2}{\lambda}-3)^2}\; \frac{8}{\lambda^2}\; d\tau =$$
$$= -32k_1\; k_2\; \int_0^{t_0} e^{\tau/\tau_i}\; e^{k_2\left((1+v_\varepsilon\tau)^2+\frac{2}{(1+v_\varepsilon\tau)}-3\right)^2}\; \frac{1}{(1+v_\varepsilon\tau)^2}\; d\tau = -32k_1\; k_2\; I_{i,\,4}^{num}\;, \tag{A.58}$$

$$I_{i,\,16} = \int_0^{t_0} e^{\tau/\tau_i}\; 2k_1\; 2k_2\; e^{k_2(\lambda^2+\frac{2}{\lambda}-3)^2}\; \frac{18}{\lambda^3}\; d\tau = \\ = 72k_1\; k_2 \int_0^{t_0} e^{\tau/\tau_i}\; e^{k_2\left((1+v_\varepsilon\tau)^2+\frac{2}{(1+v_\varepsilon\tau)}-3\right)^2}\; \frac{1}{(1+v_\varepsilon\tau)^3}\; d\tau = 72k_1\; k_2\; I^{num}_{i,\,5}\;, \tag{A.59}$$

$$I_{i,\,17} = -\int_0^{t_0} e^{\tau/\tau_i}\; 2k_1\; 2k_2\; e^{k_2(\lambda^2+\frac{2}{\lambda}-3)^2}\; \frac{24}{\lambda^4}\; d\tau = \\ = -96k_1\; k_2 \int_0^{t_0} e^{\tau/\tau_i}\; e^{k_2\left((1+v_\varepsilon\tau)^2+\frac{2}{(1+v_\varepsilon\tau)}-3\right)^2}\; \frac{1}{(1+v_\varepsilon\tau)^4}\; d\tau = -96k_1\; k_2\; I^{num}_{i,\,11}\;, \tag{A.60}$$

$$I_{i,\,18} = \int_0^{t_0} e^{\tau/\tau_i}\; 2k_1\; 2k_2\; e^{k_2(\lambda^2+\frac{2}{\lambda}-3)^2}\; \frac{8}{\lambda^5}\; d\tau = \\ = 32k_1\; k_2 \int_0^{t_0} e^{\tau/\tau_i}\; e^{k_2\left((1+v_\varepsilon\tau)^2+\frac{2}{(1+v_\varepsilon\tau)}-3\right)^2}\; \frac{1}{(1+v_\varepsilon\tau)^5}\; d\tau = 32k_1\; k_2\; I^{num}_{i,\,12}\;. \tag{A.61}$$

In the above equations, $I^{num}_{\infty,\,k}$ with $k = 1, ..., 11$ and $I^{num}_{i,\,l}$ with $l = 1, ..., 12$, denote the integrals which finally have to be solved numerically. As can be seen, although 33 integrals have been shown, finally they lead to these 23 integrals.

A.4 Combination of a neo-Hookean strain energy function and an exponential one

For the combination of a neo-Hookean strain energy function and an exponential one, the elastic response function $T^e(\lambda)$ is:

$$T^e_{\text{exp}} = 2\; \left(C_{10} + k_1\; e^{k_2(\lambda^2+\frac{2}{\lambda}-3)}\right)\; \left(\lambda^2 - \frac{1}{\lambda}\right)\;, \tag{A.62}$$

and its derivative with respect to λ:

$$\frac{dT^e_{\text{exp}}(\lambda)}{d\lambda} = 2C_{10}\left(2\lambda + \frac{1}{\lambda^2}\right) + 2k_1\; e^{k_2(\lambda^2+\frac{2}{\lambda}-3)}\left(2\lambda + \frac{1}{\lambda^2} + k_2\left(2\lambda^3 + \frac{2}{\lambda^3} - 4\right)\right)\;. \tag{A.63}$$

In this case, as equation (A.63) has 7 terms, i.e. $n = 7$, there is a total of 42 integrals in equation (A.10), 7 related to g_∞ and 7 to each g_i. Therefore, only 14 integrals have to be solved from the total of 42, as the rest are obtained just changing i from 1 to 5. Only 3 of these integrals can be directly solved because they have a closed-form solution. The rest, 11, shown below, need to be numerically solved:

$$I_{\infty,\,3} = \int_0^{t_0} 2k_1\; e^{k_2(\lambda^2+\frac{2}{\lambda}-3)}\; 2\lambda\; d\tau = 4k_1 \int_0^{t_0} e^{k_2\left((1+v_\varepsilon\tau)^2+\frac{2}{(1+v_\varepsilon\tau)}-3\right)}\; (1+v_\varepsilon\tau)\; d\tau\;, \tag{A.64}$$

$$I_{\infty,4} = \int_0^{t_0} 2k_1\, e^{k_2(\lambda^2+\frac{2}{\lambda}-3)}\, \frac{1}{\lambda^2}\, d\tau = 2k_1 \int_0^{t_0} e^{k_2\left((1+v_\varepsilon\tau)^2+\frac{2}{(1+v_\varepsilon\tau)}-3\right)}\, \frac{1}{(1+v_\varepsilon\tau)^2}\, d\tau\,, \tag{A.65}$$

$$I_{\infty,5} = \int_0^{t_0} 2k_1\, k_2\, e^{k_2(\lambda^2+\frac{2}{\lambda}-3)}\, 2\lambda^3\, d\tau = 4k_1\, k_2 \int_0^{t_0} e^{k_2\left((1+v_\varepsilon\tau)^2+\frac{2}{(1+v_\varepsilon\tau)}-3\right)}\, (1+v_\varepsilon\tau)^3\, d\tau\,, \tag{A.66}$$

$$I_{\infty,6} = \int_0^{t_0} 2k_1\, k_2\, e^{k_2(\lambda^2+\frac{2}{\lambda}-3)}\, \frac{2}{\lambda^3}\, d\tau = 4k_1\, k_2 \int_0^{t_0} e^{k_2\left((1+v_\varepsilon\tau)^2+\frac{2}{(1+v_\varepsilon\tau)}-3\right)}\, \frac{1}{(1+v_\varepsilon\tau)^3}\, d\tau\,, \tag{A.67}$$

$$I_{\infty,7} = -\int_0^{t_0} 2k_1\, k_2\, e^{k_2(\lambda^2+\frac{2}{\lambda}-3)}\, 4\, d\tau = -8k_1\, k_2 \int_0^{t_0} e^{k_2\left((1+v_\varepsilon\tau)^2+\frac{2}{(1+v_\varepsilon\tau)}-3\right)}\, d\tau\,, \tag{A.68}$$

$$I_{i,2} = \int_0^{t_0} e^{\tau/\tau_i}\, 2C_{10}\, \frac{1}{\lambda^2}\, d\tau = 2C_{10} \int_0^{t_0} e^{\tau/\tau_i}\, \frac{1}{(1+v_\varepsilon\tau)^2}\, d\tau\,, \tag{A.69}$$

$$I_{i,3} = \int_0^{t_0} e^{\tau/\tau_i}\, 2k_1\, e^{k_2(\lambda^2+\frac{2}{\lambda}-3)}\, 2\lambda\, d\tau = 4k_1 \int_0^{t_0} e^{\tau/\tau_i}\, e^{k_2\left((1+v_\varepsilon\tau)^2+\frac{2}{(1+v_\varepsilon\tau)}-3\right)}\, (1+v_\varepsilon\tau)\, d\tau\,, \tag{A.70}$$

$$I_{i,4} = \int_0^{t_0} e^{\tau/\tau_i}\, 2k_1\, e^{k_2(\lambda^2+\frac{2}{\lambda}-3)}\, \frac{1}{\lambda^2}\, d\tau = 2k_1 \int_0^{t_0} e^{\tau/\tau_i}\, e^{k_2\left((1+v_\varepsilon\tau)^2+\frac{2}{(1+v_\varepsilon\tau)}-3\right)}\, \frac{1}{(1+v_\varepsilon\tau)^2}\, d\tau\,, \tag{A.71}$$

$$I_{i,5} = \int_0^{t_0} e^{\tau/\tau_i}\, 2k_1\, k_2\, e^{k_2(\lambda^2+\frac{2}{\lambda}-3)}\, 2\lambda^3\, d\tau = 4k_1\, k_2 \int_0^{t_0} e^{\tau/\tau_i}\, e^{k_2\left((1+v_\varepsilon\tau)^2+\frac{2}{(1+v_\varepsilon\tau)}-3\right)}\, (1+v_\varepsilon\tau)^3\, d\tau\,, \tag{A.72}$$

$$\begin{aligned} I_{i,6} &= \int_0^{t_0} e^{\tau/\tau_i}\, 2k_1\, k_2\, e^{k_2(\lambda^2+\frac{2}{\lambda}-3)}\, \frac{2}{\lambda^3}\, d\tau = \\ &= 4k_1\, k_2 \int_0^{t_0} e^{\tau/\tau_i}\, e^{k_2\left((1+v_\varepsilon\tau)^2+\frac{2}{(1+v_\varepsilon\tau)}-3\right)}\, \frac{1}{(1+v_\varepsilon\tau)^3}\, d\tau\,, \end{aligned} \tag{A.73}$$

$$I_{i,7} = -\int_0^{t_0} e^{\tau/\tau_i}\, 2k_1\, k_2\, e^{k_2(\lambda^2+\frac{2}{\lambda}-3)}\, 4\, d\tau = -8k_1\, k_2 \int_0^{t_0} e^{\tau/\tau_i}\, e^{k_2\left((1+v_\varepsilon\tau)^2+\frac{2}{(1+v_\varepsilon\tau)}-3\right)}\, d\tau\,. \tag{A.74}$$

Appendix B

Safety manual

Introduction

Welcome to the Biomechanics Lab! Before you can begin working, there are many things to learn. This manual is not only to make things better and safer for you, but also for your co-workers. So take a few minutes to read it and hopefully most of your questions will be answered. Don't forget to keep it somewhere handy in case you have any problems in the future. Also, feel free to call or e-mail the laboratory, department or university staff if any matter of urgency pops up.

Thanks,

The Management

Motivation

The motivation of this manual is to establish some rules and techniques which aim is to keep you and everyone who works in the laboratory safe.

Your health is the most important concern at the Biomechanics Lab. There is a chance of transmitting infectious diseases (including Hep B and C, HIV, and staphylococcus) due to our work with human samples. This possibility is remote, because all the received specimens have been tested and we only work with those in which all the serological results are negative for those diseases. Even so, every precaution must be taken and we will always work in the lab maximizing the safety measures, because they will keep you safe and protect your co-workers as well. Additionally, any activity carried out in the lab will show the proper respect for the specimens as people have been generous to donate part of their bodies to science. As such, we must not abuse, waste, or desecrate them.

Universal precaution

Because of the threat of infectious disease, our lab works under the guidance of universal precaution. This means that even though our specimens have tested negative for certain diseases, we still handle them as if they were positive or unknown.

All human tissue or fluids should be assumed contaminated with pathogens: HIV and HBV. Protect yourself accordingly!

This means that we always wear latex or nitrile gloves when handling the specimens. Additionally, the tissues should be handled in designated areas only (the biomechanics lab) and should never contact the skin. **No food or drink permitted in these areas**.

Vaccinations

Please let us know the contact information of someone who is close to you. This will allow us to inform him in the event of an accident (unlikely if the safety measures are followed). Additionally, **everyone** that has to handle fresh human specimens has to get a Hep B vaccination. Please contact to the laboratory management if you are not vaccinated, to manage it with the Hospital.

The Hep B vaccination is administered in 3 doses. The 2^{nd} and 3^{rd} doses are given 1 and 3 months after the 1^{st} one respectively. While the 2^{nd} one has not been administered, the subject will not be considered vaccinated and he will not be allowed to manipulate human samples.

Biohazard materials

Biohazardous materials are considered to be fresh human tissue and anything that comes into contact with it. Biohazard waste (including the gloves, masks and lab coats) must be thrown in the red bin. **Never put them in the regular (black/grey) bin**. Additionally, any liquid that touches fresh human tissue must be bleached (10% bleach solution) for at least 10 minutes. Then it can be safely poured down the sinks.

Fixed (chemically preserved, normally in formaldehyde) and animal tissues are considered non-biohazardous material, but gloves are still a good idea to avoid a dirty mess. You can safely dispose of these tissues and the gloves that touch them in the regular garbage (black/grey). The liquids associated with them can be poured directly down the sink as well.

Handling biohazard

From now on, we refer as "dirty" to any person or object which has been in direct touch with the samples, and as "clean" to the contrary.

Generally, we will handle all specimens using gloves and lab coats and we will work on absorbent pads. For particularly messy operations, safety glasses, masks and hair nets are available. When in doubt, just protect you and your clothing and everyone will be okay. Please only use gloves once, we'll buy more. Safety first, always!

Use of Equipment

We have lots of equipment in this lab. You don't need to learn how to use all of them, but you will definitely use some of them. The best way to figure out how to use something is to look to see if a manual has been written for what you hope to use. These are normally located on the bookshelf in the office of the technicians responsible of the general mechanics. If not, they will know where they are.

If a manual is not available, the next best option is to find a grad student or a staff member of the department who is familiar with the equipment and get a lesson on how to use it. It is better to have someone else around the first times you use something new. Some of the larger equipment, like the MTS Minibionix hydraulic push-pull machine, are extremely dangerous (and expensive) and they should only be used by experienced people and under close supervision.

"Clean person - Dirty person" rule

Try to work in pairs in the laboratory. In this way, one person will work as "dirty", being in charge of the samples manipulation. The other one will be "clean", to the extent possible, and he will be in charge of:

1. Take notes in the lab notebook, which will always be clean.

2. Use the computer, which will always be clean.

3. Help the dirty person to avoid his contact with the areas in the lab considered as clean.

Doing so your work will be simplified, but it is not always possible to follow this procedure. If there is only one person available to work in the lab, he can apply the same rule to each hand, thus having one clean hand and one dirty hand. This is not always possible either. But don't worry, if you have to use both hands to manipulate a sample, go ahead. Afterwards, if you need to touch something clean and both your gloves are dirty, change them, we will buy more! **NEVER ECONOMIZE GLOVES. DON'T BE STINGY WHEN SAFETY IS CONCERNED**.

Areas inside the lab

Inside the laboratory it is important to distinguish two areas: a clean area, from the entry to the partition, and a dirty area, behind the partition. Make sure to take all the dirty clothes off and to throw it to the appropriate bin before passing to the clean area.

The unique exception to this rule is the freezers area. They are considered clean, but inside them there are some dirty shelves (currently, the upper shelf of the -20°C freezer). Use the "clean person – dirty person" rule (or hands) to keep your samples inside the freezer. But never touch the exterior of the freezers with dirty hands.

This is not only applicable to the freezer but also to any other furniture, machine or similar placed in the clean area or to some elements, as the computer, which should be always clean. Try not to touch or rub anything. But if you have touched something, don't worry. There is not anything that can not be disinfected, **BUT DO NOT FORGET TO DO IT**.

NEVER GO OUT OF THE LAB WITH THE PROTECTION CLOTHES. The unique exception to this rule is when throwing out the rubbish to the rubbish bin at the street. In this case, you should use one glove to carry the bag.

If you have to disinfect the computer, be meticulous but cautious. It can be cleaned with a 10% bleach solution but not soaking it. Use less quantity of liquid in this case.

The red bin is only for dirty wastes. Do not use the cover, just for convenience. It will be kept in the area where the cleaning products are stored. This bin must be always emptied at the end of the working day, regardless of the quantity of wastes.

Air circulation

As the lab is not equipped with a fume hood, please open the windows when needed. This should be used when working with chemicals that have fumes or are dangerous when inhaled (i.e. mixing PMMA, acetone) and when using the autopsy saw or Dremel tool to cut bone, because bone dust should not be breathed.

Disposal

- **Biohazard**: put into the red bin.

- **Non-biohazard**: put into the black/grey bin for disposal.

- **Sharps**: put into the red plastic container by the sink. Sharps containers must be tightly closed and changed once their contents are over the fill line. When full, call the waste control service (954485747).

- **Chemicals**: pour them into the proper place.
- **Liquids**: pour them down the sink for non-biohazard; bleach them for 10 minutes and then pour them down the sink for biohazard.

Clean up

In general, wipe down everything after you use something and wash up all the tools you have used. When done, put everything in their places. Please help us to maintain the order in the lab! However, when using biohazardous material, there are extra steps you must take to ensure everyone's safety.

1. Take the spray bottle of 10% bleach and spray down the area where the work was performed.
2. For tools you can either spray them or get a bucket and fill it with a 10% bleach solution.

3. For 1. and 2. let the bleach sit for at least 10 minutes to effectively disinfect.

4. Wipe off the bleach and spray or wash with fresh water.

5. Wipe off the water and completely dry all areas and tools.

Specimen labelling and storage

Every specimen needs to be labelled for identification purposes. It is even more important if we are going to storage them. We keep every specimen into a bottle and write on it the identification label with a permanent marker. If we do not have more bottles or you can not find any, please ask the Management for more. On each label, fill in all possible information to determine the specimen. Then, put the bottles into the freezer. In case you are carrying out a group of experiments and the specimens can be grouped in some way (for example, extraction day or similar), keep the bottles into a freezer plastic bag, with the corresponding identification which characterise the group.

Example of specimen label: DATM-01-CRD-28052013-01

- **Specimen type**: for example, "**D**isco de la **A**rticulación **T**emporo-**M**andibular".
- **Subject number**: for example, subject number one of a certain day.
- **Subject type**: for example, "**C**e**RD**o". In case of a human specimen, write **HUM**.
- **Date**: format ddmmaaaa
- **Specimen number**: in case several specimens are extracted from the same subject.
- **Notes**

Labels for human specimens will be of red colour, whereas labels for the rest of specimens will be of black colour.

In case of any accident or injury

Inform immediately the Management or the technicians responsible of the general mechanics laboratory. In the case of an emergency, call 112 for help, and if needed, the service of toxicology information (915629420). For cuts and abrasions, flush with the shower letting the blood flow and after 2 or 3 minutes, flush with hydrogen peroxide. Then, report to the Management and go to the hospital to get it checked out. For chemical contact with the body, flush with abundant water. Then, report to Management and go to the hospital for examination. In any case, give written notice to the service of health and safety at work of the University of Seville (954486163 - 954551582).

Chemical information

- **Chemical code**: Chemicals are classified in a different way depending on the standard. In Spain, warnings about the chemical product are usually on its label. In other standards, as the NFPA (United States), chemical products are classified by a colour code in the label.

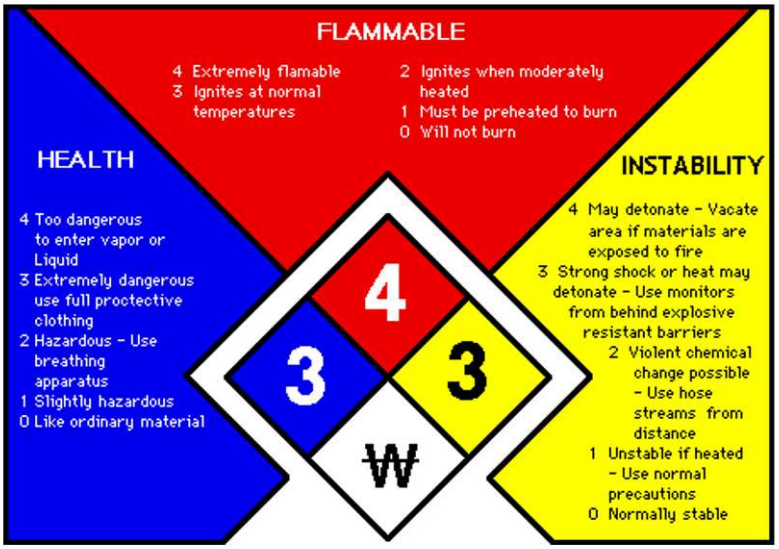

The colours indicate:

Red = flammable. Other labels:

Blue = toxic-health hazard if ingested, inhaled, or absorbed through skin. Other labels:

Yellow = reactive or oxidizing. It may react violently with air, water, or other substances. Keep it away from flammable substances and combustibles. Other labels:

White = corrosive. It may harm skin, eyes and mucous membranes. Store it away from red, blue, and yellow chemicals. Other labels:

Grey = moderate hazard.

- Labelling

  Labelling is especially important for chemical solutions that are made in the lab. All new chemical containers should be labelled with:

  1. Content.

2. Chemical concentration.

3. Chemical colour code or risks indication.

- Chemical waste disposal

  Most of the chemicals used in the lab cannot be disposed of down the sink drain. For disposal purposes, contact the waste control service of the University of Seville (954485747). Meanwhile, keep them in an appropriate container and maintain them closed and away from the work area.

Work in progress

As a general rule, the door of the lab must be always closed when working with human samples, and outside on the door we will put the international sign for biohazard materials. Exceptionally, the door will be half-closed if the air circulation in the room is needed for security reasons. In this case, the biohazard sign should be clearly shown outside.

Any person not related with the experimental tests should avoid going inside the room, to the extent possible. He will knock the door with progressive intensity to avoid shocks and he will only be able to go inside when the people working in the room authorise him. If he goes inside without permission, he should know that he is doing so under his own responsibility and that he is not only risking himself but also the rest of the lab staff.

We understand that sometimes you need to leave the lab for a little bit (lunch, for example) and have to leave your work out for a little bit. However, to protect you, your co-workers and your specimens, there are guidelines to this. You do not want to leave specimens out for too long because they will degrade and may cause an unpleasant odour. If you are leaving for more than 2 hours, then just clean up and put everything

away and continue your experiment in another moment. If it will be less than 2 hours that you will be away, put up a Work in Progress (WIP) sign and lock the door. Write WIP, your name, the time you left and whether the tissue is fresh human or not (so people will know what precautions they have to take when working around it). In any case, the staff members who are not related with the experiments will never go inside the room while the WIP sign is on the door.

As a general rule, you should do a more exhaustive cleaning of the dirty area all Fridays and/or the last working day, if the next day another person, not related with human specimen tests, is going to use the lab.

Outsiders

We get some visitors and people that collaborate with us. They need to read this manual and follow everything which is said in it. Until they get enough training and approval, all outsiders should be supervised. There should always be at least one lab member in charge of these guests of our lab. Guests should be told that they should ask for permission, generally from Dr. Jaime Domínguez or Dr. Javier Martínez Reina, to use any lab equipment. In addition, **there should be no visitors/guests in the lab, whether supervised or not, outside of normal working hours (8 am-8 pm Mon-Fri)**, unless a one-time clearance is given by Dr. Jaime Domínguez.

Computer security

All computer workstations are password protected. Ask for them to the Management or the technicians responsible of the general mechanics laboratory. Lab policy requires that you turn off the computer at the end of each working day.

Phone numbers

Here are a summary of some phone numbers you may need.

Bibliography

[1] McPherson K, Steel CM, Dixon JM. ABC of breast diseases: Breast cancer - epidemiology, risks factors and genetics. *British Medical Journal* 2000; **321**:624–628.

[2] International Agency for Research on Cancer. Globocan 2012: Estimated cancer incidence, mortality and prevalence worldwide 2012.

[3] Azar FS, Metaxas DN, Schnall MD. A deformable finite element model of the breast for predicting mechanical deformations under external perturbations. *Academic Radiology* 2001; **8**:965–975.

[4] Pianigiani S, Ruggiero L, Innocenti B. An anthropometric-based subject-specific finite element model for the human breast for predicting large deformations. *Frontiers in Bioengineering and Biotechnology* 2015; **3(201)**:1–9.

[5] Samani A, Bishop J, Yaffe MJ, et al. Biomechanical 3-D finite element modelling of the human breast using MRI data. *IEEE Transactions on Medical Imaging* 2001; **20**:271–279.

[6] Pathmanathan P, Gavaghan D, Whiteley J, et al. Predicting tumour location by simulating large deformations of the breast using a 3-D finite element model and nonlinear elasticity. *Medical Image Computing and Computer-Assisted Intervention* 2004; **2**:217–224.

[7] Han L, Hipwell JH, Tanner C, et al. Development of patient-specific biomechanical models for predicting large breast deformation. *Physics in Medicine and Biology* 2012; **57**:455–472.

[8] Schnabel JA, Tanner C, Castellano-Smith AD, et al. Validation of nonrigid image registration using finite-element methods: application to breast MR images. *IEEE Transactions on Medical Imaging* 2003; **22**:238–247.

[9] Ruiter N, Muller T, Stotzka R, et al. Automatic image matching for breast cancer diagnostics by a 3-D deformation of the mamma. *Biomedizinische Technik* 2002; **47**:644–647.

[10] Ruiter N, Stotzka R, Muller T, et al. Model-based registration of X-ray mammograms and MR images of the female breast. *IEEE transactions on nuclear science* 2006; **53**:204–211.

[11] Hopp T, Holzapfel M, Ruiter N, et al. Registration of X-ray mammograms and three-dimensional speed of sound images of the female breast. *SPIE Proceedings* 2010; **7629**:1–9.

[12] Hopp T, Baltzer P, Dietzel M, et al. 2D/3D image fusion of X-ray mammograms with breas MRI: visualizing dynamic contrast enhacement in mammograms. *International Journal of Computed Assisted Radiology and Surgery* 2012; **7**:339–348.

[13] Hopp T, Dietzel M, Baltzer P, et al. Automatic multimodal 2D/3D breast image registration using biomechanical FEM models and intensity-based optimization. *Medical Image Analysis* 2013; **17**:209–218.

[14] Mertzanidou T, Hipwell J, Johnsen S, et al. MRI to X-ray mammography instensity-based registration with simultaneous optimisation of pose and biomechanical transformation parameters. *Medical Image Analysis* 2014; **18**:674–683.

[15] Han L, Hipwell JH, Eiben B, et al. A nonlinear biomechanical model based registration method for aligning prone and supine MR breast images. *IEEE Transactions on Medical Imaging* 2014; **33(3)**:682–694.

[16] Rajagopal V, Lee A, Chung JH, et al. Towards tracking breast cancer across medical images using subject-specific biomechanical models. *Medical Image Computing and Computer Assisted Intervention* 2007; **Part I, LNCS 4791**:651–658.

[17] Rajagopal V, Lee A, Chung JH, et al. Creating individual-specific biomechanical models of the breast for medical image analysis. *Academic Radiology* 2008; **15**:1425–1436.

[18] Pérez del Palomar A, Calvo B, Herrero J, et al. A finite element model to accurately predict real deformations of the breast. *Physics in Medicine and Biology* 2008; **30**:1089–1097.

[19] Gamage TB, Boyes R, Rajagopal V, et al. Modelling prone to supine breast deformation under gravity loading using heterogeneous finite element models. *Computational Biomechanics for Medicine, P. M. F. Nielsen, A. Wittek and K. Miller.* Springer New York, 2012; 29–38.

[20] Zain-Ul-Abdein M, Morestin F, Bouten L, et al. Numerical simulation of breast deformation under static conditions. *Cumputer Methods in Biomechanics and Biomedical Enginnering* 2013; **16(S1)**:50–51.

[21] Lapuebla-Ferri A, Pérez del Palomar A, Herrero J, et al. A patient-specific FE-based methodology to simulate prosthesis insertion during an augmentation mammoplasty. *Medical Engineering & Physics* 2011; **33**:1094–1102.

[22] Rajagopal V, Chung JH, Bullivant D, et al. Determining the finite elasticity reference state from a loaded configuration. *International Journal for numerical methods in engineering* 2007; **72**:1434–1451.

[23] Vavourakis V, Hipwell JH, Hawkes DJ. An inverse finite element u/p - formulation to predict the unloaded state of in vivo biologigal tissues. *Annals of Biomedical Engineering* 2016; **44(1)**:187–201.

[24] Samani A, Bishop J, Luginbuhl C, et al. Measuring the elastic modulus of ex vivo small tissue samples. *Physics in Medicine and Biology* 2003; **48**:2183–2198.

[25] Bostwick-III J. *Plastic and Reconstructive Surgery*. Quality Medical Publishing: Missouri,USA, 1999.

[26] Shiffman MA. *Breast Augmentation*. Springer: Leipzig, Germany, 2009.

[27] Ross MH, Pawlina W. *Histology. A text and atlas*. Lippincott Williams & Wilkins: Philadelphia, USA, 2011.

[28] Gabriel A, Maxwell GP. *Breast Embryology*. Medscape, 2015.

[29] Rosebrock A, Caban JJ, Figueroa J, et al. Quantitative analysis of TDLUs using adaptive morphological shape techniques. *Proceedings of the SPIE 8676, Medical Imaging 2013: Digital Pathology* 2013; **86760N**:doi:10.1117/12.2006 619.

[30] Hassiotou F, Geddes D. Anatomy of the human mammary gland. *Clinical Anatomy* 2013; **26**:29–48.

[31] Lee HN, Sohn Y, Han KH. Comparison of mammographic density estimation by Volpara software with radiologists' visual assessment: analysis of clinical-radiologic factors affecting discrepancy between them. *Acta Radiologica* 2015; **56 (9)**:1061–1068.

[32] van Engeland S, Snoeren PR, Huisman H, et al. Volumetric breast density estimation from full-field digital mammograms. *IEEE Transactions on Medical Imaging* 2006; **25(3)**:273–282.

[33] Lu LW, Nishino TK, Johnson RF, et al. Comparison of breast tissue measurements using magnetic resonance imaging, digital mammography and a mathematical algorithm. *Physics in Medicine and Biology* 2012; **57(21)**:6903–6927.

[34] Cancer Research UK. *http://www.cancerresearchuk.org/* accessed 30-June-2016.

[35] American Cancer Society. Breast cancer 2015.

[36] Holzapfel GA. *Nonlinear solid mechanics: A continuum approach for engineering*. Wiley: Chichester, England, 2000.

[37] Weiss JA, Maker B, Govindjee S. Finite element implementation of incompressible, transversely isotropic hyperelasticity. *Computer Methods in Applied Mechanical Engineering* 1996; **135**:107–128.

[38] Holzapfel GA, Gasser TC, Ogden RW. A new constitutive framework for arterial wall mechanics and a comparative study of materials models. *Journal of Elasticity* 2000; **61**:1–48.

[39] Chen J, Akyrus U, Xu L, et al. Stress analysis of the human temporomandibular joint. *Medical Engineering & Physics* 1998; **20**:565–572.

[40] Li Z, Alonso JE, Kim JE, et al. Three-dimensional finite element models of the human pubic symphysis with viscohyperelastic soft tissues. *Annals of Biomedical Engineering* 2006; **34(9)**:1452–1462.

[41] Samani A, Plewes D. A method to measure the hyperelastic parameters of ex vivo breast tissue samples. *Physics in Medicine and Biology* 2004; **49**:4395–4405.

[42] Rubin MB, Bodner SR. A three dimensional nonlinear model for dissipative response of soft tissue. *International Journal of Solids and Structures* 2002; **39(19)**:5081–5099.

[43] Barbarino GG, Jabareen M, Trzewik J, et al. Development and validation of a three dimensional finite element model of the face. *Journal of Biomechanical Engineering* 2009; **131**:1–11.

[44] Trabelsi O, Pérez del Palomar A, Mena-Tobar A, et al. FE simulation of human trachea swallowing movement before and after the implantation of an endoprothesis. *Applied Mathematical Modelling* 2011; **35**:4902–4912.

[45] Kiapour AM, Kaul V, Kiapour A, et al. The effect of ligament modeling technique on knee joint kinematics: a finite element study. *Applied Mathematics* 2013; **4**:91–97.

[46] Gasser TC, Ogden RW, Holzapfel GA. Hyperelastic modelling of arterial layers with distributed collagen fiber orientations. *Journal of the Royal Society Interface* 2006; **3**:15–35.

[47] Sommer G, Eder M, Kovacs L, et al. Multiaxial mechanical properties and constitutive modeling of human adipose tissue: a basis for preoperative simulations in plastic and reconstructive surgery. *Acta Biomaterialia* 2013; **9 (11)**:9036–9048.

[48] Fung YC. *Biomechanics: Mechanical properties of living tissues*. Spinger-Verlag: New York, 1993.

[49] Lanczos C. *Applied Analysis*. Prentice-Hall: New Jersey, 1956.

[50] Troyer KL, Estep DJ, Puttlitz CM. Viscoelastic effects during loading play an integral role in soft tissue mechanics. *Acta Biomaterialia* 2012; **8**:234–243.

[51] Samani A, Zubovits J, Plewes D. Elastic moduli of normal and pathological human breast tissues: an inversion-technique-based investigation of 169 samples. *Physics in Medicine and Biology* 2007; **52**:1565–1576.

[52] Linde F, Sørensen HC. The effect of different storage methods on the mechanical properties of trabecular bone. *Journal of Biomechanics* 1993; **26(10)**:1249–1252.

[53] Clavert P, Kempf JF, Bonnomet F, et al. Effects of freezing/thawing on the biomechanical properties of human tendons. *Surgical and Radiologic Anatomy* 2001; **23**:259–262.

[54] Kennedy EA, Tordonado DS, Duma SM. Effects of freezing on the mechanical properties of articular cartilage. *Biomedical Science Instrumentation* 2007; **43**:342–347.

[55] Chow MJ, Zhang Y. Changes in the mechanical and biomechanical properties of aortic tissue due to cold storage. *Journal of Surgical Research* 2011; **171**:434–442.

[56] Ternifi R, Gennisson JL, Tanter M, et al. Effects of storage temperature on the mechanical properties of porcine kidney estimated using shear wave elastography. *Journal of the Mechanical Behavior of Biomedical Materials* 2013; **28**:86–93.

[57] Kiefer GN, Sundby K, McAllister D, et al. The effect of cryopreservation on the biomechanical behaviour of bovine articular cartilage. *Journal of Orthopaedic Research* 1989; **7(4)**:494–501.

[58] Hongo M, Gray RE, Hsu JT, et al. Effect of multiple freeze-thaw cycles on intervertebral dynamics motion characteristics in the porcine lumbar spine. *Journal of Biomechanics* 2008; **41(4)**:916–920.

[59] van Haaren EH, van der Zwaard BC, van der Veen AJ, et al. Effect of long-term preservation on the mechanical properties of cortical bone. *Acta Orthopaedica* 2008; **79(5)**:708–716.

[60] Nazarian A, Hermannsson BJ, Muller J, et al. Effects of tissue preservation on murine bone mechanical properties. *Journal of Biomechanics* 2009; **42**:82–86.

[61] Szarko M, Muldrew K, Bertram JEA. Freeze-thaw treatment effects on the dynamic mechanical properties of articular cartilage. *BMC Musculoskeletal Disorders* 2010; **11**:231.

[62] Wex C, Stoll A, Fröhlich M, et al. Mechanics of fresh, frozen-thawed and heated porcine liver tissue. *International Journal of Hyperthermia* 2014; **30(4)**:271–283.

[63] Torimitsu S, Nishida Y, Takano T, et al. Effects of the freezing and thawing process on biomechanical properties of the human skull. *Legal Medicine* 2014; **16**:102–105.

[64] Wieding J, Mick E, et al AW. Influence of three different preservatives techniques on the mechanical properties of the ovine cortical bone. *Acta of Bioengineering ad Biomechanics* 2015; **17(1)**:137–146.

[65] Commisso MS, Calvo-Gallego JL, Mayo J, et al. Quasi-linear viscoelastic model of the articular disc of the temporomandibular joint. *Experimental Mechanics* 2016; :1–9.

[66] Miller-Young JE, Duncan NA, Baroud G. Material properties of the human calcaneal fat pad in compression: experiment and theory. *Journal of Biomechanics* 2002; **35**:1523–1531.

[67] Andreoli A, Monteleone M, Loan MV, et al. Effects of different sports on bone density and muscles mass in highly trained athletes. *Medicine & Science in Sports & Exercise* 2001; **33(4)**:507–511.

[68] Hunziker EB, Quinn TM, Häuselmann HJ. Quantitative structural organization of normal adult human articular cartilage. *Osteoarthritis and Cartilage* 2002; **10**:564–572.

[69] Bhosale AM, Richardson JB. Articular cartilage: structure, injuries and review of management. *British Medical Bulletin* 2008; **87**:77–95.

[70] Tanner C, Schnabel JA, Hill DLG, et al. Factors influencing the accuracy of biomechanical breast models. *Journal of Medical Physics* 2006; **33(6)**:1089–1097.

[71] Wan C, Hao Z, Wen S. A comparison of material characterizations in frequently used constitutive models of ligaments. *International Journal for Numerical Methods in Biomedical Engineering* 2014; **30**:605–615.

[72] Commisso MS, Martínez-Reina J, Mayo J, et al. Numerical simulation of a relaxation test designed to fit a quasi-linear viscoelastic model for temporomandibular joint discs. *Proceedings of the Institution of Mechanical Engineers, Part H: Journal of Engineering in Medicine* 2013; **227 (2)**:190–199.

[73] Sarvazyan A, Goukassian D, Maevsky E, et al. Elastic imaging as a new modality of medical imaging for cancer detection. *Proceedings of the International Workshop on Interaction of Ultrasound with Biological Media* 1994; :69–81.

[74] Krouskop TA, Wheeler TM, Kallel F, et al. Elastic moduli of breast and prostate tissues under compression. *Ultrason Imaging* 1998; **20**:151–159.

[75] Wellman P. *Tactile Imaging*. PhD thesis: Havard University, 1999.

[76] Lorenzen J, Sinkus R, Lorenzen M, et al. MR elastography of the breast: preliminary clinical results. *Rofo* 2002; **174(7)**:830–834.

[77] Samani A, Plewes D. An inverse problem solution for measuring the elastic modulus of intact ex vivo breast tissue tumours. *Physics in Medicine and Biology* 2007; **52**:1247–1260.

[78] O'Hagan J, Samani A. Measurement of the hyperelastic properties of tissue slices with tumour inclusion. *Physics in Medicine and Biology* 2008; **53**:7087–7106.

[79] O'Hagan J, Samani A. Measurement of the hyperelastic properties of 44 pathological ex vivo breast tissue samples. *Physics in Medicine and Biology* 2009; **54**:2557–2569.

[80] Escoffier C, Rigal J, Rochefort A, et al. Age-related mechanical properties of human skin: an in vivo study. *Journal of Investigative Dermatology* 1989; **93(3)**:353–357.

[81] Serup J, Jemec GBE, Grove GL. *Handbook of non-invasive methods and the skin*. CRC Press: Florida, 2006.

[82] Jemec GB, Jemec B, Jemec BL, et al. The effect of superficial hydration on the mechanical properties of human skin in vivo: implications for plastic surgery. *Plastic and Reconstructive Surgery* 1990; **85(1)**:100–103.

[83] Veronda DR, Westmann RA. Mechanical characterization of skin-finite deformations. *Journal of Biomechanics* 1970; **3**:111–124.

[84] Agache PG, Monneur C, Leveque JL, et al. Mechanical properties and Young's modulus of human skin in vivo. *Archives of Dermatological Research* 1980; **269**:221–232.

[85] Bischoff JE, Arruda EM, Grosh K. Finite element modeling of human skin using an isotropic, nonlinear elastic constitutive model. *Journal of Biomechanics* 2000; **33**:645–652.

[86] Gambarotta L, Massabo R, Morbiducci R, et al. In vivo experimental testing and model of human scalp skin. *Journal of Biomechanics* 2005; **38**:2237–2247.

[87] Delalleau A, Josse G, Lagarde JM, et al. A nonlinear elastic behaviour to identify the mechanical parameters of human skin in vivo. *Skin Research and Technology* 2008; **14**:152–164.

[88] Annaidh AN, Bruyère K, Desdrade M, et al. Characterization of the anisotropic mechanical properties of excised human skin. *Journal of the Mechanical Behaviour of Biomedical Materials* 2012; **5**:139–148.

[89] Sutradhar A, Miller MJ. In vivo measurements of breast skin elasticity and breast skin thickness. *Skin Research and Technology* 2013; **19**:191–199.

[90] Khatam H, Reece GP, Fingeret MC, et al. In-vivo quantification of human breast deformation associated with the position change from supine to upright. *Medical Engineering & Physics* 2015; **37**:13–22.

[91] Ohl SW, Klaseboer E, Khoo BC. The dynamics of a non-equilibrium bubble near bio-materials. *Physics in Medicine and Biology* 2009; **54**:6313–6336.

[92] Riggio E, Quattrone P, Nava M. Anatomical study of the breast superficial system: the inframmamary fold unit. *European Journal of Plastic Surgery* 2000; **23**:310–315.

[93] Jinde L, Jianliang S, Xiaoping C, et al. Anatomy and clinical significance of pectoral fascia. *Plastic and Reconstructive Surgery* 2006; **118(7)**:1557–1560.

[94] Cardoso A, Santos D, Martins J, et al. Breast ligaments: an anatomical study. *European Journal of Plastic Surgery* 2015; **38**:91–96.

[95] Gefen A, Dilmoney B. Mechanics of the normal woman's breast. *Technology and Health Care* 2007; **15**:259–271.

[96] Trelease RB. *Netter's surgical Anatomy Review*. Elsevier, 2010.

[97] Kapur T, Grimson WEL, Wels-III WM, et al. Segmentation of brain tissue from magnetic resonance images. *Medical Image Analysis* 1996; **1, 2**:109–127.

[98] Kuhlmann M, Fear EC, Ramirez-Serrano A, et al. Mechanical model of the breast for the prediction of deformation during imaging. *Medical Engineering & Physics* 2013; **35**:470–478.

[99] Roose L, Maerteleire WD, Mollemans W, et al. Validation of different soft tissue simulation methods for breast augmentation. *International Congress Series* 2005; **1281**:485–490.

[100] Azar FS, Metaxas DN, Schnall MD. Methods for modelling and predicting mechanical deformations of the breast under external perturbations. *Medical Image Analysis* 2002; **6**:1–27.

[101] Temizer I, Zohdi TI. A numerical method for homogenization in non linear elasticity. *Computational Mechanics* 2007; **40**:281–298.

[102] Li X, Liu B. Quantifying breast density with a cone-beam breast CT. *Proceedings of the SPIE. Medical Imaging 2010: Physics of Medical Imaging* 2010; **7622, 762245**:1–11.

[103] Lee NA, Rusinek H, Weinreb J, et al. Fatty and fibroglandular tissue volumes in the breasts of women 20-83 years old: Comparison of X-Ray mammography and computer assisted MR imaging. *American Journal of Roentgenology* 1997; **168**:501–506.

[104] Tromans C, Brady M. An alternative approach to measuring volumetric mammographic breast density. *Proceedings of the 8th International Workshop on Digital Mammography, IWDM* 2006; :26–33.

[105] Hartmann S. Parameter estimation of hyperelasticity relations of generalized polynomial-type with constraint conditions. *International Journal of Solids and Structures* 2001; **38**:7999–8018.

[106] Hartmann S. Polyconvexity of generalized polynomial-type hyperelastic strain energy funtions for near-incompressibility. *International Journal of Solids and Structures* 2003; **40**:2767–2791.

[107] Calvo-Gallego JL, Martínez-Reina J, Domínguez J. A polynomial hyperelastic model for the mixture of fat and glandular tissue in the female breast. *International Journal for numerical methods in biomedical engineering* 2015; **31(9)**.

[108] Allen KD, Athanasiou KA. Viscoelastic characterization of the porcine temporomandibular joint disc under unconfined compression. *Journal of Biomechanics* 2006; **39**(5):312–322.

[109] Rashid B, Destrade M, Gilchrist MD. Mechanical characterization of brain tissue in compression at dynamic strain rates. *Journal of the Mechanical Behaviour of Biomedical Materials* 2012; **10**:23–38.

[110] Carew EO, Talman EA, Boughner DR, et al. Quasi-linear viscoelastic theory applied to internal shearing of porcine aortic valve leaflets. *Journal of Biomechanical Engineering* 1999; **121**:386–392.

[111] Drapaca CS, Tenti G, Rohlf K, et al. A quasi-linear viscoelastic constitutive equation for the brain: application to hydrocephalus. *Journal of Elasticity* 2006; **85**:65–83.

[112] Woo SLY, Simon B, Kuej SC, et al. Quasi-linear viscoelastic properties of normal cartilage. *Journal of Biomechanical Engineering* 1980; **102**:85–90.

[113] Lamela MJ, Prado Y, Fernandez P, et al. Non-linear viscoelastic model for behavior characterization of temporomandibular joint discs. *Experimental Mechanics* 2011; **51**:1453–1440.

[114] Koolstra JH, Tanaka E, van Eijden TMGJ. Viscoelastic material model for the temporomandibular joint disc derived from dynamic shear test or strain relaxation tests. *Journal of Biomechanics* 2007; **40**:2330–2334.

[115] Holzapfel GA, Gasser TC. A viscoelastic model for fiber-reinforced composites at finite strains: continuum basis, computational aspects and applications. *Computer Methods in Applied Mechanics and Engineering* 2001; **190**:4379–4403.

[116] Cardoso de Oliveira IR, Ferreira DF. Multivariate extension of chi-squared univariate normality test. *Journal of Statistical Computation and Simulation* 2010; **80(5)**:513–526.

[117] Katz BM, McSweeney M. A multivariate Kruskal-Wallis test with post-hoc procedures. *Multivariate Behavioral Research* 1980; **15**:281–297.

[118] Hair JF, Tatham RL, et al REA. *Multivariate Data Analysis*. Prentice Hall: New Jersey, 1998.

[119] Dillon WR, Goldstein M. *Multivariate analysis. Methods and applications*. John Wiley & Sons: USA, 1984.

[120] Riveros F, Chandra S, Finol EA, et al. A pull-back algorithm to determine the unloaded vascular geometry in anisotropic hyperelastic AAA pasive mechanics. *Annals of Biomedical Engineering* 2013; **41(4)**:694–708.

[121] Lask GP, Lee PK, Seyfzadeh M, et al. Nonablative laser treatment of facial rhytides. *Proceedings of the SPIE. Lasers in Surgery: Advanced Characterization, Therapeutics and Systems VII* 1997; **2970**:338–348.

[122] Huang S, Boone JM, Yang K, et al. The effect of skin thickness determined using breast CT on mammographic dosimetry. *Medical Physics* 2008; **35(4)**:1199–1206.

[123] Willson SA, Adam EJ, Tucker AK. Patterns of breast skin thickness in normal mammograms. *Clinical Radiology* 1982; **33**:691–693.

[124] Barbarino GG, Jabareen M, Mazza E. Experimental and numerical study on the mechanical behaviour of the superficial layers of the face. *Skin Research and Technology* 2011; **17**:434–444.

[125] Ward SR, Lieber RL. Density and hydration of fresh and fixed human skeletal muscle. *Journal of Biomechanics* 2005; **38**:2317–2320.

[126] Langer K. On the anatomy and physiology of the skin I. the cleavability of the cutis. *British Journal of Plastic Surgery* 1978; **31**:3–8.

[127] Zanon E, Harpf C. Skin cleavage lines of the female breast. *European Journal of Plastic Surgery* 1993; **16**:276–279.

[128] Evans SL, Holt CA. Measuring the mechanical properties of human skin in vivo using digital image correlation and finite element modelling. *The Journal of Stress Analysis for Engineering Design* 2009; **44 (5)**:337–345.

[129] Tepole AB, Gart M, Gosain AK, et al. Characterization of living skin using multi-view stereo and isogeometric analysis. *Acta Biomaterialia* 2014; **10**:4822–4831.

[130] Alexander H, Cook TH. Accounting for natural tension in the mechanical testing of human skin. *The Journal of Investigative Dermatology* 1977; **69**:310–314.

[131] Flynn C, Taberner A, Nielsen P. Modeling the mechanical response of in vivo human skin under a rich set of deformations. *Annals of Biomedical Engineering* 2011; **39 (7)**:1935–1946.

[132] Flynn C, Taberner A, Nielsen P. Mechanical characterisation of in vivo human skin using a 3D force-sensitive micro-robot and finite element analysis. *Biomechanics and Modelling in Mechanobiology* 2011; **10**:27–38.

[133] Diridollou S, Patat F, Gens F, et al. In vivo model of the mechanical properties of the human skin under suction. *Skin Research and Technology* 2000; **6**:214–221.

[134] Holzapfel GA, Ogden RW. *Mechanics of Biological Tissue*. Springer-Verlag: Berlin, 2006.

[135] Kuhl E, Holzapfel GA. A continuum model for remodeling in living structures. *Journal of Materials Science* 2007; **42**:8811–8823.

[136] Robling AG, Turner CH. Mechanical signaling for bone modeling and remodeling. *Critical Reviews in Eukaryotic Gene Expression* 2009; **19(4)**:319–338.

[137] Voycheck CA, Luu K, McMahon PJ, et al. Collagen fiber alignment and maximum principal strain in the glenohumeral capsule predict location of failure during uniaxial extension. *Biomechanics and Modeling in Mechanobiology* 2014; **13**:379–385.